Czech Technical University in Prague

Faculty of Electrical Engineering
Department of Electrical Power Engineering

INFLUENCE OF SUPRAHARMONICS ON AGING RATE OF POLYMERIC INSULATION MATERIALS

Doctoral Thesis

Ondřej Šefl

Prague, December 2021

Ph.D. Programme: (P2612) Electrical Engineering and Information Technology
Branch of study: (3907V001) Electric Power Engineering

Supervisor: Radek Procházka

Honour statement

I declare that I have written my dissertation thesis independently and consistently quoted the sources in the submitted work.

Ondřej Šefl

Acknowledgments

First and foremost, I wish to express my gratitude to my supervisor, esteemed colleague, and good friend Radek Procházka for the guidance during my Ph.D. studies, as well as for the “extracurricular” activities we have undertaken over the years.

I would also like to thank my family, and colleagues from the High-Voltage Laboratory and Department of Electrotechnology of FEE CTU for the unwavering support I have received over the years.

Außerdem würde ich mich gerne bei Professor Gareth J. Monkman und Professor Rainer Haller für meinen Studienaufenthalt an der OTH Regensburg bedanken.

Abstract

Pollution of electrical power systems by harmonics in the frequency range between ca. 2 to 150 kHz (supraharmonics) is becoming ever more significant in the context of the rising number of large power converters in power networks. In particular, significant distortion of the network voltage waveform can be expected in the vicinity of large renewable power sources, as they need to be supplemented by said power converters, typically of enormous installed powers. These converters can give rise to supraharmonics through resonances with local passive components or by so-called ringing distortions. Naturally, the presence of supraharmonics is partially resolved through power quality standards, but due to the distortion type's relative novelty, both the limits and measurement methods prescribed by these standards are lacking.

Concerning supraharmonics' impacts, most of the respective research works dealt with their influences on devices in low-voltage (LV) networks, especially so on the reliability of the devices' operation. Little to no attention has been paid to the supraharmonics' effects on insulation system longevity, primarily due to the lesser importance of insulation in the case of LV applications. However, supraharmonics can also propagate from the LV output side of renewable power stations' converters into the adjacent medium-voltage (MV) networks (such as off-shore wind park or photovoltaic power station interconnections). In such networks, the insulation constitutes a significant and costly part of the system, and its enhanced degradation is thus of concern.

Therefore, this dissertation strived to shed light on the issue by performing three different experiments related to the degradation of the relevant MV systems. First, long-term aging of 22-kV MV cable termination specimens was carried using reference sinusoidal electrical stress and equivalent supraharmonic-distorted electrical stress. Two out of three specimens broke down prematurely under the latter stress, while all the specimens stressed by the sinusoidal waveform withstood. The accompanying measurements (partial discharges, loss tangent, breakdown tests) also implied that the distorted waveform degrades the specimens faster.

The second experiment investigated the effect of supraharmonics on the aging rate of the main MV cable insulation, represented by thin-film unmodified cross-linked polyethylene (XLPE) specimens and nano-alumina-XLPE nanocomposite specimens of different filling percentages. Similarly, long-term electrical aging tests were carried out under sinusoidal and supraharmonic-distorted waveforms, and their results were analyzed using Weibull statistics and aging models. Likewise, an increased degradation effect of the distorted waveform was identified.

Ultimately, the third experiment aimed to analyze the impact of supraharmonics on partial discharge activity using an artificial cavity specimen. Various voltage waveforms containing a single-per-period oscillation in the supraharmonic range were applied to the test specimen, and the occurring discharge activity was recorded. An analytical PD model was constructed for the purpose of the study and subsequently employed to simulate discharge activity under identical conditions. The changes observed in the phase-resolved partial discharge (PRPD) patterns of both measured and modeled data were explained using the model. The experiment also concluded that supraharmonics could amplify the discharge activity and thus theoretically degrade the insulation systems faster.

Keywords

supraharmonics, electrical insulation degradation, aging, partial discharges, XLPE

Anotace (in Czech)

V souvislosti s rostoucím počtem velkých výkonových měničů v energetických soustavách se stává tématika znečištění síťových napětí harmonickými v rozsahu frekvencí od cca 2 do 150 kHz (tzv. supraharmonické) stále významnější. Zejména v blízkosti velkých obnovitelných zdrojů energie (OZE) lze očekávat výrazné zkreslení průběhu síťového napětí, jelikož je zapotřebí tyto zdroje doplnit zmíněnými měniči, často o enormních instalovaných výkonech. Tyto měniče mohou způsobovat supraharmonické zkreslení napětí prostřednictvím rezonancí s místními pasivními součástkami nebo tzv. „ringing distortion“. Přítomnost supraharmonických je samozřejmě částečně řešena normami kvality elektrické energie, ale vzhledem k relativní novosti tohoto typu zkreslení jsou jak limity, tak metody měření předepsané těmito normami neuspokojivé.

Co se týká dopadů supraharmonických zkreslení, většina příslušných vědeckých prací se zabývala pouze jejich vlivem na zařízení v sítích nízkého napětí (NN), zejména pak na spolehlivost provozu těchto zařízení. Vlivu supraharmonických na životnost izolačních systémů nebyla věnována téměř žádná pozornost, a to především z důvodu menšího významu izolace v případě NN aplikací. Supraharmonické se však mohou šířit i z NN výstupní strany měničů elektráren na principu OZE do přilehlých sítí vysokého napětí (VN) (např. propojení off-shore větrných parků nebo fotovoltaických elektráren). V takovýchto VN sítích představuje izolace významnou a nákladnou součást celého systému, a proto by byla její zrychlená degradace pádným důvodem ke znepokojení.

Tato disertační práce měla tudíž za cíl tuto problematiku částečně probádat provedením tří různých experimentů týkajících se degradace příslušných systémů VN. Nejprve bylo provedeno dlouhodobé stárnutí vzorků koncovek VN kabelů (22 kV) pomocí referenčního sinusového elektrického napětí a ekvivalentního elektrického napětí se supraharmonickým zkreslením. Dva ze tří vzorků předčasně selhaly při zkresleném namáhání, zatímco všechny vzorky namáhané sinusovým průběhem vydržely. Z doprovodných měření (částečné výboje, ztrátový tangens, průrazové zkoušky) rovněž vyplynulo, že zkreslený průběh degraduje vzorky rychleji.

Druhý experiment zkoumal vliv supraharmonických na rychlost stárnutí hlavní izolace VN kabelů, jež byly reprezentovány tenkovrstvými vzorky (fóliemi) z nemodifikovaného zesíťovaného polyethylenu (XLPE) a vzorky z nanokompozitu nano-alumina-XLPE s různým procentem plnění. Podobně jako předtím byly provedeny zkoušky dlouhodobého elektrického stárnutí při sinusových a supraharmonicky zkreslených průbězích a jejich výsledky byly analyzovány pomocí Weibullovy statistiky a modelů stárnutí. I v tomto případě byl identifikován zvýšený degradační účinek zkresleného průběhu.

Třetí experiment byl nakonec zaměřen na analýzu vlivu supraharmonických na výbojovou činnost pomocí vzorku s umělou dutinou. Na zkušební vzorek byly aplikovány různé průběhy napětí obsahující jeden kmit (za periodu základního napětí) o supraharmonickém frekvenci a probíhající výbojová aktivita byla zaznamenána. Pro účely studie byl sestaven analytický model PD, který byl následně použit k simulaci výbojové aktivity za stejných podmínek. Změny pozorované ve fázově rozlišených obrazcích částečných výbojů (PRPD patterns) naměřených i modelovaných dat byly vysvětleny pomocí modelu. Z experimentu také vyplynulo, že supraharmonické mohou zesilovat výbojovou aktivitu, a tím teoreticky zrychlit degradovat izolačních systémů.

Klíčová slova

supraharmonické, degradace elektroizolačních materiálů, stárnutí, částečné výboje, XLPE

List of Publications

Pertaining to the topic of the thesis

The doctoral thesis was primarily based on the following works:

First-authored journal publications

[1] O. Sefl and R. Prochazka, "Investigation of supraharmonics' influence on partial discharge activity using an internal cavity sample," *International Journal of Electrical Power & Energy Systems*, vol. 134, pp. 1–10, 2022

Co-authored journal publications

[2] M. Knenicky, R. Prochazka, J. Hlavacek, and O. Sefl, "Impact of high-frequency voltage distortion emitted by large photovoltaic power plant on medium voltage cable systems," *IEEE Transactions on Power Delivery*, vol. 36, no. 3, pp. 1882–1891, 2021

"" Ángela Espín-Delgado, S. Rönnberg, S. S. Letha, and M. Bollen, "Diagnosis of supraharmonics-related problems based on the effects on electrical equipment," *Electric Power Systems Research*, vol. 195, 2021

First-authored conference proceedings

[3] O. Sefl and R. Prochazka, "Study on aging rate of XLPE and its nanocomposites under nonstandard voltage stresses." Submitted to IEEE Conference on Electrical Insulation and Dielectric Phenomena 2021

[4] O. Sefl and R. Prochazka, "XLPE ageing under non-standard voltage stresses," in *Proceedings of the 10th International Scientific Symposium on Electrical Power Engineering, ELEKTROENERGETIKA 2019*, (Stara Lesna, Slovakia), pp. 521–524, Technical University of Kosice, 2019

[5] O. Sefl, M. Knenicky, and R. Prochazka, "Life-time of oil filled insulation paper under nonstandard voltage stresses," in *2018 International Conference on Diagnostics in Electrical Engineering (Diagnostika)*, (Prague, CZ), Czechoslovakia Section IEEE, 2018

Co-authored conference proceedings

[6] R. Prochazka and O. Sefl, "Influence of voltage distortion shape on partial discharge activity in internal voids," in *2020 International Conference on Diagnostics in Electrical Engineering (Diagnostika)*, (Pilsen, Czech Republic), pp. 1–4, IEEE, 2020

[7] R. Prochazka and O. Sefl, "Simulation model of partial discharges in internal void," in *Proceedings of the 10th International Scientific Symposium on Electrical Power Engineering, ELEKTROENERGETIKA 2019*, (Stara Lesna, Slovakia), pp. 202–206, Technical University of Kosice, 2019

[8] R. Prochazka, O. Sefl, and M. Knenicky, "Partial discharges activity within an internal void at AC voltage disturbed by high frequency components," in *Proceedings of 2018 IEEE International Conference on High Voltage Engineering and Application*, (Divani Caravel Hotel,Athens), IEEE (Institute of Electrical and Electronics Engineers), 2018

[9] M. Knenicky, R. Prochazka, and O. Sefl, "Influence of nonstandard voltage stresses on transformer insulation paper," in *Proceedings of 2017 IEEE Conference on Electrical Insulation and Dielectric Phenomena*, (Piscataway, US), IEEE, 2017

"" D. Feng, L. Yang, R. Liao, L. Zhou, and Y. Lin, "Effect of moisture content on the production and partitioning of furfural in oil-paper insulation," *IEEE Transactions on Dielectrics and Electrical Insulation*, vol. 25, no. 6, pp. 2389–2397, 2018

First-authored other publications

[10] O. Sefl, "Aging of insulation materials under nonstandard voltage stresses," 2017

Other works

Co-authored journal publications

- T. Tichy, O. Sefl, P. Vesely, K. Dusek, and D. Busek, "Mathematical modelling of temperature distribution in selected parts of FFF printer during 3D printing process," *Polymers*, vol. 13, 12 2021

Co-authored peer-reviewed articles

- P. Vesely, T. Tichy, O. Sefl, and E. Horynova, "Evaluation of dielectric properties of 3D printed objects based on printing resolution," *IOP Conference Series: Materials Science and Engineering*, vol. 461, December 2018

  "" 5 citations

First-authored conference proceedings

- O. Sefl, R. Prochazka, R. Haller, and G. J. Monkman, "Alternative approach to optical detection of partial discharges in air." Submitted to IEEE Conference on Electrical Insulation and Dielectric Phenomena 2021
- O. Sefl, P. Vesely, J. Minar, and K. Dusek, "Novel electrical insulation materials - photodegradation endurance of 3D printed polylactic acid," in *2020 International Conference on Diagnostics in Electrical Engineering (Diagnostika)*, (Plzen), Institute of Electrical and Electronics Engineers, Inc., 2020

Co-authored conference proceedings

- J. Minar, J. Pulpan, P. Vesely, O. Sefl, and K. Dusek, "Electrical properties of photopolymers for 3D printing," in *2021 44th International Spring Seminar on Electronics Technology (ISSE)*, International Spring Seminar on Electronics Technology (ISSE), (New York, US), IEEE Press, 2021
- P. Vesely, J. Minar, A. Prazanova, O. Sefl, and K. Dusek, "Novel electrical insulation materials – mechanical performance of 3D printed polylactic acid," in *2020 International Conference on Diagnostics in Electrical Engineering (Diagnostika)*, (Plzen), Institute of Electrical and Electronics Engineers, Inc., 2020
- T. Tichy, O. Sefl, P. Vesely, and T. Capal, "Application possibilities of fused filament fabrication technology for high-voltage and medium-voltage insulation systems," in *2019 42nd International Spring Seminar on Electronics Technology (ISSE)*, International Spring Seminar on Electronics Technology ISSE, (New York, US), IEEE Press, 2019

  "" 3 citations

First-authored other publications

- O. Sefl, "Design of high voltage transformer for use in electrostatic precipitator," in *Proceedings of the International Student Scientific Conference Poster – 22/2018*, (Praha, CZ), Czech Technical University in Prague, 2018

Co-authored other publications

- P. Vesely, E. Horynova, T. Tichy, and O. Sefl, "Study of electrical properties of 3D printed objects," in *Proceedings of the International Student Scientific Conference Poster – 22/2018*, (Praha, CZ), Czech Technical University in Prague, 2018

Abbreviations

AEF	Active electro-magnetic interference (EMI) filter
APF	Active power filtering
APFC	Active power-factor-correction
ATF	Active trap filtering
DC	Direct current
EGR	Electron generation rate
EHV	Extra-high voltage
EMC	Electromagnetic compatibility
EMI	Electromagnetic interference
EN	European standard
EP	Epoxy resin
EPR	Ethylene-propylene rubber
FACTS	Flexible alternating current transmission system
FEM	Finite element method
FTIR	Fourier-transform infrared spectroscopy
GPIB	General purpose interface bus
HDPE	High-density polyethylene
HV	High voltage
HVDC	High-voltage direct current
IEC	International electrotechnical commission
IEEE	Institute of electrical and electronics engineers
IGBT	Insulated-gate bipolar transistor
IPL	Inverse power law
LCC	Line-commutated converter
LDPE	Low-density polyethylene
LHS/RHS	Left-hand side / right-hand side
LLDE	Linear low-density polyethylene
MOSFET	Metal-oxide-semiconductor field-effect transistor
MTTF	Mean time to failure
MV	Medium voltage
OIP	Oil impregnated paper
PD(s)	Partial discharge(s)
PDEV	Partial discharge extinction voltage
PDIV	Partial discharge inception voltage
PE	Polyethylene
PET	Polyethylene terephthalate
PETG	Polyethylene terephthalate glycol
PFC	Power-factor corrector/-correction
PLC	Power line communication
PMMA	Poly(methyl methacrylate)
PTFE	Polytetrafluorethylene
PV	Photovoltaic
PWM	Pulse-width modulation
RMS	Root mean square
RPWM	Random pulse-width modulation
SC	(Superposed) supraharmonic components
THD	Total harmonic distortion
TSC	Thermally stimulated current
VLF	Very low frequency
VSC	Voltage-sourced converter
VSI	Voltage-sourced inverter
XLPE	Cross-linked polyethylene

Contents

Introduction

Context

The recent rapid deployment of renewable power stations brings about numerous issues in power networks. While most of the issues are related to the reduced reliability of power delivery, there are also concerns regarding power quality. Since the fundamental types of renewable power stations, such as photovoltaic and wind, cannot directly produce electric power at the network frequency (50 or 60 Hz), they need to be provided with appropriate power converters. Typically, PWM three-phase full-bridge converters are employed for this purpose.

It is well documented that such converters produce harmonic distortions at orders according to the employed number of pulses [11]. Since the magnitude of these harmonics is inversely proportional to their order, they are addressed explicitly by power quality standards only to a particular order, namely the 25^{th} by EN 50160, 40^{th} by IEC 61000-3-2, and the 50^{th} by IEEE Std. 519. However, the transistors (chiefly IGBT, but also MOSFET) employed for converter switching also produce harmonic distortions around their switching frequency and its integer multiples. Usually, these harmonics are negligible, but recently, it has been suggested that they can be magnified and spread through resonances with passive network components and by secondary emissions from other devices [12,13]. Furthermore, the regulation scheme of the converter can give rise to other harmonics well above the standard orders via so-called ringing distortions [14].

Concerning the frequency range of these specific harmonics, their lower limit is generally regarded to be the 40^{th} order (per IEC standard), and their upper limit the $3{,}000^{\text{th}}$ harmonic order. As a result, they are referred to as either "low-frequency emission" (per IEEE EMC society, standard electromagnetic emission is ca. 150 kHz and higher, hence the "low-frequency" prefix), or "supraharmonics" (placed "above" the standard harmonic orders) [15, 16]. Figure 1 illustrates the relation of the supraharmonics to their counterparts, both in terms of frequency and typical sources.

Even though numerous problems of varying severities have already been attributed to supraharmon-

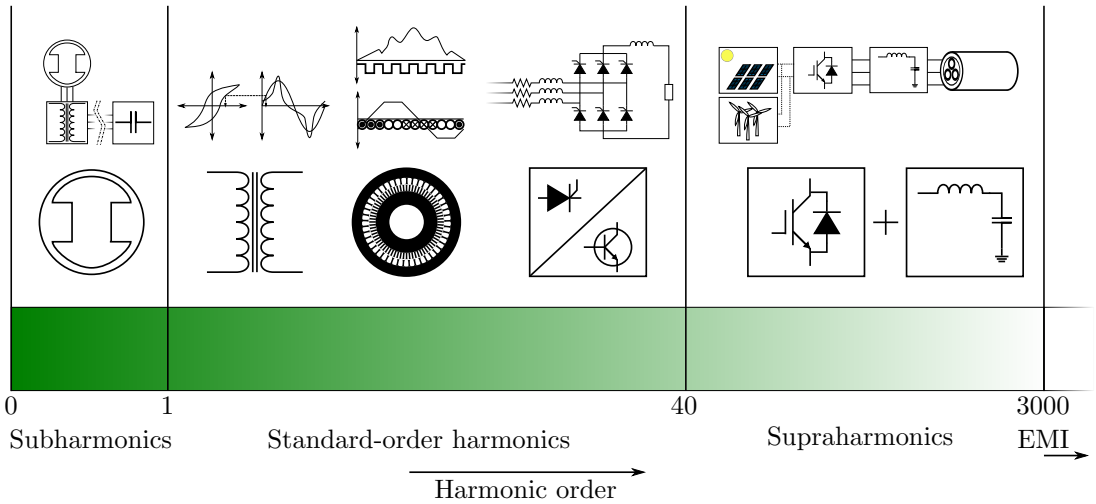

Figure 1: An overview of typical categories and sources of harmonics in power systems.

ics [16], standards have not yet been satisfactorily adjusted to address these relatively new phenomena. Obviously, that does not mean that there are no limitations, but the main issue is that supraharmonics are treated as general components, and the limits are not suited according to their impacts. Some attempts to remedy that have been made, for instance, the 2018 update of the electromagnetic compatibility standard IEC 61000-2-2:2002; however, the standard concerns only low-voltage power supply systems, and the update dealt with the supraharmonic content solely up to 30 kHz, while it ignored the higher supraharmonic orders. In addition to the unsatisfactory regulation, the actual measurement of harmonics in the supraharmonic range is not a common practice in the industry, and the methods defined in power quality standards are also lacking in this regard [17].

The above should alone imply that there is a significant gap in knowledge concerning supraharmonics. Perhaps even more poorly understood is their long-term impact on insulation of power systems, mainly due to the novelty of the topic and the long time the effects typically take to manifest. Nonetheless, the theory dictates that higher harmonic orders (frequencies), such as supraharmonics, can substantially amplify the dielectric losses and lead to uneven field distribution in non-linear stress grading materials. Short-term effects have also been proven experimentally, for instance, in the investigation of premature failures of medium-voltage (MV) cable terminations of power converter stations in [18]. Other than that, numerous indications of accelerated degradation due to effects similar to supraharmonics have also been observed (see sections 2.2.5 and 2.3.4).

However, the actual impacts of supraharmonics on insulation systems have not been thoroughly researched, despite the hints at their severity. Since substantial safety, reliability, and economic impacts are connected with unexpected premature failures of insulation systems, this thesis aims to address the said gap in knowledge and hopefully provide an incentive for further research of the issue. Due to the prevalence of the lower supraharmonic frequencies (units of kilohertz) observed in power systems [16], the work is focused primarily on these orders.

Outline of the thesis

Chapter 1 reviews the available knowledge concerning the topic of supraharmonics. Their origin as well as propagation into other parts of networks are explained, and the applicable filtering methods to combat them are listed.

Chapter 2 summarizes theoretical concepts pertinent to the phenomenon of breakdown in solid insulation materials, particularly regarding the long-term degradation of insulation systems. The main focus is paid to the electrochemical breakdown (*aging*) and erosion breakdown (*partial discharges*). The former also provides the theoretical background to the experimental part of the thesis by specifying the methodology of aging test evaluation and several chosen aging models. Analogously, due to their role in the respective experiment, the partial discharge (PD) section describes the specifics of internal cavity discharges and lists the fundamental operating principles of partial discharge models. Both sections include a literature review of the impacts of higher-frequency oscillations or impulses on the respective phenomenon, i.e., intrinsic aging or partial discharges. Ultimately, attention is paid to polyethylene-based insulation and its nanocomposites, as they also figure in the experiments.

Chapter 3 is based on publication [2], and describes the long-term combined aging experiment performed on cable termination specimens. Test station configuration and aging test parameters are presented, and the results obtained from accompanying loss tangent, partial discharge, and short-term breakdown tests and measurements are discussed. Experimental evidence for substantially accelerated aging of cable terminations under supraharmonic-polluted voltage waveforms was obtained.

Chapter 4 is based on publications [3–5, 9, 10], and describes the long-term electrical aging experiment performed on base and nano-alumina-filled cross-linked polyethylene (XLPE) film specimens. Similarly, test station configuration and aging test parameters are given. The obtained results were treated using Weibull statistics, and the resulting aging data were fitted by aging models. These aging models also indicated accelerated aging under supraharmonic-polluted waveforms, albeit to a smaller degree than in the previous experiment. Furthermore, the employed 5wt% alumina-XLPE nanocomposite showed better insulation performance than the unmodified material.

Chapter 5 is based on publications [1, 6–8], and describes the partial discharge experiment performed on 3D-printed test specimens with a single, spherical internal cavity. Test station, specimen preparation method, and the employed voltage waveforms are described. The analytical PD model constructed for

the investigation of changes in PD activity due to the presence of a supraharmonic oscillation is mentioned next. Both the experimentally measured and modeled results are discussed afterward. Increased discharge activity and possible stimuli for accelerated degradation were identified for several waveforms that contained supraharmonic oscillations.

Chapter 1

Supraharmonics

1.1 Origin & fundamental filtering methods

1.1.1 Power converter switching harmonics and their suppression

Power generation that does not utilize power-frequency synchronous generators (such as from solar or wind energy) needs to be supplemented with power converters that can transform the generated power to conform to the power quality standards. The conversion is principally achieved through high-power voltage source inverters (VSIs; eventually converters – VSCs), which also find use in pulse-width modulation (PWM) controls of AC motor drives. The VSIs, however, significantly pollute the output current with harmonics of two types – low-order ones from the distorted network voltage and those originating from the switching of the converter (switching harmonics). The latter is typically in the range of units of kHz up to 20 kHz (per the employed IGBTs), i.e., in the supraharmonic range [19].

Both types of distortions can be suppressed by *LCL* / *LLCL* filters passively or by active power filtering (APF) and active trap filtering (ATF) actively; a combination of the two is preferred in most cases [19,20]. Figure 1.1 shows two examples of the filtering methods: an inductance-capacitance-inductance (*LCL*) passive filter connected to the output of a VSI and a hybrid power conversion system that combines a line-commutated converter (LCC) with active filtering by an auxiliary VSI.

The simplest passive filter is a filtering inductor of suitable inductance for suppression of the network current distortions. However, such a configuration tends to be costly due to the considerable size of the inductor. One alternative is an *LCL* filter, shown in Figure 1.2a, which can suppress higher-frequency oscillations (supraharmonics) from the switching processes even better. On the other hand, strong resonances might occur in the system due to the combination of large capacitive and inductive components [20]. An additional resonance inductor can be added in the capacitor branch to form an *LLCL* filter (Figure 1.2b). This inductor filters out the switching-frequency harmonic components at the cost of reduced attenuation at higher frequencies. Because of the reduced attenuation, harmonics at low integer multiples of the switching frequency are often insufficiently suppressed [21]. The advantages of the two

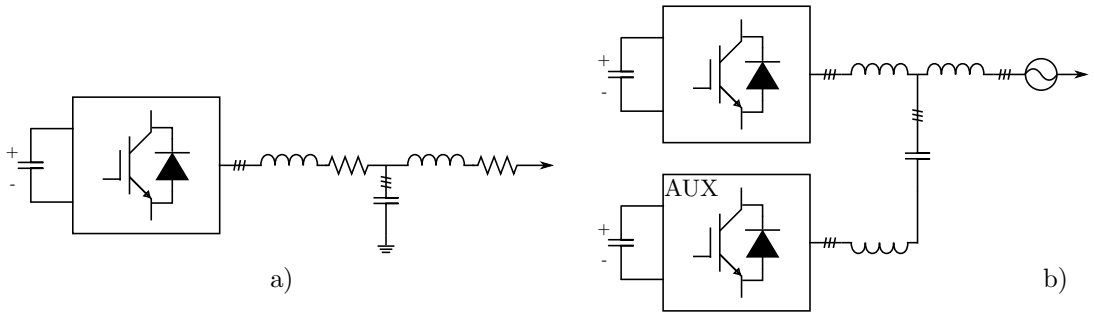

Figure 1.1: A VSI with an *LCL* filter at its output (a); hybrid power conversion system composed of an LCC and an active filter, i.e., an auxiliary (AUX) VSI (b).

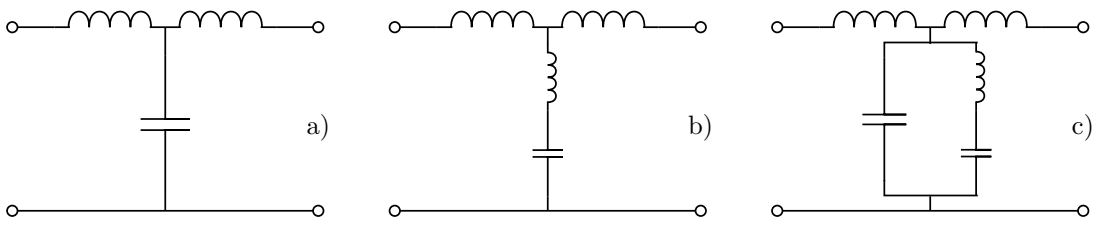

Figure 1.2: Fundamental low-order / switching harmonic filter types: *LCL* (a), *LLCL* (b), and *LCL-LC* (c).

filter types (*LCL* and *LLCL*) can be combined in a so-called *LCL-LC* filter (Figure 1.2c). Therein, a series connection of a filtering inductor and capacitor is placed in parallel to the original capacitor of an *LCL* filter.

Shunt damping resistors can be added to an *LCL* filter to reduce the damping losses and improve the high-frequency attenuation. A branch consisting of one such resistor and a blocking capacitor can be connected in series to the filtering capacitor to increase the attenuation further. The *LLCL*-type filter serves as a passive trap (minimal impedance at given frequencies) due to the resonance between the components. Analogously, a shunt resistor, or its combination with a blocking capacitor, can be added to improve the filter's parameters. Multiple branches of filtering inductor-capacitor series connections may be used to form a multitoned passive trap filter. When designed correctly, such a filter strongly attenuates both the low-order harmonics and the harmonics at multiples of the switching frequency [22]. The actual choice of a filter type depends on the intended use and, naturally, on the cost of the implementation.

Filtering of low-order and switching harmonics can be carried out actively by the APF and ATF techniques. Both methods can be employed if the configuration shown in Figure 1.1b is present, but each filtering method requires its own control loop.

The APF technique serves primarily to suppress the low-order harmonics. Its operating principle is based on the creation of an opposite-polarity (180° phase shift) compensation current that is injected into the line, where it cancels out the unwanted harmonic content [23]. This technique also finds use, for example, as an alternative to the well-established hybrid combinations of high-power current-source inverters (CSIs, in this case serving as an LCC) and auxiliary VSIs in PWM-control of electric drives [24]. The advantage of the APF solution is that the auxiliary VSI has a much low power rating (about 10 % of the load size [23] and can hence run at higher switching frequencies, which are easier to filter out by passive *LC*-based filters. However, the filtered device cannot be operated without the APF, as the low-order harmonics would reach inadmissible values.

An ATF modifies its output impedance using an *LLCL* filter connected to an auxiliary VSI to provide a low-impedance path for the select frequencies (mainly the multiples of the converter switching frequency). The prime advantages of such a solution are a lower power rating and DC-link voltage of the auxiliary VSI and a greatly simplified design of the respective current controller. On the other hand, the system is sensitive to background harmonics of the network voltage [19].

1.1.2 Leading-phase and ringing distortion harmonics and their suppression

Network-connected power converters are also supplemented with power-factor correctors (PFC) and inverters to achieve not only sufficiently low levels of harmonic distortion and electromagnetic interference (EMI) but also a high power factor. Both devices modulate the current in-phase with the voltage to meet all three goals. The drawback of this approach is the periodic occurrence of high-frequency currents that create substantial conducted EMI [25]. Hence, EMI filters need to be employed as well. Fundamentally, EMI filters are low-pass filters composed of L and C elements intended to suppress noise in the frequency range from 150 kHz to 30 MHz (radio and TV broadcast) [23]. They are generally designed independently of the power filters [26]. Recently, novel filter designs for specific purposes and increased frequency range have been proposed [21, 27].

The main goal of EMI filters is to attenuate the distortions strongly while maintaining low input impedance to dampen transient events. Naturally, these filters are designed to provide as high attenuation as possible. However, at high attenuations, it was observed that strong interactions between diode bridge rectifiers or unfolders with the EMI filters could take place and manifest as unexpected

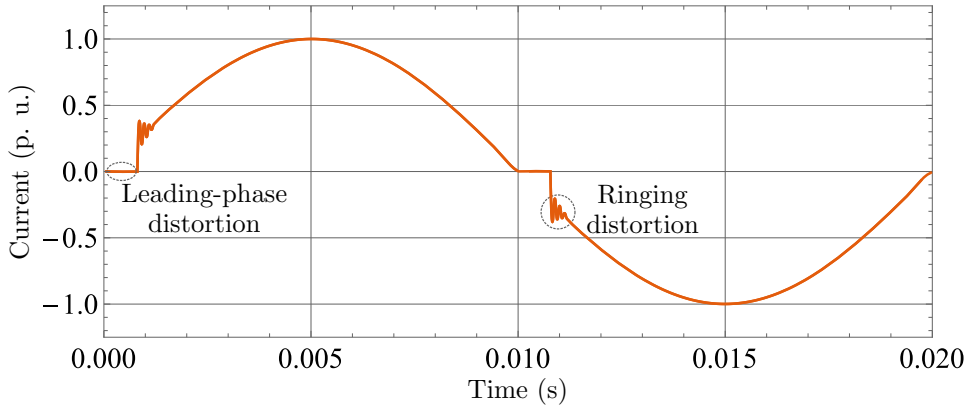

Figure 1.3: Fundamental causes of supraharmonic distortions; output current trend of PFC/micro converter containing EMI filter. Recreated from [25].

harmonic content in the supraharmonic range [25]. The source of these supraharmonics can be traced to two fundamental distortions occurring periodically during the operation of a converter: *leading-phase distortion* and *ringing distortion* [16]. A theoretical output current trend of a PFC/micro converter – EMI filter combination showing both types of these distortions can be seen in Figure 1.3. The magnitude of the distortion effects is slightly increased for illustration purposes.

The leading-phase distortion is caused by a slight phase shift between the current and voltage waveforms due to the average-current regulation operation principle of the converter. In [14], the relation between a leading-edge modulation PFC's input current and voltage was given as:

$$\frac{I_{\mathrm{in}}(s)}{U_{\mathrm{in}}(s)} = \frac{gR_{\mathrm{l}}}{R_{\mathrm{s}}} \cdot Q(s) \tag{1.1}$$

where s is the complex frequency (Laplace transform), g represents the load connected to the converter (invariable with s) and hence defines the constant ratio between current and voltage, R_{l} and R_{s} are the resistances adjusting current flowing into the regulator, and $Q(s)$ is the s-variable ratio between the current and voltage, defined by the converter's parameters. By substituting the parameters with their typical values, it was shown in [14] that $Q(s)$ is not always equal to unity (i.e., the right-hand side of Eq. 1.1 is variant with complex frequency), and hence a non-zero phase lead of current can, and in practice does, occur.

Due to their characteristic behavior, diodes cannot lead current when a reverse-bias voltage is still applied to them. Naturally, this behavior becomes troublesome when a converter employs diode bridges, and a phase shift between the input current and voltage waveforms is present (i.e., a PFC/micro converter). With a non-zero current phase lead, the current reaches its zero value prior to the voltage. At this moment, the other pair of diodes is still reverse-biased, and the current cannot thus flow through them and must remain at zero. Only after the polarity shifts and the forward voltage of the other diode pair reaches the turn-on value, the current can flow once again. The event during which the current is forced to remain at zero is referred to as a leading-phase distortion [14].

Since the regulator demands a sinusoidal current waveform, there is a substantial difference between the target value and the actual value (zero) of the current at the end of the leading-phase distortion. This discrepancy forces a sudden increase in the current when the diodes become forward-biased due to the voltage polarity shift. The triggered (current) transient event is typically an underdamped harmonic oscillation, whose frequency is determined by the poles of the overall input admittance of the device (in other words, resonance); most of the time, this frequency is of units to lower tens of kHz [14, 25]. The resulting current distortion is then known as a ringing distortion.

Specialized design methods that can suppress the distortion effects are available. Among the traditional use of a proper filter capacitor, the parameters of the EMI filter can be designed in a way to reduce the phase lead of the current or to achieve critical damping of the ringing distortion event. However, these alterations come at the cost of reduction of its other qualities, be they power factor correction, low-order harmonics suppression, or attenuation [25].

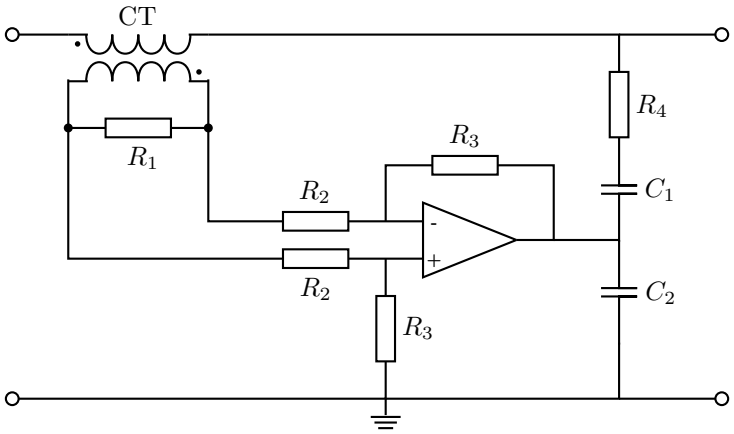

Figure 1.4: A typical design of an AEF. Recreated from [27].

An active EMI filter (AEF) can also be employed to suppress these types of distortions. A typical circuit diagram of such a filter is shown in Figure 1.4. The current transformer (CT) transfers a fraction of the current in the EMI range into the filter circuit. The current is then transformed to voltage via the resistor R_1. Subsequently, the voltage is amplified and inverted by the operational amplifier, transformed back to current via the resistor R_4, and injected into the line. Since the injected current is of opposite polarity, it cancels out the EMI noise on the line in the ideal case. Capacitor C_1 provides a high-impedance block between the filter and the line for low-frequency components [27].

However, there are two principal issues with the use of an AEF for the filtering of ringing distortions in the supraharmonic range. Firstly, the AEFs are typically designed to suppress EMI above the frequency of 150 kHz. Naturally, the low cut-off frequency (given by the current transformer) can be lowered, as was shown in [27], but that also reduces attenuation at lower frequencies, which can lead to the overloading of the filter. The overloading is connected to the second issue, which is the filter's low power rating due to the use of the operational amplifier [26]. These issues principally constrict the application of AEFs to low-voltage, low-power systems.

In the medium- and high-voltage power systems, an APF can be used to reduce the ringing distortion harmonics. A special design needs to be employed, as APFs primarily serve to suppress only the low-order harmonics. Simultaneously, a complementary ATF is used to filter out the switching frequency multiples.

1.1.3 Methodology of supraharmonic suppression at the point of origin

One approach to combat the presence of supraharmonics in power networks was described concisely above. The use of passive or active filters is well-established for low-order harmonics, as well as for the integer multiples of the converter switching frequencies. As mentioned, filters are not typically adjusted to filter out the supraharmonics originating from ringing distortions, which can be particularly troublesome if a resonance with the components of the local network occurs at lower (supraharmonic) frequencies. Naturally, the best solution would be to identify the problematic frequencies and design trap filters to eliminate these components.

However, if done only passively, changes in the network may result in shifting of the resonance frequencies, and hence reduction of the filtering efficiency. Furthermore, the passive traps generally reduce the attenuation at higher frequencies unless damping systems are added [22]. The overall arrangement may then become rather costly and complex. Similarly, the increasing number of components can be detrimental to the system's stability, especially in the case of an island power system [28].

On the other hand, active filtering is expected to perform better, as it can be adapted to the network changes. In addition, the number and dimensions of passive components are reduced, which might lower the total cost of the filtering system [26]. Although appealing, such an approach would most likely require constant monitoring of the network voltage waveform and adjustment of the ATF. Moreover, as mentioned earlier, the active filtering method requires uninterrupted operation and is sensitive to background noises from the network. All in all, these drawbacks illustrate that the supraharmonic filtering issue cannot be resolved through trap filters only.

Consequent to the above, the methodology should be viewed as an extended design of filters. Combinations of passive and active filters of all types should be planned in a way that ensures simultaneous suppression of the low-order harmonics, switching frequency multiples (supra)harmonics, and ringing distortion supraharmonics. Concurrently, strong attenuation needs to be maintained for higher-order supraharmonics as well as EMI, and resonances between the passive components in the supraharmonic range should be strictly avoided. The available tools are primarily damped LC filters and modified APFs or ATFs, eventually modified AEF if applicable.

The other approach to suppression of supraharmonics is the change of the switching pattern and control algorithm of the power converter. Multi-level converters ensure a broader range of control capabilities so that the interactions between the converter and passive filter elements can be reduced [16]. Random pulse width modulation (RPWM) can also be used to suppress the harmonic pollution and EMI noise from the converter. Principally, the length of the switching and sampling cycles of the PWM is randomized, and consequently, the original discrete harmonic spectrum with significant peaks is transformed to a continuous spectrum of moderate harmonic magnitudes [29]. The EMI is then significantly reduced [30], which lowers the demands on the corresponding filter and, in turn, possibly decreases the severity of ringing distortion supraharmonics. Naturally, the demands on the EMI filter can be further lowered by employing fundamental methods that hinder the propagation of the EMI from the point of their origin, such as grounding, shielding, or reduction of electromagnetic coupling [23]. Ultimately, the commonly employed average-current regulation scheme of the converter should be avoided to prevent the emergence of the leading-phase / ringing distortion events.

1.2 Propagation

Whereas the previous section described the origin of supraharmonics and the methods used for their filtration, this section is focused on the phenomenon of propagation of supraharmonics into other parts of the local network or the adjacent network. Three basic types of propagation of supraharmonic components are recognized: propagation between devices, propagation through resonances, and secondary emission. A detailed description of each of these methods is given below. Universally, propagation of voltage harmonic components of a frequency f in a network consisting of N nodes can be described by the following formula [16]:

$$\hat{U}_r(f) = \sum_{s=1}^{N} \hat{Z}_{rs}\,(f) \cdot \hat{I}_s\,(f), \tag{1.2}$$

where $\hat{U}_r$ is the voltage in node r, $\hat{Z}_{rs}$ is the transfer impedance between buses r and s, and $\hat{I}_s$ is the current in node s (an algebraic sum of all currents flowing into and out of the node). Practically in every case, all the terms are complex numbers variable in time. It should be noted that any additional device connected to the network changes the transfer impedance between adjacent devices, and hence the aggregation rules per IEC 61000-3-6 are not applicable in such a case [31].

1.2.1 Propagation between devices

Propagation of harmonics between devices occurs in a local network system, whereas only a part of the propagated harmonic emissions can be detected as the current flowing into the adjacent network. In [31], a simple model describing the effect of switching frequencies, number of devices, and EMI filter capacitor size on this type of harmonic propagation was proposed. The harmonic-emitting device was also equipped with active power-factor-correction (APFC) to better represent the systems used in practice. For sufficiently low frequencies (including supraharmonic range), the device could be modeled as a current source with a capacitor connected in parallel, as shown in the circuit diagram of the said model in Figure 1.5. In the frequency domain, the current flowing through the interface between a single device and the network can be written as:

$$\hat{I}_{\mathrm{em}(1)} = \frac{1}{1 + \mathrm{j}\alpha}\hat{I}_{\mathrm{L}}, \tag{1.3}$$

where j is the complex unit, $\hat{I}_{\mathrm{L}}$ is the current emitted by the device, and $\alpha = \omega RC$ with $\omega = 2\pi f$ being the angular velocity of the examined harmonic, R the resistance of the network and C the filter capacitance.

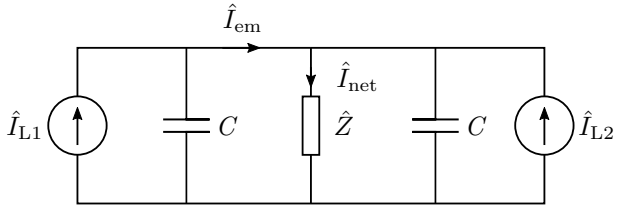

Figure 1.5: A simplified circuit scheme for the modeling of harmonic emission propagation between two devices connected to an adjacent network represented by an impedance $\hat{Z}$. Recreated from [31].

It should be noted that the model was proposed for low-voltage networks, in which the resistance of the adjacent network is predominant when compared to the other passive parameters.

The situation changes when two similar devices (with APFC and EMI filters) are present in the local network, as the current emitted from one device is now also influenced by the other device. Using the model shown in Figure 1.5, Eq. 1.3 becomes:

$$\hat{I}_{\mathrm{em}(1)} = \frac{1+\mathrm{j}\alpha}{1+2\mathrm{j}\alpha} \cdot \hat{I}_{\mathrm{L1}} - \frac{\mathrm{j}\alpha}{1+2\mathrm{j}\alpha} \cdot \hat{I}_{\mathrm{L2}}, \tag{1.4}$$

where $\hat{I}_{\mathrm{L1}}$ and $\hat{I}_{\mathrm{L2}}$ are the currents emitted by the respective devices (internal emission). The first term is known as *primary emission*, whereas the second term is known as *secondary emission*. Principally, the primary emission is the emission originating from the device itself, and secondary emission is the emission from the device caused by the presence and operation of another device in the local network.

Conversely, the current flowing into the adjacent network can be expressed as:

$$\hat{I}_{\mathrm{net}} = \frac{1}{2\mathrm{j}\alpha} \cdot \hat{I}_{\mathrm{L1}} + \frac{1}{2\mathrm{j}\alpha} \cdot \hat{I}_{\mathrm{L2}}. \tag{1.5}$$

If the devices produce emission currents of similar amplitude I_{L} with only a slight difference in frequency, the amplitude of the total emission current at the device–network interface can be obtained using Parseval's theorem as:

$$I_{\mathrm{em}} = \sqrt{\frac{1+2\alpha^2}{1+4\alpha^2}} \cdot I_{\mathrm{L}}. \tag{1.6}$$

Analogously, the amplitude of the total emission current flowing into the adjacent network is:

$$I_{\mathrm{net}} = \sqrt{\frac{2}{1+4\alpha^2}} \cdot I_{\mathrm{L}}. \tag{1.7}$$

At low values of α, i.e., at low frequencies, the emitted current observed at the device–network interface (Eq. 1.6) is identical to the internal emission of the device. For high frequencies, i.e., for $\alpha \to \infty$, the contribution of the internal emission reduces only to about 70,7 %, indicating weak overall dependence on frequency. Naturally, for frequencies of hundreds kHz or higher, the model in Figure 1.5 does not hold, as, for example, the network resistance/impedance needs to be replaced by wave impedance [31]. Nevertheless, the conjecture illustrates that the current observed at the device–network shows not only a marginal dependence on frequency but also on the capacitance of the employed EMI filter.

However, different behavior is present for the emission current flowing into the adjacent network (Eq. 1.7). The α term is present only in the denominator of the right-hand-side term. Hence, the emission current flowing into the network as a result of the internal emission of the devices is inversely proportional to their (switching) frequency and the capacitance of their EMI filters.

Furthermore, the above equations can be generalized for N devices in the local network. They then become:

$$I_{\mathrm{em}} = \sqrt{\frac{1 + N(N-1)\alpha^2}{1 + N^2\alpha^2}} \cdot I_{\mathrm{L}}, \tag{1.8}$$

and

$$I_{\mathrm{net}} = \sqrt{\frac{N}{1 + N^2\alpha^2}} \cdot I_{\mathrm{L}}. \tag{1.9}$$

Eq. 1.8 illustrates that the current emitted from a single device (observed at its interface) is magnified for low numbers of devices in the network, especially at higher frequencies. However, the effect gradually diminishes as the device count N rises. Conversely, at low frequencies, the emission current flowing into the adjacent network, per Eq. 1.9, is proportional to the square root of the total number of devices N in the network. At high frequencies, the current becomes **inversely** proportional to the square root of N.

The experiment performed in [31] shows that the amplitude of the current flowing into the adjacent network is indeed smaller than the amplitudes of emission currents measured at the respective network–device interfaces. Furthermore, the extensive measurements carried out in [32] also confirm the behavior anticipated by Eq. 1.8. Therein, the spectrum of the current flowing at the network–device interface was gathered for various devices. Comparison of the current emission spectra of a photovoltaic (PV) inverter confirmed that secondary emissions from the other two inverters in the network increase the emission current at the interface, especially at higher frequencies. Unfortunately, the emission current into the adjacent network was not measured.

To sum up, this section should postulate primarily the following: secondary emissions lead to the propagation of additional harmonic pollution between the devices in a network. The two principal currents, i.e., current at the device–network interface and current flowing into the adjacent network, show vastly different dependences on switching frequency, filter capacitance, and the number of devices in the network. This difference can cause major discrepancies between the two current spectra (and harmonic content), which may not be revealed by a single measurement. In theory, substantial harmonic pollution of the network may be perceived as insignificant if, for instance, only the emission into the adjacent network is measured. Therefore, harmonic filter design should also encompass the analysis of waveform spectra in various nodes of the network to ensure correct functionality.

1.2.2 Resonances

In medium-voltage networks, a much more characteristic type of harmonic propagation is the propagation via resonances [16]. The modus operandi of the propagation is the presence of resonance frequencies in the examined network. These resonances originate from the various combinations of passive RLC components found in the system. Such a component can be, for example, the inductance, resistance, or capacitance of a passive or active filter. Even without any additional device, major passive components, such as the inductance of a transformer, the inductance of overhead lines, or the capacitance of cable systems, are already present in the network.

The issue of resonances in MV networks is illustrated, for instance, in [12]. This research paper dealt with propagation of harmonics in a medium-voltage cable network interconnecting a total of ten wind turbines, each with a rated power of 3 MW. A model originally proposed in [33] was applied to determine the overall transfer function of the emissions into the adjacent network. It was found out that resonance of the turbine and power collection systems occurs at around 1.55 kHz (resonances at higher frequencies were not the subject of the work). In the worst-case scenario, i.e., when the phase angle of emissions from each turbine was identical, the transfer function reached a maximum of about 16 (p.u.).

A moderate, more authentic estimation was determined by a Monto Carlo simulation, which took random samples of the actual currents measured at the output of a wind turbine and created a representation of an average complex current output from each turbine. Due to the various phase shifts between the individual currents, the magnitude of the transfer function was reduced. Nevertheless, the maximum transfer ratio still reached about 5 (p.u.). Another metric, called the aggregation factor, was also employed to illustrate the actual propagation into the adjacent network better. The aggregation factor is calculated as a ratio between the overall emission from the system to the emission current from a single device multiplied by the total number of devices (i.e., tenfold the single-device emission in this case). The factor also reached

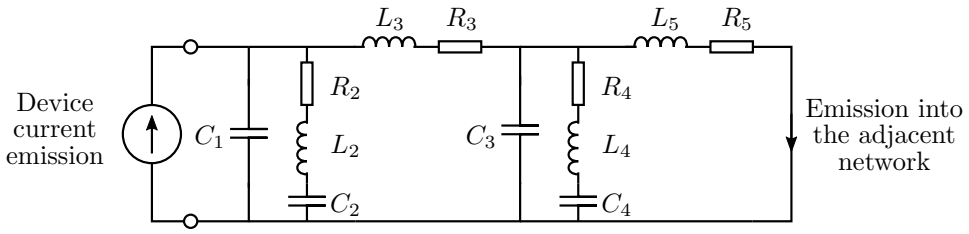

Figure 1.6: A resonance emission circuit model consisting of a single device, a medium voltage (collector) cable system, and an upstream transformer. Recreated from [12].

a maximum of about 5 in the vicinity of the resonance frequency, indicating magnified propagation of harmonics into the adjacent network.

Figure 1.6 shows the model used for the determination of resonance frequencies per [12]. The device is connected to a feeder cable system, through which the current flows into an upstream transformer and further into the adjacent network. A π-model of the cable system is employed to describe the behavior of the system at supraharmonic frequencies better. Definition of the individual passive parameters can be found, for example, in [34]. The transfer function (ratio of the emission into the adjacent network to the device current emission) is given as:

$$\hat{H}_{\mathrm{tg}}(\omega) = \frac{\hat{Z}_{34}}{\hat{Z}_{34} + \mathrm{j}\omega L_5 + R_5} \cdot \frac{\hat{Z}_{12}}{\hat{Z}_{12} + (\mathrm{j}\omega L_3 + R_3) + \frac{\hat{Z}_{34}\cdot(\mathrm{j}\omega L_5 + R_5)}{\hat{Z}_{34} + (\mathrm{j}\omega L_5 + R_5)}}, \tag{1.10}$$

where the impedance $\hat{Z}_{12}$ represents the combination of passive parameters C_1, C_2, R_2, and L_2. Analogously, $\hat{Z}_{34}$ represents the combination of C_3, C_4, R_4, and L_4.

As mentioned above, the power station network of [12] consisted of ten wind turbines. Two identical cable feeder systems were present, each collecting power from five equidistant turbines. By employing a similar configuration with slightly changed parameters, harmonic emission transfer functions for four various input points were determined using Eq. 1.10. The results are shown in Figure 1.7.

The obtained transfer functions suggest that the transfer ratio remains equal to one for the entire spectrum of intraharmonics and standard harmonics (up to the 40^{th} order) for all four configurations. However, multiple resonances take place in the supraharmonic range, pushing the transfer ratio into lower tens. Following the last resonance, the transfer function quickly drops to minimal values as the frequency rises. The drop occurs at frequencies below the boundary between supraharmonics and EMI (150 kHz), indicating a minimal spread of conducted EMI into the upstream network.

All in all, the simulation illustrates that harmonic emission from devices in a medium-voltage network may be amplified through resonances exclusively in the unsatisfactorily regulated supraharmonic band. Furthermore, the transfer function reaches substantial values at resonance frequencies, which predicts that even weak harmonic emission might be amplified to high levels. Therefore, a similar analysis should always be performed for systems susceptible to such phenomena, i.e., mainly renewable power stations interconnected to the network via medium-voltage cable systems.

1.2.3 Secondary emissions

The term secondary emission has already been introduced in the subsection 1.2.1. Fundamentally, it represents the part of the emission current spectrum of a single device, which originates from the presence and operation of another device in the same network. A simple analytical model describing the behavior of both primary and secondary emissions was proposed in [13]. Compared to the model mentioned in the said subsection, this one describes the emission spectrum of just one general device, with no regard to the propagation into the **adjacent** network. The circuit from which the behavior of both types of emission is derived is shown in Figure 1.8.

Principally, the circuit is split into the device part (components denoted by index 1) and the rest of the local network (index 2). Two sources are present: a current source, $\hat{J}_1$ representing internal emissions, and a voltage source, $\hat{E}_2$ representing background voltage from the network. Impedance $\hat{Z}_1$ simulates

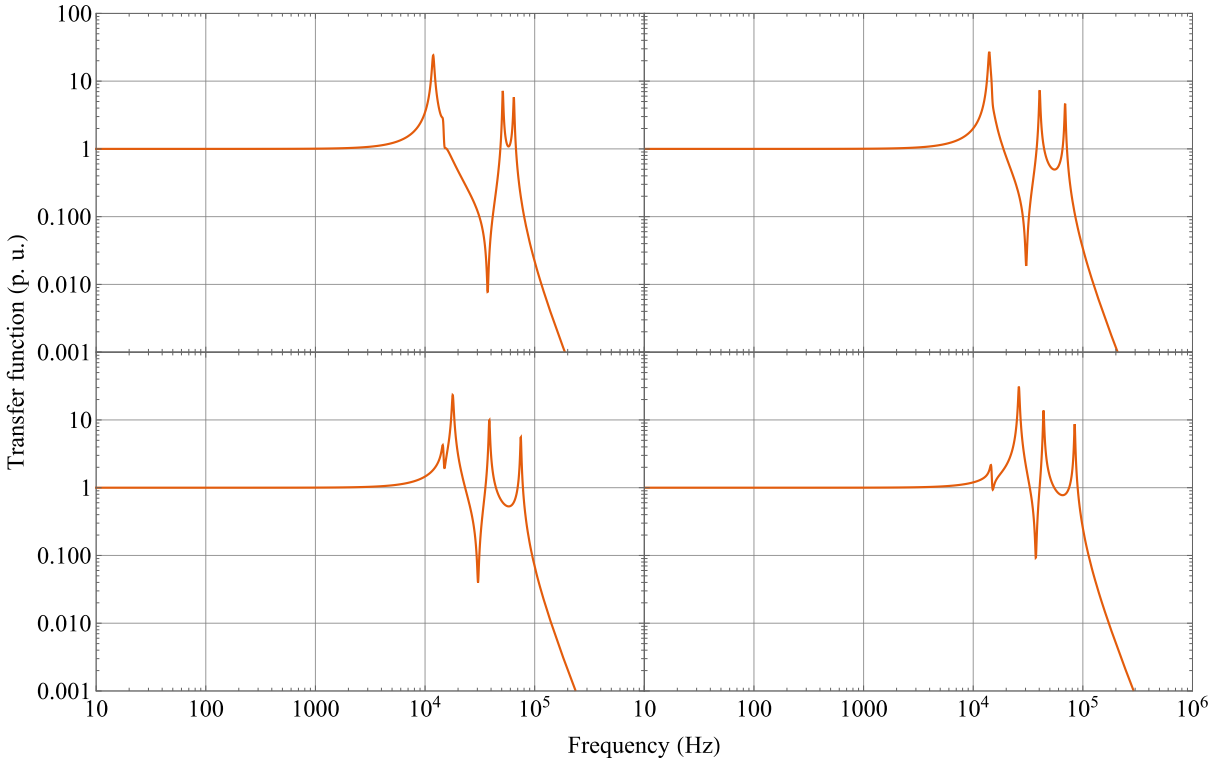

Figure 1.7: Transfer function between a wind turbine and the upstream network at four different locations. Modeled per [12].

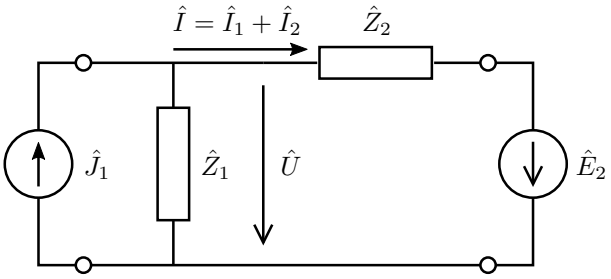

Figure 1.8: A diagram of the circuit used to determine primary and secondary emission in the model per [13].

the impedance of the device, whereas $\hat{Z}_2$ simulates the network impedance. Voltage $\hat{U}$ is present at the terminals of the device, and emission current $\hat{I}$ flows from the device into the local network.

In practice, all the elements, i.e., sources and impedances, are expected to be non-linear to at least some degree. However, for the purpose of the behavior analysis of emissions, the researchers in [13] first assumed the best-case scenario, in which all the components are linear, and voltages are sinusoidal and nominal, and subsequently dropped some of these assumptions in a thought experiment. The following contributions to the harmonic emission from the device were determined:

- If the network impedance is non-zero: part of the emitted current flows through the device impedance, distorting the voltage at the device terminals and changing the emission spectrum.
- If the supply voltage is distorted (even without the influence of the device): change in the current flowing through the device impedance results in the change of the emission spectrum, analogous to the previous point.
- If the network is non-linear: network impedance and background voltage change with the voltage at the device terminals.

These contributions indicate that the emission behavior is complex and that numerous (non-linear) relations between the quantities need to be established to describe the behavior in detail. Nevertheless, three basic definitions can be formed, of which the first two can be written mathematically as:

$$\hat{I}_1 = \frac{\hat{Z}_1}{\hat{Z}_1 + \hat{Z}_2} \cdot \hat{J}_1, \tag{1.11}$$

$$\hat{I}_2 = -\frac{1}{\hat{Z}_1 + \hat{Z}_2} \cdot \hat{E}_2, \tag{1.12}$$

where $\hat{I}_1$ represents the current flowing from the device to the network as a result of its internal emission (*primary emission current*), and $\hat{I}_2$ represents the contribution to the emission current at the device terminals that originates from the presence or operation of other devices in the local network (*secondary emission current*). The third definition, *harmonic interaction*, is proposed for the non-linear phenomena mentioned in the bulleted list above.

If the emission is to be measured, one needs to remember that standard online measurements can only gather the total current $\hat{I}$, which can be expressed as the sum:

$$\hat{I} = \hat{I}_1 + \hat{I}_2. \tag{1.13}$$

In other words, the obtained emission spectrum contains both primary and secondary emissions, with no way to discern them from each other. Specialized, long-term measurements need to be employed to obtain the individual emission types.

One such example was shown in [34], where the output current spectrum of a single wind turbine in a medium-voltage wind park was measured for about ten days. Since the turbine was at certain times turned off, the measurement could gather the harmonic emission produced only by the other devices in the local network, i.e., the secondary emissions. After performing harmonic analysis of the current and voltage measured at the terminations of the observed device, the dependence of the gathered (inter)harmonic voltage on the (inter)harmonic current was plotted (see Figure 5.9 in [34]). At all the observed (inter)harmonic orders, two distinct data point clusters emerged, each having a different slope if fitted by a line. The steeper of the two was almost vertical, indicating simultaneous strong harmonic distortion of the voltage and minor distortion of the current. This cluster consisted only of data gathered when the observed turbine was shut down and therefore showed the secondary emission solely. The other cluster consisted of data gathered in the on-state of the turbine and hence showed both the primary and secondary emission.

Another experiment [13] examined the supraharmonic emission at the terminals of a PV inverter in a household installation. A total of 45 measurements were performed, where each measurement consisted of a different combination of typical (household) devices connected to the network. In contrast to the measurement performed in [34], the observed device (PV inverter) was in the on-state over the entire

duration of the data acquisition, whereas each other device was at least once in the off-state. Therefore, the emission spectral components common for each measurement iteration represent the primary emission of the PV inverter. In the gathered spectrogram (see Figure 4 in [13]), one such common component (line) is evident at about 16 kHz. The line most likely represents the switching frequency of the inverter. Since two less clear lines are present at about 32 and 48 kHz, i.e., at multiples of two and three of the assumed switching frequency, the claim is supported further.

A similar measurement, albeit in a shopping mall, was carried out in [35]. Therein, the measuring instrument was placed on the terminals of the lighting circuits fuse box to gather a voltage spectrogram over twenty hours. The obtained spectrogram (see Figure 13 in [35]) shows a distinct part between 19:30 and 8:40, during which the lights were turned off. Some components were present throughout the entire measurement, such as the lines at 24 and 27 kHz and the harmonic band below 10 kHz. These should therefore represent the secondary emissions from other devices, as their relative content increased when the primary emission source (lighting) was switched off.

1.3 Chapter summary

The main goal of this chapter was to illustrate that the voltage waveform found in various types of low- to medium-voltage systems can be substantially polluted, even when conforming to the power quality standards. A subtype of harmonics, supraharmonics, was identified as the most potent factor of such pollution, mainly due to the lacking regulation per the mentioned standards.

Section 1.1 presented individual devices and configurations prone to the creation of supraharmonic pollution. The basis of all the identified problematic configurations was a power converter with PWM regulation. Apart from emitting low-order harmonics, the converter was shown to produce supraharmonics at integer multiples of its switching frequency. Suitable harmonic filters that can combat these distortions, as well as their operating principle, benefits, and shortcomings, were mentioned. Next, the phenomenon of ringing distortions was described and attributed to the joint action of both the converter and its harmonic filter and the presence of passive components in the local network. The difficulties stemming from the complex optimization of a harmonic filter concerning all the desired qualities (low-order, switching and ringing distortion harmonics suppression, maintenance of high power factor) were enumerated. Ultimately, the methodology of such optimization regarding supraharmonics was summarized.

Conversely, section 1.2 described the three fundamental ways in which supraharmonics can propagate into other elements of the local network, as well as into the adjacent network. It was shown that supraharmonics emitted by a single device (primary emission) could be further magnified through the presence and operation of other devices in the network (secondary emissions). Firstly, a model describing the propagation of supraharmonics between devices in a low-voltage network with regard to their frequency, the total number of devices, as well as fundamental parameters of EMI filters was mentioned. The principal use of the model was to illustrate that substantial supraharmonics pollution of the local network may be present, whereas only a fraction of this pollution may be detected at its terminals to the adjacent network. Next, the primary source of propagation of supraharmonics in medium-voltage networks, resonances, was analyzed. In the same spirit, a model of this type of propagation was presented. Frequency-dependent transfer functions between a single device and the adjacent network were determined for a sample wind park installation. It was shown that the resonances might amplify some component in the supraharmonic range by a factor of over ten. Ultimately, both primary and secondary emissions were further analyzed using yet another model. Some specialized methods of their detection were mentioned as well.

Chapter 2

Breakdown & aging of solid insulation materials

2.1 Overview of breakdown types

Solid electrical insulation materials have numerous unique traits that predetermine them as the only choice for specific insulation systems. In the context of the three (employable) states of matter, solid materials show on average the highest dielectric and mechanical strength, but they simultaneously become unusable if their breakdown occurs [36]. The breakdown is always a result of one or more stresses exerted on the given insulation material during its operation. In electric systems, the clear majority of such stresses are either directly or indirectly connected to the presence of an elevated electric field in their insulation. Depending on the magnitude of the electric field, different types of degradation processes take place.

Regarding the predominant mechanism that leads to the breakdown, several breakdown subtypes are recognized [37], as shown in Figure 2.1. The first three types, *intrinsic*, *electromechanical*, and *avalanche*, are briefly described in the subsections below. In contrast, *thermal breakdown*, *aging*, and *erosion breakdown* are explained in greater detail, as they play vital parts in all three experiments performed within this doctoral thesis.

2.1.1 Intrinsic (electrical) breakdown

The intrinsic breakdown represents an extreme case in which the applied electric field causes the electrons in the material to cross from the valence band over to the conduction band. Such transition quickly increases the number of free electrons, which are then accelerated via the applied field. Due to the mutual interactions, the electron temperature increases, which also increases the temperature of the material. At higher temperatures, the bandgap is reduced, and hence more electrons can cross over to the conduction band. This process forms a positive-gain loop, which eventually leads to thermal instability. As the temperature rises above all limits, the "high-temperature" breakdown takes place. The adjective is used to distinguish the breakdown from thermal breakdown, during which thermal instability is also reached, but the process is substantially slower.

The transition of bound (valence) electrons into the conduction band in an ideal non-conductive crystal is illustrated in Figure 2.2. In a normal state (Figure 2.2a), i.e., without an applied electric field, the electrons are bound in potential wells given by lattice atoms. At room temperature, the forbidden band is too wide to be crossed over, and the crystal thus retains its insulating nature. However, if a sufficient electric field is applied, the energy levels of the conduction band become distorted enough for a quantum tunneling effect to release a valence electron into the conduction band (Figure 2.2b) [36].

A necessary condition of an intrinsic breakdown is the prevalence of the energy gained by conduction electrons from the electric field over the energy lost to the lattice. In pure crystals, the number of conduction electrons is very low, and hence their mutual interactions are minimal compared to the electron–lattice interactions. The electron temperature is, therefore, often almost equal to the temperature of the lattice. On the other hand, in amorphous dielectrics, the interactions between conduction electrons overshadow

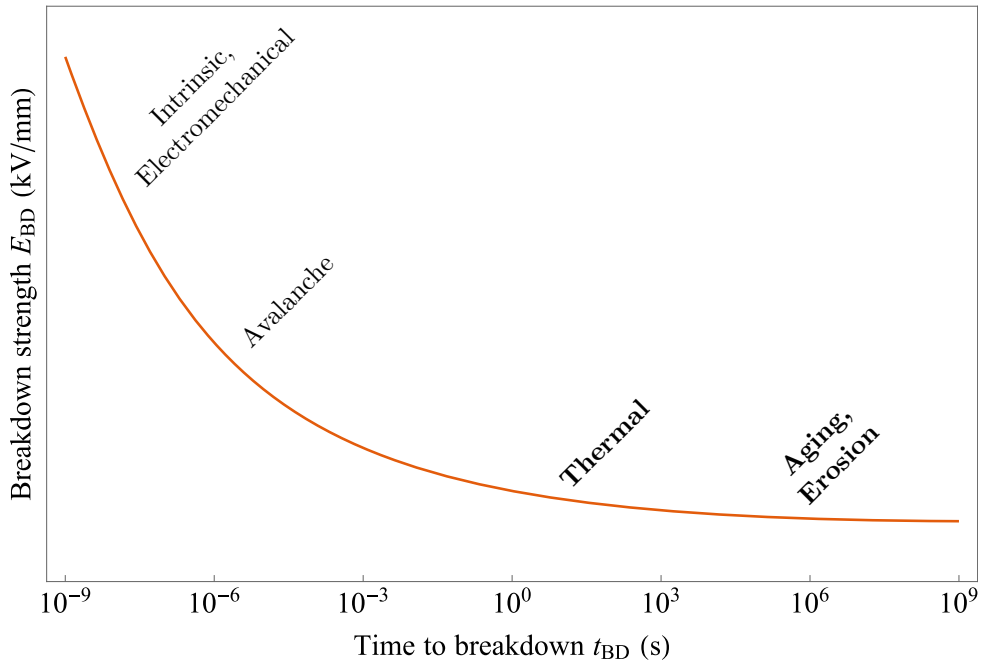

Figure 2.1: A life curve of a general solid insulation system illustrating the fundamental types of electrically induced breakdowns.

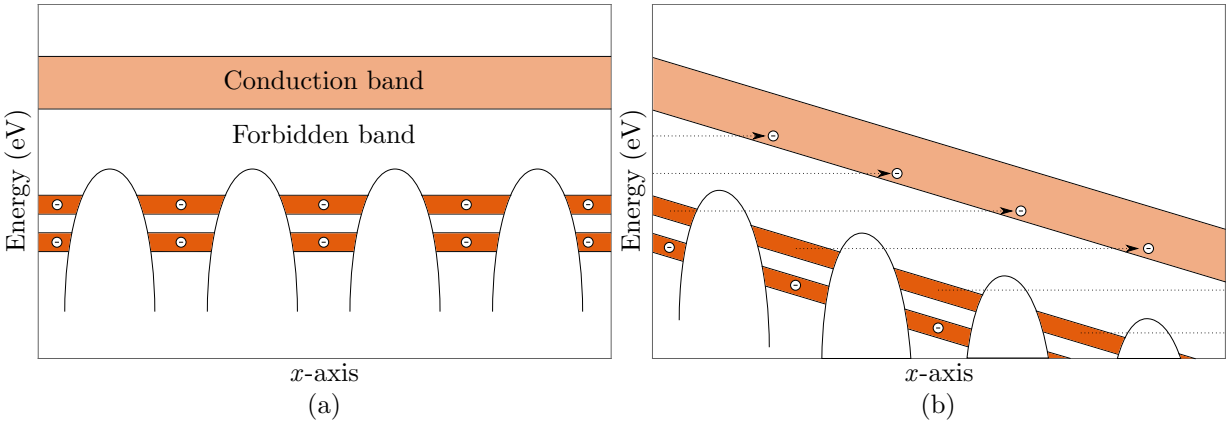

Figure 2.2: An illustration of the high-field electron release principle (electronic bandstructure model). Recreated from [36].

the electron–lattice ones, and the electron temperature is typically higher than its counterpart. In any case, if the applied electric field provides more energy to the electrons than they lose to the lattice, the breakdown process will be triggered. The process lasts about 10^{-8} s and requires electric field strengths well above 100 kV/mm [37].

2.1.2 Electromechanical breakdown

This type of breakdown can occur if the stressed material can be deformed to a large extent without fracturing. In general, the applied electric field exerts electrostatic compression force on materials. If the material is resilient enough not to fracture, the electrostatic compression force might surpass its mechanical compressive strength. Should that occur, the material will disintegrate, and the insulation system will be broken down.

For each applied voltage (electric field), the material reduces its volume so that the force it exerts under strain counterbalances the electrostatic compression force. The equilibrium of the two acting forces can be written as:

$$\varepsilon_0 \varepsilon_\mathrm{r} \frac{U^2}{2d^2} = Y \ln\left(\frac{d_0}{d}\right), \tag{2.1}$$

where ε_0 and ε_r are the vacuum and relative permittivities, respectively, U is the applied voltage, d and d_0 are the actual and initial material sample thicknesses, respectively, and Y is Young's modulus. The left-hand side of the equation represents the acting electrostatic force, whereas the right-hand side defines the force the material exerts under strain.

Eq. 2.1 can be understood in the following way: the electrostatic force acting upon the material leads to its deformation so that $d_0/d > 1$. Such a response increases the force the material exerts under strain (RHS of Eq. 2.1), which strives to stabilize the system. However, as the material thickness d decreases, the electrostatic force increases due to the rise in the applied field strength $E = U/d$ (valid for homogenous fields; LHS of Eq. 2.1). This dependence suggests that at a high enough voltage, the increase in electrostatic force will be greater than the increase in the force exerted by the material under stress. The system will become unstable, and the material will disintegrate. The limit value of compression ratio d_0/d can be calculated if Eq. 2.1 is rewritten as:

$$U^2 = d^2 \frac{2Y}{\varepsilon_0 \varepsilon_\mathrm{r}} \ln\left(\frac{d_0}{d}\right) \tag{2.2}$$

and differentiated with respect to the thickness d. The differentiation reveals that the maximum of the RHS of equation 2.2 occurs when $d0/d \approx 0.6$, as shown in Figure 2.3. Hence, any voltage above the one, which compresses the material to such a degree, must lead cause electromechanical breakdown. In terms of applied electric field strength, the limit value can be expressed as:

$$E_\mathrm{bd} = \frac{U}{d_0} = 0.6\sqrt{\frac{Y}{\varepsilon_0 \varepsilon_\mathrm{r}}}. \tag{2.3}$$

Naturally, such a definition describes only the ideal case, in which no irregularities in the material are present. Furthermore, the dependence of Young's modulus on time and stress, as well as on plastic flow, is neglected [37]. The duration and the applied electric field strength of an electromechanical breakdown are similar to those of an intrinsic breakdown.

2.1.3 Avalanche (streamer) breakdown

An avalanche breakdown is a particular type of breakdown that takes place only if specific conditions are met. The applied electric field must be uniform, and both electrodes must be embedded in the insulation system. At a sufficient electric field, a free electron may be present at the cathode interface (either externally emitted from the electrode or internally by a transition from the valence band). The electron can then be accelerated via the electric field in the direction toward the anode. Due to the energy gain, the free electron might cause collision ionization if its free path is long enough. The ionization produces

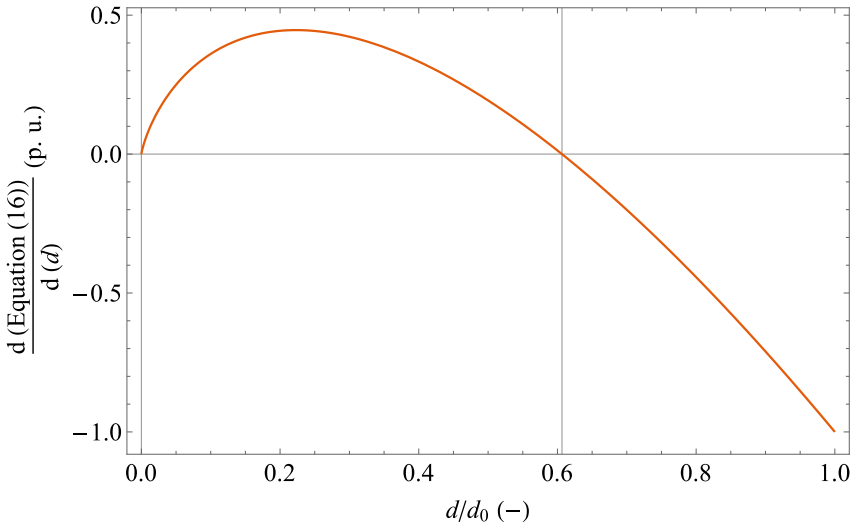

Figure 2.3: Determination of the limit value of d/d_0.

another free electron, which is then also accelerated by the applied field. Should these electrons cause a chain reaction (form an electron avalanche), the breakdown of the material will occur.

The minimum field required for an avalanche breakdown to occur is lower than in the case of intrinsic and electromechanical breakdowns. Nevertheless, its typical values (∼100 kV/mm) are still much larger than the standard operating conditions of insulation systems. Although the avalanche mechanism in solids is similar to the one occurring in gases, the required field is much higher due to the significantly reduced mean free path of electrons [38]. The breakdown event lasts for about 10^{-6} to 10^{-5} s [37].

2.1.4 Thermal breakdown

A thermal breakdown occurs when the heat generated by an insulation system is greater than the heat removed from the system. In such a case, thermal instability is reached, and the temperature rises above all limits. The heat supplied to the system originates either from dielectric losses in the insulation material or ohmic losses in an adjacent conductor. By contrast, the heat is removed from the system through conduction, convection, or a combination of both.

In general, dielectric losses can be determined using the following formula:

$$P_\delta = V^2 \omega C \cdot \tan\delta\,(T), \tag{2.4}$$

where V is the RMS value of the applied voltage, ω is the angular frequency of the voltage, C is the capacitance of the insulation system, $\tan\delta$ is the loss tangent of the insulation material, and T is the thermodynamic temperature of the insulation system.

From Eq. 2.4, five factors that lower the threshold at which the thermal breakdown occurs can be identified:

- the high relative permittivity of the material/capacitance of the insulation system,
- the high loss tangent of the insulation material,
- strong positive dependence of the insulation material loss tangent on its temperature,
- harmonic distortion of the voltage waveform and
- **presence of high-frequency oscillations in the voltage waveform** (supraharmonic pollution, EMI).

Regarding the other mechanisms at play, two additional factors can worsen the situation:

- the high ohmic losses of the adjacent conductor and

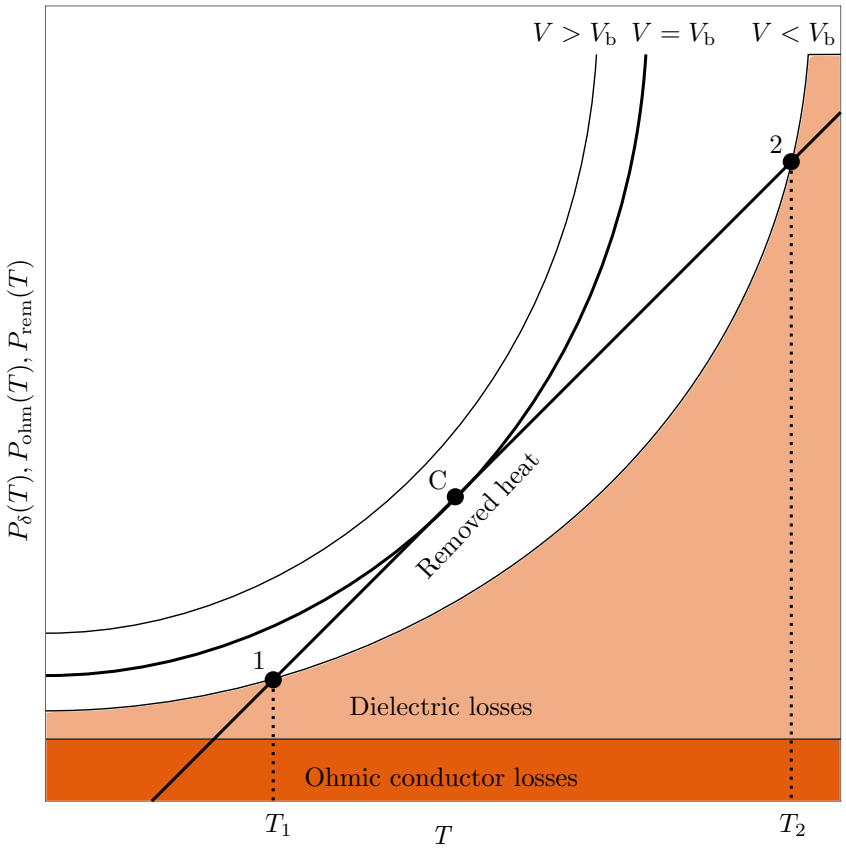

Figure 2.4: A simplified illustration showing temperature dependencies of heat gained/lost by an insulation material in an electric field. Recreated from [36].

- poor removal of heat from the insulation system.

Typical configurations prone to the development of the thermal breakdown are compensation capacitors (high permittivity), epoxy resin bushings (poor heat removal), and aged mineral oil impregnated paper insulation of transformers (large dissipation factor) [36].

Both the dielectric losses and heat removal are temperature-dependent. If an infinitely long insulation system is assumed, i.e., its length h is much larger than its thickness d, the heat removal can be expressed as:

$$P_{rem} = \lambda \cdot A\,(x) \cdot \frac{\partial T}{\partial x}, \tag{2.5}$$

where λ is the thermal conductivity of the insulation material, $A(x)$ is the heat-transmitting surface, and x is a spatial variable in the direction of the material thickness d.

From the above, it should be evident that the *thermal breakdown voltage* must be determined specifically for each case. The breakdown voltage can be expressed from the gained/lost heat dependence on the temperature, whose example is shown in Figure 2.4 (material temperature is assumed constant for simplicity, hence the linear dependence of lost heat on temperature).

If the voltage applied to the insulation system is lower than its respective thermal breakdown voltage, two thermal equilibrium points can be determined. In the figure, these are located at the two intersections between the $V < V_b$ curve and "removed heat" line (area below the $V < V_b$ curve shows the total losses at voltage V – depicted in dark and bright orange). Point 1 represents a stable thermal equilibrium – should the temperature increase, the removed heat will be higher than the heat generated, and therefore the temperature will return to its original value T_1. Analogously, should the temperature drop, the heat generation will be greater than its dissipation, and the temperature will increase back to the value T_1. On the other hand, point 2 is unstable as any change in temperature will result either in a thermal runoff

(increase) or its reduction to the temperature of a stable point, i.e., to T_1 (decrease). Point 2 can be reached if an appropriate transient event increases the temperature to T_2. Such an event can be, for example, a short-circuit and its resulting overcurrent and ohmic losses. The critical point C represents a semi-stable state that is present only when the voltage is equal exactly to the breakdown voltage of the system. While the decrease in temperature will lead to the stabilization of the system, any increase in losses (voltage) will inevitably cause a thermal runoff, which results in the thermal breakdown of the material.

A unique trait of a thermal breakdown mechanism is its independence on the material thickness d in some instances. One such case is a configuration in which the heat is generated in the insulation material globally, and the surrounding electrodes generate no heat through ohmic losses. The only source of heat is, therefore, the dielectric losses (Eq. 2.4). Now, if the insulation thickness is doubled, the dielectric losses are reduced in half owing to the resulting capacitance decrease ($C \sim 1/d$). Conversely, the thermal resistance of the insulation is doubled, which means that the heat dissipation from the system will be halved as well. All in all, the decrease in heat generation and dissipation will cancel each other out, and therefore the insulation thickness will play no role in the determination of the thermal breakdown voltage of such an insulation system.

The above needs to be considered when designing high-voltage insulation systems that utilize materials with either high permittivity or loss tangent. One example is polyvinyl chloride, whose thermal breakdown voltage is as low as 0.1 to 0.2 MV, rendering it unusable for high-voltage cable insulation. Polyethylene and capacitor paper show more promising behavior with thermal breakdown voltages of about 3 to 5 MV. Nevertheless, one needs to consider the heat dissipation in the intended system, as, for example, in cables, heat is also generated in the cable core, and it can be thus dissipated through one side only. Furthermore, the heat dissipation in large capacitors is generally poorer, and owing to the strong electric field, the insulation system might quickly degrade to a point at which the thermal breakdown voltage becomes low enough for the breakdown to occur [36].

Attention must also be paid to the thermal equilibrium temperature, as the dielectric losses may quickly increase when the temperature of the insulation system rises above the glass transition point of the employed insulation material. Indeed, the glass transition point limits the maximum operating temperature of practically all polymer-based insulation systems. Examples of operating temperatures include 260 °C of polytetrafluorethylene (PTFE), 50 up to 160 °C of epoxy resins (EP), or 90 °C of XLPE [36]. These are set well below the respective glass transition points to ensure that the insulation system temperature does not reach such a value even during transient events (overcurrent).

The thermal breakdown was described in greater detail mainly due to its mutual relation to the aging mechanism described in the next section. The processes transpiring during the aging of the given insulation system generally worsen its insulating properties. Such a worsening often leads to a rise in thermal generation (losses) of the material or a decrease in its thermal conductivity, which reduces the thermal breakdown voltage of the system. Furthermore, all the chemical (degradation) processes taking place in the material can be described by transition state theory (see section 2.2.4.3), which states that the probability, or rate, of a given chemical reaction is strongly dependent on the thermodynamic temperature. Therefore, heat generation/dissipation also plays a significant role in this regard [39].

2.2 Aging

2.2.1 Stress types & levels

While the mechanisms of the previously mentioned breakdown types are relatively straightforward, the aging processes that steadily degrade the given insulation system to the point of its breakdown are much more complex. Numerous constituent aging processes of various natures can be identified throughout the insulation system's lifetime, with each playing a different role in the ultimate failure of the insulation system. Some examples include [36]:

- chemical, mechanical, and thermal stresses, as well as environmental influences and radiation that lead to embrittlement of the material, which can result in the formation of cracks,
- changes in insulation material structure by hydrolysis due to ingress of water,
- creation of conductive tracks due to the concurrent effects of moisture and electric field (water treeing),

- creation of conductive tracks due to strong electric field at the electrode–insulation interface (electrical treeing), often connected with increased partial discharge activity [40],
- the rise in conductivity and loss tangent of the insulation material leading to unfavorable field redistribution (DC), or thermal instabilities (AC) or
- formation or enlargement of defects, in which partial discharges might reach inadmissible magnitudes, eventually causing an erosion breakdown of the material.

Under normal operating conditions, these processes must be either avoided entirely or at least slowed enough so that the electric device or system remains operational over its planned lifetime. Specific methods to combat the progression of each degradation type are available, whereas, for electrically induced aging, the universal approach lies in the reduction of electrical stress. For a planned lifetime of 30 years, electrical stresses should be kept below the following values: 3 to 7 kV/mm for PE-based cable systems; 40, 20, and 3 to 7 kV/mm for mineral oil-impregnated paper capacitors, cables, and transformers, respectively; 1 to 3 kV/mm for porcelain insulators; and 1.5 to 4 kV/mm for epoxy resin in general [36].

The listed limits for the long-term endurance of insulation materials often represent only a fraction of their short-term breakdown strength. Apart from the assumed general dependence of electrochemical degradation processes on the applied field strength (see [41] for XLPE cable insulation), the admissible field strength is also significantly reduced by electrode surface roughness and material inhomogeneities in industrial settings [38]. The latter is in stark contrast with the laboratory conditions under which the short-term breakdown strengths are typically obtained.

Determination of the limiting values of stresses exerted on a given insulation system is crucial in terms of its economization. On the one hand, oversized insulation will decrease the chance of failure and thus extend the lifetime of the given electric device or system (unless thermal breakdown is of concern). On the other hand, the cost of such a device will be significantly increased, and due to continuous technological advancements, excessively prolonged lifetimes may not always be welcomed. Further inconveniences include the increased weight of the device, as well as its size due to the larger insulation clearances. In practice, the insulation system is designed to ensure that its failure probability is much below 1 % at the end of its technical life [36]. The respective threshold can only be established if a prediction of the system lifetime at the planned stress levels is available. To obtain an accurate prediction, one needs to employ a suitable aging model (see section 2.2.4) on the statistically evaluated results of aging tests (see sections 2.2.2 and 2.2.3).

If an insulation system is designed and produced well and operated under prescribed conditions, most degradation processes become insignificant in the scope of its planned lifetime. Nevertheless, some processes, usually of chemical nature, cannot be entirely avoided. Noteworthy examples include the scission of polymer inter and intramolecular chains through thermally accelerated oxidation [42] or free electrons accelerated by the electric field in free volumes of the polymer [43,44]. While not strictly chemical, partial discharges that cause erosion of the insulation system are often also present, especially toward the end of the planned lifetime of the device. More information about the partial discharge phenomenon is given in section 2.3.

A common factor of (electrochemical) aging processes is the presence of an electric field, from which stems the frequently used term electrochemical degradation. Furthermore, as was said earlier, chemical reactions can be described using the transition state theory, which quantifies the strong dependence of reaction rates on thermodynamic temperature. Since electrical and thermal stresses are bound together, it should be evident that both play the leading role in the aging of a well-designed insulation system. Any lifetime prediction should thus be based primarily on these two factors, that is, if the other factors can be considered irrelevant.

2.2.2 Aging data acquisition

Prior to any attempts at estimating an insulation system's lifetime, relevant aging data must be acquired. Naturally, it would be ideal to carry out aging tests under the same conditions, under which the system's lifetime is sought after. However, due to their impractical lengths (tens of years for standard operating conditions), they need to be carried out in an accelerated fashion. The critical component to extrapolating the accelerated aging results is the knowledge of the acceleration factor between the sought-after and actual (test) conditions. The acceleration factor can be estimated through aging models, but relevant aging data must be obtained first. The aging data are represented by data points consisting of a pair

of values: the magnitude of the applied stress and the mean time-to-failure under the applied stress. In the case of multi-stress aging, the data points are extended to include all the applied variable stresses. Specifically for electrical aging, the applied stress is represented by RMS voltage or (RMS) electric field strength.

2.2.2.1 Mean value, standard deviation

Whereas the magnitude of the applied stress is clearly defined and easily measurable, the mean time-to-failure needs to be determined from the aging test results. Due to the stochastic nature of breakdown, statistics need to be employed to obtain an expected mean value of the gathered times-to-breakdown. A statistical analysis of the results assumes that each tested specimen represents a random sample of an unknown (infinite) basic population, governed by some (continuous) probability distribution function [36]. The goal of the statistical analysis is then to find the distribution which would describe the behavior of the examined insulation system in terms of reliability.

For self-regenerative (gaseous or liquid) insulation, the test specimens are represented by successive (flashover) tests of the same arrangement, whereas for solid insulation, each aging/breakdown test requires an individual sample. Naturally, the total number of performed tests is limited and cannot thus exactly describe the basic population. Every set of tests will therefore provide only an estimate of the examined actual mean value (time-to-breakdown / breakdown strength), known as the arithmetic mean value.

Apart from the mean value, the standard deviation of the basic population, or rather sample set, needs to be determined to obtain the complete picture of the insulation system behavior. The standard deviation determines the difference between various failure probabilities (the mean arithmetic value corresponds to a failure probability of 50 %) in terms of the examined times-to-breakdown or stress parameter values (voltage/electric field strength). In an ideal case, the standard deviation would be zero, and all failures would occur simultaneously (aging tests) or at the same stress value (breakdown tests). The insulation system's operating voltage could then be placed just below the arithmetic mean value with the certainty of no premature breakdown. The worst-case scenario would be with the standard deviation approaching infinity, effectively yielding the same failure probability (50 %) over the entire range of stresses, even for times-to-failure/stress values close to zero.

2.2.2.2 Confidence intervals of estimated parameters

Since the number of performed tests (*master list*) is always smaller than the respective basic population, the estimated parameters of the governing distribution will never provide an exact match to the actual, unknown parameters. The accuracy of a parameter estimate can be quantified by a *confidence interval* of the desired probability p. The confidence interval represents a range of values, between which the actual distribution's parameter is located with a probability of p. For the standard normal distribution, the confidence interval boundaries of the mean value can be obtained from the following expression:

$$\bar{x} \pm z\frac{\sigma}{\sqrt{n}}, \tag{2.6}$$

where $\bar{x}$ is the mean value of the parameter gathered in the master list (breakdown strength/applied stress), z is the p-quantile of the standard normal distribution, σ is the corresponding standard deviation, and n is the size of the master list. Most often, intervals with a confidence level of 90 % are used. The interval can be constructed for the standard deviation estimate as well. If the Weibull distribution is used instead, one needs to employ the expressions listed in the section 2.2.3.

2.2.2.3 Methodology of insulation system design per statistical analysis

From the practical point of view, the statistical analysis of an insulation system for design purposes consists of several steps, as described, for example, in [36]. Firstly, a random sample, referred to as a master list, must be collected from the unknown basic population (time-to-failure/breakdown values). The number of performed tests depends on the availability of specimens, ease and length of their testing, and available resources. As a rule of thumb, at least ten tests should be performed. The obtained data are then sorted in ascending order, and each value is provided with a failure probability. The expression for failure probability depends on the chosen theoretical distribution (normal, lognormal, Weibull), through which the statistical parameters are estimated. Next, the sorted data pairs are fitted

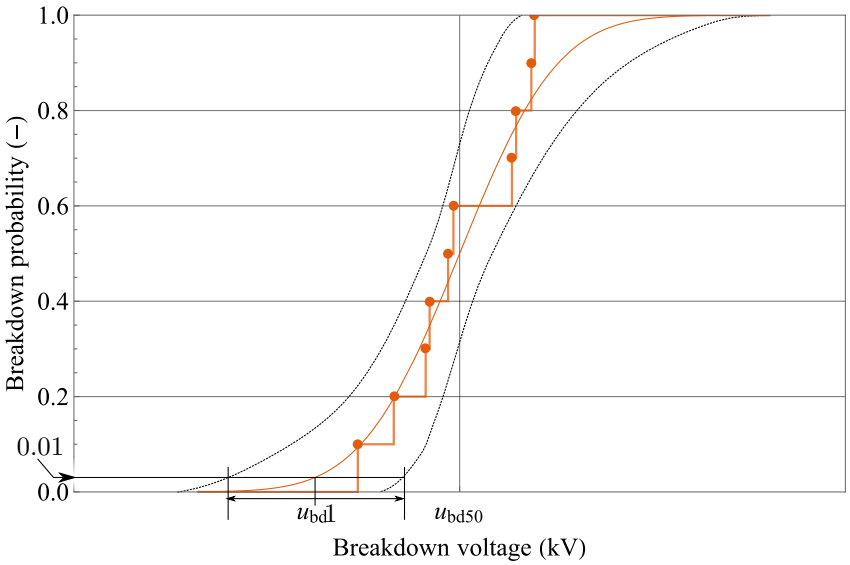

Figure 2.5: Fitting of illustrative breakdown data by cumulative frequency polygon and cumulative distribution function of normal distribution (90% confidence intervals are shown as well). Note how the mean breakdown voltage u_{bd50} and the long-term withstand voltage estimate u_{bd1} are determined. Recreated from [36].

by a cumulative frequency polygon to obtain rough estimates of the cumulative distribution function of the total population. The cumulative frequency polygon is constructed by a simple interconnection of the data points by a staircase function, as shown in Figure 2.5.

A suitable distribution function needs to be fitted to the data to obtain more accurate estimates. Figure 2.5 also illustrates the use of the Gaussian normal distribution function (thin orange line) on breakdown data. In practice, the Weibull distribution function is often preferred, especially for aging data, as recommended by IEC 62539 (IEEE 930). The parameters of the chosen distribution are estimated using an appropriate mathematical method. Most often, the maximum likelihood method is employed, but in more complex cases, other methods might be more viable. Further information about the various parameter estimation methods is given, for example, in [41].

Next, the confidence intervals are calculated, usually at the confidence level of 90 %. The confidence intervals can be calculated for numerous quantiles (apart from the 50 %, i.e., mean value) so that confidence limits (curves fitted to the quantile boundaries) can be plotted. Example confidence limits are shown in Figure 2.5 as the thin dashed curves that envelop both the normal distribution and cumulative frequency polygon. Ultimately, the desired percentile u_x and its confidence interval may be extracted from the plot. For applications where the withstand voltage is of concern, the 1% breakdown voltage (u_{bd1}) is commonly sought after, whereas for aging prediction, the u_{bd50}, eventually u_{bd63} if the Weibull distribution was used, is of interest.

2.2.3 Weibull statistics

2.2.3.1 Weibull distribution

The Weibull statistics are based around the Weibull distribution, which represents a generalization of the exponential distribution. The Weibull distribution provides more utility in terms of shape than is possible for the single-shape exponential distribution, which made it greatly popular in reliability engineering, as well as in the description of the strength of various materials [45]. Similar to the normal distribution, the Weibull distribution is a two-parameter continuous probability distribution. Its cumulative probability function is:

$$F(t) = \begin{cases} 0 & \text{if } x < 0 \\ 1 - e^{-(t/\alpha)^{\beta}} & \text{if } x \geq 0 \end{cases}, \tag{2.7}$$

where t is the measured variable, $F(t)$ is the probability that a random variable from the basic population will be lower than or equal to t, $\alpha > 0$ is the scale parameter, and $\beta > 0$ is the shape parameter. In the context of reliability engineering, $F(t)$ represents the probability of failure at a stress value or time lower than or equal to t. Furthermore, the scale parameter can be interpreted as a failure probability of 63.2 % $(1 - e^{-1})$ and is analogous to the mean value of the normal distribution. Similarly, the shape parameter determines the range of observed times-to-failure and is analogous to the inverse of the standard deviation of the normal distribution.

The mean value and variance (square of the standard deviation) of the Weibull distribution can be expressed respectively as:

$$\mu = \alpha\Gamma\left(1 + \frac{1}{\beta}\right) \tag{2.8}$$

and

$$\sigma^2 = \alpha^2\left[\Gamma\left(1 + \frac{2}{\beta}\right) - \left(\Gamma\left(1 + \frac{1}{\beta}\right)\right)^2\right], \tag{2.9}$$

where Γ is the gamma function.

2.2.3.2 Weibull probability data

Whereas the assignment of failure probabilities to the ordered times-to-failure is straightforward for the normal distribution, a specific expression needs to be used when employing the Weibull distribution. Per IEC 62539, the expression is defined as:

$$F\left(i, n\right) \approx \frac{i - 0.44}{n + 0.25} \cdot 100\ \%, \tag{2.10}$$

where i is the *rank* of the given time-to-failure (1 to n), and n is the total number of tested specimens (master list size).

Eq. 2.11 is valid for so-called *complete data*, i.e., when all test specimens break down over the observed period. If some of the samples withstand, then the term singly censored data is used. Long-term aging tests often provide singly censored data, as it might be impractical or impossible to continue the tests until the failure of the last specimen. In such a case, the failure probability expression is unchanged; only the rank i goes from 1 to r, where $r < n$.

If the data are progressively censored, i.e., some of the samples were suspended at different points of the test, the so-called *rank function* $I(i)$ must be used instead of the simple rank i. The rank function can be expressed as (IEC 62539):

$$I\left(i\right) = I\left(i - 1\right) + \frac{n + 1 - I\left(i - 1\right)}{n + 2 - C_\mathrm{i}} \cdot 100\ \%, \tag{2.11}$$

with $i > 0$ and $I(0) = 0$. The term C_i is equal to the number of broken down and suspended specimens when the i^{th} breakdown occurs. The respective failure probability is then determined from Eq. 2.11, where rank i is replaced by the rank function $I(i)$.

The suitability of the Weibull distribution's use for the given test results can be verified either by eye or by determination of the correlation coefficient. The latter can be performed by transforming the obtained sorted results so that the Weibull distribution fit results in a line. Each parameter is transformed differently; the time-to-breakdown becomes:

$$Y_i = \ln\left(t_i\right), \tag{2.12}$$

whereas the failure probability becomes:

$$X_i = \ln\left(-\ln\left(1 - \frac{F\,(i,n)}{100}\right)\right). \tag{2.13}$$

The correlation coefficient can be established using the least square regression method as the square root of the R^2 value obtained from the X-Y data's linear fit. Its value is then compared to the values extracted from Figure A.8 in IEC 62539 for the given number of broken-down specimens r. If the calculated correlation coefficient is equal or larger, then the use of Weibull distribution is adequate.

2.2.3.3 White method

If the total number of breakdowns in an aging test is lower than 20, IEC 62539 suggests using the White method for parameter estimation. The White method assigns weight w_1 to each data point depending on its order i and the total number of breakdowns r, whereas the respective weight values can be found in Table A.6. of the IEC standard. The modified parameter estimates are determined from the weighted averages of X_i and Y_i (per Eq. 2.12 and 2.13), which can be calculated using the following formulae:

$$\bar{X} = \frac{\sum_{i=1}^{r}(w_i X_i)}{\sum_{i=1}^{r}(w_i)}, \tag{2.14}$$

$$\bar{Y} = \frac{\sum_{i=1}^{r}(w_i Y_i)}{\sum_{i=1}^{r}(w_i)}. \tag{2.15}$$

If the data are progressively censored, the integer value closest to $I(i)$ (employed instead of i) shall be used instead. With $\bar{X}$ and $\bar{Y}$ known, the shape parameter β can be estimated as:

$$\hat{\beta} = \frac{\sum_{i=1}^{r}\left(w_i\left(X_i - \bar{X}\right)^2\right)}{\sum_{i=1}^{r}\left(w_i\left(X_i - \bar{X}\right)\left(Y_i - \bar{Y}\right)\right)}. \tag{2.16}$$

Ultimately, the scale parameter α estimate can be expressed as:

$$\hat{\alpha} = \exp\left(\bar{Y} - \frac{\bar{X}}{\beta}\right). \tag{2.17}$$

2.2.3.4 Weibull percentiles

The scale factor of the Weibull distribution represents the 63.2^{nd} percentile (failure probability of 63.2 %). If an arbitrary percentile t_p is sought after, for instance, for the determination of 1% failure chance, the following expression can be employed to estimate it:

$$\hat{t}_p = \hat{\alpha}\left(-\ln\left(1 - \frac{p}{100}\right)\right)^{1/\hat{\beta}}, \tag{2.18}$$

where p is the probability expressed as a percentage. Significant failure probabilities include 0.1, 1, 5, 10, 30, 63.2, and 95 %.

2.2.3.5 Weibull confidence intervals

As was briefly mentioned above, the expressions for determining confidence intervals use slightly different values in the case of Weibull distribution. The 90 % confidence interval boundaries of the shape parameter β are given as:

$$\begin{aligned} \hat{\beta}_\text{l} &= W_\text{l}\hat{\beta}, \\ \hat{\beta}_\text{u} &= W_\text{u}\hat{\beta}, \end{aligned} \tag{2.19}$$

where the indexes l and u denote lower and upper limits, respectively, and W is a multiplication factor.

Analogously, one needs to employ multiplication factor Z to obtain the confidence intervals for different failure percentiles. The general form of the expression is:

$$\begin{aligned} \hat{t}_{\mathrm{l}} &= \hat{\alpha} \exp\left(Z_{\mathrm{l}}\left(p\right)/\hat{\beta}\right), \\ \hat{t}_{\mathrm{u}} &= \hat{\alpha} \exp\left(Z_{\mathrm{u}}\left(p\right)/\hat{\beta}\right), \end{aligned} \tag{2.20}$$

where $\hat{t}_{\mathrm{l}}$ and $\hat{t}_{\mathrm{u}}$ are the lower and upper bounds of the 90 % confidence interval for the p^{th} percentile. The 63.2^{nd} percentile is used to determine the confidence interval of the scale parameter. The values of W and Z must be extracted from Figures A.14 to A.29 in IEC 62539 for the given r and n.

If the confidence intervals for 0.1^{st}, 1^{st}, 5^{th}, 10^{th}, 30^{th}, 63.2^{nd}, and 90^{th} percentiles are obtained, confidence limits can be plotted by a simple connection of the upper and lower limit points by a smooth line, respectively.

2.2.4 Aging models

2.2.4.1 Introduction

Consequent to the above, the lifetime of a given insulation system can be estimated from the expected thermoelectrical stresses using an aging model. The obtained estimation can be either relative to already known lifetime–stress data or absolute. The former is typical for empirical models, whereas physical models should provide a lifetime estimate without the need for reference data (they are still helpful for model verification). These data are sometimes available from the industry, but more often, they need to be obtained from accelerated aging tests.

Empirical models can be simplified by disregarding the thermal stress if the reference and expected temperatures are identical. For practical applications, the expected temperature is often taken as the maximum operating temperature of the given insulation system to provide the worst-case scenario prediction. Analogously, the same can be done with electrical stress to obtain a single-stress, thermal aging data. However, in contrast to electrical aging, the dependence of reaction rate on temperature is well-known from the transition state theory, on whose correctness there is a general agreement (both the Arrhenius and the Eyring equations that describe the dependence are established in physical chemistry for almost a century). For practical purposes, thermal aging is treated as a single degradation process described by the Arrhenius [46] or the modified Arrhenius [47] equations (empirical forms of transition state theory equation). Since both these equations utilize an empirical constant (preexponential term), reference data are also required. It is worth mentioning that in some relatively rare cases, mechanical stresses might also be considered.

Hence, if the chosen stress can be singled out by following the logic above, one can employ single-stress aging models to predict the lifetime of a given system. If not, the use of multi-stress empirical or physical models is necessary. The greatest pitfall of the multi-stress empirical models is the mutual cumulative effect of the considered stresses, meaning that individual single-stress data cannot be simply combined to predict the combined degradation effect, that is, unless the stresses are purely sequential [48]. A large number of reference data is typically required to obtain the lifetime n-dimensional surface. More information about each model type, including examples, is given below.

2.2.4.2 Single-stress (electrical) empirical aging models

An early yet essential example of single-stress empirical models is the inverse power law (IPL) model of the early 1970s, which represented a significant output of the first decade of initial basic research on the breakdown in solids [38]. Publications of import concerning the IPL include the works of W. Nelson [49] and L. Simoni [50]. Per the publications, the IPL for electrical (single-stress) aging can be expressed as:

$$\theta(U/E) = \frac{1}{K(U/E)^n}, \tag{2.21}$$

where θ is the characteristic life of the examined system, U/E is the voltage/electrical stress, and K and n are (positive) empirical parameters specific to the material and test method. An example of the

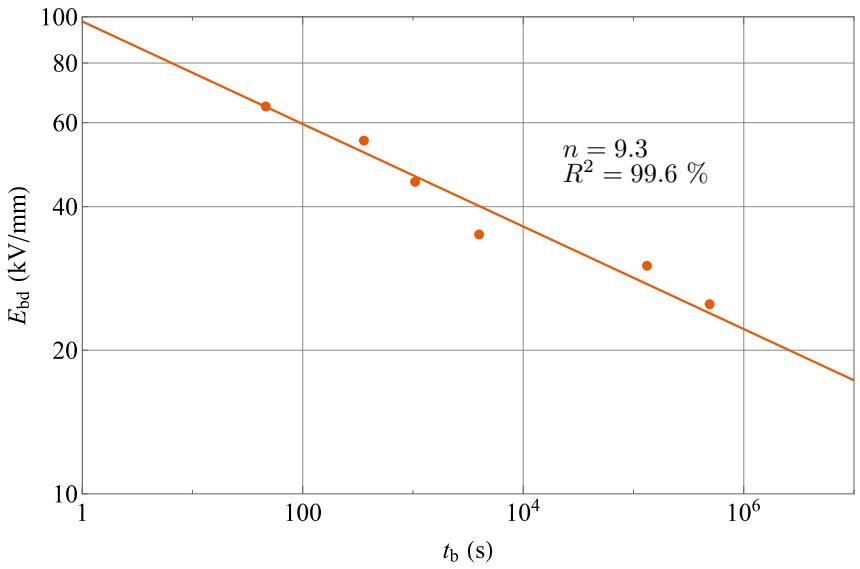

Figure 2.6: The inverse power law fitted to aging data obtained from accelerated electrical aging tests of oil impregnated paper performed in [10]. Plotted in logarithmic–logarithmic coordinates.
Note: only the parameter n *is typically stated, as it defines the slope of the lifeline, and thus provides an easy way to compare aging data from different experiments.*

application of IPL on aging data is shown in Figure 15. The data are plotted in an $\ln(E)$ vs. $\ln(t)$ coordinate system so that the IPL model fit produces a line.

Due to its simplicity, the IPL became widely used, and as a result, reference data for various stress-insulation system combinations are available in great numbers. Critique of the IPL is mainly aimed at its tendency to give too optimistic predictions from laboratory measurements performed at high fields, its disregard for other stress types, and its occasional ambiguity [43]. Furthermore, when the model was applied to aging data obtained from accelerated tests of extruded polymeric cables, it did not fit the data well due to the presence of a low-field aging regime, which drastically reduces the aging rate when the test voltage is below a particular threshold value [51]. The authors of the study thus proposed a modification to the IPL model, which would also consider the low-field aging regime:

$$t_\mathrm{b} = \left[f_1 b_1 \left(e^{b_2 (E - E_\mathrm{th})} - 1 \right) \left(e^{b_3 E_\mathrm{bd}} + b_4 \right) \right]^{-1}, \tag{2.22}$$

where t_b is the expected time to breakdown (identical to characteristic life), f_1 is the frequency of the applied AC field or the number of applied transients, b_1 to b_4 are empirical constants, and E, E_th, and E_bd are the applied, threshold, and breakdown field strengths, respectively. Although the modified equation describes the aging data of extruded polymeric cables well, the high number of unknowns limits its use only to large datasets, whose fitting will most likely provide ambiguous results.

Another single-stress empirical model type was proposed in 1978 by T. W. Dakin and S. A. Studniarz. Following the assumption that electrical aging follows similar exponential dependence as thermal aging [52], a so-called *exponential electrical aging model* was published in [53]. Apart from the "standard" high-stress aging regime, a threshold due to the cessation of partial discharge activity (assumed to be the primary degradation mechanism) at weak fields was incorporated. The model predicted the dependence of time-to-breakdown of the given system on the applied field strength to be:

$$t_\mathrm{b} = \frac{(Af)^{-1}}{E - E_\mathrm{th}} \exp\left[\frac{E - b\,(E - E_\mathrm{th})}{kT} \right], \tag{2.23}$$

where A is the fraction of electrons reaching the (cavity) surface and causing degradation, f is the frequency, E and E_0 are the applied and threshold electric field strengths, k is the Boltzmann constant, T is the thermodynamic temperature, and b is "a factor containing the electric charge and an equivalent mean distance it must move in the field to give the mean energy reduction obtained by the mean applied

field" [53]. Especially from the latter's definition, it should be evident that although the terms A and b have physical meaning, their definition is somewhat impractical. Hence, the exponential model is listed among the empirical ones.

The exponential model managed to describe the change in the lifeline observed at low field stresses (so-called "tail") quite well. However, the fundamental premise of the model was later disproved in [54], where no space charge injection into the aged and later broken-down samples was observed, indicating that partial discharges were not the cause of the failure. It was also observed that purely mechanical lifelines are similar to those obtained solely under electrical stresses, including the transition at low-stress levels [43]. This fact led J.-P. Crine, L. Dissado, G. C. Montanari, L. Simoni, and others to edit the exponential model further according to the transition state theory, as they suspected that the similarity between the two stress types originates therein. These new exponential model iterations technically represented physical models, and they are hence listed below.

2.2.4.3 Crine (physical) aging model

Although the contributions of the authors mentioned above to the revamp of the exponential model were also significant, this thesis deals further only with the model proposed by J.-P. Crine (Crine model), as it was explicitly derived for extruded polymeric insulation – the subject of two out of three experiments performed in the scope of this work.

The Crine model [44,55–57] is based on the existence of so-called molecular holes in the amorphous phase of semicrystalline PE/XLPE materials (PE: 35 to 94 %; dicumyl-peroxide-crosslinked XLPE 35 to 41 % crystallinity [58]). As opposed to the crystalline phase, where individual polymeric chains are densely and regularly stacked, the chains in the amorphous phase are disordered and have thus relatively large empty spaces (molecular holes) in between [59]. Under mechanical stresses (among others also exerted by electrostatic forces), the free volume might be rearranged to form submicrocavities (also referred to as submicrocracks) [60]. In these submicrocavities, injected free electrons may obtain enough kinetic energy through electric field acceleration to break the relatively weak van der Waals intermolecular bonds, whose bond energies are typically between 0.1 to 0.4 eV. In this stage, the free electron energies cannot reach sufficient values to break the intramolecular bonds (3.6 to 3.9 eV), which hold together individual monomers of the long polymer chains [44].

However, as the intermolecular bonds break, additional free volume is created in the amorphous phase. Consequently, the injected free electrons can be accelerated to higher energies due to the longer mean free paths. The Crine model theory supposes that more and more intermolecular bonds are gradually broken, and therefore the mean free path becomes longer, and the electrons can obtain more energy. This stage represents the aging process, which is subsequently concluded by the breakdown of the insulation system. The breakdown is expected to occur shortly after the free electrons are able to obtain enough energy to break the intramolecular bonds [44]. Apart from the ultimate failure of the system, the (pre)breakdown phase is marked by a quick worsening of the system's insulating properties.

Using the transition state theory, the authors proposed that an energy barrier between the unaged (no bond broken) and aged (van der Waals bond broken) states controls the aging process. The height of the energy barrier is equal to the standard Gibbs energy of activation of the bond scission for zero electrical stress $\Delta G_0^{\ddagger}$. Without any applied electrical stress, the probability that the scission process takes place can be expressed as:

$$p \simeq \left(\frac{kT}{h}\right) \exp\left(-\frac{\Delta G_0^{\ddagger}}{kT}\right), \tag{2.24}$$

where h is the Planck constant. Since the bond scission process is reversible, i.e., the broken bonds can be rebounded, and since the model assumes that the Gibbs free energy of both states is the same, the probability of the reverse process in the absence of stress must be identical (transition state theory).

When an electric field of strength E is applied to the system, the barrier height $\Delta G_0^{\ddagger}$ is reduced by deformation work W, carried out on the molecular chains over the submicrocavity size λ. The deformation work can be calculated as $W = e\lambda E$, where e is the elementary charge. Since the deformation makes the bond scission easier, its probability (marked by a +) will be increased to:

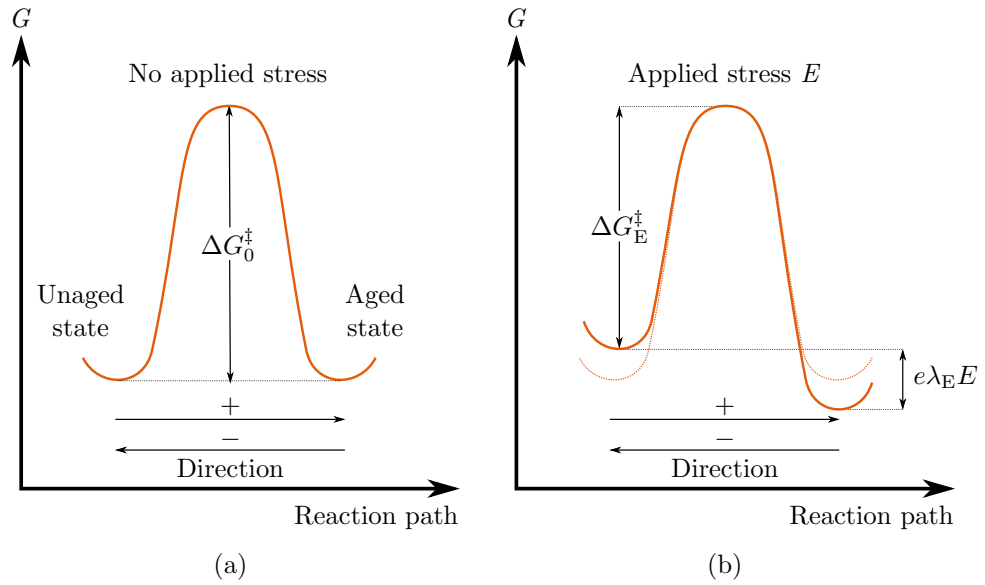

Figure 2.7: The energy barrier between the unaged and aged states of an insulation system under no applied stress (a) and applied electrical stress E (b). Recreated from [44].

$$p_+ \simeq \left(\frac{kT}{h}\right) \exp\left(-\frac{\Delta G_0^{\ddagger} - e\lambda E}{kT}\right), \tag{2.25}$$

whereas the probability of the bond rebounding (marked by a $-$) will be reduced to:

$$p_- \simeq \left(\frac{kT}{h}\right) \exp\left(-\frac{\Delta G_0^{\ddagger} + e\lambda E}{kT}\right). \tag{2.26}$$

Figure 2.7 illustrates the situation in terms of Gibbs free energy of individual states – the energy of the unaged state is increased by $e\lambda E/2$, while the energy of the aged state is reduced by $e\lambda E/2$. The barrier between the states is thus smaller in the $(+)$ direction and simultaneously larger in the $(-)$ direction. The indexes E mark the influence of the applied electric field.

The net probability of scission reaction can be expressed using the hyperbolic identities as:

$$p = p_+ - p_- \simeq \left(\frac{2kT}{h}\right) \exp\left(-\frac{\Delta G_0^{\ddagger}}{kT}\right) \sinh\left(\frac{e\lambda E}{kT}\right), \tag{2.27}$$

while the expected lifetime of a given insulation system can then be estimated by inverting Eq. 2.27:

$$t \simeq \left(\frac{h}{2kT}\right) \exp\left(\frac{\Delta G_0^{\ddagger}}{kT}\right) \operatorname{csch}\left(\frac{e\lambda E}{kT}\right). \tag{2.28}$$

Two different aging regimes are incorporated in the lifetime prediction: the high-field regime, in which the hyperbolic cosecant part behaves as an exponential (*exponential regime*), and the low-field regime, where the cosecant starts to approach infinity as the applied field E approaches zero (*non-exponential regime*).

Parameters $\Delta G_0^{\ddagger}$ and $\lambda_{\max}$ can be determined from the slope and intercept of the exponential regime. The latter represents the maximum submicrocavity size (scattering length) due to the mechanical strain, which is, however, not identical to the λ term employed in the model. In [44], the authors proposed

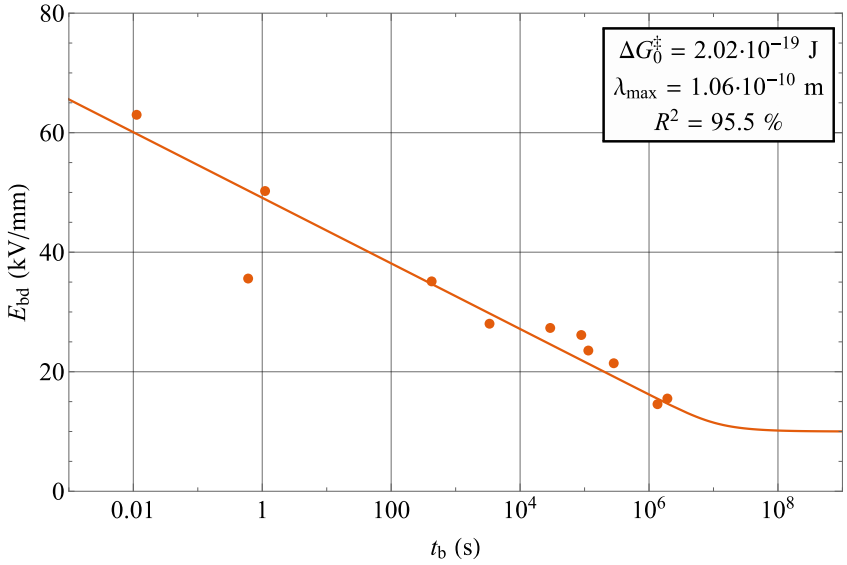

Figure 2.8: An example fit of Crine model (submicrocavity size) to XLPE cable sample aging data gathered in [61]. Plotted in logarithmic–linear coordinates.

that the submicrocavity size is more or less constant and equal to λ_{max} throughout the exponential aging regime, whereas it sharply drops to very low values below a certain threshold, which corresponds to the change of aging regime to non-exponential. The threshold is represented by a critical field strength E_c, below which it is assumed that bond scission and rebounding are equiprobable. To provide a physical meaning to the term, the authors attribute the aging regime transition to the exceeding of deformation work over the polymer's cohesion energy E_{coh}. The critical field strength can then be defined as:

$$E_c \simeq \frac{E_{coh}}{e \cdot \lambda_{max}} = \frac{\Delta H_{vap} - kT}{e \cdot \lambda_{max}}, \tag{2.29}$$

where ΔH_{vap} is the heat of vaporization of the polymer. As evident, the cohesion energy reduces with increasing temperature, indicating that the critical field strength will be lowered as well. Consequently, the intensive exponential aging regime will be reached at weaker fields, and the expected lifetime at such fields will thus be shortened significantly.

The comparison of calculated and experimentally obtained values of critical field strengths performed in [44] revealed that the values obtained by Eq. 2.29 are in some cases slightly inaccurate. Nevertheless, the values determined for XLPE (5 to 12 kV/mm experimentally, 6 to 16 kV/mm from calculation) are shown to be in a good agreement with the field values above which charge injection into the polymer starts taking place, and thus such estimations can be readily used for lifetime model fitting. An example fit of the Crine model to the data obtained from aging of XLPE cable samples in [61] using $T = 293.15$ K and $E_c = 10$ kV/mm is shown in Figure 2.8.

The critique of the Crine model was aimed mainly at the unclear dependence of the employed parameters on both temperature and electric field [62]. Indeed, the authors of the original work, in which the Crine model is proposed, dedicated several sections to the explanation of dependence of the parameters on temperature, electric field, impurities, and environment (humidity), and the mutual dependence of the parameters. However, the clarification is somewhat complex and does not answer all the questions. A further endeavor to remedy the shortcomings was made in [55], where the barrier height reduction was attributed to Maxwell stress creating surface tension in submicrocavities. Apart from introducing the activation volume term ΔV, the dependence of the barrier reduction on the applied electric field strength was proposed to be quadratic instead of linear. The new iteration of the model takes the form:

$$t \simeq \left(\frac{h}{2kT}\right) \exp\left(\frac{\Delta G}{kT}\right) \operatorname{csch}\left(\frac{\Delta V \cdot \varepsilon \cdot E^2}{2kT}\right). \tag{2.30}$$

where ΔG is the height of the energy barrier for $E = E_c$, and ε is the permittivity of the material. The

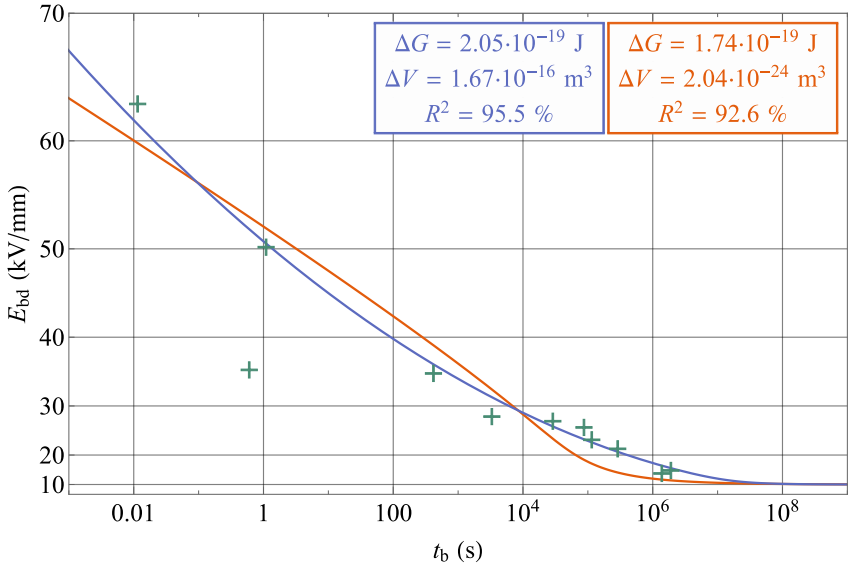

Figure 2.9: Example fits of Crine model (activation volume) to XLPE cable sample aging data gathered in [61]. Two different "best" fits were obtained, with each showing a significant difference between the obtained and expected value of parameters. Plotted in logarithmic–quadratic coordinates.

activation volume ΔV represents the sum of the volumes of the microcavities formed over the total aging time t. In this case, the transition between the two aging regimes is determined from the dependence of the activation volume on the total aging time. By retrofitting older XLPE cable aging data, it was shown in [55] that the activation volume increases with aging time up to the value corresponding to $E = E_c$, above which the volume drops sharply (practically no microcavities are formed). Analogously to the former model iteration, the critical field value can be calculated from the polymer's cohesion energy as:

$$E_c = \sqrt{\frac{2E_{\mathrm{coh}}}{\Delta V \cdot \varepsilon}}. \tag{2.31}$$

The prime advantage of this iteration of the Crine model is the known (or measurable) dependence of permittivity on temperature. Although the situation is more complex for the activation volume, it nonetheless represents a parameter with a clear physical definition, as well as some degree of measurability.

Two example fits of the modified Crine model to XLPE aging data are shown in Figure 2.9. Both fits were obtained using the linear least-square regression method for relative permittivity $\varepsilon_r = 2.3$, thermodynamic temperature $T = 293.15$ K, critical field strength $E_c = 10$ kV/mm, and various initial value estimates of the parameters ΔG and ΔV. The figure illustrates the occasional unambiguity of the model, which stems from the extremely low values of the exponent/hyperbolic cosecant arguments. Some parameter estimates can result in argument values below machine precision, which may cause false identification of extreme values during the best fit calculation.

Two subsequent iterations of the Crine model were presented in [56] and [57]. While the changes to the lifetime estimation formula are minimal – addition of a term describing frequency for DC and higher AC/impulse frequencies and a slight alteration to the Maxwell stress term – the works make significant contributions to the theory behind the primary aging process. Although it was proposed that low-energy intermolecular bonds are disrupted by accelerated free electrons and are hence the cause of the long-term aging, it was still unclear how the electrons can reach enough energy to cause scission of intramolecular bonds (C–C) in the (pre)breakdown phase. Although the C–C dissociation energy is in a normal state too high (3.6 to 3.9 eV), it is expected to be reduced by the gradual relaxation of the bonds when an electric field is applied [63]. The dependence of dissociation energy D_E on time due to the relaxation at a given applied electric field strength E can be written as [56]:

$$D_E = D_0 \exp\left(-\frac{t}{\tau_E}\right), \tag{2.32}$$

where D_0 is the dissociation energy of the bond in the normal state. If one supposes that the bonds will be completely relaxed at $t = \tau_E$, where τ_E is the time to breakdown at the given applied field, the dissociation energy will be reduced to about $2.1 \cdot 10^{-19}$ J. Such a value is similar to the typical barrier heights ΔG obtained from XLPE aging data, suggesting that the typical free electron energies might be sufficient to break the **intramolecular** bonds toward the end of the aging process. This observation further confirms that the acceleration of free electrons inside the microvoids and the subsequent bond scission might be the primary degradation mechanism if the others (electrical treeing, water treeing, intense partial discharge activity) are sufficiently suppressed.

Caution needs to be exercised when comparing activation volumes extrapolated from samples of different sizes, as it was shown in [56] that the obtained activation volumes of XLPE samples are linearly dependent on the sample volume. Lower activation volumes predict slower aging, which can be dangerous if the same activation volume is used for lifetime prediction of the much larger insulation systems used in practice.

Ultimately, the last model iteration [57] suggests adding a frequency-dependent term a to the denominator of the preexponential term. The term represents the number of power cycles per second (i.e., $a = 2f$) and should provide direct comparability between DC and AC electrical aging in terms of lifetime. A further reduction (by a factor of four) of the DC lifetime due to the application of AC stresses of the same voltage (AC RMS equal to DC average) is assumed from the difference in dissipation losses. The subsequent model application on both AC and DC aging data of similar XLPE samples provides a decent fit to both. Nevertheless, the main contribution of the frequency term in the context of this dissertation is the definition of the lifetime dependence on waveform frequency, as it may be used in the estimation of the effect of supraharmonics' presence.

Overall, the Crine model represents a long-standing effort to explain and describe the physicochemical origin of electrical aging of extruded polymers. Due to its continuous development as new aging data and diagnostic methods were becoming available, as well as its strong link to physical chemistry, the model was considered vital to this thesis, and hence it was described in greater detail at the expense of others.

2.2.4.4 Multistress empirical aging models

As is evident from the previous paragraphs, even the latest iterations of physical aging models cannot directly describe the effect of temperature on the aging rate. The same conclusion, albeit for older iterations, was reached already in 1984 by L. Simoni in [64]. Instead of further commitment toward the physical (physicochemical) description of electrothermal aging, the author proposed an empirical multi-stress aging model that was based on the two well-established models of each of the two stresses – inverse power law (electrical) and Arrhenius model (thermal). The following equation defined the general form of the model:

$$\left(\frac{ES}{ES_0}\right)^{n^*-1} = 1 - \frac{t}{L_0}\left(\frac{E}{E_0}\right)^{n^*} \exp\left(B \cdot DT\right), \tag{2.33}$$

where ES is the *electric strength* of the system following prestressing (aging) for time t (index 0 marks no prestressing) and the exponent $n^* = n - b \cdot DT$ with n being the voltage endurance coefficient, b a material constant determining the combined-stress behavior, and $DT = 1/T_0 - 1/T$ the applied thermal stress. The electric strength of the system is reduced by (prestress) time t, applied electrical stress E, and thermal stress DT, modified by the constant B. Electrical stress has a threshold E_0, below which the electrical aging is expected to cease. At room temperature and below the threshold E_0, the insulation lifetime L is equal to its maximum value L_0. To obtain the estimated lifetime of the insulation, one needs to put $t = L$ and $ES = 0$ (breakdown conditions) and rearrange the equation to express either L/L_0 or directly L. Individual single-stress aging models can be obtained by putting $T = T_0$ (room temperature), or $E = E_0$. An illustrative plot of the Simoni multi-stress model is shown in Figure 2.10. Note the single-stress lifelines due to the use of the linear–logarithmic–logarithmic coordinate system.

The ultimate iteration of the Simoni multi-stress model was published a decade later by a collective of authors from the University of Bologna in [65]. The new model was intended to be as general as possible to reliably describe the aging of materials both with and without the threshold behavior. It takes the following form:

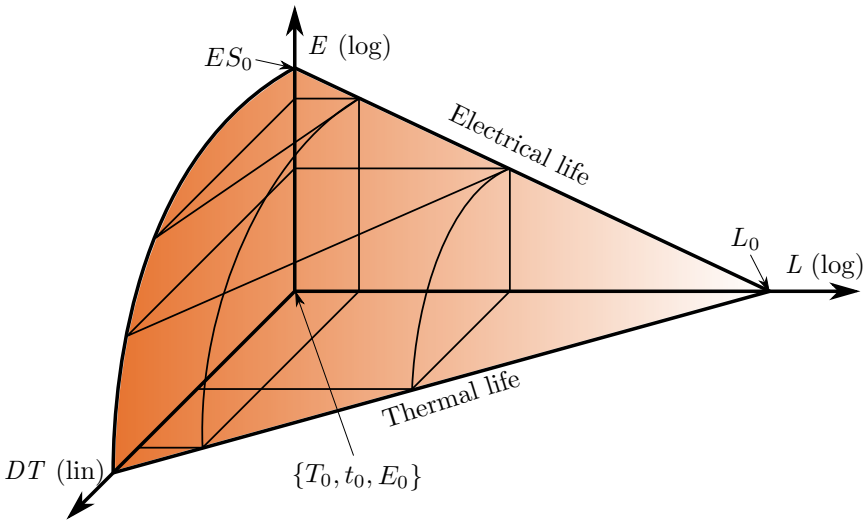

Figure 2.10: An illustration of a Simoni multi-stress model plot. The expected lifetime of the system under given conditions (temperature, applied field strength) can be obtained from the "life surface" marked in the orange gradient.

$$L = L_0 \frac{\exp\left[-n\log\left(E/E_0\right) - BT + bT\log\left(E/E_0\right)\right]}{\left[\frac{\log\left(E/E_0\right)}{\log\left(E_{t0}/E_0\right)} + \frac{T}{T_{t0}} - k\frac{\log\left(E/E_0\right)}{\log\left(E_{t0}/E_0\right)} \cdot \frac{T}{T_0} - 1\right]^{\beta}}, \tag{2.34}$$

where k is a constant describing the threshold line shape, E_{t0} is the electrical aging threshold at room temperature T_0, T_{t0} is the thermal aging threshold at electric field strength E_0, below which the electrical aging can be neglected, and β is an exponent determining threshold behavior of the aging. If $\beta = 0$, the expected insulation lifetime is identical to the one obtained by rearrangement of Eq. 2.33. An illustrative plot of the Simoni multi-stress model for insulation system showing threshold behavior is shown in Figure 2.11.

The general Simoni multi-stress aging model (Eq. 2.34) employs a total of seven parameters with one additional complementary parameter that can be readily determined from the others. Four parameters, namely n, B, E_{t0}, and T_{t0} can be determined from single stress measurement, and another parameter, L_0, should be typically available from reference data or can be estimated as the intersection of thermal lifeline and ambient temperature from purely thermal aging tests [65]. Therefore, the fitting of "life surface" is achieved chiefly through b and β only. Naturally, the model fitting becomes much easier if the threshold behavior is not present or is neglected.

To obtain the "life surface" of a given insulation system with as few aging tests as possible, one should proceed methodically. The single stress tests provide the outline of the graph surface, as well as rough (maximum) estimates of the lifetime at the given combination of stresses. The multi-stress tests should be designed to provide more (reasonably spaced) data points at higher stresses, where the curvature of the graph surface is considerable and the test times are short, which ensures that only a few points are needed at lower stresses, where the curvature is minimal and test times are much longer.

With the necessary tools for the evaluation of accelerated aging tests revised, let us proceed to the actual topic of aging under non-standard electrical conditions.

2.2.5 Aging & high-frequency oscillation/repetitive impulse phenomena

A review of works and respective findings concerning the effect of high-frequency oscillations on the aging rate of insulation systems is presented in the following paragraphs. The review is limited to aging phenomena not directly connected to partial discharges, as those are listed separately as a part of section 2.3. Since research articles on the direct impact of supraharmonics on the aging of insulation materials are scarce, the review also deals with the effect of chosen repetitive impulse overvoltages and square waveforms, whose characteristics are deemed to be similar to those of supraharmonics.

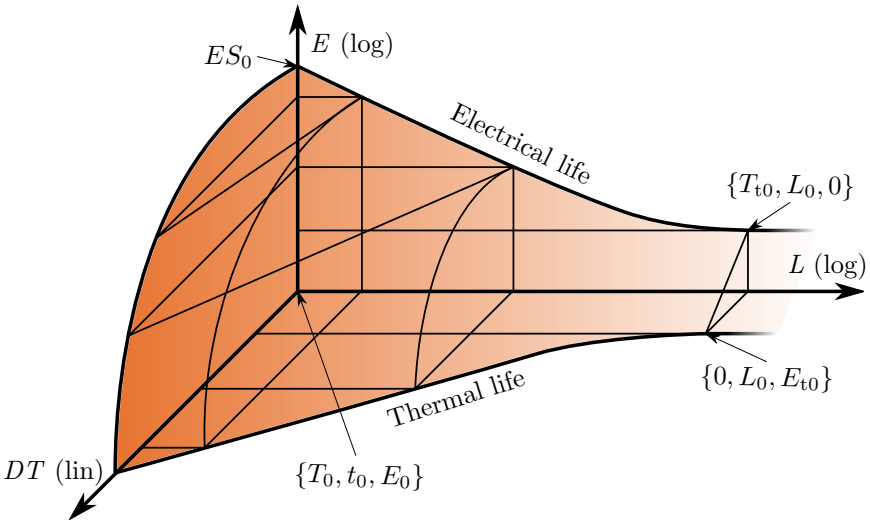

Figure 2.11: An illustration of a Simoni multi-stress model plot of an insulation system showing threshold behavior. The expected lifetime of the system under given conditions (temperature, applied field strength) can be obtained from the "life surface" marked in the orange gradient. The threshold curve (between points $\{T_{t0}, L_0, 0\}$ and $\{0, L_0, E_{t0}\}$) is a line, meaning that $k = 0$ for this particular case.

The section is split into three parts – the first two are concerned with the additional aging mechanisms associated with the presence of high-frequency oscillations: changes in the local field distribution and increases in dielectric losses. These phenomena were often identified in experiments carried out on cable terminations, which bore an analogy to the one performed within the framework of this thesis. Since the second experiment conducted within the thesis investigated the accelerated aging of thin polymeric film specimens, the last part reviews the works dealing with this topic.

2.2.5.1 Changes in the local electric field distribution

Repetitive impulse voltages were identified as a cause of the premature breakdown of insulation systems already in 1956 [66]. The authors of the study implemented the use of accumulative effect for repetitive impulses, which had not seen usage until the 1990s when PWM-type inverter-fed motors became widespread [67]. Later works, such as [68], illustrated that these inverter-fed motors could cause premature breakdown of their insulation systems due to the emergence of PWM-induced repetitive impulse voltage stresses. The electric field distribution between the turns of inverter-fed motor windings was shown to be substantially distorted by these stresses, owing to the strong transient response determined from the windings' passive parameters [69]. Furthermore, the local field would be gradually strengthened due to the long-term application of non-standard voltage waveforms, as was concluded in [70]. The work investigated electrical aging of twisted pair enameled wires under 50-Hz sinusoidal and 10-kHz square pulse voltage waveforms. Subsequently performed thermally stimulated current (TSC) measurements revealed that the square pulse waveforms indeed enhance the deposition of space charge.

Similarly, high-frequency oscillations and fast voltage rises substantially alter the local field distribution in power transformers due to their large inter-turn and turn-to-ground capacitances [71]. A rather extreme example of the issue is shown in [72], where the model of a 4-kV MV medium-frequency transformer predicts that the electric field in the vicinity of its turns might reach dangerous values of up to 2.5 kV/mm if PWM voltage with very-fast rise times is fed to the transformer (see Figure 9 in [72]). Inter-turn and interlayer voltage calculations in a power transformer were performed for voltages with fast and very-fast rise times in [73] and [74], respectively. Both works concluded that such waveforms could substantially enhance the respective local electric fields.

Due to the use of stress-grading layers, cable terminations (see section 2.4.2.2) are also prone to developing strong local electric fields. In 2003, [18] was published as one of the first complex studies of the phenomenon. The study investigated the cause of a series of rapid failures of XLPE cable terminations (four failures within the first three days after commissioning) in the Eagle Pass installation at the border between the USA and Mexico. Analysis of the voltage waveforms revealed an unexpectedly large content of supraharmonics (particularly at 12.4 kHz). It was shown that these supraharmonics, as well as

high-order standard harmonics, substantially alter the local electric field distribution in the stress-grading layers of the cable terminations (compare Figure 6 and 9 in [18]). The sequence of processes leading to the cable termination failure was identified to start with the drying-out of silicon grease (the result of local hotspots due to the strong fields), followed by migration of the grease and the associated formation of cavities, in which partial discharges are incepted. Electrical treeing then takes place and creates a conductive channel, through which the breakdown ultimately propagates. The work also proposed a specific design of the stress-grading layer to solve the issue. In the same spirit, articles [75] and [76] investigated the topic further. The last article proposed the addition of a semiconductive layer with a lower conductivity and high relative permittivity in between the stress grading and original semiconductive layers to optimize the electric field for a broad range of frequencies.

Development of larger-than-usual space charge due to pulsed voltages representing the PWM-distorted voltage waveforms was observed in [77]. The experiment was carried out on 25-µm thick polymeric samples (two types of polyester and one type of polyimide) representing standard insulation systems used in LV rotating machines. Similarly, internal space charge distribution resulting from the application of repetitive voltage surges was examined on 125-µm thick polyimide specimens representing the same insulation systems in [78]. The pulsed electro-acoustic method (PEA) was used to measure space charge accumulation under positive and negative unipolar impulses of various repetition frequencies (10 to 500 Hz). The polarity effect seemed to play a vital role in the process, as the positive space charge deposited faster at lower repetition frequencies, whereas the negative one accumulated quicker at higher frequencies. The maximum observed increase in the local field was about 19 % for the negative voltage and about 16 % for the positive voltage.

The above paragraphs should illustrate that the internal space charge redistribution due to high-frequency oscillations or fast rise voltages can cause issues in many insulation systems used in the power engineering industry. Fundamentally, the locally strengthened electric field accelerates the degradation processes via the increased electrical stress, as clearly predicted by aging models. The inception of PDs that would not normally take place is of concern as well, mainly due to the subsequent development of electrical treeing – these topics are discussed later in the respective section. In line with the intrinsic aging topic, increased dielectric losses, which are partly caused by the strengthened local electric fields, are reviewed next.

2.2.5.2 Increases in dielectric losses

When examining the fundamental dielectric losses formula, it should be evident that superposed harmonic oscillations, such as supraharmonics, must increase the overall heat generation. The research report of CIGRE working group D1.43 defined the contribution of an h^{th} harmonic component toward the total dielectric losses as:

$$P_h = h\omega_1 C_h V_h^2 \tan\delta_h, \tag{2.35}$$

where ω_1 is the fundamental frequency, C_h and $\tan\delta_h$ are the insulation's capacitance and loss tangent at h^{th} harmonic, respectively, and V_h is the magnitude of the h^{th} harmonic of the applied voltage. A simple summation of Eq. 2.35 over the considered harmonic range provides the total dielectric losses. The process can be applied to determine losses under any periodic waveform, as such waveform can always be expressed in sinus terms via a Fourier transform.

Inverter-type voltages can significantly complicate the calculation of dielectric losses, as their typical waveforms are trapezoidal and therefore contain non-marginal harmonic content up to a very high order. A simplified calculation resolving the issue has been proposed in [79] (see Eq. 5.51 and 5.53): instead of the summation, which requires the knowledge of C_{h} and $\tan\delta_{\text{h}}$ for all the components, the thesis offered an expression demanding only a total of four parameter values. The author's other work, [80], also proposed an equation that would directly estimate the hotspot temperature of a polyethylene terephthalate (PET) foil due to dielectric heating. Analogous to the former article, [81] has suggested an expression for calculating dielectric losses under a trapezoidal voltage waveform, defined by four time-parameters. To further simplify the calculation, the expression employed (voltage) weighting coefficients p_{n}, determined from the spectrum of a trapezoidal waveform (see Figure 2 in [82]). The dielectric losses under an ideal square and square-like (exponential rises and falls) waveforms were investigated in [83]. Two loss regimes were identified – one below the cut-off frequency f_{c} and one above it. In the latter, the dielectric losses would decrease with the cube of frequency, indicating quick convergence to the sought-after total value of losses. Depending on the ratio between the waveform's rise time and its period, only dielectric

losses components up to a particular harmonic order would have to be calculated to obtain a reasonable estimation of the total losses (see Figure 2 in [83]).

Several experiments concerning the topic of increased dielectric losses were also performed with cable terminations. The temperature distribution on the surface of a cable termination was modeled and measured in [75]. It was shown that the dielectric losses under a 22-kHz sinusoidal waveform increase the maximum surface temperature by about 8 K when compared to the standard 50-Hz waveform. Square pulse, PWM, and impulse voltage waveforms were applied to cable termination specimens in [84]. Similarly, the measurements revealed increases in the maximum surface temperature under all waveforms by units of Kelvin. Another article [85] further investigated the influence of square wave pulses on the dielectric losses of cable terminations using *finite element method* (FEM) modeling and temperature distribution measurements. Two different cable termination designs were employed in the study, whose FEM models predicted an increase in the hotspot temperature by about 6.5 and 14 K, respectively. Surface temperature distribution measurements subsequently verified these estimations.

Suffice to say, the combination of locally strengthened electric fields and increased dielectric losses (which are often intertwined) was repeatedly shown to cause substantial issues to various insulation systems of devices used in the electrical power industry. Some additional degradation mechanisms of polymers due to the non-uniform AC fields had already been proposed before the topic became crucial: bond scission by energetic photons released by electroluminescence [86], bond scission by energetic charge carriers injected into the material [87], and Maxwell-stress-induced formation of cracks, from which electrical trees may propagate [88]. It is, therefore, useful to examine the aging of thin-film specimens under the considered voltage stresses since the uneven distribution of electric field and dielectric losses are expected to play a lesser role in their degradation. Other effects, such as the ones mentioned above, might be thus identified more easily. A review of experiments concerned with such aging is given next.

2.2.5.3 Experiments on thin-film specimens

Electroluminescence of 100-µm thick transparent epoxy specimens under repetitive voltage surges was investigated in [89]. The resulting observations were subsequently put into the context of degradation in [90] by performing short-term aging experiments under unipolar (positive or negative) voltage surge waveforms, during which the electroluminescence of specimens was measured. Interestingly enough, more electroluminescent activity was observed for specimens stressed by the negative voltage surges, even though their times-to-failure were longer on average. No breakdown occurred within the experiment timeframe in samples, where electroluminescence was not detected.

No additional effects (apart from the increased dielectric losses) were proposed for the intrinsic aging of layered thin plastic foils with thin fleece layers under 50 Hz and 50 kHz AC voltage performed in [91]. Curious contraindicative results were also obtained from the short-term aging tests of PET foils in [80]. The lifetime of specimens stressed by mixed-frequency (DC and superposed AC) voltages below the respective PD inception value did not show any dependence on the rise time of the superposed PWM square pulses, suggesting that neither dielectric losses nor any other additional effect played a significant part in the specimens' breakdown. However, it should be noted that the applied electrical stress was very high (above 400 kV/mm DC) and that the peak value was identical for both the pure DC and mixed-voltage stresses.

On the other hand, short-term aging under trapezoidal voltage substantially increased the loss tangent of 50-µm thick oil-impregnated paper (OIP) specimens in [81]. The greatest extent of the effect was observed for waveforms with rise times of 0.9 and 1.2 µs at frequencies around 1 Hz. Similarly, short-term aging of OIP, albeit using 50-Hz and 1500-Hz AC waveforms, was carried out in [92]. The aging and the accompanying breakdown tests revealed that failure occurs at much lower electric fields under the 1500-Hz waveforms. No explanations of the difference in breakdown or time-to-failure values were offered.

Furthermore, short-term aging of OIP insulation under pure 50-Hz AC and 50-Hz AC with superposed 6-kHz sinusoidal bursts of repetition frequency of 700 Hz was investigated in the author's master thesis [10]. The RMS values of both employed types of waveforms were always identical so that the possible acceleration effect would be unambiguous. A definitive decrease in the specimens' lifetime was observed under the latter aging regime (supraharmonic representation). While no direct explanation was proposed in the work, it is the author's privilege to add one in retrospect. Since relaxation processes in OIP generally occur at frequencies well below the employed 6 kHz [93], changes in surface potential distribution

should not be of concern, as was shown in [77]. Due to the AC character of the voltage, the internal space charge should not play a significant role either.

Moreover, even though [80] was carried out on polymeric insulation, the work identified no evident dependence of (short-term) time-to-failure of specimens on the repetition frequency of pulses. Likewise, thermal degradation via increased dielectric losses is expected to be marginal due to the use of thin samples and large, (thermally) well-conductive electrodes. With these possibilities ruled out, the explanation should be sought elsewhere.

Due to the typical predominant process of OIP and extruded polymeric insulation degradation – depolymerization [36], it is the author's opinion that parallels can be drawn between the two to a certain degree. Particularly enticing is the theory of breakdown proposed by J. P. Crine (see section 2.2.4.3), where free electrons are accelerated via electric field to cause scission of the intramolecular bonds (depolymerization). Naturally, increases in the mean free path, or rather the free volume, would be hindered due to the presence of oil. Nevertheless, the free electrons' kinetic energy would be increased if the (supraharmonic) bursts were located at the peak of the fundamental waveform. Such an effect can be expected to matter more toward the end of the OIP's lifetime when free electrons can obtain more energy in general. Still, the magnitude of the effect would be small; however, that agrees with the experimental results rather well.

2.2.5.4 Review summary

This entire review section should emphasize that additional degradation effects due to non-standard waveforms were indeed observed and measured, both for insulation system and film specimens and in the absence of PDs. Such a conclusion prompted the long-term aging experiment on XLPE specimens carried out as a part of this dissertation (see Chapter 4). The main idea was to provide a counterweight to the other aging experiment performed on cable termination specimens, in which partial discharges undoubtedly played a significant role (see Chapter 3).

2.3 Partial discharges (erosion breakdown)

It is not within the scope of this work to describe the fundaments of partial discharges, such as their origin, types, detection methods, or interpretation, in their entirety. They are thus mostly omitted so that attention can be paid to the theory pertinent to the experiment described in Chapter 5.

Firstly, since the experiment was carried out on internal cavity specimens, the particularities of partial discharge development in such configurations are stated. As the leitmotif of the thesis and the experiments carried out within is insulation system degradation, the impacts of partial discharges on an insulation system's integrity are discussed next. A brief overview of methods of partial discharge modeling, with a focus on the analytical/finite element methods, follows. Ultimately, the partial discharge complement to the section 2.2.5 review is given.

2.3.1 Specifics of internal cavity discharges

2.3.1.1 Internal electric field

Internal cavity discharges exhibit unique properties since they occur in gas-filled areas enclosed in liquid (bubbles) or solid insulation material. The relative permittivity of the gas is equal to one [36], which implies that the internal electric field will be strengthened as the surrounding material's permittivity is always higher (see the example showing air-filled cavity in epoxy resin in Figure 2.12). This phenomenon is especially problematic due to the comparatively weak dielectric strength of gases, which can be as low as 2 to 3 kV/mm under atmospheric conditions (air). If local breakdowns of the gas (partial discharges) occur in such a cavity, they can erode its surface and create micro defects, from which conductive channels (treeing) can develop. These channels can eventually spread over the entire electrode span and cause an erosion breakdown of the system.

2.3.1.2 Partial discharge inception voltage

Due to the insulative character of the cavity's surface, its *partial discharge inception voltage* (PDIV) does not precisely follow Paschen's law, as Paschen's theory assumes initial electron release from electrodes.

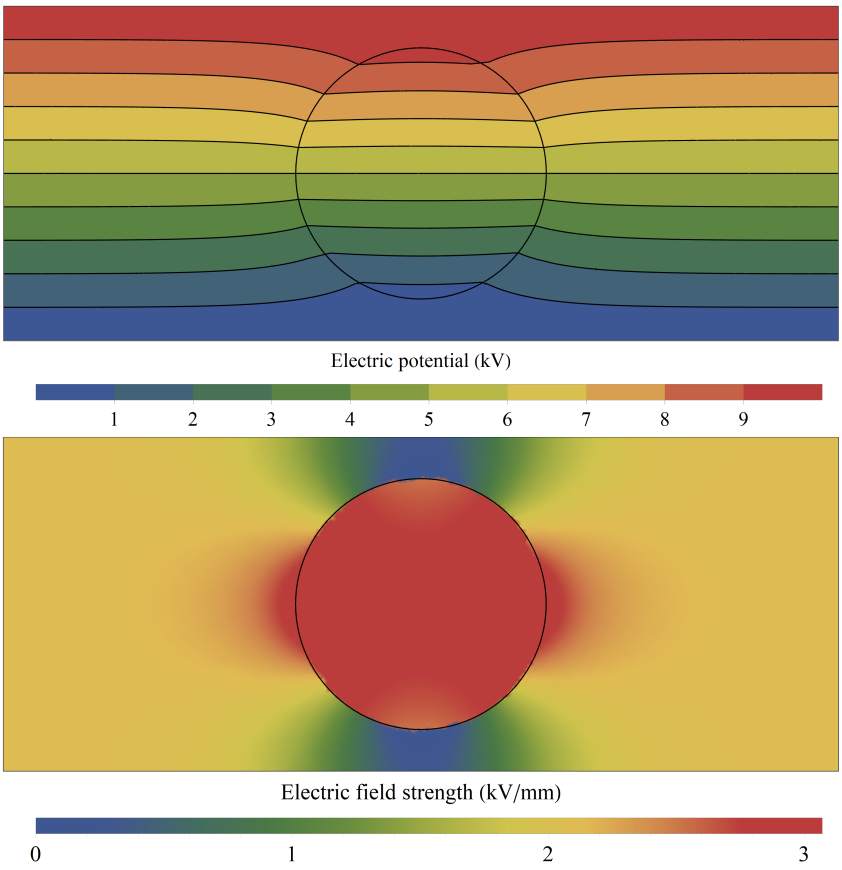

Figure 2.12: A FEM model of electric potential and field strength prior to the first PD occurrence in an internal cavity inside of an epoxy disc specimen ($h = 4$ mm, $d_{\mathrm{disc}} = 50$ mm, $d_{\mathrm{cav}} = 2.5$ mm, $\varepsilon_{\mathrm{r,epoxy}} = 3.2$, $U_{\mathrm{app}} = 10$ kV); electrodes not shown.

The initial electron thus needs to be supplied from elsewhere (see section 2.3.1.4), which results in the increase of PDIV by about 10 %. In this case, the discharge development follows the streamer mechanism, and the PD impulses last units of nanoseconds. A specialized formula (see Eq. 2.40) is frequently used to calculate the respective inception field strength and thus the PDIV. Due to the occurring degradation processes, the surface of the cavity might become so conductive that the discharge mechanism changes to the Townsend type. The respective PDIV then follows Paschen's law and is equal to:

$$U_{\mathrm{bd/inc}} = \frac{B \cdot pd}{\ln \frac{A \cdot pd}{\ln(1+1/\gamma)}}, \tag{2.36}$$

where A and B are the gas constants, γ is the second Townsend ionization coefficient, and pd is the pressure-electrode distance product. In addition, the half-value width of discharge impulses increases to 80 to 800 ns [36].

2.3.1.3 Space-charge field

Another particularity of internal discharges is the surface charge accumulation on the cavity surface via discharge channels. Since the surface is insulative (excluding cavities at the electrode interfaces), the charges remain thereon for prolonged times and significantly deform the local electric field for the subsequent discharge. A discharge always transfers a positive charge to the surface closer to the cathode and vice versa. If another subsequent PD of identical polarity is to occur in the same (AC) voltage halfwave, the applied field must overcome not only the PDIV field equivalent but also the opposite-polarity local field due to the accumulated space charge. Conversely, a PD of opposite polarity might occur more easily, as the space-charge field's polarity matches the applied field's one, effectively strengthening it. Therefore, the PDIV field equivalent will be overstepped earlier in the phase of the applied AC waveform.

Naturally, space charges also play a role in the development of external PDs. However, they tend to vanish very quickly in comparison to the power frequency. A suitable example is the development of same-polarity Trichel pulses even when the absolute value of AC voltage starts to fall (i.e., between phase angles 90° to 180° or 270° to 360°). This phenomenon indicates that the space-charge field must weaken much faster than the main (source) field, else the same-polarity PDIV could not be reached. On the other hand, charges deposited on the insulative surface of internal cavities are longer-lasting since the respective removal/recombination processes have much larger time constants. These processes include surface emission and subsequent recombination via ion drift through the gas, recombination via surface conduction, and recombination via conduction through the bulk of the insulation material [94]. Effective charge decay time constant is often used to represent the combined effect of all the processes. Reverse engineering of experimental measurements through modeling can be employed to estimate this time constant, as was shown for epoxy specimens in [95]. Typical values can thus be expected in units of milliseconds, whereas [94] estimates the value to be in the range of units of microseconds for external discharge configuration in SF_6 gas.

2.3.1.4 Initial electron availability

While external discharges often occur as soon as the PDIV of the given configuration is reached, the situation is considerably different in the case of internal discharges. Alongside the PDIV, the parameter determining the discharge inception behavior is the initial electron availability. In large volumes, typical for external discharge configurations, volume generation of initial electrons via (cosmic) radiation is substantial. Surface generation can be extensive as well when semiconductive or conductive surfaces delimit the defect configuration.

On the other hand, the volume of internal cavities is very small in general, and so is the respective volume generation of initial electrons. Prior to the first-ever (so-called *virgin*) PD in a cavity fully enveloped by insulation, the initial electron can be, in most cases, obtained exclusively through volume generation. In such case, the average (PD) inception delay can be described by the following formula:

$$\Delta t_{\mathrm{inc}} \approx \left[C_{\mathrm{rad}} \cdot \Phi_{\mathrm{rad}} \cdot \left(\frac{\rho}{p}\right)_0 \cdot p \cdot \frac{4}{3}\pi ab^2 \cdot \left(1 - \nu^{-1/n}\right) \right]^{-1} \tag{2.37}$$

where C_{rad} defines the interaction of the radiation with the cavity gas, Φ_{rad} is the radiative cosmic and radioactive quantum flux density, $(\rho/p)_0$ the pressure reduced gas density, $(4/3)\,\pi ab^2$ is the volume of

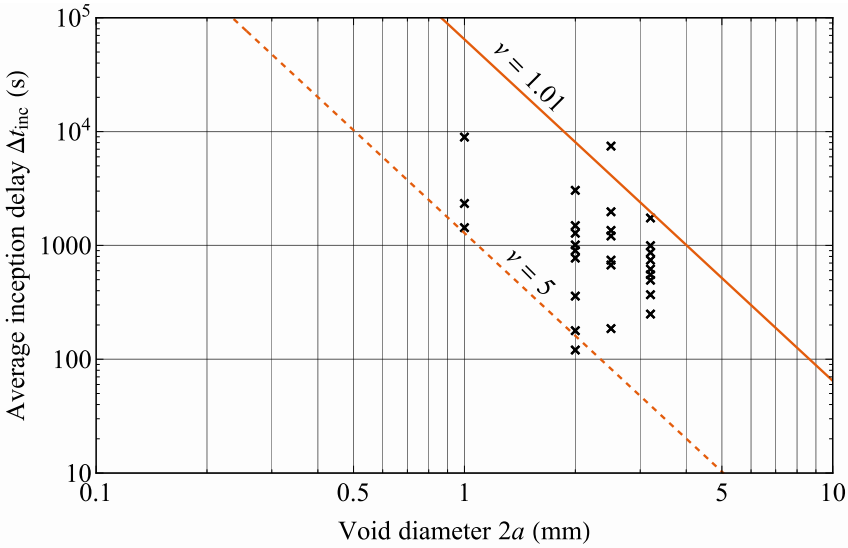

Figure 2.13: Dependence of the average inception delay on the cavity diameter (air-filled, spherical). The data points show experimental results gathered in [95], whereas the orange lines are plotted according to Eq. 2.37 using the typical values for air and $p = 75$ kPa for two different values of ν. Recreated from [95].

the cavity, ν the overvoltage ratio (applied voltage to inception voltage ratio), and finally n a parameter characterizing the ionization process. For air, the typical values are $C_{\mathrm{rad}} \cdot \Phi_{\mathrm{rad}} \approx 2 \cdot 10^6$ kg^{-1}s^{-1} (natural irradiation, can vary locally by a factor of at least two), $(\rho/p)_0 \approx 10^{-5}$ kg/m^3, and $n = 1/2$ [95]. For small cavity diameters, one might expect the average PD inception delay of tens of seconds up to tens of hours long (see Figure 2.13).

The inception delay could cause issues in diagnostic tests, such as the *one-minute AC voltage tests*, since cavities up to a specific size would not be detected due to their respective inception delay being longer than the test duration. "Luckily," there would be a large number of such cavities in practical applications, and hence the inception delay would be much shorter than according to Figure 2.13. Furthermore, the tests are usually conducted at voltages well above the eventual PDIV, which also decreased the delay further [36].

2.3.2 Impacts

2.3.2.1 Erosion

When an internal discharge occurs, the resulting movement of charged particles can degrade the cavity surface. The reason for that is because free electrons may obtain enough energy to cause bond scission in the surface material, whereas the much larger positive ions may produce local thermal instability when they bombard the (cavity) cathode. Additionally, the discharge typically produces free radicals such as ozone, O_3, and nitrogen dioxide, $NO_2^{\bullet}$, which are highly reactive and hence also deteriorate the surface material via chemical reactions.

Due to the above effects, pits and channels may be formed in the insulation material surrounding the cavity. These structures are filled with gas, which has both lower relative permittivity and dielectric strength than the solid insulation, and their surface is highly irregular with a large number of microtips, or rather micropits, due to the erosion. Strong local electric fields are thus present inside these formations, and if discharges are incepted, the resulting charge concentration at the tip of a discharge channel can magnify the field to the order of 1 MV/mm, i.e., well above the intrinsic breakdown strength of the surrounding material [37]. Numerous local breakdowns of the surrounding material then ensue, forming a branched structure of eroded channels. Due to its resemblance to a tree, the phenomenon is referred to as *treeing*.

2.3.2.2 Treeing

The formation of eroded channels from a defect represents a severe threat to insulation systems, mainly because their subsequent propagation is driven by the direction of the applied electric field. In other words, the channels propagate mainly transversally through the insulation, which eventually forms at least one channel connecting both electrodes. Since this channel will be filled with (dielectrically) weaker gas, and since a triple point of electrode-solid insulation-gas will now exist, the dielectric strength of the insulation system will be significantly reduced, in virtually all cases well below the operating field strength. Needless to say, once that occurs, the power system will be rendered unusable.

So far, two different mechanisms of treeing have been identified: *electrical treeing* and *water treeing*. Electrical treeing transpires solely due to the enhanced local electric field, and its development follows the course of action described above. Characteristic traits include long hollow channels, absence of water, and very rapid growth in the span of hours to weeks. The electrical trees are often initiated by DC, surge, and impulse voltage stresses [96].

Conversely, *water treeing* is characterized by the formation of discreet voids around insulation defects, the necessary ingress of water into the insulation, and a prolonged growth rate (months to years). Water trees are also difficult to spot if the structures are not stained. The water treeing process is influenced by several parameters, including moisture, contaminants, ionic impurities, temperature and its gradient, aging time, voltage stress, and pH of the ingressed water [96].

Whereas the electrical treeing directly causes the afflicted (insulation) system to fail, it was observed in power cables that water treeing does not necessarily lead to the same result. In fact, water-treed cables were repeatedly shown to remain serviceable for prolonged periods. Nevertheless, subsequent DC voltage stress, surges, and impulses led to the transformation of water trees into their electrical counterparts, which naturally caused the system's failure. Several explanations of such a transformation are available, of whose the more commonly accepted one is the movement of charges trapped in the tree walls, which can bore tunnels between individual defects due to heat or mechanical motion. When such tunnels are connected over the entire electrode span, the breakdown in the manner of electrical treeing ensues [96].

It should be noted that water treeing is less of a concern in modern power cable systems, mainly due to the high quality of cross-linked polyethylene manufacturing and the use of longitudinal and radial water seals (see section 2.4.2).

2.3.3 Partial discharge modeling

Four different fundamental approaches to modeling of partial discharges have been established over the last decades. In general, the complexity and accuracy of the models increased with the improving computational technology [97]. Nevertheless, due to the frequent demands of PD activity simulation over prolonged periods, even the older, less accurate, but easy-to-calculate models still find use. The model types ordered chronologically are *capacitance models*, *electrostatic models*, *conductance models*, and *plasma models*.

2.3.3.1 Capacitance models

These models are based on an equivalent circuit of an internal cavity, where each part (cavity, upper and lower part of the surrounding solid insulation, and the rest bulk insulation) is represented by its capacitance. The discharge occurrence is simulated by a switch S placed parallel to the cavity capacitance, which switches on when the discharge conditions are met and switches off afterward. Both the equivalent circuit and its simplified version are shown in Figure 2.14. Using the simplified circuit, the physical, true charge transferred during a discharge, q_{phys}, is expressed from the difference in voltage on the cavity c prior to and after a PD, ΔU_{c}, and the ratio of the individual capacitances as:

$$q_{\mathrm{phys}} = \Delta U_{\mathrm{c}} \left(C_{\mathrm{c}} + \frac{C_{\mathrm{a}} C_{\mathrm{b}}}{C_{\mathrm{a}} + C_{\mathrm{b}}} \right), \tag{2.38}$$

where C_{a}, C_{b}, and C_{c} represent the respective capacitances of the equivalent circuit, as defined in [98]. The observable, apparent charge can be readily obtained from the total capacitance of the configuration, C_{tot}, and the difference in voltage across the electrodes prior to and after a PD, ΔU, as:

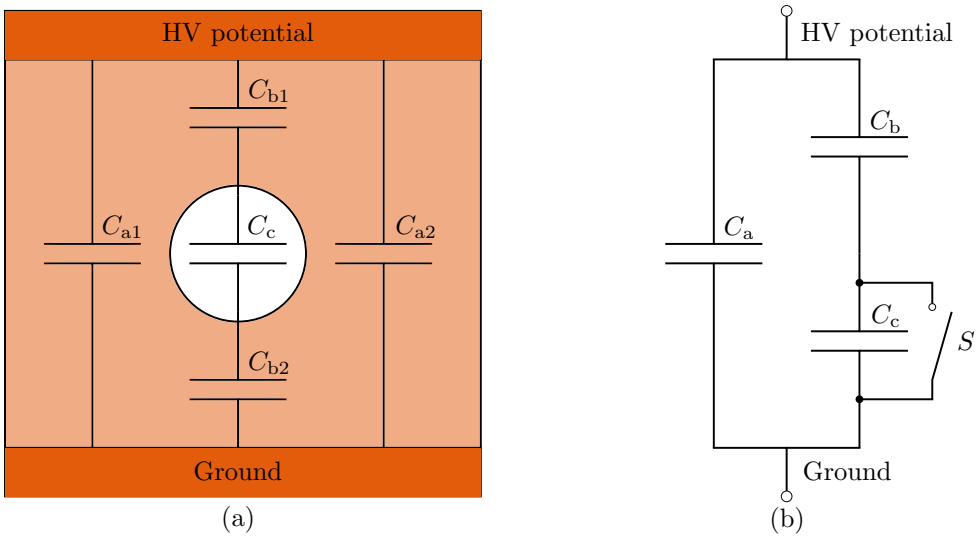

Figure 2.14: Capacitance model: equivalent (a) and simplified (b) circuit of an internal cavity. In (a), dark orange marks the electrodes, light orange solid insulation, and white the cavity. In (b), S denotes a switch that short-circuits the capacitance C_c during a discharge. Inspired by [97].

$$q_{app} = \Delta U C_{tot}. \tag{2.39}$$

Only these two quantities are measurable in real systems, and hence all PD instruments show the apparent charge solely.

The original capacitance model was subsequently reworked and extended to incorporate the effects of space charge generated by the PDs, the resistance of the discharge channel, insulation resistance, or to model two cavities at the same time or both cavity and surface discharges. Due to its simplicity, the computation speed of the model is exceptional, and it can be used with sufficient accuracy for power equipment, such as cables [97]. However, the issue of the capacitance model is that it employs the concept of cavity capacitance, which is only valid when the cavity surface is equipotential [99]. Naturally, this fundamental assumption is erroneous due to the deposition of space charge on the cavity surface. As a result, electrostatic models, which directly calculate the internal cavity field, were developed. Nevertheless, modified capacitance models still find their use, as is, for example, evident from a recent publication [100].

2.3.3.2 Electrostatic models

The long-term (in respect to the time between discharge events) deposition of space charge on a cavity's surface due to PDs is not just consistent with the theoretical assumptions, but it has also been directly observed in experiments (see Figures 3 to 6 and 8 in [101]). With the knowledge of electrode potentials φ, the spatial distribution of (space) charge ρ and permittivity ε, Laplace's equation for electrostatics can be used to calculate the field distribution, from which both the time of inception as well as the magnitude of a PD can be determined. As was stated, the time of inception also depends on initial electron availability, but in any case, the internal cavity field must be in at least one point larger than the inception field strength, which is defined in [95] for internal spherical cavities filled with air as:

$$E_{inc} = 25.2 \cdot p \cdot \left(1 + \frac{8.6}{\sqrt{2pr_{cav}}}\right), \tag{2.40}$$

where p is the cavity gas pressure and r_{cav} is the radius of the spherical cavity. Furthermore, the article also provides an equation to calculate the apparent (induced) charge q_{app}, i.e., the discharge magnitude, which takes the following form:

$$q_{app} = -4\pi\varepsilon_0\varepsilon_r r_{cav}^3 \left(E_{c,bef} - E_{ext}\right) \nabla\lambda, \tag{2.41}$$

where $E_{\mathrm{c,bef}}$ is the cavity field strength prior to a discharge, E_{ext} is the extinction field, and λ is a dimensionless function representing the solution of Laplace's equation with unit voltage applied to the measurement electrode and zero voltage to all the other electrodes [95].

Eq. 2.41 is valid only for uniform surface charge distributions, which represents a substantial simplification of the issue. Nevertheless, its accuracy for ideal spherical cavities was shown to be sufficient [7]. FEM can be used to include the effect of non-uniform space charge distribution, as was done, for example, in [102]. In fact, the calculation of the cavity electric field via FEM allows for a much more precise determination of the PD inception criterion, both in terms of inception field strength and free electron availability.

An expression for the initial electron availability in a FEM electrostatic model was proposed in [103]. Therein, the availability is considered to originate solely from surface charge detrapping since the volumetric initial electron generation is typically very low and random, which makes it challenging to model. The expression calculates the so-called *electron generation rate* (EGR; identical to initial electron availability) using the field strength in the center of the cavity as:

$$N_{\mathrm{es}}\left(t\right) = N_{\mathrm{es,0}} \left| \frac{E_{\mathrm{cav}}\left(t_{\mathrm{PD}},0,0\right)}{E_{\mathrm{inc}}} \right| \exp\left[\frac{-\left(t-t_{\mathrm{PD}}\right)}{\tau_{\mathrm{dec}}} \right] \exp\left| \frac{E_{\mathrm{cav}}\left(t,0,0\right)}{E_{\mathrm{inc}}} \right|, \tag{2.42}$$

where $N_{\mathrm{es,0}}$ is the initial value of EGR (per model parameters), $E_{\mathrm{cav}}\left(t_{\mathrm{PD}},0,0\right)$ is the electric field strength in the center of the cavity, where t_{PD} denotes the time of the last PD event, and τ_{dec} is the effective (space) charge decay constant. The three variable factors consider the effect of the number of available electrons to be detrapped, space charge decay with time, and enhancement of the detrapping process due to a stronger field, respectively. The use of field strength in the center of the cavity is a simplification undertaken to improve the calculation speed of the model. Nevertheless, the internal cavity field calculated by the model in [104] was shown to be quasihomogeneous, and hence the decrease in the model's accuracy due to this simplification is expected to be minimal. It should be mentioned that Eq. 2.42 was derived from expressions pertaining to the individual phenomena, which were proposed back in the 1990s by L. Niemeyer, F. Gutfleisch, G. C. Crichton, and others.

The initial electron availability through surface detrapping is also influenced by the polarity of the previous PD event. Generally, an electron can be detrapped more easily from a positively charged surface (same polarity) than from its counterpart (opposite polarity). This imbalance leads to the frequently observed split of PRPD pattern clusters into a long, narrow, and dense vertical part and broad, sparser part resembling the sinusoidal waveform (so-called *rabbit ear*), as shown in Figure 23. In [104], this polarity effect is considered by splitting the $N_{\mathrm{es,0}}$ term into two values: $N_{\mathrm{es,0L}}$ if the subsequent PD polarity is opposite, and $N_{\mathrm{es,0H}}$ if same. For modeling purposes, this division can be denoted mathematically as:

$$N_{\mathrm{es0}} = \begin{cases} N_{\mathrm{es0L}} & \text{if } E_{\mathrm{cav}}\left(t\right)/E_{\mathrm{cav}}\left(t_{\mathrm{PD}}\right) \geq 0 \\ N_{\mathrm{es0H}} & \text{otherwise.} \end{cases} \tag{2.43}$$

Even though the electrostatic models resolve the central issue of the capacitance models, which is the effect of the (uneven) distribution of space charge and its role in both internal cavity field and EGR, they still disregard the actual discharge process and consider only its aftereffects. Furthermore, the effect of space charge recombination via cavity conductance is overly simplified and incorporated only as a part of the effective charge decay constant. Both these drawbacks are eliminated in conductance models.

2.3.3.3 Conductance models

In the dischargeless state, the cavity gas has very low conductivity, and hence virtually no (volumetric) current flows through it. However, the situation changes when a discharge develops since numerous free charge carriers will be present in the discharge channel due to ionization processes. As a result, electric current flows through the discharge channel (detected via PD measuring instruments per IEC 60270) and deposits space charge on the insulative cavity surface. The former cannot be modeled solely by Poisson's equation for **electrostatics**, as the name suggests, and therefore an alternative approach is required. An expression that combines the current continuity equation and Poisson's equation was initially proposed in [105] to model the space charge recombination via surface conductance. The derived expression is:

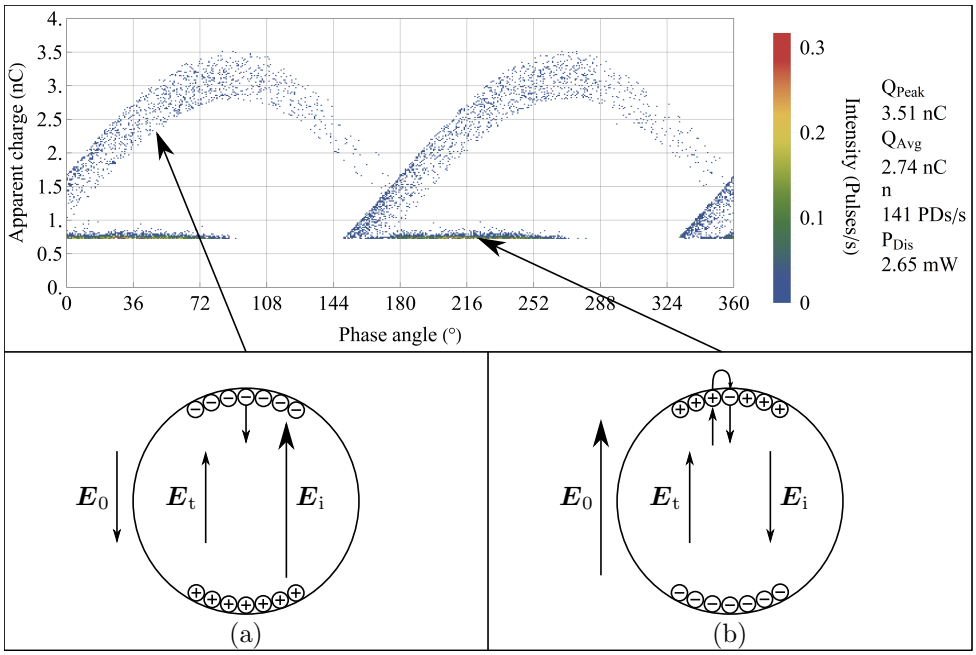

Figure 2.15: Electrostatic model – polarity effect of initial electron detrapping: (a) total field $\boldsymbol{E}_\mathrm{t} = \boldsymbol{E}_0 + \boldsymbol{E}_\mathrm{i}$ (vector sum of voltage source field and internal field) is in the opposite direction of the voltage source field $\boldsymbol{E}_0$ (rabbit ear in the PRPD pattern), electrons are detrapped from the negatively-charged surface. (b) total field $\boldsymbol{E}_\mathrm{t}$ is in the direction of the voltage source field $\boldsymbol{E}_0$ (long, dense, narrow cluster in the PRPD pattern), electrons are detrapped from the positively-charged surface. Inspired by [95].

$$\nabla \cdot \left(-\sigma \nabla \varphi - \frac{\partial}{\partial t} \left(\varepsilon_0 \varepsilon_\mathrm{r} \nabla \varphi \right) \right) = 0. \tag{2.44}$$

In [104], this equation was also used to model the cavity (volumetric) conductance, which was set to $\sigma_\mathrm{cav} = 0$ S/m in the dischargeless state, and to $\sigma_\mathrm{cav,max} = 5 \cdot 10^{-3}$ S/m during a discharge. The latter value was estimated using the expression for electron conductivity in plasma. Furthermore, a surface conductance condition was added to prevent surface charge decay through recombination when the total cavity field acts against the intended movement of surface charges (i.e., when the total field forces the charges to move to the nearest cavity poles instead of the opposite).

Conductance models can be used to simulate PD activity in more than one cavity [106] and in power equipment [107]. Moreover, the temperature distribution inside the cavity due to PDs can be modeled as well [97, 104]. The increase in the model's accuracy over the electrostatic variant comes at the cost of calculation speed, which is significantly reduced due to the miniature step size required to model the transfer of charge during the swift discharge events (units of nanoseconds for streamer mechanism, as mentioned above). Nonetheless, the occurring phenomena are still significantly simplified, and if an accurate description of partial discharge activity in a cavity is required, plasma models need to be employed.

2.3.3.4 Plasma models

To better simulate the physical processes occurring during and after a PD, the respective structures pertinent to the discharge (electron gas, avalanche, streamer) can be treated as fluids (plasma) and described using the fluid equations. Since these equations are well beyond the scope of this thesis, they are not listed or further discussed, and the reader is suggested to seek out more information in the respective publications (see, for example, the overview in section 3.4 Plasma models in [97], or the entirety of [108]), if necessary. The discharge development is considerably complex and apart from the primary free electron generation processes, secondary processes, such as cathode secondary emission and photoionization, also need to be modeled.

The reward for constructing such a plasma model is an accuracy incomparably higher than those of the

previous model types. However, due to the limitations of contemporary computational technology, only very short sequences (several discharges) of PD activity can be obtained in a reasonable time. Since the longer statistical behavior of PDs is predominantly sought after, plasma models are used only rarely. Nevertheless, the benefit of such a powerful tool is, among others, the ability to verify whether the simplifications considered in other models are permissible. For instance, it was shown in [108] that for low relative permittivities of the solid insulation, the discharge propagates through the center of a cavity, as is assumed in electrostatic models.

2.3.4 Partial discharges & high-frequency oscillation/repetitive impulse phenomena

The effects of various high-frequency voltage components on insulation systems' intrinsic aging rate were reviewed in section 2.2.5. Since PDs fundamentally alter the degradation processes and the overall aging rate, they are reviewed separately in this section.

In terms of insulation diagnostics, one of the most remarkable differences between the two degradation types is their detectability. Whereas enhanced intrinsic degradation, such as additional dielectric losses, might be impossible to detect, partial discharges, if present, can be identified relatively easily. Also, the latter's insulation degradation mechanisms are understood more clearly (see section 2.3.2). Hence, this review focuses more on the magnification of the degradation effect (PD activity) rather than its impacts. The search is split into three subsections describing the effects of different voltage waveforms (mixed voltage, (semi)square and PWM, harmonics and impulses superposed on AC) on the PD activity.

2.3.4.1 Mixed voltage

The term mixed voltage encompasses various waveforms consisting of significant DC and AC components [79]. A subset of the mixed voltage is the DC periodic voltage, which combines DC and AC of power frequency and primarily establishes the period for (PR)PD measurements [109]. While not precisely a high-frequency issue, the DC periodic voltage can be viewed as a parallel to fast transients superposed on power-frequency waveform (the voltage change rate of the latter is insignificant to the one of the former) and was hence included. Similar parallels can be drawn for the combination of DC and low-order harmonics, whose effects on PD activity were investigated in [110] and [111]. In contrast, the DC-biased square pulse waveforms generated by a PWM-driven inverter, employed in [79] and [80], had very fast rise times ($\tau_\mathrm{r} = 40$ ns) and thus indeed simulated the high-frequency phenomena.

The DC periodic voltage experiments revealed that including even a tiny power-frequency AC component results in much more intensive PD activity than in the case of pure DC [109]. The investigated waveforms had a similar peak value determined by the AC waveform, whose parts below the threshold δ were replaced by unipolar (positive) constant DC. For the pure DC stress ($\delta = 1$), the peak voltage had to be increased to 14 kV so that PDs would occur at all, and yet the resulting PD repetition rate was meager (0.084 PDs/s). When the threshold δ was decreased, the repetition rate grew, and the PDIV decreased, with their values ultimately reaching 55.37 PDs/s and 2.2 kV, respectively, at $\delta = 0$. The PRPD patterns constructed in the subsequent article [112] indicated that the discharges occur almost exclusively in the phase range corresponding to the presence of the AC component. The authors attribute this phenomenon to the steep increase in the $\mathrm{d}V/\mathrm{d}t$ ratio at the transition between DC and AC parts of the waveform. Although the voltage was always unipolar (except the pure AC stress), PDs of both polarities have been observed, especially in Kapton and XLPE specimens. Since such effect is not uncommon in internal cavities (substantial memory effect), especially when the voltage reaches multiples of the PDIV, the observation is not entirely surprising.

The PD activity on twisted pair specimens under waveforms representing the output voltage of modular multilevel converters with significant DC offset was investigated in [110]. Three different values of converters' switching frequencies were employed: 2, 5, and 10 kHz. For the 2-kHz switching frequency, configurations of three, five, and seven submodules were respectively employed to generate the waveform. In the other two cases, only the five-submodule configuration was employed. Reference PD measurements (PDIV, pulses per second measured at PDIV + 0.5 kV, and mean discharge magnitude) were carried out on pure AC and pure DC waveforms. The lowest PDIV (1.3 kV) and most pulses per second (557) were measured under the AC waveform. No PD activity occurred up to the maximum test voltage of 9.5 kV for the DC waveform. In the case of the five-submodule configuration, the PDIV decreased, and pulses

per second rose with the increasing switching frequency. Conversely, the higher number of submodules increased the PDIV and decreased the pulses per second.

Combinations of first to ninth odd harmonic voltage waveforms with different amplitudes and (HV)DC offsets were applied to a needle electrode embedded in ethylene propylene diene monomer (EPDM) specimens in [111]. Electrical treeing ensued, and after development over a given timeframe, the trees' morphology was photographed and subsequently analyzed. An apparent increase in tree length and accumulated damage to the insulation (measured as the number of "damaged" pixels in the photograph) with the rising harmonic order of the AC components was identified. Concerning the tree length, the increase between the first and ninth harmonic was about 80 % for negative DC offset (-15 kV_{DC} with 10 kV AC amplitude) and circa 75 % for positive offset (+15 kV_{DC} with identical AC amplitude). The negative voltage created bush-like trees, for which the total accumulated damage due to the higher harmonic order was about ten times larger, whereas the magnitude of the effect was substantially smaller for the positive voltage, mainly due to the formation of branch-like trees. In this case, the increase in the accumulated damage was circa fourfold. Similar waveform configurations consisting of HVDC and superposed 6^{th}, 12^{th} and 18^{th} harmonics were employed in the article [113], which focused on modeling of PD activity in an artificial void under the given waveforms. The model proposed an increase in PD repetition rate due to the harmonic components' rising relative magnitudes, and the subsequent experiments confirmed this assumption.

Mixed voltage (DC + 50-Hz AC and DC + 600-Hz AC) was applied to epoxy-resin-impregnated paper and insulating paper specimens with an artificial cavity in [114]. Both the modulation of the resulting PRPD patterns and long-term degradation of the specimens under these voltage waveforms were examined. The occurring PD activity was substantially magnified due to the inclusion of AC components on the DC waveform, and it was further shown via resistance mapping of the aged specimens that degradation due to PDs took place. Furthermore, higher AC-to-DC peak voltage ratios reduced the PDIV, which indicated that the AC components play a crucial role in its determination.

Water treeing of polyethylene specimens under various voltage waveforms was examined in [115]. The speed of the degradation process was shown to be strongly correlated to the number of the applied voltage waveform's zero crossings. Under mixed voltages, the highest measured water tree length was 560 µm for 3 kV_{DC} + 2-kHz 3 kV_{RMS} combination (4,000 zero crossings per second). Surprisingly, the effect was present even for waveforms with DC offset larger than the AC component's magnitude (effectively unipolar voltage with no zero crossings). In fact, one such combination (5.6 kV_{DC} + 2-kHz 3 kV_{RMS}) resulted in a water tree length of 500 µm, which entirely eclipsed the tree length of 60 µm detected under a 50-Hz 13-kVRMS waveform (100 zero crossings per second). The authors concluded that the water tree propagation under mixed voltages is enhanced due to effective zero crossings at the tip of the water tree, determined solely from the high-frequency component. Further information and additional references concerning the topic are available, for example, in section 2.2 of [116].

2.3.4.2 (Semi)square and PWM voltage

PD activity on twisted pair test specimens under PWM voltage waveforms was investigated in [117]. It was identified that the waveform parts most likely to incept PDs are the voltage flanks between individual voltage levels. The employed waveforms were thus varied by the rise time of these critical flanks (0.2, 5, and 100 µs; controlled via added resistance) and by the number of the inverter's voltage levels (three and five) so that the PD activity during these transitions could be analyzed in greater detail. Shorter rise times increased the number of PDs and decreased the *partial discharge extinction voltage* (PDEV), whereas the addition of two inverter levels weakened these impacts substantially. The smoothest critical voltage flanks were present for the five-level inverter and rise time of 100 µs – in this case, the obtained PD parameters were very similar to those of a standard 50-Hz waveform. Most PD events were clustered around the phase angles where transitions between individual voltage levels occurred, suggesting a close connection to the dV/dt parameter. The smoother transitions between individual voltage levels were also shown to weaken the PD activity in [118].

Similar research of PD activity on twisted-pair specimens was conducted in [119], which showed that the decreasing duty cycle of semi-square waveforms reduces the PDIV. In contrast to [117], lower rise times (70 vs. 150 ns) slightly increased the PDIV; however, these rise times were much shorter than the second shortest value employed in the former research (5 µs), which could indicate saturation and subsequent reversal of the dV/dt parameter effect. On the other hand, larger overshoot values (60 % vs. 28 %) of the semi-square waveforms decreased the PDIV, especially for longer duty cycles. In the same

spirit, single-contact crossed pair copper wires insulated by polyamide-imide enamel were subjected to various semi-square waveforms [120]. The conducted experiments focused on the effect of the waveform's duty cycles on PD activity and specimen endurance. Shorter impulse lengths (duty cycles) resulted in an asymmetric PD activity at rising and falling voltage flanks. A PD during the rising flank was always present, while the probability of a PD event during the negative flank reduced with the decreasing impulse length. Nevertheless, this asymmetry vanished for impulses longer than 25 µs. The endurance experiment revealed that the same number of impulses of different lengths has a more significant degradation effect on the specimens if the impulses are longer. Such revelation indicated a close correlation to the measured PD activity, which was more potent in terms of PD magnitude for longer impulses.

The common theme of several works dealing with the PD activity due to PWM-driven inverters is the examination of PDIV or PDEV. Failure mechanisms of induction motors due to PDs were reviewed in [121]. The work discussed the maximum operating voltages concerning the PDIV of respective configurations and failure mechanisms. The influence of the rise time on PDEV of various insulation system specimens was investigated in [122]. OIP and needle (corona discharge) specimens' PDEV showed none or minimal dependence, while the PDEV of twisted-pair specimens strongly correlated with the rise time. Issues with the detection of PDs due to the high-frequency voltage components passing through the coupling capacitor were also identified and discussed. Similar issues were also briefly reviewed in [123]. The effect of square waveform's rise times on the PDIV of wire specimens was assessed in [124]. Longer rise times (500 µs) increased the PDIV by about 17 % compared to the shorter rise times (0.75 µs). Moreover, electrical treeing due to the PD activity was observed. The shorter rise times seemed to create thinner branches, but no further analysis of this observation was given.

OIP specimens were subjected to square voltage waveforms of various rise times (200 to 1,000 ns) and repetition frequencies (1 to 10 kHz) in [125]. The PDIV of the specimens generally reduced with the decreasing rise time; however, a saturation effect of the PDIV decrease was observed at short rise times for the 8-kHz and 10-kHz repetition frequencies. Similar behavior was detected for the breakdown voltage of the specimens. In fact, the two parameters were shown to be strongly correlated.

2.3.4.3 Harmonics and impulses superposed on AC voltage

In an earlier investigation of PD activity under waveforms consisting of either solely 50-Hz sinusoid, or 50-Hz sinusoid with superposed eleventh harmonic, the authors concluded that the increased $\mathrm{d}V/\mathrm{d}t$ parameter of the latter modified the PRPD and increased the values of descriptive parameters of the occurring discharge activity [126]. The investigation was later extended to incorporate waveforms with combinations of the third, fifth, and seventh harmonics of various phase angles [127] and to observe the phenomena on various specimens representing transformer insulation [128]. In the last article, it was shown that the number of pulses under the tested waveforms is mostly similar when compared to the fundamental waveform in the case of micro blade protrusion specimens. Conversely, the tests on internal cavity specimens revealed that the number of pulses substantially decreases for all the non-fundamental waveforms. The influence of the third harmonic on the PD activity was shown to be the strongest for a phase angle of 180°, closely followed by 270°. Ultimately, the authors emphasized the knowledge of the applied voltage waveform's harmonic content so that the impact of PDs can be adequately assessed. It was pointed out that the test voltage and the actual voltage waveform are often dissimilar, which could lead to erroneous conclusions.

Numerous strong switching impulses (150 J each) were consecutively applied to EPR and XLPE cable specimens in [129]. The study investigated the influence of these impulses on various parameters of PD activity, including the PDIV, PDEV, and the distribution of discharge events in PRPD patterns. Both the PDIV and PDEV reduced significantly, with the former reaching only about 55 and 61 % of its original value for XLPE and EPR, respectively, following the application of 10,000 switching impulses. Ten-second long PRPD patterns were shown to be sufficient to reveal the differences characteristic for various stages of the degradation due to the impulses. Furthermore, the study proposed a lifetime prediction based on the exponential model of PDIV vs. the number of applied impulses. In this case, the practical lifetime would be determined from the intersection between the PDIV "lifeline" and the system's operating (nominal) voltage.

A detailed analysis of PDs in cable joins under waveforms composed of fundamental AC and superposed switching-like impulses (2.8/526 µs) was carried out in [130]. The experiments were performed on two artificial cable joint defects. Depending on the peak values of both components, different PD activities were observed: no PDs, initiation of PDs only during the impulse, initiation only after the impulse, and

initiation both during the impulse and afterward. Each of these activities was examined and explained via an analytical PD model. Ultimately, the authors concluded that superposed switching impulses might incept PDs at otherwise non-discharging defects and that these discharges would increase the probability of PD occurrence, as well as decrease the delay time and thus accelerate the aging process. It was also pointed out that many PDs occur only during the impulses, and therefore an online monitoring system with high enough time resolution to detect fast transient should be employed.

A similar experiment on a 150-kV XLPE cable model with an artificial defect was conducted in [131]. In this case, a broader range of waveform parameters, including impulse front and half-tail times, polarity, and superposition phase angles, was employed. It was shown that the front and half-tail time setting mainly influences just the time of PD inception, whereas the number of PDs depends primarily on the impulse peak value. Furthermore, the increasing phase angle between the AC crest and the superposed impulse reduced the number of discharges. In most cases, the initiated PDs also persisted following the impulse. Issues with the decoupling of the PD signal from the impulse remnant were identified. These were chiefly discussed in the authors' previous article, [132], where the employed measurement configuration was described in its entirety.

2.3.4.4 Review summary

From the above paragraphs, it should be clear that various voltage components superposed on both AC and DC waveforms greatly influence the PD activity and the degradation rate. The mixed voltage waveforms mentioned at the beginning of the review are related to the examined supraharmonics rather loosely; however, the transition between DC and AC can be understood as an analogy to the superposition of supraharmonics on AC waveforms. Most of the mentioned works investigated the effect of this transition on the PDIV, which was shown to be substantially reductive in all cases. The transition was quantified by the $\mathrm{d}V/\mathrm{d}t$ parameter, and it became evident that the higher the values of this parameter, the lower the PDIV. In the case of PWM mixed voltages, a lower number of modules resulted in rougher voltage transitions, which in turn incepted PDs earlier.

The works concerning the effect of (pure) semisquare and PWM voltages reached the same conclusions. Shorter rise times of semisquare waveforms reduced the PDIV and increased the total number of discharges. These effects were also observed for waveforms with rise times of up to 500 µs, which corresponds to the lower definition limit of supraharmonics (2 kHz). Moreover, larger overshoots during the transient event between two voltage levels of a PWM voltage waveform were also shown to decrease the PDIV. The investigations focused on the effect of low-order harmonics superposed on the fundamental AC waveform also concluded that their presence substantially modulates the PD activity and that caution needs to be exercised when performing PD measurements, as the test voltage waveform might not always fully represent the actual operational stresses. Ultimately, stand-alone and superposed impulses were reviewed. Consecutive application of strong switching impulses to insulation systems gradually decreased the PDIV and modified the occurring PD activity. Superposition of switching-like impulses on the AC waveform often resulted in the inception of PDs, which would normally not occur. In some cases, the PD activity would continue even in the absence of the impulses.

In any of the above cases, the presence of additional components on the reference waveform resulted in a noticeable increase in the discharge activity. Nevertheless, since no work (to the author's knowledge) examined the influence of supraharmonics on PD activity, such an investigation was deemed necessary to complement this dissertation. The respective experiment along with the employed analytical model and discussion of the identified effects, are given in Chapter 5.

2.4 Polyethylene-based insulation

A short overview of the fundamentals of polyethylene-based insulation systems is given below. That is mainly because the experiments in Chapter 3 and 4 employ some form of cross-linked polyethylene as specimens. Since Chapter 4 utilizes nanocomposite materials, a brief introduction to the topic is also made in section 2.4.4.

2.4.1 Basic characteristics, manufacturing method

Polyethylene represents a highly polymerized thermoplastic, which exhibits excellent electrical insulation properties. Two fundamental types of polyethylene are used in the electrical insulation industry: *high-*

density polyethylene (HDPE) and *low-density polyethylene* (LDPE). Both types are produced by the polymerization of ethylene molecules, but the individual manufacturing processes differ.

HDPE is produced by the low-pressure polymerization method, which takes place at ambient temperatures, under the pressure of only a few bars, and in the presence of catalysts. The resulting molecular chains are linear and are thus densely packed in a parallel arrangement, only occasionally interrupted by amorphous regions. Due to the dense stacking, higher density is achieved, hence the name. Thermal degradation of the crystalline regions starts to occur at temperatures above 100 °C [36].

Conversely, LDPE is produced by the high-pressure polymerization method at temperatures around 200 °C and under pressures up to 3,000 bars. LDPE's molecular chains are partly branched, resulting in the formation of larger amorphous regions (hence the lower density). LDPE electrical insulation can be continuously operated at maximum temperatures of about 70 °C [36]. The branching of LDPE can be reduced by modifying the manufacturing process, namely by reducing the pressure and temperature of the copolymerization. The obtained polymer is then referred to as *linear low-density polyethylene* (LLDPE). LLDPE exhibits better mechanical properties and elevated operating temperature (by about 20 °C) compared to the standard LDPE [133].

Concerning the main electrical insulation properties, polyethylene's dielectric constant is relatively low at $\varepsilon_\mathrm{r} = 2.3$, and its loss tangent $\tan\delta < 10^{-4}$ results in minimal dielectric losses [36]. Furthermore, polyethylene has a high dielectric strength of about 100 kV/mm for 1-mm thin films, which only drops to 40 to 50 kV/mm for HV crosslinked polyethylene cables of length $l = 100$ m [134].

MV, HV, and possibly EHV cables represent one of the main applications of (crosslinked) polyethylene in the electric industry. Specialized manufacturing methods, which extrude the insulation system directly on the cable core, are thus available. Among other parts, the insulation system consists of an internal conducting layer, an insulation (PE/XLPE) layer, and an external conducting layer. These three layers are advantageously deposited one by one on the constantly moving cable core using a triple extruder. High quality of the manufacturing is ensured by purification of the supplied granulate using pneumatic sifters and magnetic separators in the cleanroom environment [36].

In modern cable systems, crosslinked polyethylene is preferred due to its higher operating temperature and shape stability, which prevents creepage. Crosslinking is typically carried out using the so-called horizontal method, in which the cable core with extruded insulation layers is pushed through a heated crosslinking tube. Before entering the tube, internal lubricant is applied to the cable. Crosslinking then takes place at elevated temperatures (200 °C) in peroxide vapors inside the tube [36, 135]. It should be noted that although the XLPE insulation is superior to the non-crosslinked polyethylene insulation, the crosslinking process transforms the polymer into a thermoset, which practically eliminates its recyclability. Due to environmental concerns, the replacement of XLPE by its predecessor, the easily recyclable (thermoplastic) polyethylene insulation, has been proposed [136]. Naturally, improvements of the PE-based insulation would be required.

2.4.2 Medium-voltage XLPE cable systems

2.4.2.1 Main insulation

Cable insulation systems of power networks can be divided into two distinct subgroups – main insulation and accessories (cable terminations/joints). Starting with the former, Figure 2.16 depicts a typical construction of an XLPE water-tight 22-kV cable (single-core). Such a configuration is present throughout the entire cable system apart from its joints and terminations, hence the term main insulation. The innermost part of the main insulation is the cable core, which is made of stranded conductor wires (copper or aluminum). Its first layer consists of a single strand, whereas each additional layer is composed of $6(n–1)$ strands.

Next comes the insulating part, which comprises the inner and outer semiconductive layers and bulk XLPE insulation. Whereas the XLPE layer carries out the insulating function, the semiconductive layers homogenize the electric field and reduce the applied electrical stress. Increased demands are placed on insulation layers' extrusion and crosslinking quality, as it impacts the system's lifetime significantly. The main threats include the formation of voids during the extrusion process, which leads to the occurrence of partial discharges, and the creation of suitable conditions for the development of water trees due to improper crosslinking [137]. The latter can be further combated by adding water-swellable tape on the outer semiconductive layer, which functions as a longitudinal water sealing.

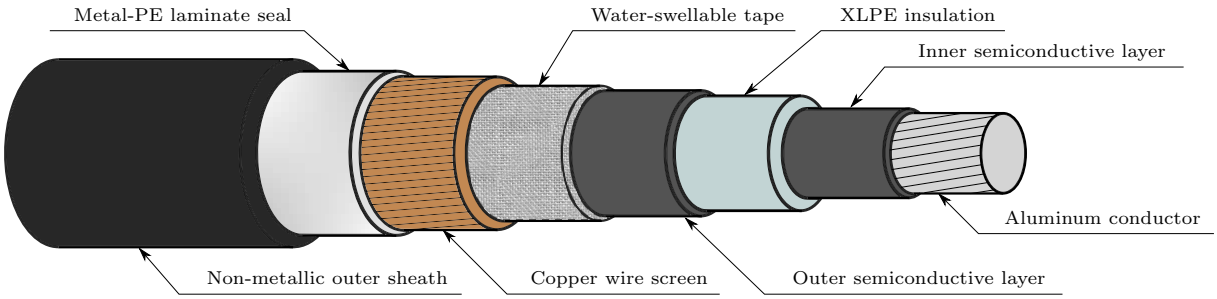

Figure 2.16: Construction of a typical 22-kV water-tight XLPE cable.

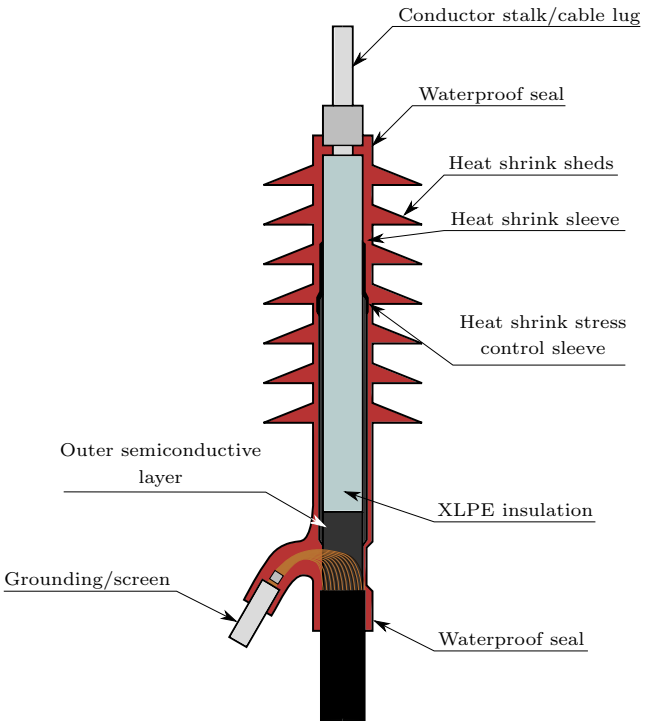

Figure 2.17: Construction of a typical 22-kV XLPE cable termination.

Either copper wire or copper tape screen forms the next layer of the cable system. The screen is grounded, and apart from fulfilling the role of the counter electrode to the cable core, it also suppresses the outgoing and incoming electromagnetic interference, which is particularly important in densely built-up areas. Cable designs that utilize a lead sheath instead of the copper one are available as well. In water-tight cables, a metal-PE laminate layer is added on top of the sheath to serve as a radial water sealing [138]. Ultimately, all the layers are enveloped in a non-metallic outer sheath, made of either PE or PVC.

2.4.2.2 Cable terminations

Figure 2.17 shows the typical construction of an XLPE cable termination. Whereas the clear majority of a cable system consists of regular, continuous main insulation, its interconnections to other systems (terminations) must be fashioned in a specific way. The chief cause of issues with terminations is the necessity to separate the conductive cable core and the grounded screen and lead them out to different places. The core is usually terminated by a cable lug, which, for example, interconnects an underground cable system to overhead lines through an outdoor transformer. Naturally, the cable lug is a live part, and due to the relative proximity to the grounded screen lead-out, the development of surface discharges between the two parts is of concern.

Surface discharges start to occur when the longitudinal electric field component surpasses the discharge inception value determined by the triple interface (conductor, first insulation – gas, second insulation – solid). Both the inception and breakover values of such a configuration are generally very low, and hence

special techniques to suppress the discharges need to be employed. In the case of the cable construction shown in Figure 2.16, the suppression is achieved by minimization of the longitudinal field strength by adding a heat shrink (semiconductive) stress control sleeve. The sleeve is electrically connected to the screen and is thus grounded. The optimal length and shape of the sleeve can be determined from an electrostatic model of the termination. Furthermore, a heat shrink waterproof seal envelops the termination to prevent ingress of humidity into the cable, which is of particular concern due to the frequent outdoor usage of terminations. The waterproof seal is equipped with (rain) sheds to reduce the probability of external surface discharge flashovers by increasing the surface distance between the live and grounded parts.

The necessity of tight contact between the individual interfaces is emphasized in CIGRE Brochure 210. The brochure concludes that the interface surfaces must be smooth enough to reduce the size of cavities to at most one µm and that sufficient pressure must be exerted on the interface via heat shrinking. Rubber material elasticity or spring pressure are used instead if stress cones or conical epoxy castings are respectively employed to optimize the electric field distribution in other cable variants [137].

Cable joints are in many ways similar to cable terminations, particularly regarding the implementation of stress grading. However, since cable joints are not a part of the experiments conducted within the framework of this doctoral thesis, they are not discussed further.

2.4.3 Medium-voltage cable system diagnostics

Numerous testing methods for MV cables are proposed and defined in the IEC 60502 standard. The clear majority of those are sample and type tests, both electrical and non-electrical, performed prior to the installation of a cable system, while the rest consists of electrical diagnostic methods performed after the installation. Since the cable termination specimens investigated in Chapter 3 had already been installed and tested by the manufacturer, only the after-installation cable (termination) diagnostics are mentioned further.

Two such diagnostic methods were employed to observe the progress of the cable termination specimens' degradation: *partial discharge tests* and *loss tangent measurements*. Ultimately, *breakdown tests* were carried out as well. Due to the relatively small length of the specimens, the tests could be performed directly using a power frequency (50 Hz) sinusoidal waveform instead of the often employed very low frequency (VLF) sinusoid. The VLF method is used due to the immense power requirements on the test power source due to the large capacitance of a typical-sized cable system. As the sinusoidal waveform frequency is reduced, the impedance of the cable system reduces as well, and hence less power is required to energize it. Frequencies below 1 Hz are used, as prescribed, for example, in IEEE 400.2-2013 standard. An alternative approach would be using a series resonance power source, whose inductance can be adjusted to lower the overall impedance of the examined cable system substantially and reduce the required power drastically.

2.4.3.1 Partial discharge tests

As stated before, cavities can be formed during the extrusion process as well as during a cable termination assembly. These cavities can be detected via the discharges that occur inside them, as the internal gaseous insulation has a significantly lower dielectric strength. Sensitive partial discharge tests should be performed following the assembly since even relatively weak discharges of a few picocoulombs might cause failure within the range of hours [137]. Typically, elevated voltage is used during these tests – IEEE 400.2-2013 Standard, for example, suggests performing a VLF AC withstand test of a cable system at the triple of its operational voltage (30 or 60 min) simultaneously with partial discharge tests. Per IEC 60502, both the withstand and partial discharge tests should be performed at the operational voltage if a power frequency waveform is utilized. The criteria are usually agreed upon between the manufacturer and the customer [36].

For the cable termination types examined in this work, the upper limit of the apparent charge measured after a certain period following the installation is, in most cases, ten picocoulombs. Such a delay in the measurement should eliminate the influence of after-installation processes (post-crosslinking, minor spatial rearrangements) that take place due to the long-term application of voltage and thermal stresses. The time delay is usually referred to as settling time, and its recommended value typically ranges from tens to hundreds of hours.

2.4.3.2 Loss tangent measurements

Whereas partial discharge tests reveal the local weak points of a given cable system, loss tangent measurements provide information about its global state. Similarly, the tests can be performed either using VLF or power frequency voltage waveforms. The cable system is deemed problem-free if the loss tangent obtained using VLF is lower than $4 \cdot 10^{-3}$. Unfortunately, no unified criterion is defined for the power frequency measurements [139]. Nevertheless, one might employ, for example, the IEC 60502 standard, which proposes the same limit as in the case of the VLF. IEEE 400.2-2013 advises further study if the VLF loss tangent is between $4 \cdot 10^{-3}$ and $50 \cdot 10^{-3}$ and prompts action if larger than $50 \cdot 10^{-3}$.

Moreover, in some cases, it is necessary to measure the loss tangent at elevated temperatures, as little to no differences might be observed at the room temperature, whereas significant differences would be present at around the system's operating temperature. The rise of loss tangent is particularly troublesome due to the resulting increase in heat generation, which further accelerates the aging process, causes overheating, and can even trigger a thermal breakdown [36].

2.4.3.3 Breakdown tests

Concerning the cable termination breakdown tests, although they are not directly standardized (owing to their destructive nature), their results should provide a clear indication of an insulation system's integrity. The breakdown tests can be conducted either by *linear* or *stepwise* increasing of the test voltage. Analogously to the partial discharge tests, the breakdown tests identify the weakest point as the breakdown propagates through it. Direct localization of the breakdown path can be carried out by disassembly or X-ray scanning. The obtained breakdown voltage should be, in general, comparatively lower for more degraded samples. An exception to this rule is, for example, aging via gamma irradiation, which, by contrast, can even increase the breakdown strength of XLPE (at the cost of its mechanical resilience) [140]. During the early phases of a cable system's aging, gaseous byproducts of internal discharges can also (temporarily) increase the breakdown strength [141].

2.4.4 Polymeric nanocomposites

2.4.4.1 General traits

Polymeric nanocomposites consist of at least two constituent materials, of which one is a *polymeric matrix* and the other a *nanofiller*. Per the general nanocomposite definition, at least one nanofiller's dimension must be smaller than a hundred nanometers. Like the larger microcomposites, the filler alters the resulting material's parameters primarily via the interface between its structures (particles) and the polymeric matrix. Since a structure's volume-to-surface ratio increases with its decreasing size ($3/r$ for spherical nanofiller particles), the interfacial area and the magnitude of its effect are more prominent for the same filler *weight percentage* (wt%) when smaller structures are employed.

The interface of (polymeric) nanocomposites draws numerous parallels to colloids, where the constituent immiscible substances also form a similar structure. In colloids, various forces, such as excluded volume repulsion, electrostatic, van der Waals', entropic, and steric, are at play, and the resulting net force determines the spatial distribution and properties of the mutual interface. Among these forces, mechanisms such as physical and chemical adsorption, surface tension are involved as well. Since most of these phenomena had been understood well before the first attempts at creating nanocomposites, the knowledge concerning colloidal interfaces proved pivotal for the research of the topic [142].

2.4.4.2 Multi-layered model

Specifically for polymeric composites, the interface is formed by a so-called bound polymer layer. Its size depends on the strength of the interaction forces, and it typically reaches values between several nanometers to several hundreds of nanometers [142]. The interface can be modeled in greater detail using a multi-layered core model, which consists of two additional *mesoscopic* layers and an *electric double layer* (see Figure 2.18). The innermost bonded layer, situated around the nanoparticle, represents a transition layer tightly bonded to substances via coupling agents (such as silane). Outward in the radial direction, next comes the immobile bound polymer layer that represents the interfacial region. Inside this region, the polymeric matrix's chains are strongly bound to the particle's surface or the bonded layer. Last comes the outermost loose layer, which embodies a transition region between the bound layer and the surrounding polymeric matrix. The layer differs from the matrix in its polymer chain

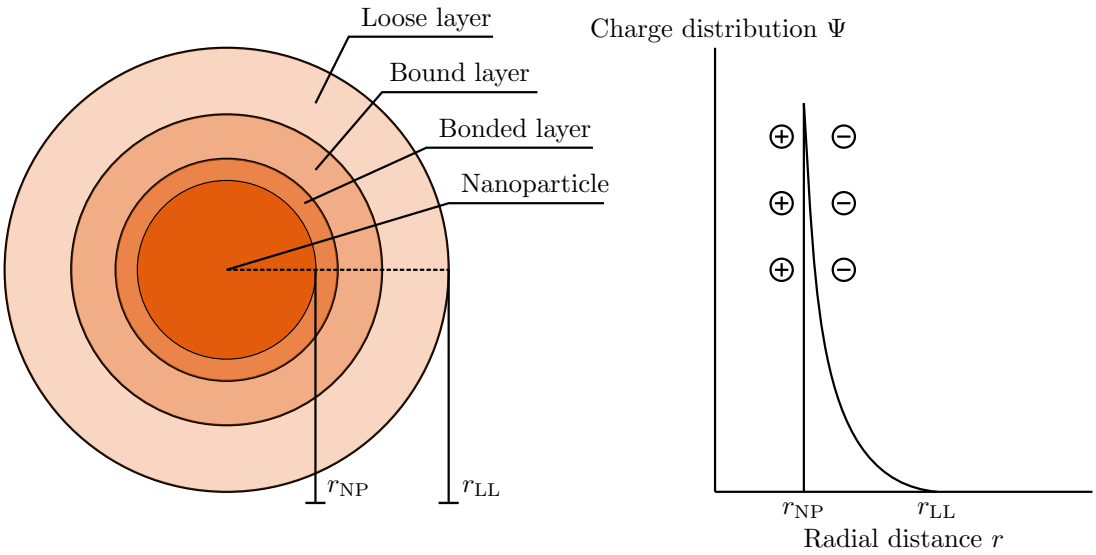

Figure 2.18: Multi-layered core model of a nanoparticle in a polymeric matrix showing the individual mesoscopic layers of the interface (left) and the electric double layer (Gouy-Chapman diffuse layer for a positively-charged nanoparticle; right). Inspired by [143].

conformation, mobility, free volume, and also crystallinity. Its coupling to the bound layer is generally weak. Since electrical forces also determine the morphology, they are included in the model via the electric double layer. The double-layer (*Gouy-Chapman diffuse layer*) is formed via charge injection due to the triboelectric effect between the matrix and the filler [143].

2.4.4.3 Affected parameters, manufacturing methods

Concerning the electrical insulating properties, the addition of inorganic nanostructures can alter a number of the material's characteristics to a substantial degree. Examples of these characteristics include resistance to PDs and tracking, lifetime reduction via treeing, internal and surface space charge accumulation, dielectric strength, dielectric constant or DC conductivity [36, 144]. Non-electrical properties, such as thermal conductivity, thermal expansion, mechanical strength, or elongation, can be modified as well.

The extent to which the properties of the original polymer are changed depends on several factors. Apart from their chemical composition, the nanofillers also differ in shape. In this regard, *quasi-spherical* and *layer-structured* nanofiller types are distinguished. Quasi-spherical nanofillers are particles of a single compound, typically a metal oxide (silica, titania, zirconia, aluminum oxide, barium titanate). On the other hand, nanofillers with layered structures, also referred to as clays, are formed by layers consisting of several compounds (for example, montmorillonite consists of seven different metal oxides) and metal ions placed in-between. Multiple manufacturing methods are available for each nanofiller type. Nanocomposites with quasi-spherical filler are produced by mixing or sol-gel methods, whereas clays are made by the intercalation mixing method. The manufacturing process must be carried out thoroughly as the nanofiller's spatial distribution, orientation, and dispersion strongly impact the nanocomposite's resulting parameters [36, 144].

2.4.4.4 Polyethylene nanocomposites

Polyethylene and cross-linked polyethylene are typically coupled with quasi-spherical nanofillers. A key issue with their manufacturing is the strong agglomeration of the nanofillers due to cohesion forces between the individual nanoparticles. A silane coupling agent and a surface preparation agent are applied to the nanoparticles' surfaces to suppress the agglomeration. Furthermore, specialized dispersion devices such as double spindle screw extruders, high-pressure homogenizers, or ultrasonic wave homogenizers are employed to disperse the nanofiller particles as homogeneously as possible. For instance, the latter utilizes ultrasonic waves to disrupt large agglomerates of particles. Any possibly remaining agglomerates can be subsequently removed by application of a centrifugal force to the composite [144].

Nanofiller materials for PE/XLPE nanocomposites are primarily *nano-silica* (SiO_2) and *nano-magnesia* (MgO). Whereas nano-silica is used to improve the dielectric strength of XLPE in HVAC power cables, nano-magnesia can reduce the accumulation of space charge and is hence employed in HVDC power cables [144]. In particular, nano-silica has been studied extensively. A comprehensive experimental investigation of its influences on electrical insulating parameters of XLPE was conducted by CIGRE work group D1.24 [145]. The performed experiments confirmed the following beneficial effects of the addition of nano-silica: reduction of permittivity in the low-frequency region, reduction of dielectric losses over the entire frequency spectrum, reduction of DC conductivity, change of space charge from heterocharge to homocharge, and increased PD resistance.

Furthermore, no significant change in the lifetime of DC XLPE specimens was achieved by adding 1wt% of nano-silica [146]. However, specialized surface treatment methods of the nano-silica in 5 wt% XLPE nanocomposites were shown to increase both the DC breakdown strength (by up to 20 %) and DC voltage endurance of the material [147]. Conversely, the addition of nano-magnesia increased LDPE's PD resistance [148] and inhibited water tree propagation [149]. An extensive investigation of electrical insulation performance of nano-magnesia commercial-grade XLPE for ±320-kV HVDC cables was performed in [150]. It was observed that the addition of nano-magnesia had the following effects: an increase in the DC breakdown strength by about 20 %, a drastic decrease in space charge accumulation, and a slightly reduced DC conductivity. The changes were primarily connected to the increased deep trap density due to the nanofiller.

Naturally, other nanofiller compounds for LDPE/XLPE have also been examined. The effect of nano-titania on DC insulation performance was analyzed in [151]. Similar to the investigation of nano-magnesia's effects mentioned above, an increase in the DC breakdown strength and a decrease in the injected homocharge density were identified. The work also analyzed the influence of nanoparticle dispersion on charge characteristics, which are deemed pivotal to improving the material's insulation properties. Non-specified XLPE nanocomposites were examined for use in HVDC cables in [152]. In this case, the addition of nanofillers achieved an increase in the material's resistivity, which was explained using the multi-core model and Schottky emission. An extensive study of the effects of graphene nanofiller on the trap properties and charge transmission in LDPE is given in [153]. Since graphene is semiconductive, only small filler contents (fractions of wt%) were employed to preserve the material's insulative character. The smaller filler contents increased the polymer's DC breakdown strength and reduced its conductivity. Analogous to the studies performed for nano-silica, magnesia, and titania, space charge accumulation was suppressed, and the density of deep potential traps rose.

Ultimately, it should be mentioned that although nanocomposite insulation is still rather new and its long-term stability could not have yet been verified, it has already been employed in a large-scale power apparatus. Perhaps the most representative example of such a system is the ±250-kV HVDC cable link between Hokkaido and Honshu islands in Japan, described in [154]. Even though the exact composition of the nanocomposite insulation has not been publicized, it can be expected that one of the above-mentioned nanofillers was used. So far, the link has been in operation (for ca. eight years) with no reported issues. With the continuous improvements in manufacturing technologies, more realizations of power systems utilizing nanocomposite insulation can be anticipated in the future.

2.5 Chapter summary

The leitmotif of the extensive second chapter was insulation degradation. At first, various types of breakdowns concerning the applied voltage stress and time-to-breakdown were covered. Since long-term degradation, or aging, represents the main topic of this dissertation, it was discussed to the greatest extent. Following a concise overview of fundamental traits of long-term degradation, the evaluation of accelerated aging (and breakdown) tests was described. Aging models employed for lifetime predictions based on aging data were discussed subsequently. A particular focus was paid to the Crine aging model, as it is specifically suited for extruded polymeric cables. As this thesis aims to evaluate the effect of supraharmonics on the degradation rate, a review of similar research articles was given next. Two main phenomena due to the presence of higher-frequency components in the examined waveforms were identified: strengthening of the local (internal) electric field and increased dissipation losses. The review was limited to intrinsic aging, i.e., in the absence of partial discharges.

Naturally, partial discharges had to be discussed next. A concise overview of specifics of internal partial discharges introduced the topic. An emphasis was put on the impact of PDs on the degradation rate

of materials. Due to the inclusion of an analytical PD model in the experimental part of the thesis, various ways to model PD activity were listed and briefly described. Analogous to the intrinsic aging section, the effects of higher-frequency voltage waveform components (on PD activity) were reviewed. A definitive decrease in the PDIV of various test configurations owing to such components was observed in the searched publications. In numerous cases, an amplification of the PD activity was recorded as well. These changes were assumed to originate from the various additional voltage components' heightened $\mathrm{d}V/\mathrm{d}t$ ratios.

Basic properties and manufacturing methods of polyethylene-based insulation were described afterward. Since an experiment on XLPE cable terminations was also carried out within this dissertation, their construction and characteristics were mentioned. Chosen diagnostic methods of cable systems were briefly reviewed next. Due to the use of nanocomposite XLPE in the second experiment, nanodielectrics were also included in this chapter. Apart from the fundamental characteristics of nanocomposites and the multi-core model, their manufacturing methods and issues related to these processes were discussed. Ultimately, the effect of different nanofiller compounds on the insulation performance of PE or XLPE was reviewed.

Aim of the Work

The presence of supraharmonics in power networks (Chapter 1) should theoretically enhance the aging rate of the respective insulation systems (Chapter 2). The review of research works concerning the additional impact of phenomena **similar** to supraharmonics on insulation systems' performance identified minimal effects in the case of aging in the absence of partial discharges (section 2.2.5). In contrast, severe effects were detected in the case of aging in the presence of partial discharges (section 2.3.4). Specifically for cable XLPE insulation, the respective review (section 2.4.4.4) identified ways to improve the insulation performance of PE or XLPE by adding nanoparticles, which could help to mitigate said impacts.

Nonetheless, virtually none of the found research articles investigated the effect of fundamental AC waveforms with a considerable content of supraharmonics. Since such voltage waveforms can be present in power networks, especially with the boom of renewable power stations, this work aimed to provide a better understanding of their impacts on insulation systems. For this purpose, the following goals were set:

- determine how supraharmonic-polluted waveforms can affect the critical parts of insulation systems in such networks (MV cable terminations),
- specify whether the bulk insulation (non-critical parts) would also be affected (XLPE specimens),
- investigate if the insulation performance of the bulk insulation, both general and supraharmonic-specific, can be improved by a novel manufacturing process such as the addition of nanoparticles (nano-alumina-filled XLPE specimens),
- and analyze to what degree can one of the major degradation factors, partial discharges, be influenced by the presence of supraharmonics in the fundamental AC waveform (experimental measurement and analytical modeling of discharge activity in a sample cavity).

Ideally, the work would investigate all the constituent phenomena of the presence of supraharmonics and formulate a methodology to address them. However, when considering the scope of a single doctoral thesis, it is clear that only a partial contribution toward this desired goal can be achieved. Nonetheless, by meeting the above goals, perhaps a sufficient incentive for further research of the impacts of supraharmonics on insulation systems will be provided.

Chapter 3

Aging of Medium-Voltage Cable Termination Specimens

This chapter is based on publication [2].

The photovoltaic power station model and the conducted experiment, including the construction of the test station, were an integral part of doctoral thesis [155]. For the purposes of this work, these parts are listed only briefly per the co-authored publication [2]. The author's original contribution lies in the visualization and analysis of the results within the context of the other chapters of this thesis.

Abstract

The work investigated the influence of supraharmonic voltage components on the aging rate of XLPE cable termination specimens. At first, a model of a 1-MW photovoltaic power station was constructed so that an estimation of an actual voltage waveform at its output could be obtained. The waveform had a significant content of supraharmonic components, which were not suppressed by the commonly used harmonic filters. Combined thermal and electrical accelerated aging on a total of nine 3-m long cable termination specimens was performed afterward. The electrical stress was represented by either a 50-Hz AC waveform or a waveform analogous to the one obtained from the model, whereas the thermal stress was designed to keep the cable core at its maximum operating temperature of 90 °C. Three diagnostic methods were employed to analyze the degradation state of the specimens – loss tangent measurement, PD measurement, and breakdown voltage measurement. A clear tendency for premature failure was identified for the specimens aged by the waveform with significant supraharmonic content. Only one of the three specimens withstood the aging test. Conversely, all three specimens under the 50-Hz AC stress withstood. The diagnostic measurements subsequently performed on the remaining specimens confirmed this tendency to some degree.

Introduction

The aforementioned study of the Eagle pass back-to-back tie [18] (see section 2.2.5) was one of the first works that illustrated the adverse effects of unregulated supraharmonics on the degradation rate of insulation systems. In this regard, the examined cable terminations, interconnecting large power converters to the network, were the ideal "victim" – the field redistribution inside the terminations due to the higher frequency of supraharmonics was virtually as unfavorable as possible, and the supraharmonic content was enormous. In fact, the enhancement of the aging rate was so immense that not one but **four** terminations failed within a few days after their commissioning. The authors attributed the failures to dielectric losses, which would naturally be magnified by both the higher frequency and strengthened local field due to its redistribution inside the terminations' stress-grading layers. While the exact magnitude of the effect was unknown, the resulting temperature increase was sufficient to cause migration of silicone grease in the stress-grading layer, which initiated partial discharges that led to the quick erosion breakdown of the terminations.

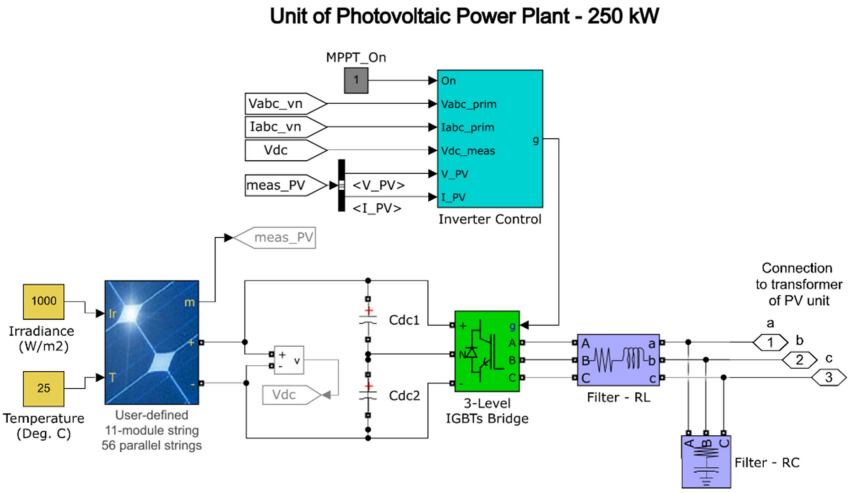

Figure 3.1: Elements of a single PV unit of the employed model. Adopted from [2].

Numerous research papers concerning the topic outlined in the Eagle pass investigation have been published over the following years. Specialized cable termination designs that maintained satisfactory field distribution up to hundreds of kHz have been proposed. However, these designs have not been indeed implemented in the industry, as the installations that would cause similar issues were very rare back then. Nevertheless, with the ever-increasing demand for renewable energy, power converter stations that transform and transfer the power generated by renewable power stations into the network are becoming ubiquitous. Although these stations are not exactly identical to the Eagle pass installation, it was shown that supraharmonic voltage components could reach substantial values in their local and adjacent networks (see section 1.2.2). Furthermore, the clear majority of such converter stations are relatively new when regarding the cable systems' expected technical lifetime.

Nonetheless, some unexplained premature failures have already been (confidentially) reported for such installations, at least in the author's country of origin. Thence came the motivation for this experimental investigation and the two main questions to be answered: *Can significant supraharmonics be present in networks close to converter stations of renewable power stations? If yes, what are their effects on the aging rate of cable systems?*

3.1 Model of a photovoltaic power station

3.1.1 Model topology, parameters

A photovoltaic power station was chosen to represent the renewable power station. As mentioned above, the model's main goal was to determine the shape of the voltage waveform at the station's output. The Matlab – Simulink software was employed for the simulation, which consisted of four smaller PV units (blocks), each connected to a single 3-level IGBT inverter with RL and RC standard harmonic filters at its output. An MV transformer was placed at the output of each inverter to increase the voltage level to 22 kV. All four transformers were subsequently brought out to a single common node (PV node), which was further connected to a block representing the self-consumption of the power station and an interconnecting MV cable/overhead line link. The link led to the primary of an upstream HV transformer (G node), which was connected to a block representing the adjacent HV power network. Individual elements of a PV unit are shown in Figure 3.1, whereas the entire model topography, including transformer voltage levels, wirings, and nominal powers, can be seen in Figure 3.2. Table **??** lists the parameters of the selected elements.

3.1.2 Worst-case scenario analysis, resulting waveforms

Two model parameters were variable: the length of the cable link and the length of the overhead line link. The reason for such a choice was to provide a means to observe the influence of the links' passive parameters on the upstream propagation of higher-frequency components. A worst-case scenario analysis was performed for the extended (over all frequencies) voltage THD index in the PV (=output) node.

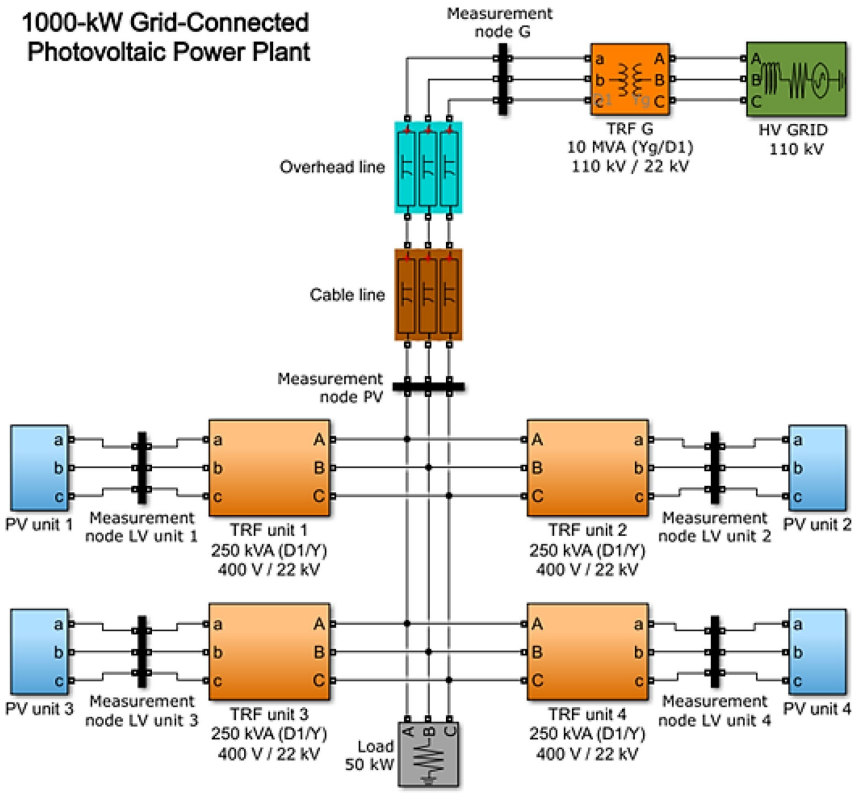

Figure 3.2: Topography of the modeled photovoltaic power station, including the adjacent elements. Adopted from [2].

Table 3.1: Overview of model element parameters

Element	**Parameter**	**Value**
PV array	Number of module strings	11
	Number of parallel strings	56
	Installed power	250 kW_{peak}
	Irradiance	1,000 W/m^2
	Panel temperature	25 °C
Inverter	Type	IGBT
	Number of levels	3
	DC (input) voltage	770 V
	AC (output) voltage	400 V_{RMS}
	Switching frequency	3 kHz
Passive filter	Series phase inductance	300 µH
	Parallel capacitance	500 µF
	THD power quality standards compliance	Yes
Power station	Number of blocks	4
	Installed power	1,000 kW_{peak}
	Power factor	0.95
Cable link	Resistance	0.32 Ω/km
	Inductance	0.4 mH/km
	Capacitance	0.31 µF/km
	Equivalent circuit type	π
Overhead line	Resistance	0.24 Ω/km
	Inductance	1.1 mH/km
	Capacitance	4.5 nF/km
	Equivalent circuit type	π

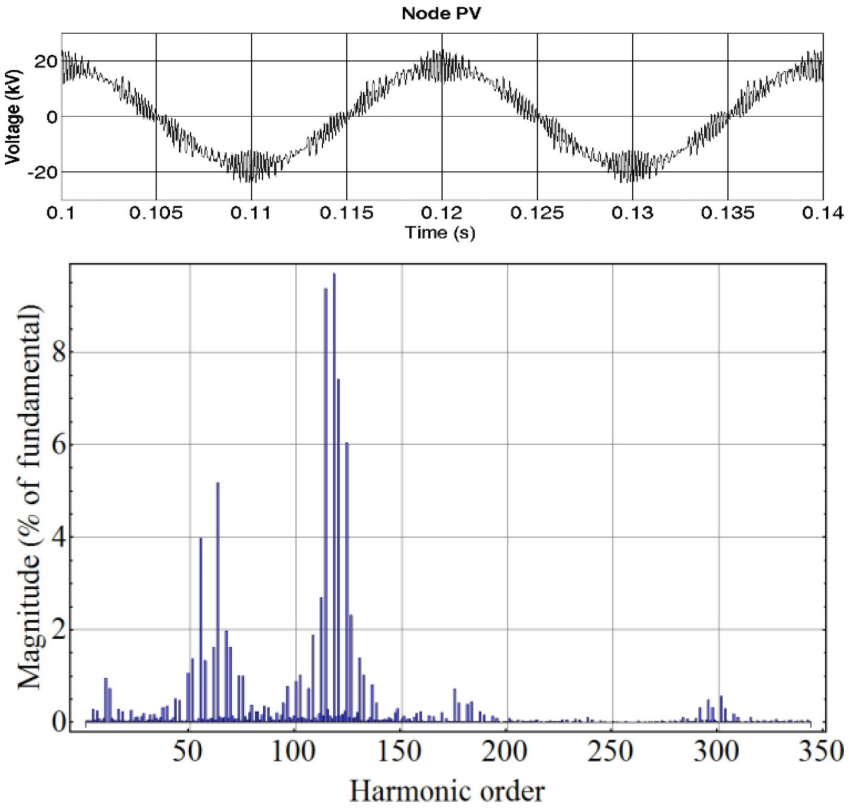

Figure 3.3: Results of the simulation for the worst-case scenario: voltage waveform in the PV node and its frequency spectrum. Adopted from [2].

Per its definition, the extended THD index could reasonably quantify the content of the investigated voltage components. In the analysis, cable length limits were chosen as 20 m and 1 km, while the length of the overhead line could vary between 5 and 30 km. In any scenario, the standard voltage THD index (up to the 40^{th} harmonic order) had to comply with the respective power quality standards. The length boundaries corresponded to the common practice of PV power station connection, in which a shorter cable link brings out the produced power to a nearby longer overhead line.

Simulations revealed that the worst-case scenario is present for a 20-m long cable and a 10-km long overhead line (see Figure 50 in [155]). In this case, the extended voltage THD index reached a value of about 20 %. The obtained voltage waveform and its frequency spectrum are shown in Figure 3.3. Note that such a significant distortion is present in the *PV* mode, i.e., at the MV sides of the PV unit transformers.

3.2 Experimental configuration

3.2.1 Accelerated aging test parameters

A critical decision to ensure that an accelerated aging test provides meaningful results is the choice of stress levels. Stress levels matching an insulation system's nominal operating conditions should not cause its failure during the stated technical lifetime. In the case of MV cable systems, the technical lifetime is most frequently given as at least 30 years. However, due to time constraints and common sense, the maximum aging time had to be limited to 24 weeks (about 4,000 hours). Since observable changes of the insulation state were necessary to quantify the effect of the distorted waveform, the aging rate had to be enhanced accordingly.

Concerning the temperature stress, the maximum operating temperature of XLPE cables, 90 °C, was employed. Although higher temperatures have also been used in other experiments, it was deemed safer regarding the regulation method to stay at such a level so that the glass transition point (about 105 °C) would not be overstepped. Besides, more reference XLPE aging data, including data from combined

Table 3.2: Parameters of the distorted waveform used in the experiment.

Waveform parameter	**Value**
50-Hz AC voltage	38.1 kV_{RMS}
SC amplitude (15 % of AC peak)	8.08 kV_{PP}
SC natural frequency	7.2 kHz
SC repetition frequency	800 Hz

aging experiments, were available at the chosen temperature of 90 °C.

These combined aging data provided the basis for the designation of voltage stress levels. In regard to the design of electrical stress, all the cable termination samples were prepared from the same 22-kV XLPE single-phase cable. Since the thickness of the insulation layer was 5.5 mm and the nominal phase voltage was 12.7 kV, the resulting nominal electrical stress corresponded to about 2.3 kV/mm. Suitable reference data, available in [43, 156, 157], predicted a very long to "infinite" lifetime for such a configuration, which was in line with the expectations for the nominal operating conditions. By increasing the voltage stress to 300 % (6.9 kV/mm), the following predictions can be obtained: a time-to-breakdown of about 10,000 hours for XLPE aged by thermal cycles between 22 and 90 °C in air (Figure 8 in [43]) as well as by constant 75 °C in air (Figure 13 in [43]); upper thousands to lower tens of thousands hours for XLPE cable samples aged at 90 °C in air (Figure 3 in [156]); and about 200 days (4,800 hours) for XLPE cable samples aged in water under 8 kV/mm electrical stress and with cable core kept at 90 °C (cumulative failure probability of 63.2 % in Figure 1 of [157]).

All in all, the available data predicted a time-to-failure of upper thousands of hours for the chosen stress levels. It should be noted that the articles are of older date and that the manufacturing technology has improved since then. Longer lifetimes for contemporary cable samples can be therefore expected. Furthermore, the lifetimes obtained from the aging tests performed in water might be substantially reduced due to water treeing, which should naturally not be the case when the tests are conducted only in air. On the other hand, the cable samples employed in this experiment included cable terminations, which are generally regarded as the area most prone to failures. It was, therefore, speculated that these effects more or less cancel each other and that the predicted time-to-failure is valid. In that case, degradation under the standard sinusoidal waveform stress should not cause a breakdown within the timeframe of the experiment, but its impacts should be apparent. Since such an impact was sought after, the triple nominal voltage stress was employed.

3.2.1.1 Distorted waveform

The waveform obtained from the simulation (Figure 3.3) would have been complicated to generate unless a similar PV power station unit had already been available. Instead, an analogous waveform consisting of fundamental AC 50-Hz voltage and superposed supraharmonic components (SC) representing the obtained distortions was employed. The waveform's parameters are listed in Table II, and its actual shape, including the effect of the test station's passive parameters, is shown in Figure 3.4.

3.2.2 Test station

A specialized combined aging test station had to be assembled for the purpose of this experiment. A series combination of an MV 50-Hz test transformer and an MV high-frequency transformer was employed to generate the voltage stress. Conversely, the thermal stress was created by a toroidal current transformer, which was galvanically decoupled from the circuit. The current loop was formed by two separate copper busbars that the cable specimens would interconnect during the experiment. Two capacitors and an inductor were added into the circuit to suppress high-frequency components at the secondary of the 50-Hz test transformer and, analogously, power frequency components at the HF transformer secondary. The circuit diagram of the electrical parts of the test station is shown in Figure 3.5, whereas the actual realization of the test station is depicted in Figure 3.6. Parameters of the individual components are listed in Table 3.3.

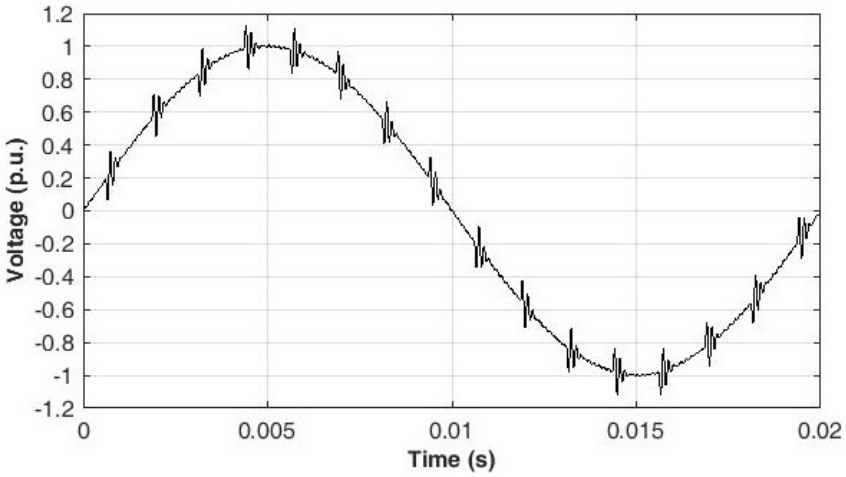

Figure 3.4: The distorted waveform used in the experiment. Adopted from [2].

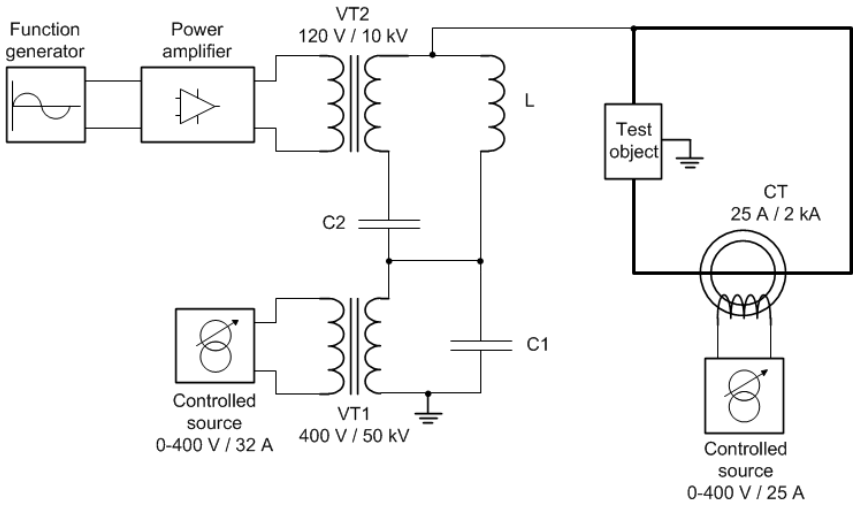

Figure 3.5: A circuit diagram of the test station. The generic test object is, in this case, represented by the cable termination specimens. VT1/2 – voltage transformer: 50-Hz (1), high-frequency (2); CT – current transformer. Adopted from [2].

Table 3.3: Parameters of the test station components.

Component	**Parameter**	**Value**
Test transformer V1 (50-Hz)	Nominal voltage	400 V/50 kV
	Nominal power	40 kVA
Test transformer V2 (HF)	Nominal voltage	120 V/10 kV
	Nominal power	6 kVA
	Main insulation withstand voltage	$\geq$ 60 kV
	Frequency range	5 to 120 kHz
Current transformer CT	Construction	Two parallel toroidal cores
	Supply current	Up to 25 A
	Supply voltage	Up to 400 V
	Output current	Up to 2 kA (short-circuit)
	Main insulation withstand voltage	$\geq$ 60 kV
Air-core inductor L	Inductance	11.7 H
HV capacitor C1	Capacitance	10 nF
MV capacitor C2	Capacitance	0.05 µF

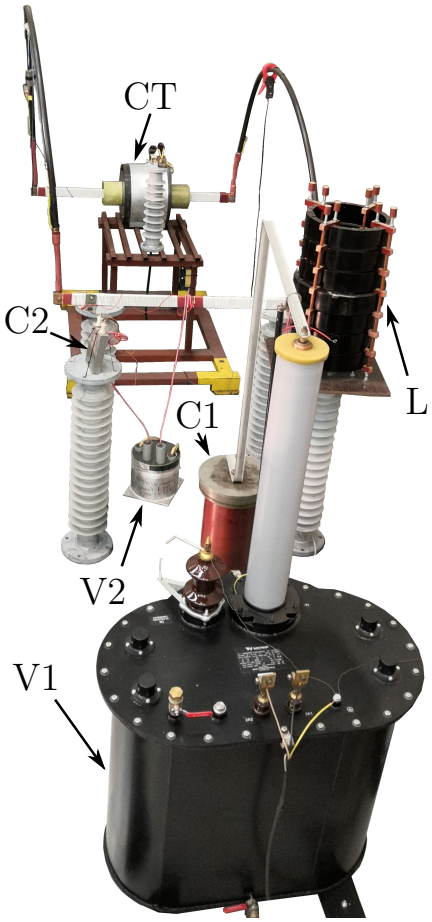

Figure 3.6: The realized test station. The nomenclature corresponds to Figure 3.5.

Figure 3.7: One of the tested cable termination specimens; the figure also depicts the test configuration employed in loss tangent measurements.

3.2.3 Cable termination specimens

The cable termination specimens consisted of a 3-m long section of a standard 22-kV shielded one-core XLPE cable (cross-section of 150 mm^2), which was equipped with a heat-shrink termination on each end. One of the specimens is depicted in Figure 3.7 (the photo was taken during the loss tangent measurement). The conditions of the reference work, [18], were replicated by employing terminations with a non-linear stress grading layer. For thermal stress regulation purposes, temperature sensors were placed on the cable jacket. A measurement calibration in accordance with the IEC 61442 standard was subsequently performed to obtain the current required to increase the cable core temperature to 90 °C. A current of about 480 A was determined to be sufficient for such a purpose.

A total of nine specimens was prepared. Of these nine, three were not stressed to provide reference data, whereas the other six were stressed both thermally and electrically. The thermal stress was identical for all these samples, but three samples were stressed electrically using a standard 50-Hz waveform, while the other three were stressed by the distorted waveform. An overview of the specimens listing their codename and respective aging parameters is given in Table 3.4.

3.3 Results and discussion

3.3.1 Partial discharge measurements

Extensive partial discharge measurements were performed on the specimens before, during, and after the accelerated aging tests using an Omicron MPD 600 PD measuring instrument. In each run, the PDIV and PDEV were determined, and PRPD patterns at different test voltage levels were recorded. The employed test voltage protocol consisted of six levels, each with a dwell time of one minute. The initial voltage level of 40 kV was sequentially reduced by 5 kV down to 15 kV. Afterward, the entire sequence was repeated two more times. 60-s long PRPD patterns were recorded at each voltage dwelling of each iteration, and the obtained apparent charge was written down. The first measurement was conducted prior to the aging test to provide reference data and to confirm the correctness of the termination mounting. Subsequent measurements were performed every three weeks throughout the experiment and,

Table 3.4: Aging parameters of individual specimens.

Codename	Thermal stress (core)	Electrical stress	Distorted?
T1	90 °C	6.9 kV/mm	Yes
T2	90 °C	6.9 kV/mm	Yes
T3	90 °C	6.9 kV/mm	Yes
T4	90 °C	6.9 kV/mm	No
T5	90 °C	6.9 kV/mm	No
T6	90 °C	6.9 kV/mm	No
T7	20 °C (room)	0 kV/mm	No
T8	20 °C (room)	0 kV/mm	No
T9	20 °C (room)	0 kV/mm	No

where possible, afterward. The PDIV and apparent charge metrics were employed to evaluate the extent of degradation, whereas the recorded PRPD patterns were used primarily to verify that the PD activity is not of an external origin.

3.3.1.1 Partial discharge inception voltage

Figure 3.8 depicts the time development of the samples' PDIV. The upper part shows samples T1 to T3, aged by the distorted waveform, while the lower part shows samples T4 to T6, aged using the standard AC waveform. Third-degree polynomials fitted the data to represent the tendency of cable termination to "settle" in the initial period after the installation. This phenomenon should be observable by reduced PD activity and slightly increased PDIV due to the thermally induced structural rearrangements that instigate the collapse of some of the internal cavities.

Indeed, such a tendency is observable in the trends, particularly in those of specimens T4 to T6, but it manifested first after several weeks had passed. The intermediate period was marked by a sharp decrease in the PDIV in comparison to the initial measurement. It can be speculated that such an increase was due to the strong applied electric field, which incited intensive charge detrapping combined with enhanced charge deposition on cavity surfaces. Were that the case, the PD measurements, which were always performed within a maximum of three hours after removal from the test station, could have been influenced by the remaining trapped charges. Naturally, these charges would have been easier to detrap so that the PDIV would have been reduced.

Another explanation of the initially decreasing PDIV might be the development of surface discharges inside the samples due to delamination or on the cable jacket. External corona discharges cannot also be ruled out entirely. Nevertheless, the gathered PRPD patterns were reviewed, and their shapes corresponded to those of internal cavities, showing multiple combined PD activities distinguished by the typical "rabbit ears." Strong memory effect, characteristic for internal discharges, was also identified from the presence of both same- and opposite-polarity discharges in a single test voltage halfwave.

The increase in PDIV, attributed to the "settling processes," varied in extent from specimen to specimen. In any case, the parameter started to decrease afterward, indicating a worsening of the insulation state. In the case of specimens T1 and T2, the decreasing tendency manifested around the 13^{th} week of aging. Shortly afterward, failure of both specimens ensued. Hints of such a decrease are present toward the end of the aging test for specimens T3 and T4, suggesting that their breakdown could have occurred soon if the test were to be continued, that is, if the observed PDIV trend is to be trusted. Conversely, the development of the PDIV of T5 and T6 specimens predicts that the "settling" PDIV peak has not yet been reached. Therefore, no imminent breakdown of the specimens should be expected.

It is worth mentioning that the PDEV of the specimens was also measured, but it mostly followed the trend of the PDIV, only with a slight shift of a few kV downward. Hence, the respective trends are not depicted.

3.3.1.2 Average charge

Concerning the average charges, their time development (at the 40-kV test voltage level) is depicted in Figure 3.9. In this case, the parameter should be taken inversely to the PDIV – the higher the value,

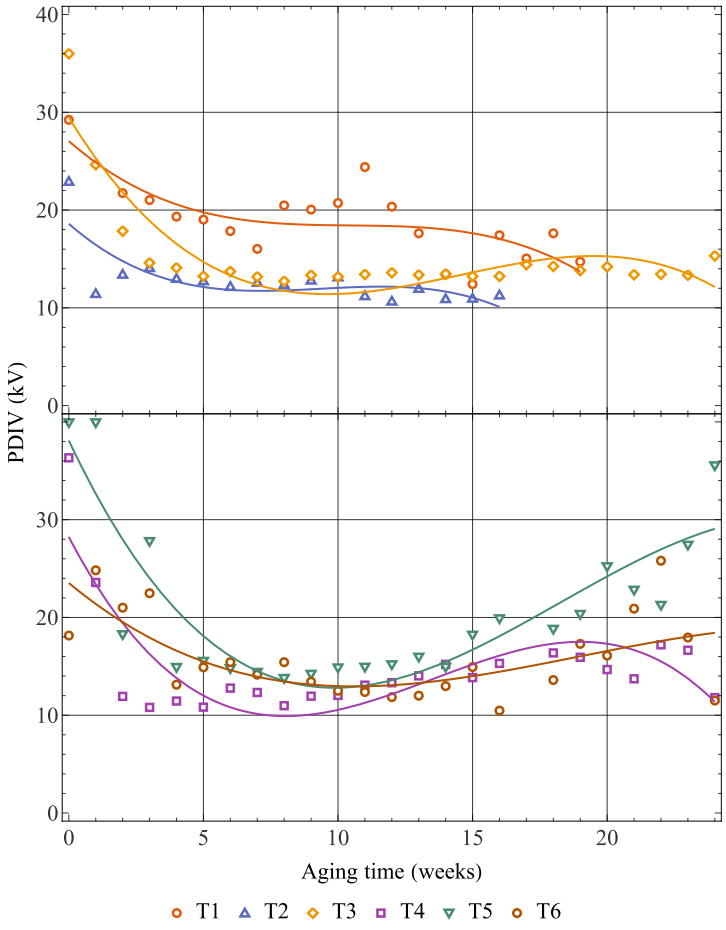

Figure 3.8: The evolution of samples' PDIV with aging time.

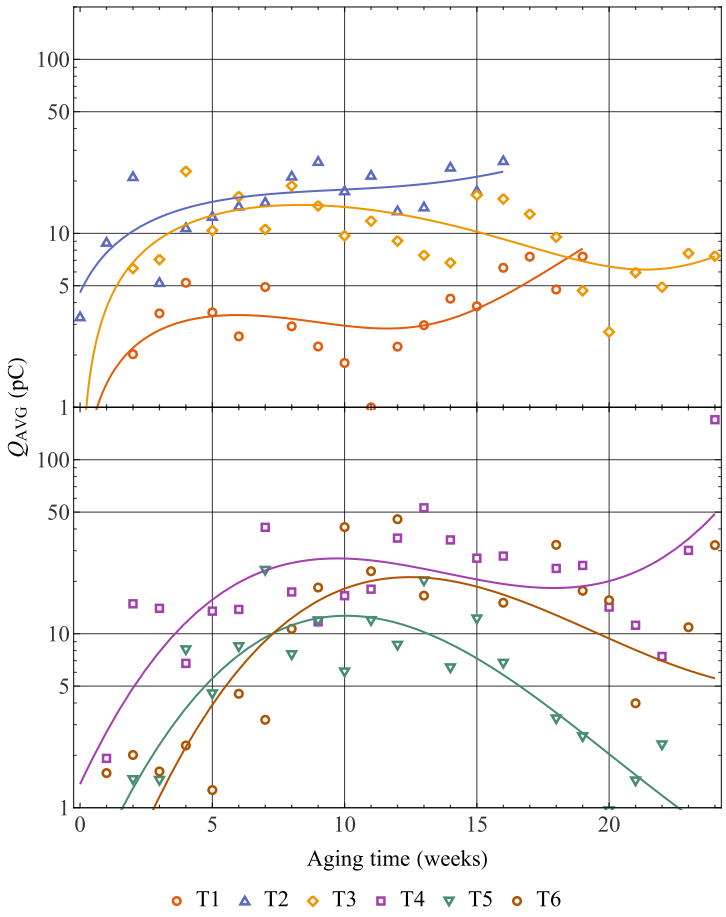

Figure 3.9: The evolution of specimens' average charge with aging time. Measured at a test voltage of 40 kV.

the worse in terms of insulation state. Based on this assumption, one can see that the average charge trends are similar to those of the PDIVs. At first, a significant increase in the average charge is observed, in which most of the specimens overstep the 10-pC threshold during the first few weeks. Afterward, the "settling" processes most likely manifest as the charge starts to reduce gradually. As is evident from the trends of samples T1 and T2, the average charge starts to rise again in the next phase, which is ultimately concluded by the specimens' failures. It should be noted that the assumed transition due to the "settling" is not apparent for the T1 specimen, both from the PDIV and average charge trends. It can be argued that due to the significantly reduced lifetime (T1 specimen's time-to-failure was the shortest), the transition was not captured to its greatest extent due to the weekly basis of the measurements.

Nonetheless, even the other samples, T3 to T6, exhibit the above-described behavior. In contrast to the prediction from the PDIV trends, specimen T3 does not seem to be about to fail, as the pre-breakdown increase in the average charge was not detected. However, the readings gathered in the last few weeks of the aging test show high discrepancy, which seems to influence the polynomial fit substantially. On the other hand, rising tendencies toward the end of the aging test are evident not just from the trend of specimen T4, as was the case for PDIV, but also from the trend of specimen T6. The behavior of specimen T5 was in line with the tendency observed in its PDIV measurement, as the average charge also gradually decreased, eventually reaching values below the reliable lower measurement threshold of 1 pC. Both metrics indicate that the T5 specimen was the least degraded one out of the entire set.

Ultimately, it is vital to mention that the PDIV of all specimens was well below the aging test voltage of $3 \cdot U_{\mathrm{n}}$, i.e., 38.1 kV. Therefore, the primary degradation mechanism is assumed to have been partial discharges. Such an observation perhaps conflicts to a certain degree with the findings of the Eagle-pass installation investigation, where the failures attributed to PDs occurred almost lightning-fast compared to those in this experiment. Nonetheless, the occurrence of PDs should also be viewed through the lens of their average charge, which was for most parts of the experiment within reasonable boundaries (10 to

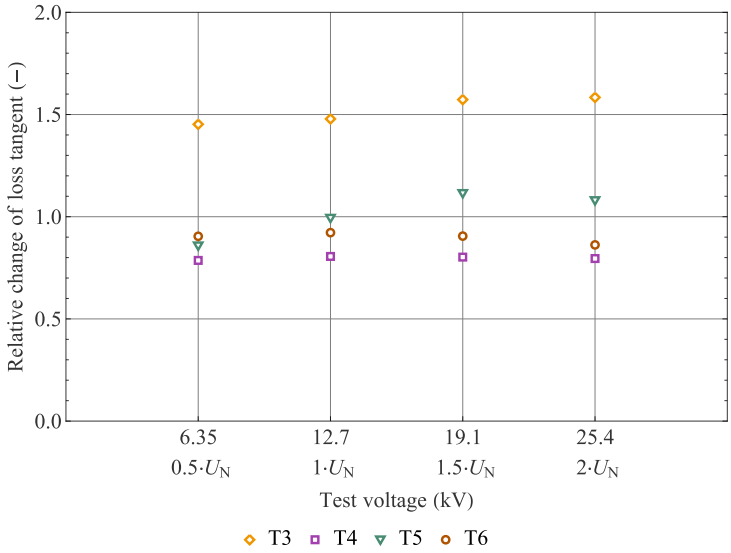

Figure 3.10: Results of the loss tangent measurements carried out at different multiples of the specimens' nominal voltage. The y-values represent the ratio of individual loss tangent readings obtained after and before the aging test.

50 pC). However, such data are not available for the Eagle-pass investigation, which could very well mean that the PD activity was substantially more prominent in that case. Furthermore, the waveforms gathered in the installation had a much larger content of standard-order harmonics as well as supraharmonics (see Figure 2 in [18]), which makes it entirely plausible that the degradation-enhancing effect, observed for specimens T1 and T2, was magnified to such a degree, that premature failures occurred within hours to days instead.

3.3.2 Loss tangent measurements

The individual specimens' loss tangents were recorded at various multiples of the nominal voltage both before and after the execution of the aging test. Figure 36 depicts the change in the specimens' loss tangent as a single value determined from the ratio of readings obtained after the test to the readings obtained prior to it. Unfortunately, due to equipment limitations, the measurements had to be performed at room temperature, which might have reduced the results' representability drastically, as mentioned briefly in section 2.4.3.2.

Before drawing any conclusions from the results, it is vital to acknowledge that the inception of partial discharges impacts the value of measured loss tangent. In a dischargeless state, insulations systems are generally linear, and hence the loss tangent readings should be invariant to the employed test voltage. However, when PDs are incepted, the discharge currents are suddenly added to the equation. Since loss tangents of a typical insulation system are very low, and since the discharge current is frequently distributed over a wide range of phase angles, the new loss tangent reading will be higher. Hence, a sudden rise in the loss tangent with increasing test voltage is often a preliminary indication of partial discharges. Such a rise in the loss tangent vs. test voltage trend is referred to as an "ionization knee" [37].

Since partial discharge diagnostics have also been performed, it might be advantageous to dedicate the loss tangent measurement to determining the "integral" insulation state of the specimens. By looking at the individual PDIV values, the test at a voltage of 6.35 kV seems to be the only common ground, at which no partial discharges were occurring both before and after the aging test. Hence, these readings were most likely not impacted by PDs, and therefore the observed change in loss tangent should provide the sought-after "integral" insight.

At the above-stated voltage level, the loss tangent of the specimens aged under the standard waveform stress, T4 to T6, slightly decreased, which would correspond to the supposed "settling" processes. Conversely, only the T3 specimen's loss tangent increased noticeably. Such an increase indicates worsening of its insulation system's state, likely marking the transition to a later degradation phase. Fundamentally, these observations are in agreement with the assumed degradation acceleration effect of the distorted

Table 3.5: Results of the step-up breakdown tests.

Codename	Accelerated aging time	Breakdown voltage
T1	136 days	N/A
T2	112 days	N/A
T3	168 days	104 kV
T4	168 days	108 kV
T5	168 days	108 kV
T6	168 days	108 kV
T7	0 days	108 kV
T8	0 days	112 kV
T9	0 days	108 kV

waveform. However, the results also imply that specimens T4 and T6 are degraded to a much lesser degree than the T3 specimen. Such an implication contrasts with the inferences of both PDIV and average charge measurements, which also predicted impending failures of specimen T4, or eventually T6 as well. The explanation could lie in the different approach of each measurement, where partial discharge highlight the weak points of the insulation system, whereas loss tangent is determined by the entirety of the system and is hence less sensitive to local defects.

By the above logic, it is plausible that the distorted waveform substantially accelerated the aging of the T3 specimen's bulk (cable) XLPE insulation, which then manifested as the increase in the loss tangent value. While the applied electrical stress was low (∼7 kV/mm) in comparison to the short-term AC breakdown strength of XLPE (∼100+ kV/mm), one needs to remember that the field inside the cable insulation is inhomogeneous due to its concentric configuration and that the reference breakdown strength was obtained for much thinner film specimens in laboratory conditions. On the other hand, the cable insulation is relatively thick (5.5 mm), and its volume, as well as defect concentration, is incomparably higher. With the aging time of almost half a year, during which high thermal stress was also present, some degradation of the bulk insulation can be expected, seemingly in particular when the voltage waveform is distorted in such a manner. Among other things, this assumption also instigated the subsequent aging experiment conducted on XLPE film specimens, which is described in Chapter 4.

Nevertheless, as was expected, the premature failures and the failures during the subsequent breakdown test all occurred in the cable terminations, i.e., at the specimens' weak points. This fact gives greater weight to the PD measurements, as the discharges almost certainly occurred exclusively in the terminations. In any case, both diagnostic methods are in unison regarding whether the distorted waveform accelerates the aging process. Moreover, the loss tangent measurement was shown to be a suitable complement to its PD counterpart, as it could offer another point of view on the specimens' insulation system states.

3.3.3 Step-up breakdown tests

After the accelerated aging experiment had been concluded and the final partial discharge and loss tangent measurements had been taken, the surviving samples' breakdown voltage was determined via step-up breakdown tests. These tests were carried out using a step-up voltage protocol with an initial voltage of 40 kV, a dwell time of 20 s, and a voltage step size of 4 kV. Naturally, both terminations of each specimen had to be immersed in insulating oil to prevent surface flashovers. The results of the step-up breakdown test are listed in Table 3.5.

Out of the specimens aged by the distorted waveform, only the specimen T3's breakdown voltage could be tested, as the others had already broken down during the aging test. The respective breakdown occurred at a lower voltage level than in the case of specimens aged under the sinusoidal waveform stress (T4 to T6). While the decrease is equal to just a single voltage step, it nonetheless stands out in the context of the other specimens, including the unaged ones. Naturally, a more significant decrease in the breakdown voltage would be expected for samples T3 to T6 due to the accelerated aging. However, such an assumption was disproved in [158], where the breakdown voltage dependence of XLPE cables on their aging time was constructed. The trend indicated that the breakdown voltage reduces minimally with the aging time (see Figure 4 in [158]). Therefore, the slight decrease in the breakdown voltage of specimen

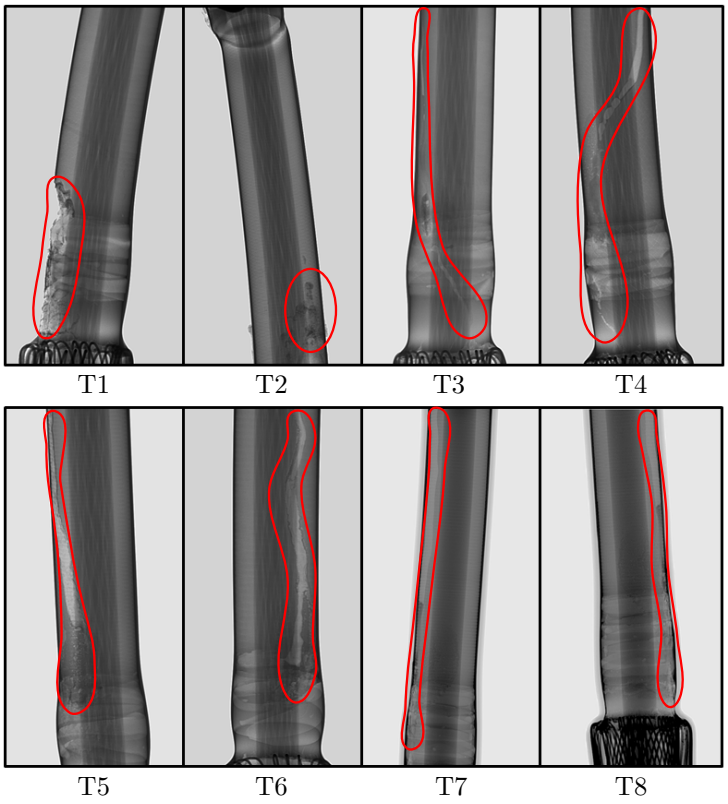

Figure 3.11: X-ray images of the broken-down terminations. Individual breakdown trajectories are highlighted in red. Adopted and edited from [2].

T3 could very well correspond to its substantial degradation.

3.3.3.1 X-ray scanning

Additionally, the specimens' failures were further examined via X-ray scanning, which revealed the breakdown trajectories inside the terminations. The X-ray images of the broken-down terminations of specimens T1 to T8 are shown in Figure 3.11. In the case of the prematurely failed specimens, T1 and T2, the breakdown propagated from the end of the shielding wires directly through the XLPE insulation into the cable core. A different trajectory was observed for specimens T4 to T9, where the breakdown also developed from the shielding wires, but it instead propagated alongside the non-linear stress-grading layer until it ultimately reached the cable lug. T3 specimen's breakdown trajectory represented a combination of the two – it also initiated from the shielding wires and propagated alongside the semiconductive layer; however, before reaching the cable lug, it swerved off through the XLPE insulation into the cable core (not depicted in the figure, as it was outside the boundaries of the X-ray image).

Regarding the interpretation of these breakdown trajectories, the propagation along the stress-grading layer indicates that the insulation system (XLPE) was durable enough to withstand the electrical stress and was not substantially degraded. On the other hand, propagation of the breakdown through the XLPE layer implies the presence of a weak spot, most likely a result of severe degradation. In the case of the T3 specimen, this weak spot was presumably located further away from the shielding wires. Nevertheless, the fact that the breakdown eventually pierced through the main insulation layer still infers that the specimen was degraded to a greater extent than its counterparts T4 to T6.

3.4 Conclusion

This chapter sought to answer the two questions formed in its Introduction. Concerning the first question, i.e., if substantial supraharmonic distortion can be present in the vicinity of a renewable power station, the constructed model of a PV power station provided a positive answer. To answer the follow-up question – if such distortions can accelerate the aging of the employed cable systems – an extensive experimental

study had to be performed. By looking at the results of the accompanying diagnostic measurements, the following conclusions can be drawn:

- The premature failures of two out of three cable specimens aged by the distorted waveform indicated their quicker degradation.
- The trends of both the PDIV and the average charge of the specimens implied that the distorted waveform degraded the specimen(s) to a greater degree. Conflicting predictions were obtained for the other specimens.
- Loss tangent measurements performed at room temperature and 50 % of the specimens' nominal voltage projected further degradation of the specimen, which survived the distorted waveform aging.
- Step-up breakdown voltage tests and accompanying X-ray diagnostics infer that the surviving specimen aged by the distorted waveform was degraded to a greater extent.

Naturally, each of the employed diagnostic methods is susceptible to interpretation errors. Partial discharges might have been occurring in the semi-conductive layer or at its interface with the cable's sheath. Such discharges would have also been detected, even though they do not represent an immediate threat to the cable [129]. Similarly, loss tangent readings could have been impacted by undetected partial discharges, and breakdown voltage readings might have been misinterpreted due to their minor differences. Nevertheless, since each diagnostic method points in the same direction, that is, toward the enhanced degradation effect of the distorted waveform, the answer to the second question must also be "yes."

Such a conclusion was expected when considering the results of the frequently-referred Eagle pass installation study. However, the distortion content was much lower in this case, and also about 20 years have passed since the study was published, meaning that there was enough time to incorporate the formerly proposed solutions into the standard cable termination design. As evident, the issue has not been successfully resolved yet, and due to the increasing number of power converter installations, it is perhaps necessary to highlight it once again.

Chapter 4

Aging of XLPE and Nano-XLPE Specimens

This chapter is based on publications [3–5], and [9, 10].

Abstract

This experimental work aimed to determine whether voltage waveforms with supraharmonic components degrade cross-linked polyethylene insulation faster than their purely sinusoidal counterparts. For this task, long-term aging tests of ca. 200-µm thin XLPE film specimens were performed at different voltage stress magnitudes using two waveform types – sinusoidal and distorted. Alumina-XLPE nanocomposite specimens with different filler weight percentages were also included in the experiment to cover novel polymeric insulation systems. The aging time was limited to 720 hours for each test run, except for the pure XLPE aging test at the lowest stress level, which was prolonged to 4,320 hours.

After the tests had been concluded, the gathered results were treated by Weibull statistics. Next, the calculated mean times to failure (MTTF) of each material-stress type combination were fitted by various aging models, and the obtained lifelines were subsequently analyzed. The lifelines obtained by employing the frequently used inverse power law (IPL) implied that the 1wt% and 3wt% alumina nanocomposite specimens degraded faster than the pure XLPE specimens, especially under the distorted waveform stress. On the other hand, the degradation of 5wt% specimens under both waveform stresses seemed to transpire slower than in the case of the pure specimens. A slight increase in the aging rate was detected for the 5wt% specimens aged under the distorted waveform stress. Regarding the reference pure XLPE specimens, their lifelines indicated that the degradation under the distorted waveform stress had been more intensive. Two variants of the Crine model were subsequently applied to the aging data. Both variants implied similar conclusions as the IPL. Ultimately, an explanation of the observed phenomena was proposed, and possible sources of errors in the predictions were identified.

Introduction

The main idea behind this investigation was already described in detail in the Introduction to the previous chapter. However, the chapter paid attention mainly to the accelerated aging of cable terminations, while the topic of main insulation (XLPE) degradation was barely touched due to insufficient data. Therefore, this chapter aims to remedy these shortcomings and provide a more extensive insight into the phenomenon of accelerated degradation due to supraharmonic distortions.

Regarding the additional effect of distorted waveforms on the aging rate of film specimens, the search of similar works, given in section 2.2.5.3, found mostly disapproving verdicts. Of particular interest is work [80], which meticulously analyzed the effect of mixed voltage electrical stress on the aging rate of polymeric foil specimens. In the case of intrinsic aging, no apparent effect of the mixed voltage waveform's shape ($\mathrm{d}V/\mathrm{d}t$ ratio) on the degradation rate was observed. Similarly, no such effect was unequivocally identified in the author's master thesis [10].

However, there are some fundamental differences between the individual experimental configurations, making the works' conclusions not directly applicable to the investigation intended (and performed) for this chapter. Concerning the former work, the waveforms employed therein were mixed voltage (a combination of DC and AC components) with identical peak values. In contrast, the distorted waveforms used in both the master thesis and this investigation were made up of two AC components – fundamental 50-Hz and single-frequency supraharmonic – with the waveforms' RMS voltage identical instead. Moreover, in the master thesis, OIP specimens were investigated. While OIP bears a certain similarity to polymeric electrical insulation, particularly in terms of degradation processes, it is nonetheless a different material, and the conclusions obtained in the thesis are thus not transferable.

In the previous chapter, the loss tangent changes in the cable termination specimens (see section 3.3.2) indicated a possible intensification of the aging rate due to supraharmonic components in the waveform. As the increase was relatively significant (∼50 %), it can be speculated that degradation of the specimen's cable part main (XLPE) insulation also took place. Even though such speculation could not be verified, it nevertheless motivated this investigation.

Ultimately, as mentioned above, alumina-XLPE nanocomposites were also examined. Such inclusion was partially driven by the possible modification of the aging rate, as the incorporation of nanoparticles results in changes in materials' dielectric and thermal behavior. For example, reference data in [144] showed an increase of about 5 to 15 % in the relative permittivity of LDPE due to the addition of different weight percentages of magnesia nanoparticles (magnesia's relative permittivity of about nine is analogous to alumina's). Similarly, a slight increase in the loss tangent at room temperature was identified (see Figure 5.6 in [144]). On the other hand, the integration of alumina nanoparticles into epoxy resin decreased the relative permittivity by about 7.5 % compared to the unmodified material (see Figure 5.8 in [144]).

Regarding the thermal behavior, the heat dissipation of the unmodified XLPE specimens is expected to be improved by the presence of alumina nano particles, as alumina has a much higher thermal conductivity. This assumption was based on work [159], where the thermal conductivity of epoxy resin increased with the rising alumina nanofiller content. All in all, these changes could change the specimens' internal temperature, which should, in theory, alter their degradation rate. Naturally, the magnitudes of individual effects depend on the nanofiller content, meaning that multiple nanofiller contents had to be employed to analyze the phenomenon better. Apart from observing the net effect of electro-thermal parameter changes on the specimens' longevity, the influence of the supraharmonic distortions was also examined.

4.1 Experimental configuration

4.1.1 Accelerated aging test parameters, distorted waveform

In contrast to the experiment of Chapter 3, the XLPE film specimens were aged solely by electrical stress. Since the experiment was performed in a laboratory that also contains inhabited offices, the ambient temperature stayed mostly within the boundaries of room temperature, and hence the thermal stress could be disregarded. Concerning the electrical stress, two different voltage waveforms were employed – a standard 50-Hz sinusoidal and a 50-Hz sinusoidal with superposed supraharmonic components. Parameters of each waveform are listed in Table 4.1, and the distorted voltage waveform is shown in Figure 4.1, including a detailed depiction of the supraharmonic oscillation. Since the film specimens used in the experiment were relatively thin (∼200 µm), a slight deviation in their thickness could result in a significant difference in the applied field strength. Hence, the electrical stress levels were defined using electric field strength values rather than their voltage counterparts. Furthermore, in the case of thin films, the specimens' thickness can significantly affect their resulting breakdown strength. Therefore, the stress levels were in every case recalculated to 200-µm field strength equivalent using the ASTM D-149 standard.

4.1.1.1 Number of test runs, duration

Regarding the evaluation of the waveform's effect on the specimens' aging rate, three runs of long-term aging tests were performed for each specimen material – waveform combination. The respective trios of electrical stresses were designed so that the highest stress level would not cause the specimens to break down immediately, and simultaneously most of the specimens would fail within 720 hours at the lowest stress level. The reason for such a decision was to provide sufficient spacings between individual data points in field strength vs. MTTF plots for the subsequent aging model fitting. Unfortunately, the upper

Table 4.1: Parameters of the employed voltage waveforms.

Waveform	**Parameter**	**Value**
Sinusoidal	RMS voltage	1 p. u. (per designated stress)
	Peak voltage	1 p. u.
	Frequency	50 Hz
Distorted	RMS voltage	1 p. u. (per designated stress)
	Peak voltage	up to 1.1 p. u.
	1st harmonic frequency	50 Hz
	Supraharmonic oscillation frequency	8 kHz
	Oscillation repetition frequency	700 Hz
	Oscillation peak voltage	0.1 p. u.
	Number of oscillation periods	1

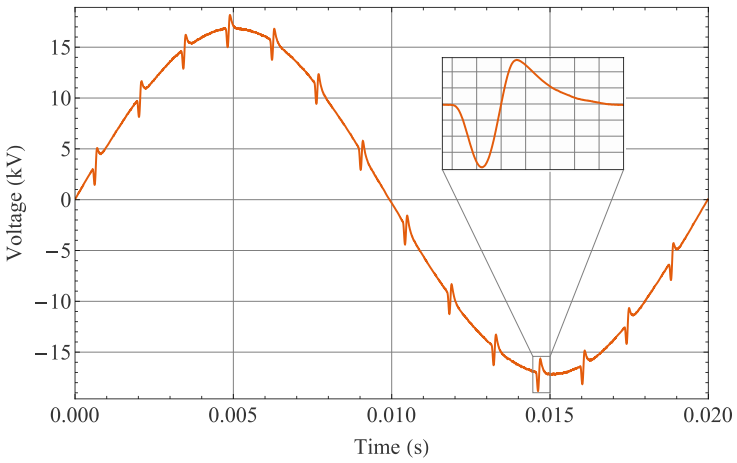

Figure 4.1: Trend of the distorted waveform recorded using a voltage probe and an oscilloscope. A single supraharmonic oscillation is shown in detail.

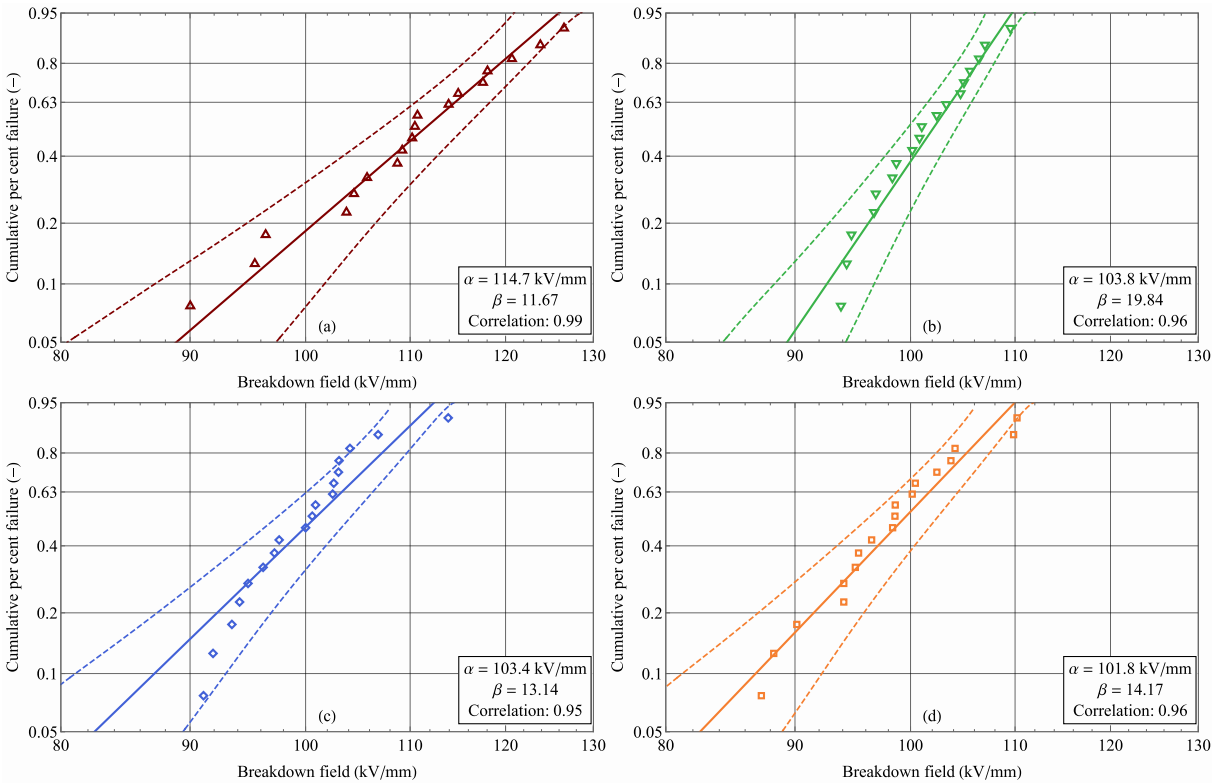

Figure 4.2: Results of short-term breakdown tests of the specimens evaluated according to IEEE/IEC 62539-2007 standard: (a) pure XLPE; (b) nano-alumina-XLPE, 1wt%; (c) nano-alumina-XLPE, 3wt%; (d) nano-alumina-XLPE, 5wt%. Estimated Weibull parameters are listed in the right-bottom corner of each plot. Confidence limits (90 %) are also plotted.

time limit had to be constrained due to a large number of test runs. An exception was made for both waveform types at the lowest stress levels of the (reference) pure XLPE specimens, at which the tests were run for 4,320 hours.

Ten specimens were tested for each combination to ensure that the obtained results would be statistically significant, bringing the total number of specimens to 240 (ten specimens per each of the three stress levels, four materials, and two waveform types). Combined with the long-term character of the aging tests, such a high number of specimens demanded that the aging tests would be as efficient as possible. Therefore, each set of specimens (10) was aged in parallel, and two test stations, each for one waveform type, were employed. As a result, the projected duration of the experiment was significantly reduced, but it would have still taken more than a year in the best case. In reality, due to idle times and the necessity to redo specific test runs, the actual duration was close to two years.

4.1.1.2 Choice of initial stress levels

Short-term breakdown tests were performed on the samples to provide an initial estimation of suitable stress levels. The gathered results, treated by Weibull statistics according to IEEE/IEC 62539-2007, are depicted in Figure 4.2. As evident, pure XLPE specimens had a mean breakdown strength of ca. 115 kV/mm, while the strength of all nano-alumina XLPE specimens was lower by about 10 kV/mm. The individual aging stress levels were then estimated as approximately 50 % of the specimens' breakdown strength. In the case of the pure XLPE specimens, the chosen stress levels were 60, 65, and 70 kV/mm. Due to the lower breakdown strength, the stress levels of nano alumina XLPE specimens were designated as 55, 60, and 65 kV/mm. Throughout the experiments, two alterations to the latter had to be made. For the 1wt% XLPE nanocomposite specimens, all the stress levels were reduced by 5 kV/mm in the case of the distorted waveform aging tests, as numerous instantaneous breakdowns took place at the original highest stress level. Conversely, the stress levels of the 5wt% nanocomposite specimens were increased by 5 kV/mm for both waveform types since exceptionally long times to failure were obtained at the formerly designated values.

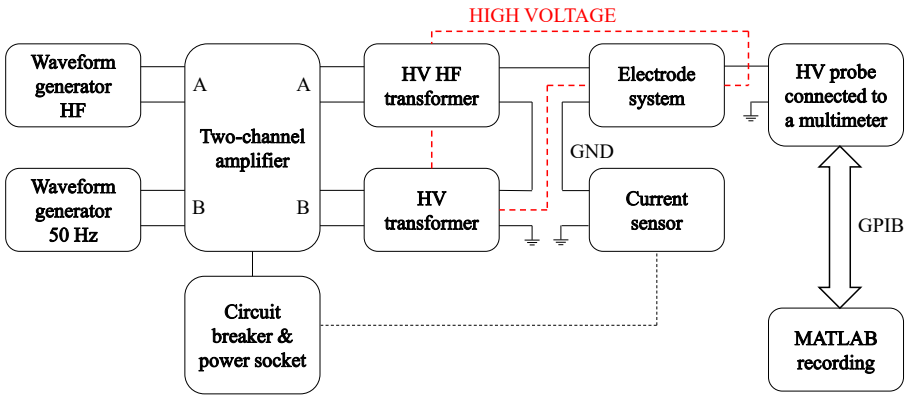

Figure 4.3: A block diagram of the distorted waveform accelerated aging test station. GND – grounded; GPIB – general-purpose interface bus.

4.1.2 Test stations

4.1.2.1 Voltage waveform generation

Similar to the cable termination experiment, a duo of test transformers was employed to generate the voltage stresses. A standard 100-kV HV test transformer supplied the 50-Hz stress, while the supraharmonic components were added using a specialized high-frequency HV transformer with a maximum output voltage of 15 kV_{RMS}. Since the transformers would be connected in series, as was the case in the previous experiment, the main insulation of the HV HF transformer was designed to withstand a much higher voltage than the 15 kV. The operating frequency of the HV HF transformer ranged from upper hundreds of Hertz to about 100 kHz (i.e., the transformer had a constant transfer ratio in this range), which was more than sufficient for the intended use.

An arbitrary waveform generator was employed to supply the test transformer's primary to ensure that temporal changes in the local power network would not influence the 50-Hz voltage stress. Another arbitrary waveform generator was employed to generate the supraharmonic oscillations via the HV HF transformer. Since both generators' output voltages were too low to excite sufficient stress levels via the transformers, a two-channel power amplifier was added in-between. A block diagram of the entire voltage generation configuration and the other elements of the test station is shown in Figure 4.3, while its actual realization is depicted in Figure 4.6. As an additional 50-Hz test transformer was available for use, another similar test station was constructed, albeit without the high-frequency channel.

4.1.2.2 Automated test shutdown & data collection

Due to the character of the aging tests, a large number of breakdowns was expected to take place, and therefore the test stations had to be designed for frequent serviceability. Furthermore, to reduce the overall time demands and suppress the influence of repeated test configuration energization, the experiments were kept running also in the absence of personnel, which meant that an automatic shutdown system, as well as a time-of-failure recording system, had to be implemented. Concerning the former, a current sensor was installed on the electrode system's earthing wire to detect overcurrent due to the breakdown of one of the specimens. In such a case, the sensor would trigger the circuit breaker of the power socket, effectively de-energizing the test station. Only the power amplifier was plugged into the switched power socket to eliminate the need for a repetitive configuration of the arbitrary waveform generators.

The test voltage was measured every ten seconds and saved along with the measurement's timestamp to an Excel file using a Matlab data-logging program to record the specimens' times of failure. By listing through the file, the failure could be easily identified as a sudden drop of test voltage to zero. Naturally, the test station had to be manually reenergized after each breakdown, and it was therefore necessary to keep track of the total uptime of the experiment. Regarding the test voltage, it was measured using a

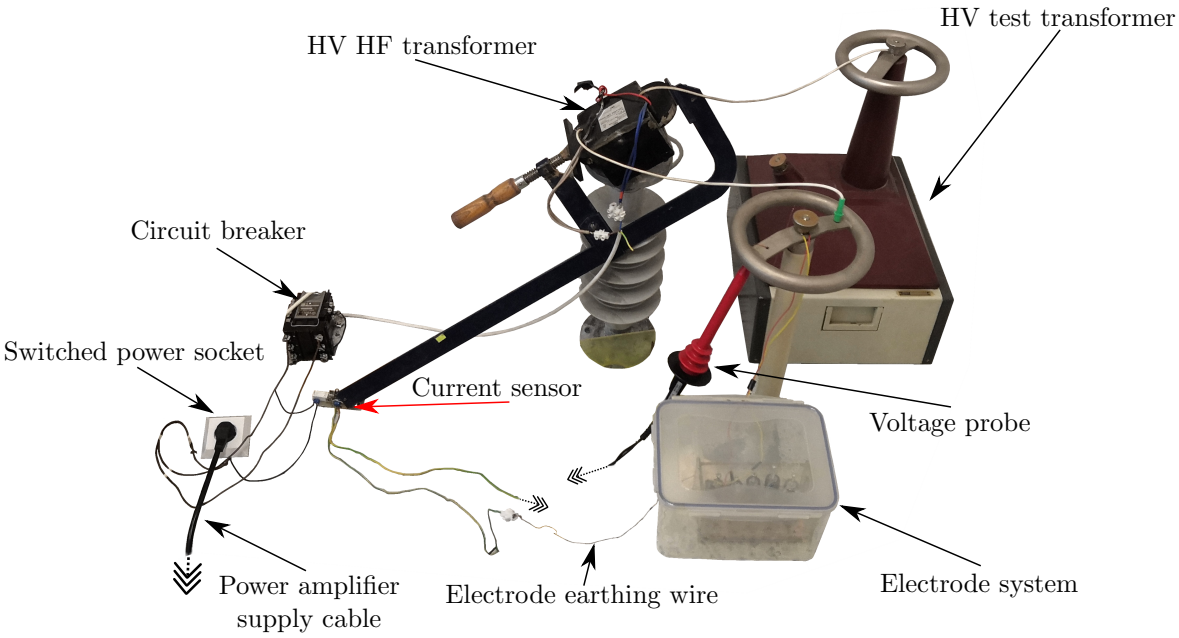

Figure 4.4: The actual realization of the XLPE specimen accelerated aging test station (distorted waveform).

1:1,000 HV probe connected to a multimeter. A GPIB cable was used to interconnect the multimeter with the (data-logging) PC to ensure that the EMI emitted by the breakdowns would not interfere with the recording devices.

4.1.2.3 Electrode system

Ten individual electrode pairs were employed in each electrode system to adhere to the demand of the simultaneous aging of ten specimens. Naturally, due to the specimens' size, the size of the electrodes had to be reduced from the standard dimension used for testing film specimens. Normally, both electrodes should be cylindrical, with a diameter of 2.5 cm for the upper and 7.5 cm for the lower. For this experiment, the diameter of the upper cylindrical electrode was reduced to 8 mm, while the lower was replaced by a large, grounded copper plate (ca. 15 cm by 6 cm). The copper plate provided a common ground for each of the upper electrodes, which were distributed equidistantly along the plate surface (in a two-by-five formation). A FEM electrostatic model of the electrode arrangement was constructed to verify that the spacing of electrodes is sufficient to eliminate mutual interactions. Regarding the upper electrodes, their edges were rounded (rounding radius of about 0.5 mm) to provide as homogeneous field as possible. The specimens and electrodes were immersed in insulating oil to improve the electric field conditions further. Apart from having a higher dielectric strength than air, the insulating oil also had a relative permittivity similar to XLPE (ca. 2.5 vs. 2.2, respectively).

Sufficient compressive force was exerted on the specimens by adding a 4-cm tall brass cylinder with a diameter of 3 cm atop the stainless-steel electrode. The two parts were held together by a stainless-steel bolt, which was subsequently connected to the voltage sources. A poly(methyl methacrylate) (PMMA) stand was used to secure the electrodes in their correct place. Due to the immersion in oil, the ground plate, specimens, and electrode stand were placed inside an open-top PMMA vessel to prevent the oil's leakage into the surroundings. Furthermore, as oil rapidly loses its insulating properties due to the ingression of water, the electrode system was sealed in an air-tight vessel, partially filled with silica gel, to combat the condensation of water vapors from the air. The actual realization of the entire system is depicted in Figure 4.5.

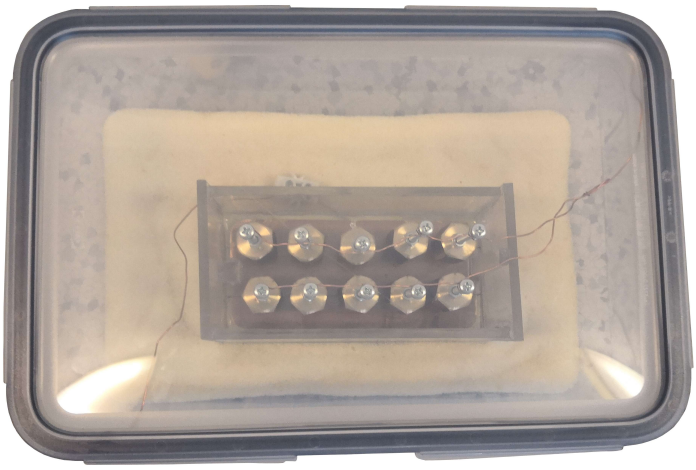

Figure 4.5: The electrode system employed for the parallel long-term aging of XLPE film specimens. The electrodes are placed inside of the smaller open-top PMMA vessel, which is surrounded by silica gel. Humidity ingress was prevented by placing the system into an air-tight polymeric container.

4.1.3 XLPE film specimens

All specimens were prepared in the same laboratory using identical procedures. Initially, industrial-grade LDPE granulates were extruded by a twin-screw extruder, and the created material was subsequently crosslinked over 10 minutes at a temperature of 120 °C in the presence of a dicumyl peroxide crosslinking agent. In the case of the nanocomposite specimens, the LDPE granules were mixed with the respective amount (weight percentage) of unmodified nano-alumina particles, while the crosslinking was performed at 10 rpm to ensure good dispersion of the nanoparticles. Afterward, the obtained (nano-)XLPE material was hot-pressed at a temperature of ca. 170 °C into 200-µm thick 15 cm by 15 cm films. The quality of the nanoparticle dispersion was verified through SEM imaging. As evident from Figure 4.6, no microscopic lumps of nanoparticles were present for either nanofiller content.

Since the XLPE films' thickness slightly differed from the required 200 µm at some places, the films were cut into approximately 2.5 cm by 2.5 cm pieces and sorted according to their thickness, which was measured by a digital caliper. For each test run, specimens of the same thickness were employed to ensure that identical electrical stress would be present.

4.2 Results and discussion

4.2.1 Statistical treatment of aging data

The results obtained from the accelerated aging experiments were evaluated according to the IEEE/IEC 62539-2007 standard. In specific test runs, not every specimen broke down during the prescribed time, and hence the respective data needed to be evaluated as single-censored. Furthermore, in some cases, fewer than five breakdowns were attained, which would substantially skew the fitted distribution. Thus, artificial breakdowns were added to the aging data so that at least five data points would be present. The time to breakdown of these fictional data points was equal to the duration of the test run, representing a pessimistic outlook, in which the "missing" number of failures would have occurred just after the experiment had been concluded. Since the total number of specimens of each test run was lower than twenty, the data were evaluated as smaller sets using *the White method*, described in section 2.2.3.3.

Starting with the aging test of the reference pure XLPE specimens, the treated breakdown data and their respective Weibull distributions, including the 90% confidence limits, are illustrated in Figure 4.7. At first sight, it is evident that the 70 kV/mm and 65 kV/mm stress levels significantly increased the degradation rate of the specimens aged by the distorted waveform. The aging data obtained at these stress levels for both waveform types showed minimal statistical spread, as can be seen from the narrow confidence limits. Nevertheless, the fitted Weibull distributions determined almost identical MTTF (cumulative per cent failure of 63.2 %) for the sinusoidal 70 kV/mm and 65 kV/mm stress levels. Regarding the degradation

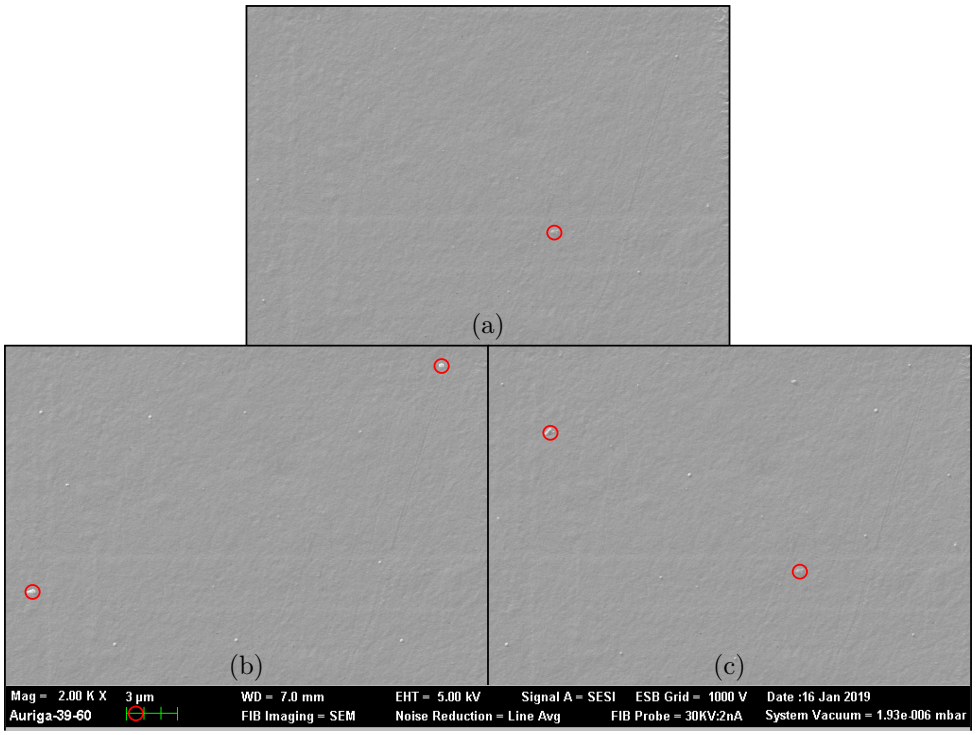

Figure 4.6: SEM images of the nanocomposite XLPE specimens: (a) 1wt% of nano-alumina; (b) 3wt% of nano-alumina; (c) 5wt% of nano-alumina. The largest detected clusters are highlighted in red circles. Each circle has a diameter of 1 µm, as evident from the green scale line below, meaning that the clusters were mesoscopic at most.

rate at the 60 kV/mm stress level, no apparent effect of the distorted waveform was observed. While the second to sixth breakdowns occurred in (logarithmically) regular intervals under the distorted waveform stress, the second to fourth failures occurred almost back-to-back for the sinusoidal waveform. As a result, the slope of the fitted distribution (shape factor) was substantially gentler for the former, resulting in a larger statistical spread, as demarked by the respective confidence limits.

As mentioned above, the stress levels needed to be reduced for the aging tests of the 1wt% and 3wt% nano-alumina XLPE specimens. Specifically for the distorted waveform aging test of the 1wt% nanocomposite specimens, the stress levels had to be reduced even further, in total, by 10 kV/mm in comparison to the unmodified specimens. Naturally, the need for such a reduction indicates that both the 1wt% and 3wt% nano alumina specimens degraded quicker than their pure XLPE counterparts. The results of the respective aging tests are shown in Figure 4.8 (1wt%) and Figure 4.9 (3wt%).

Ultimately, the results of the accelerated aging tests of the 5wt% nano alumina specimens are depicted in Figure 47. Even with the stress levels increased to those of pure XLPE specimens, the total number of attained breakdowns was lower. Similarly, the degradation rate of specimens aged by the distorted waveform seems to be enhanced, particularly at the two higher stress levels, while the effect diminishes at the stress level of 60 kV/mm. Once again, the Weibull distributions obtained for the distorted waveform stress regimes have steeper slopes in general, resulting in thinner confidence limits. Since both aging tests at the 60 kV/mm stress level were conducted at the end of the entire experiment, they were kept running as long as possible to obtain more data points.

The scale and shape parameters of each of the Weibull distributions fitted to the gathered data are listed in Table 4.2. Additionally, the correlation coefficients for each data set are also shown. While the majority meets the criterion of a good fit according to the IEEE/IEC 62539-2007 standard, there were some cases where the correlation indicated a bad fit. These were, however, limited to the cases where the artificial breakdowns were added, which was mostly expected.

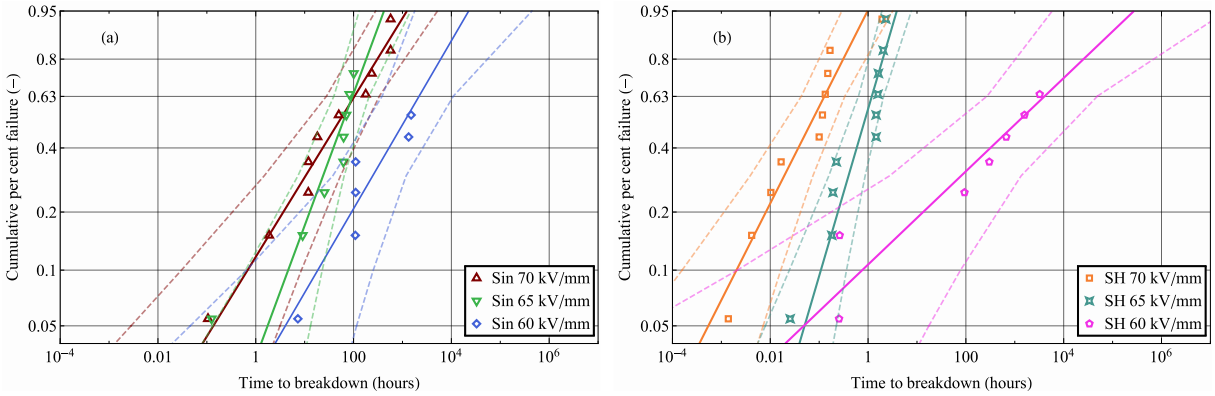

Figure 4.7: Results of the accelerated aging tests of the pure XLPE specimens for: (a) sinusoidal waveform; (b) supraharmonic-distorted waveform (SH).

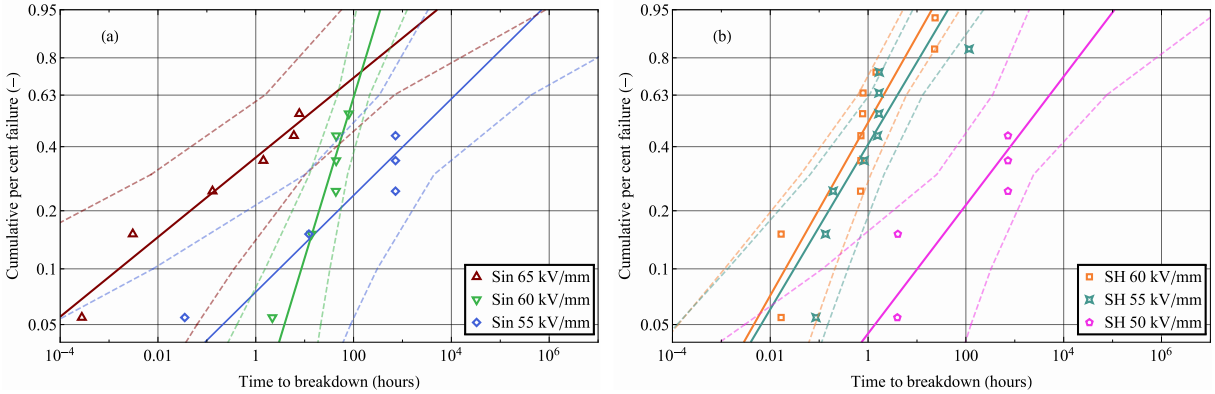

Figure 4.8: Results of the accelerated aging tests of the 1wt% nano alumina XLPE specimens for: (a) sinusoidal waveform; (b) supraharmonic-distorted waveform (SH).

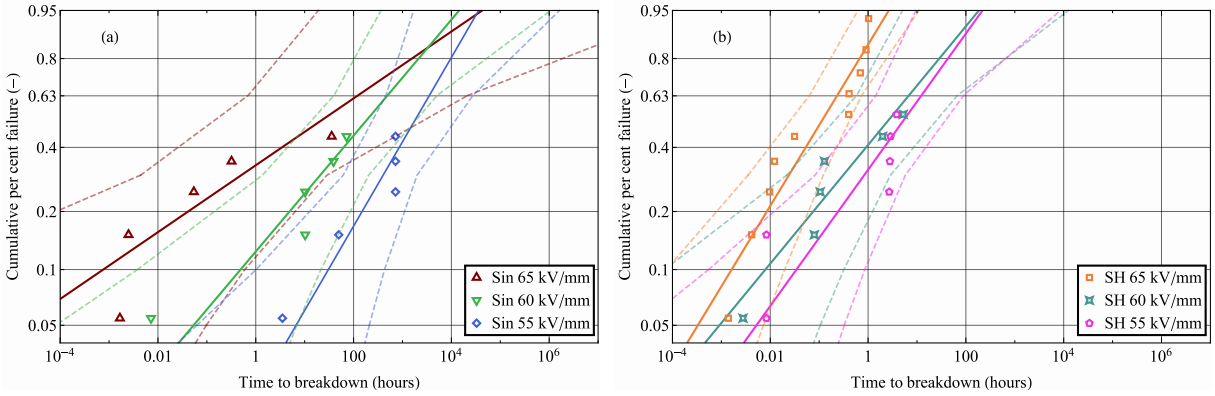

Figure 4.9: Results of the accelerated aging tests of the 3wt% nano alumina XLPE specimens for: (a) sinusoidal waveform; (b) supraharmonic-distorted waveform (SH).

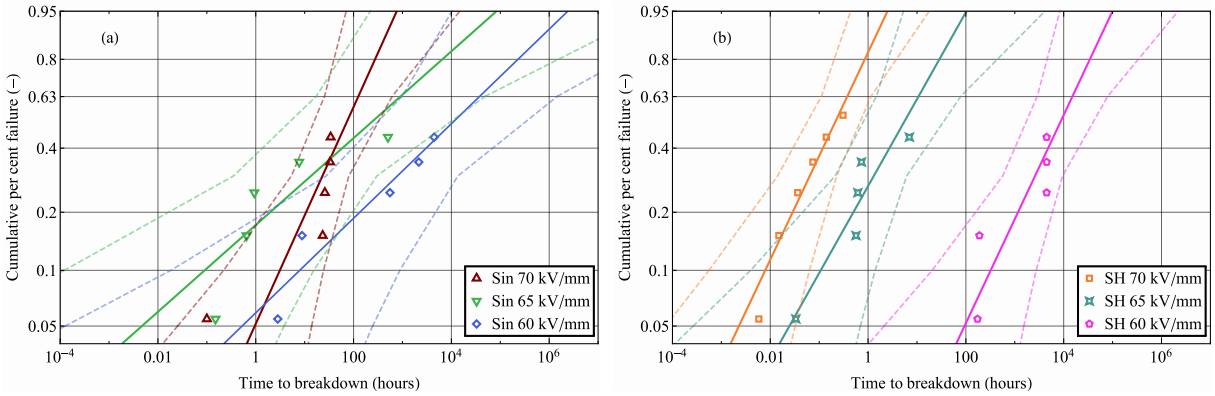

Figure 4.10: Results of the accelerated aging tests of the 5wt% nano alumina XLPE specimens for: (a) sinusoidal waveform; (b) supraharmonic-distorted waveform (SH).

Table 4.2: Overview of Weibull parameters obtained for each aging test.

Specimen material	**Stress level (kV/mm)**	**Scale parameter α (hours)**		**Shape parameter β (-)**		**Correlation (-)**	
		Sin	**SH**	**Sin**	**SH**	**Sin**	**SH**
Pure	60	2,200	4,130	0.47	0.26	0.93	0.94
	65	95.5	1.20	0.74	0.94	0.93	0.95
	70	105	0.13	0.45	0.54	0.99	0.96
Nano-alumina 1wt%	50	-	5,220	-	0.36	-	0.87
	55	12,200	4.02	0.27	0.46	0.96	0.84
	60	104	2.1	0.9	0.49	0.97	0.92
	65	37.8	-	0.22	-	0.98	-
Nano-alumina 3wt%	55	3,550	12.4	0.47	0.38	0.96	0.88
	60	495	6.85	0.33	0.33	0.94	0.95
	65	123	0.24	0.19	0.45	0.87	0.95
Nano-alumina 5wt%	60	38,300	15,200	0.27	0.58	0.95	0.88
	65	927	10.8	0.24	0.49	0.85	0.93
	70	126	0.38	0.61	0.58	0.89	0.98

Sin = sinusoidal waveform; SH = supraharmonic-distorted waveform

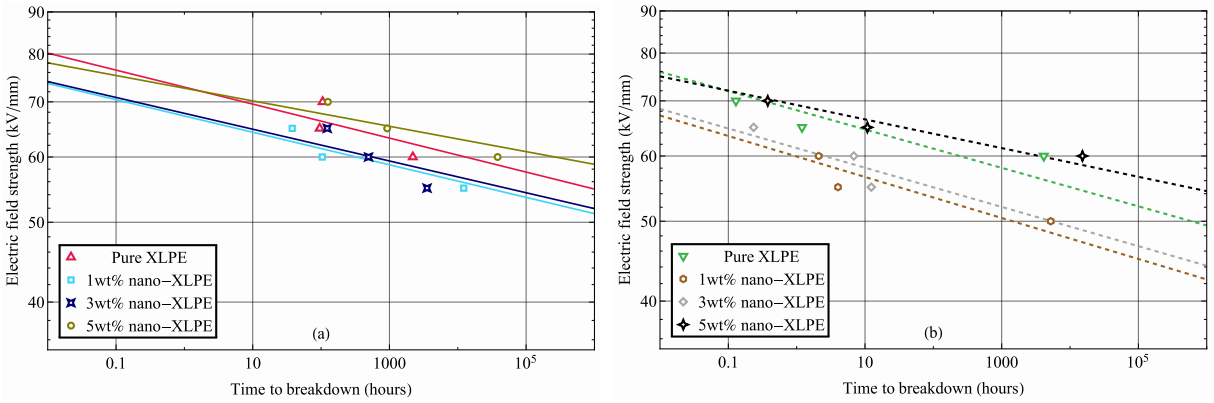

Figure 4.11: The lifelines obtained by fitting inverse power model to the aging data of the: (a) sinusoidal waveform stresses; (b) distorted waveform stresses. Plotted in logarithmic–logarithmic coordinates.

4.2.2 Application of aging models

Initially, the short-term breakdown test results were incorporated into the aging data to ensure better aging model fits. The electric field strength of the data points was put equal to the respective material's breakdown strengths, while the time to breakdown was estimated as 10^{-6} s. This estimation was based on the typical duration of short-term breakdown mechanisms (see section 2.1). Unfortunately, the breakdown tests could not have been performed using the distorted waveform, but the reference sinusoidal waveform values were nonetheless deemed to be a viable tool for the fitting of the distorted aging data. The remaining data points were constructed from the obtained scale parameters and the respective stress levels.

4.2.2.1 Inverse power law

First, the frequently used inverse power law model (see section 2.2.4.2) was fitted to the aging data. The respective aging plots of each waveform type are depicted in Figure 4.11. Even though a larger scale parameter was obtained at the lowest stress level of the pure XLPE specimens for the distorted waveform, the fitted lifelines predict a longer lifetime under the sinusoidal waveform stress. In fact, similar observations can be made for the other specimen materials. An apparent decrease in the expected life is present for the 1wt% and 3wt% nano-filled specimens. Their lifelines are almost identical, and both are shifted from the reference XLPE lifeline downward by ca. 3 to 5 kV/mm for the standard waveform and by ca. 5 to 7 kV/mm for the distorted waveform. Conversely, up to a field strength of about 70 kV/mm, both lifelines of the 5wt% nano-filled specimens predict a longer expected life than in the case of the pure XLPE. Due to the gentler slopes of the 5wt% nanocomposites' lifelines, the difference in the expected life further grows in its favor with the decreasing field strength.

The slope n of each estimated IPL lifeline and the adjusted coefficients of determination (R^2) of each fit are listed in Table 4.3. Clearly, for each specimen material, the slope n was consistently larger in the case of the sinusoidal waveform aging, which is in line with the observations stated above.

4.2.2.2 Crine model (I)

As was mentioned in the theoretical introduction to the aging models (see section 2.2.4), IPL tends to give too optimistic results at low stresses. Hence, it was deemed suitable also to employ a threshold model to provide another point of view, from which different conclusions might be perhaps obtained. The prime candidate for such a model was the Crine model, as it was described in detail in the theoretical part due to its intended use on XLPE. Since two model variants were highlighted, i.e., Eq. 2.28 and 2.30, they were both employed. The earlier iteration, Eq. 2.28, was fitted to the data first. Even though the model uses only two physical variables, ΔG, and λ, it also needs to be supplemented with the critical (threshold) field strength.

The critical field strength determines when the hyperbolic cosecant part of the equation comes into play and turns the lifeline perpendicular to the time axis. Although the term is not identical to the operating field strength, it can be treated so if one makes a small concession by regarding the (cable) XLPE systems'

Table 4.3: Overview of the parameters of the fitted aging models.

Model	Parameter	Pure XLPE		1wt% nano		3wt% nano		5wt% nano	
		Sin	SH	Sin	SH	Sin	SH	Sin	SH
IPL	Slope n	48.5	42.9	50.6	40.2	51.9	42.0	64.9	57.4
	Adjusted R^2	0.998	0.998	0.999	0.999	0.998	0.999	0.999	0.999
Crine1	λ (nm)	13.9	12.6	16.0	13.4	16.3	13.3	19.9	18.1
	ΔG (10^{-19} J)	2.08	2.07	2.15	2.13	2.17	2.15	2.30	2.28
	"Critical field" (kV/mm)	50	42.5	45	33.5	45	32.5	50	44
	Adjusted R^2	0.987	0.928	0.994	0.968	0.988	0.991	0.994	0.974
Crine2	ΔV (10^{-24} m^3)	1.54	1.39	1.99	1.72	2.04	1.66	2.43	2.18
	ΔG (10^{-19} J)	2.13	1.96	2.16	1.94	2.18	1.89	2.42	2.21
	Critical field (kV/mm)	15	15	15	15	15	15	15	15
	Adjusted R^2	0.994	0.891	0.991	0.945	0.998	0.995	0.999	0.948

IPL = inverse power law (Eq. 2.21); Crine1 = Crine model per Eq. 2.28; Crine2 = Crine model per Eq. 2.30 ($\varepsilon_r = 2.2$)

lifetime (ca. 30 years) to be "infinite" from a technical point of view. In fact, [36] lists the operating field strength of XLPE cable systems as 15 kV/mm, which is very close to the critical field values mentioned in section 2.2.4.3.

Naturally, the value is valid for the much thicker insulation of cable systems as opposed to the employed specimens' thickness of 200 µm, and it is also limited by the systems' weak points, namely cable terminations. Standard ASTM-D149 suggests recalculating the breakdown (field) strength values when the thicknesses of the compared insulation specimens are not identical. While the dependence of breakdown strength on the insulation thickness is most likely not identical to the aging rate's dependence, the expression should nonetheless provide a rough estimate. Using the ratio of inversed square roots of the thicknesses suggested by the standard, one might obtain about 2.3 times larger operating (i.e., "critical") field strength for the 200 µm thick specimens (reference thickness of 1 mm).

Furthermore, suppose the higher homogeneity of the specimens (prepared in laboratory conditions) and the much lower thermal stress ($T \simeq 293.15$ K as opposed to cable systems' maximum operating $T_{\max} = 363.15$ K) are factored in. In that case, an operating field strength of around 50 kV/mm does not seem entirely unreasonable. It must be reiterated that the use of such a value as the "critical field strength" is incorrect in the strictly physical sense, as injection of electrons via the Schottky effect certainly already takes place.

By looking at the experimental results, it can be speculated that since a good half of the specimens withstood the accelerated aging at the lowest stress level (60 kV/mm, pure XLPE) for over six months, a decrease in the electrical stress by 10 kV/mm would increase the expected lifetime to tens of years. The same conclusion can be reached by looking at the IPL model fits in Figure 4.11.

Therefore, the initial estimation of the "critical field strength" was chosen to be 10 kV/mm below each material's and aging regimes' lowest stress. The suitability of the estimations was verified via the adjusted coefficient of determination, which, however, showed no apparent dependence on the critical field strength in the case of sinusoidal aging. Hence, the initial estimations were employed to determine the other model parameters.

The overall quality of fits in the case of the distorted waveform aging was relatively poor (see Figure 4.12), indicating that the "critical field strength" had been chosen unsatisfactorily. Therefore, the parameters were altered with respect to the adjusted coefficient of determination of the fits. The new "critical field strengths," obtained through the adjusted R^2 optimization, were substantially smaller (by 6 to 12.5 kV/mm, as shown in Table 4.2) than their sinusoidal aging equivalents. Similar to the conclusions of the IPL model, this fact postulated a magnified degradation effect of the distorted waveforms. The resulting model fits of the Crine model (Eq. 2.28) are depicted for all specimen materials and waveform types in Figure 4.13.

After this optimization, the newly obtained Gibbs free energies and the mean free paths (see 4.3) matched those obtained for XLPE in the reference work [44] relatively well. Also, the estimated Gibbs free energies of the individual stress regimes of each material were almost equal. Since the Gibbs free energy

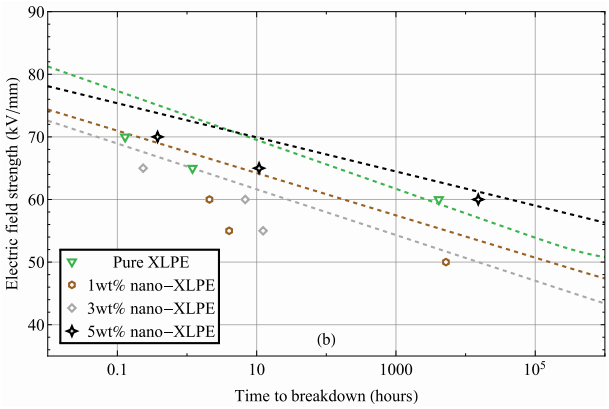

Figure 4.12: The lifelines obtained by fitting the Crine model (per Eq. 2.28) to the aging data of the distorted waveform stresses prior to the "critical field strength" optimization. Plotted in logarithmic–linear coordinates.

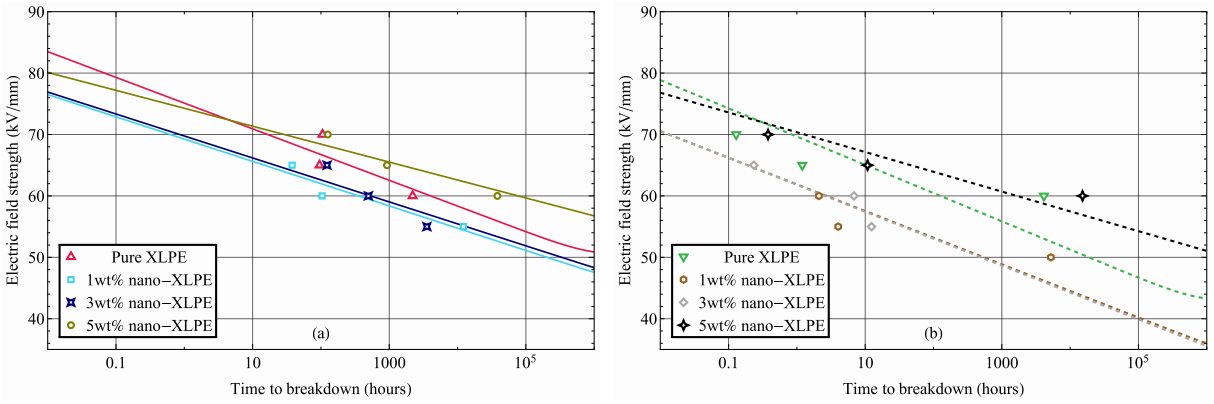

Figure 4.13: Lifelines obtained by fitting the Crine model (per Eq. 2.28) to the aging data of the: (a) sinusoidal waveform stresses; (b) distorted waveform stresses. Plotted in logarithmic–linear coordinates.

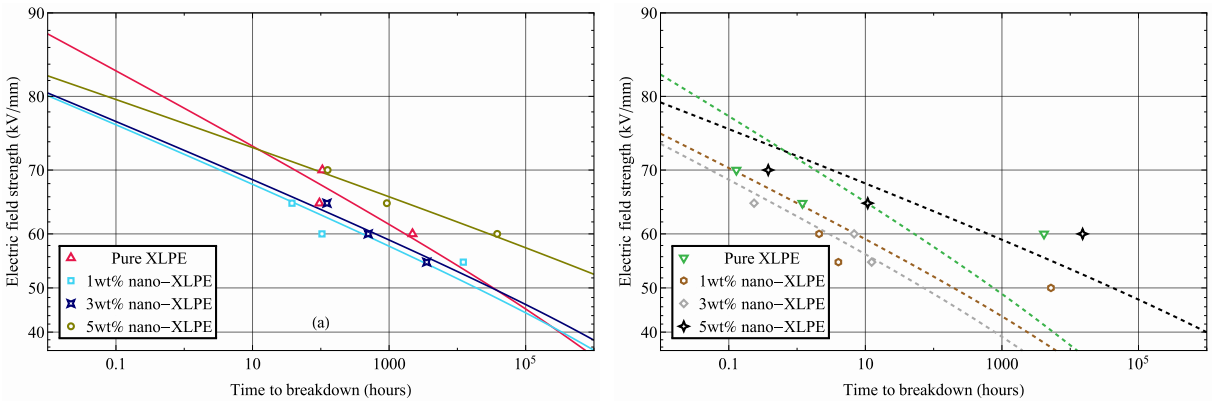

Figure 4.14: Lifelines obtained by fitting the Crine model (per Eq. 2.30) to the aging data of the: (a) sinusoidal waveform stresses; (b) distorted waveform stresses. Plotted in logarithmic–quadratic coordinates.

of an insulation system (material) should not depend on the electrical aging regime, such a result was expected. Conversely, the mean free paths were slightly shorter for the distorted aging data, contrary to the assumption that the supraharmonic waveform components should elongate the free paths. However, that can be attributed to the effect of the reduced "critical field strengths" on the model fit, as the original, unoptimized fits yielded longer mean free paths in the case of distorted waveform aging.

4.2.2.3 Crine model (II)

Afterward, the newer iteration of the Crine model, Eq. 2.30, was fitted to the aging data. As can be seen from the lifelines depicted in Figure 4.14, the main difference between the two iterations is that the latter's fit is slightly curved in the transition region between the low-field and high-field aging regimes. This curvature stems from the model's quadratic dependence on the field strength, which is particularly pronounced when the hyperbolic cosecant term's contribution increases. Other than that, the iterations also differ in the second employed parameter – in this case, the mean free path is replaced by the system's activation volume ΔV, with typical values of 10^{-24} m^3.

In contrast to the previous Crine model iteration, the critical field strengths of the sinusoidal aging were set to the actual estimated value of 15 kV/mm. The reason for that was, apart from the physical correctness, the non-sensical values of the initial Gibbs free energies estimates ($\geq 3 \cdot 10^{-19}$ J). The parameters estimated using these correct critical field strengths are listed in Table 4.3. While the coefficients of determination slightly improved for the sinusoidal aging, they worsened for the distorted waveform equivalents. Concerning the Gibbs free energy, the sinusoidal estimates mostly agreed with the expected value of $\sim 2.1 \cdot 10^{-19}$ J. Conversely, those of the distorted waveform aging were slightly lower (by about $0.2 \cdot 10^{-19}$ J) but were still within reasonable tolerance around the expected value.

Similar to the previous model, the values of the second parameter, activation volume, were slightly lower in the case of the distorted aging regime, but still in agreement with the reference data [56]. By setting the respective Gibbs free energies equal to the ones obtained for the sinusoidal aging, it can be shown that the activation volumes would be indeed larger, as expected. Such an approach would be consistent with the theoretical assumptions, where the absolute height of the potential between the unaged and aged state should be constant. Nevertheless, the respective "best fit" lifelines fitted the data very poorly, as shown in Figure 4.15, and hence the original Gibbs free energy estimates were employed instead.

The reason for the discrepancy between the values of the Gibbs free energy obtained for each aging regime presumably stems from the spatial distribution of the data points, where, in the case of the distorted aging regime, the three points obtained from the long-term aging experiments are located in the transition region (compare Figure 4.14a and b). In contrast, only the single short-term breakdown data point determines the slope of the high-field part of the lifeline. Since this point was obtained for sinusoidal stress (thus most likely at a higher breakdown field), the high-field region slope should be steeper, as the distorted waveform aging data were generally shifted toward shorter times to breakdown. Due to the employed model's definition, a higher slope corresponds to lower Gibbs free energy, which could explain the slightly reduced estimates of the distorted waveform aging data fits. In comparison,

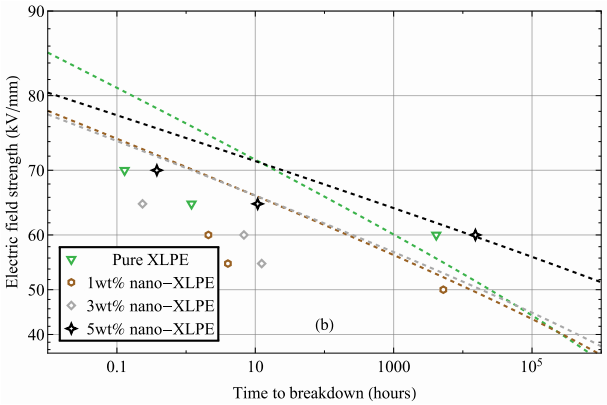

Figure 4.15: The lifelines obtained by fitting the Crine model (per Eq. 2.30) to the aging data of the distorted waveform stresses by setting the ΔG equal to the respective sinusoidal aging data equivalents. Plotted in logarithmic–quadratic coordinates.

the situation was different for the previous iteration of the Crine model, as the transition part was much narrower, and most of the points were already located in the high-field region in both cases. As a result, the Gibbs free energy estimates were almost identical.

Therefore, it would be beneficial to also perform short-term breakdown tests of the specimens by employing the distorted waveform instead. Unfortunately, such a task could not have been carried out due to equipment limitations.

In any case, the lifelines shown in Figure 4.14 more or less imply the same as the previous two aging model results. All the distorted aging regime lifelines are shifted toward shorter times to breakdown compared to their sinusoidal equivalents. Similarly, the 5wt% nanocomposite specimens seem to have performed the best, followed by the unmodified, pure XLPE. The insulation performance of the 1wt% and 3wt% nanocomposites was the worst and almost identical. The only exception seems to be the lifeline of the unmodified XLPE in the case of the sinusoidal aging regime, which intersects those of 1wt% and 3wt% nanocomposite at about 400,000 hours (about 46 years) and 30,000 hours (only about 3.5 years), respectively. While the former is mostly irrelevant, since the time of the intersection is much longer than the typical technical life of insulation systems, the latter might indicate a better insulation performance of the 3wt% nanocomposite under typical industrial electrical stresses.

Ultimately, an attempt was made at employing the ultimate variant of the Crine model (per [57]) mentioned at the end of section 2.2.4.3, defined as:

$$t \simeq \left(\frac{h}{2akT}\right) \exp\left(\frac{\Delta G}{kT}\right) \operatorname{csch}\left(\frac{\Delta V \cdot \varepsilon \cdot E^2}{2kT}\right). \tag{4.1}$$

Where a is the number of power cycles of the voltage waveform per second. The main idea behind its use was to quantify the waveform distortions via the higher value of the a term (i.e., an increased number of power cycles). However, all the model fits were unsatisfactory even for the well-defined sinusoidal aging ($a = 100$), and this idea was hence dropped.

4.2.3 Fourier-transform infrared spectroscopy (FTIR) analysis

An attempt was made to investigate the degree of degradation of the specimens that withstood the aging test. The main idea of such an investigation was to provide more apparent indications of the distorted waveform's enhanced degradation effect. Since the specimens were in the form of thin films, an FTIR analysis seemed to be an ideal choice and was thus performed. The obtained FTIR spectrum of an unaged and degraded pure XLPE specimen can be seen in Figure 4.16a and b, respectively. Typical peaks of XLPE are highlighted in the upper spectrum.

Per [160], a major degradation mechanism of XLPE is its oxidation, which manifests in the spectrum as peaks around the wavenumbers of 3,300 cm^{-1} (hydroxyl stretching band) and 1,740 cm^{-1} (carbonyl stretching band). Concerning the former band, a slightly decreased transmittance in the respective area

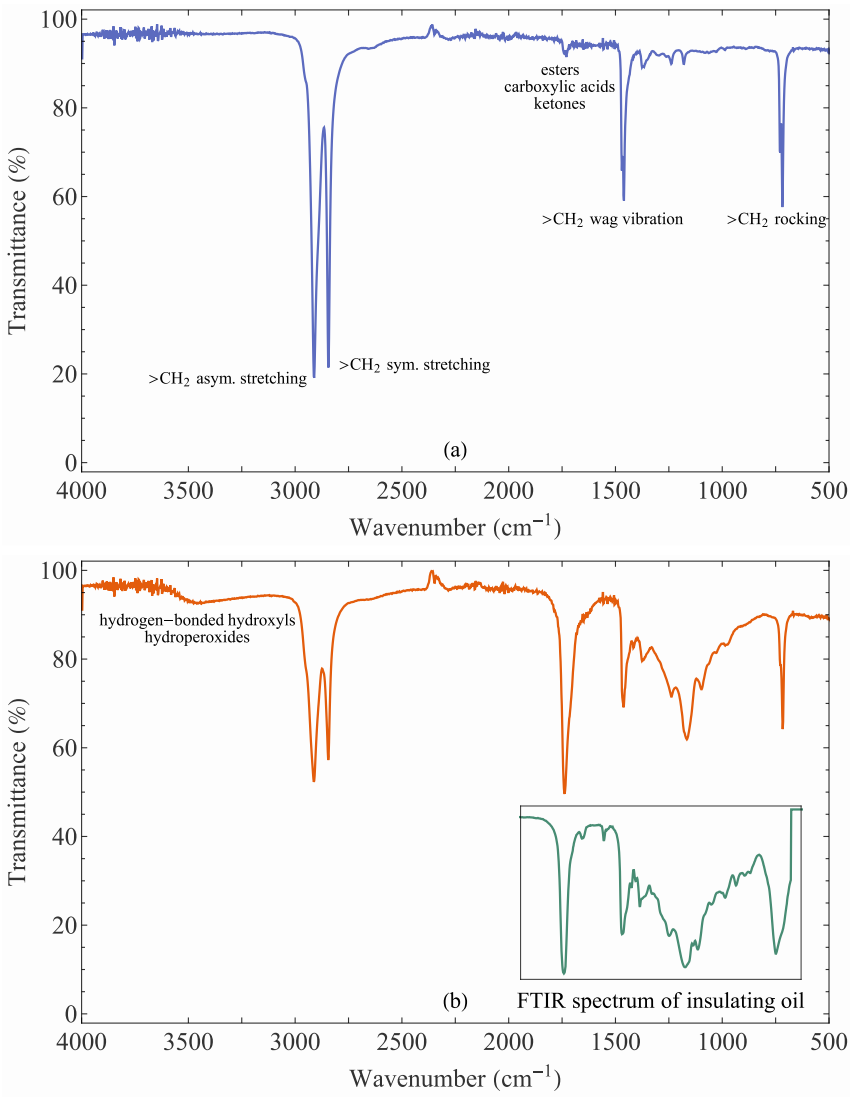

Figure 4.16: FTIR spectrograms of an XLPE specimen before (a) and after (b) its aging test. The latter includes an FTIR spectrum of the insulating oil, in which the specimens were immersed during the test.

is apparent from the degraded XLPE spectrum. However, the transmittance in the entire double bond region (1,500 to 2,000 cm^{-1}), which includes the carbonyl stretching band, and the fingerprint region (500 to 1,500 cm^{-1}) seems heavily distorted. Investigation of this phenomenon revealed that the distortion was most likely due to the partial ingress of insulating oil into the specimens. As a result, the specimen's spectrum was heavily influenced by the presence of the oil, as is evident from the oil's FTIR spectrum inset in Figure 4.16b. Naturally, attempts were made to remove the ingressed oil from the specimens, such as wiping and drying or cleaning using isopropanol, but no better results could have been obtained.

Due to this limitation, no convincing conclusion could be drawn from the results of the FTIR analysis, and they hence had to be disregarded.

A measurement of the oil ingress was also performed to investigate whether it could affect the specimens' insulation performance. The specimens were thus weighted and immersed in the oil for a prolonged period. Only a slight increase in their weight of about a percent was detected after their removal and subsequent cleaning. Such an ingress was deemed irrelevant to the insulation performance, but it was clearly sufficient to alter the overall absorbance of the specimen.

4.3 Conclusion

The primary intent of this chapter was to answer the question of whether supraharmonic-distorted waveforms can also substantially enhance the intrinsic aging rate of cable systems' main insulation. For this purpose, long-term aging tests of unmodified and nano-alumina-filled XLPE film specimens under sinusoidal and supraharmonic-distorted waveform stresses were performed. By analyzing the obtained results, the following conclusions can be drawn:

- A comparison of the total number of specimen failures at equivalent stress levels indicates a magnified degradation effect of the distorted waveform for the 1wt% and 3wt% nanocomposite specimens. Conversely, no clear implications are present for the pure XLPE and 5wt% nanocomposites specimens.
- The scale parameters, determined from a Weibull analysis of the aging data, also imply an enhanced aging rate of the specimens stressed by the distorted waveform. In general, all sinusoidal aging data scale parameters were larger than those of the distorted waveform aging data. The only exception was the scale parameter of the distorted, 60 kV/mm stress' dataset of pure XLPE, which was substantially larger than its sinusoidal stress' counterpart.
- The IPL lifelines of the sinusoidal aging data are, in all cases, situated above their distorted waveform counterparts. Regarding the specimen materials, the least longevity is predicted for the 1wt% and 3wt% specimens. The reference XLPE specimens seem to have performed substantially better but still slightly worse than the 5wt% nanocomposite specimens.
- Due to the tendency of the IPL to give too optimistic predictions for low-field stresses, two different iterations of the Crine model were also fitted to the data. Both models also imply that the distorted waveform aged the specimens faster than the sinusoidal waveform for all materials. The parameters determined by fitting the two variants of the Crine model were in good agreement with the available reference data, and the overall quality of the fits was decent.

While the above implications almost unanimously hint at the enhanced intrinsic aging rate due to the supraharmonic-distorted waveform, the conclusions must be understood in the context of the experiment and its limitations. For example, an objection can be made that even though the distorted waveform was analogous to the one modeled in the previous chapter, it still represented a rather extreme case. Furthermore, the specimen set size of each test run was not ideal, which stemmed from the equipment limitations. Naturally, sources of errors could also be located in the manufacturing quality of the specimens, both regarding inhomogeneities and variable thickness. Due to fewer aging plot points, errors could naturally arise from the subsequent interpretation of fitted aging models. Similarly, the inclusion of breakdown test results into the aging data was prone to errors, especially concerning its time to breakdown estimation.

Be that as it may, the above implications of enhanced intrinsic aging rate could (and perhaps should) instigate further research of the topic, as most of the identified analogous works, albeit for different waveform configurations, dismiss the idea. While the previous chapter pointed at similar effects, they were thought to originate from the uneven field distribution and enhanced dielectric losses of the examined cable terminations. The issue's solution had already been proposed but apparently not widely implemented.

However, in this case, the inferences of the experimental work could be substantially more severe, as they indicate that the longevity of the cable system's main insulation would also be affected. Concerning the costs of the entire cable systems and the relevant excavation works, a suitable dimensioning might be preferred to address the issue.

Chapter 5

Impacts of Low-Order Supraharmonics on Partial Discharges

This chapter is based on publications [1], and [6–8].

Abstract

With the effect of distorted waveforms already examined for aging both in the presence and the absence of PDs, this chapter strived to complement the previous two by analyzing the waveforms' effect on the PD activity. A 3D-printed specimen with a single artificial, spherical cavity was employed as the reference defect. The PD activity inside the cavity was gathered for various waveforms consisting of a single oscillation superposed on a 50-Hz sinusoidal. Both the oscillation's natural frequency (2 to 9 kHz) and position (phase angle 324° to 108°) were altered throughout the experiment. Three 1-minute long PRPD patterns with the accompanying statistics were recorded for each combination. Subsequently, an analytical electrostatic PD model was used to simulate the measured discharge activities. By comparing the experimental and simulation results, the changes in both PRPD patterns and statistics due to the oscillations could have been analyzed.

The most apparent changes in the PD activity were observed when the oscillations had a lower natural frequency and were placed in the peak of the sinusoidal waveform. Although to a lesser extent, similar changes were also present for the other waveforms. A change in the employed analytical model had to be implemented to account for the oscillation-induced intensive clustering of discharge events in the experimental PRPD patterns. The phenomenon was resolved by providing the model's fundamental equation with a free electron availability term based on the $\mathrm{d}V/\mathrm{d}t$ value of the instantaneous voltage.

Introduction

An introduction to the topic was mostly made in the review of effects of various high-frequency transients, oscillations, and impulses in section 2.3.4. In this case, the searched works unanimously concluded that the PD repetition rate is increased or the system's PDIV is reduced due to the presence of various components in the voltage waveform. Since both effects lead to faster degradation of insulation systems, an analogous investigation of supraharmonics' impacts on PD activity was deemed integral to the thesis' main topic. The investigation was further motivated by the fact that even though similar works have been already performed, none examined the impacts of a sinusoidal waveform with superposed supraharmonic oscillations

Furthermore, most of the searched works did not employ a PD model as a tool to analyze the recorded discharge activity. Exceptions, and perhaps the thematically closest works, were [130–132], which investigated PD activity in cable accessories due to repetitive impulses superposed on sinusoidal voltage waveforms. Like the other research articles, the works implied that additional PDs might occur, in this

case, due to the superposed impulses. Concerning the choice of PD model for the intended analysis, a basic overview of available types and their respective pros and cons was given in section 2.3.3. The electrostatic variant based on [103] was utilized due to its decent accuracy and fast computing speed. Since PD activity over ca. 51 minutes needed to be calculated using short step sizes, the model was transformed from its original FEM variant to an analytical variant. Such a simplification could be made owing to the specificity of the employed artificial defect, which was represented by a single, sizeable spherical cavity.

Lastly, the area of applicability of this investigation should be defined. In contrast to the previous two, this chapter's implications and conclusions are applicable to a considerably broader range of insulation systems. In fact, since the general behavior of PDs in an internal cavity is examined, the inferences should be valid for all solid insulation systems, which are prone to the presence of internal voids. This area thus naturally covers all polymeric material due to their manufacturing method. By intersecting the set of polymeric material by the set of networks susceptible to strong supraharmonic content, one might identify that in addition to (XLPE) cable systems, the conclusions drawn from this investigation can also be valid for epoxy resin encapsulated transformers.

5.1 Experimental configuration

5.1.1 Employed waveforms

Initially, research articles were reviewed to identify the shapes of a typical supraharmonic-distorted waveform. Four examples are depicted in the upper part of Figure 5.1; the individual waveforms were obtained: at the busbar of a self-commutated converter (measured, Figure 3 of [161]), in the MV node of a PV power station (modeled, Figure 5 of [2]), at the output of an *LCL-LC* type inverter system (measured, Figure 21 of [21]), and at the input of a boost single-phase PFC converter (measured, Figure 1 of [14]). Even though some of these examples are current waveforms, the supraharmonic distortions can be transferred to the voltage at passive elements of the respective network, particularly at transformers, as was illustrated in section 1.2.

A voltage component in the form of a single sinusoidal oscillation (per fundamental waveform's period) in the supraharmonic frequency range was chosen to represent the identified waveforms. Since the individual distortions were present in various phase angles of the fundamental waveform, the position of the oscillation would be altered throughout the experiment (phase angle placement from 324° to 108° with steps of 18°) to address the fact. Similarly, the identified distortions were of different frequencies in each case, and hence the natural frequency of the oscillation would also be changed (2 to 9 kHz with steps of 1 kHz).

On the other hand, despite the variations in the magnitude of the reference distortions, the peak-to-peak voltage of the experimental waveforms' oscillations was fixed to 10 % of the fundamental waveform's peak-to-peak value. The reason for that was the already high number of possible waveform configurations. Furthermore, the initial test runs revealed that the most prominent effect on the PD activity would be present with the oscillation placed in the fundamental waveform's peak (phase angle of 90°). Hence, the oscillations' frequency would be varied only at this position, whereas it would be set to 8 kHz (the most common value of identified distortion frequencies) otherwise. These restrictions reduced the total number of waveform configurations to 17, as shown in the lower part of Figure 5.1 (8 kHz, 90° phase angle waveform is shown twice while the reference purely sinusoidal waveform is not depicted).

5.1.2 Test station

5.1.2.1 Voltage generation

Analogous to the previous chapter, the desired test voltage was produced by a series connection of a 120-kV 50-Hz (PD-free) HV transformer and a 50-kV HV HF transformer (also employed in Chapter 3), whose primaries were excited by a two-channel power amplifier. The input of each of the amplifier's channels was supplied from an arbitrary waveform generator. Since the exact placement of the supraharmonic oscillation was essential to the experiment, the waveform generators' outputs needed to be interlocked in phase. For this purpose, one generator's internal 10-MHz reference clock was used to produce an external trigger signal for the other one. The voltage generation configuration is depicted in the block diagram of the test station in Figure 5.2.

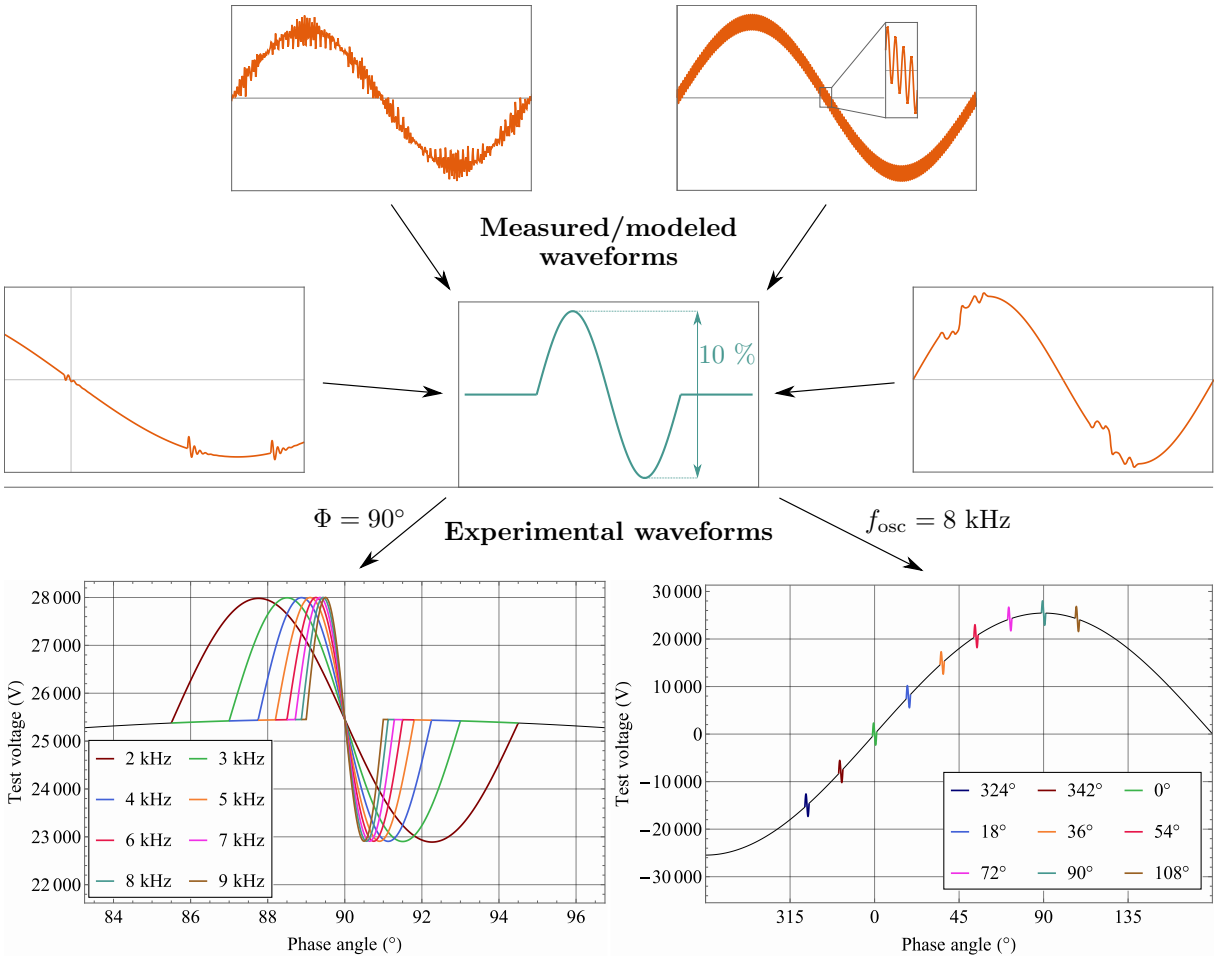

Figure 5.1: Overview of waveforms measured or modeled in works investigating the topic of supraharmonic in juxtaposition with the waveforms employed in the experiment. Clockwise from left (9 hours), the reference waveforms originated from works [161], [2], [21], and [14]

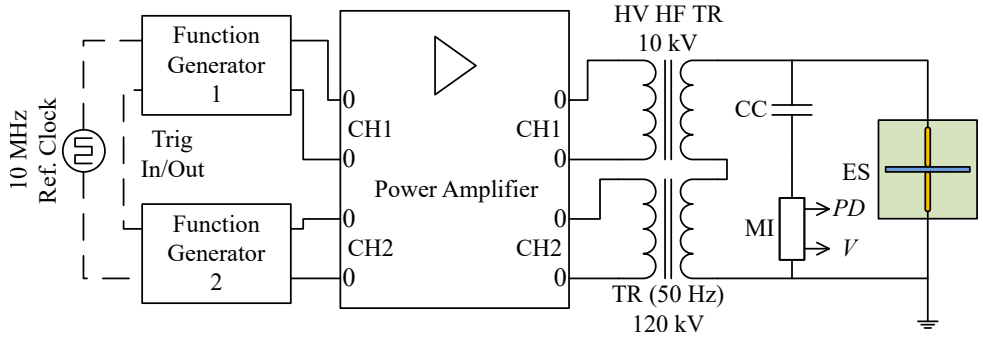

Figure 5.2: A block diagram of the test station. CH1 / 2 – channel 1 / 2, TR – transformer; HV HF – high-voltage, high-frequency; CC – coupling capacitor; MI – measuring impedance; PD / V – partial discharge / voltage output channel; ES – electrode system. Adopted from [1].

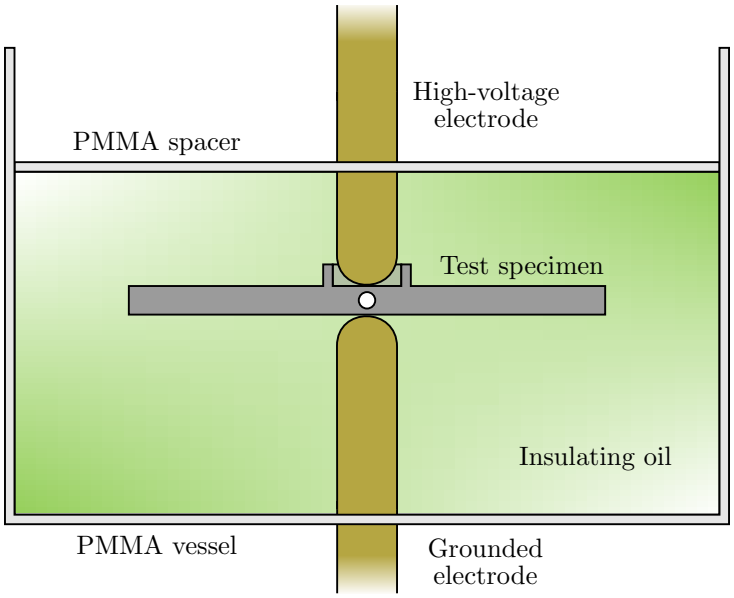

Figure 5.3: An illustration of the employed electrode system.

Apart from the above components, the test station also consisted of an electrode system (described below) and a coupling capacitor (300 nF) connected to an MPD 600 partial discharge measurement system. Regarding the PD measurement, a shortcoming of the employed voltage generation solution was the relatively high noise produced by the power amplifier, which manifested as intensive discharge activity with an apparent charge of about 100 pC. Nevertheless, the test specimens' internal cavities were designed to be large enough to attain a high degree of shape regularity (due to the limited resolution of the 3D-printing preparation method), which also ensured that the minimum discharge magnitude of the occurring PD activity would be about 600 pC. As a result, the sensitivity (threshold) of the PD measurement could be set above the power amplifier's noise without affecting the reading of the cavity PDs. Even though other methods, such as static/dynamic gating of the noise or use of different integration ranges, were available, the decreased sensitivity was deemed sufficient and perhaps most suitable, as it preserved the simple reproducibility of the experiments.

5.1.2.2 Electrode system

The employed electrode system consisted of two long, brass cylindrical electrodes with a diameter of 8 mm. Both electrodes had rounded edges to prevent the development of surface discharges on the specimen inserted in between them. Since a test voltage of up to 20 kV_{RMS} was required, the system was immersed in natural insulating oil to suppress the inception of surface discharges further. An open-top PMMA vessel was used to contain the oil and fix the electrodes in place. The lower, grounded electrode was led out of the vessel through a hole drilled in its bottom, which was sealed by epoxy glue that also fixed the electrode's placement. The upper HV potential electrode was secured in its position using a PMMA spacer. Sufficient compressive force on the specimen was exerted by the weight of both the upper electrode and the gooseneck interconnection to the HV transformer. A schematic depiction of the electrode system is shown in Figure 5.3.

5.1.3 Test specimens

5.1.3.1 Preparation method

Preparing solid insulation specimens containing just a single regular cavity can be arduous. Typically, such specimens are fabricated from epoxy glue by injecting it with a defined amount of air at a suitable moment during its curing process. Since the choice of such a moment can be difficult, multiple specimens are frequently cast at once using smaller molds to improve the chance of success. Suitable specimens are then put individually into larger molds, which are again cast using the same epoxy glue. This way, a specimen of sufficient size for the intended PD measurement is obtained.

Nevertheless, an alternative preparation method was employed in this experiment. Instead, the test

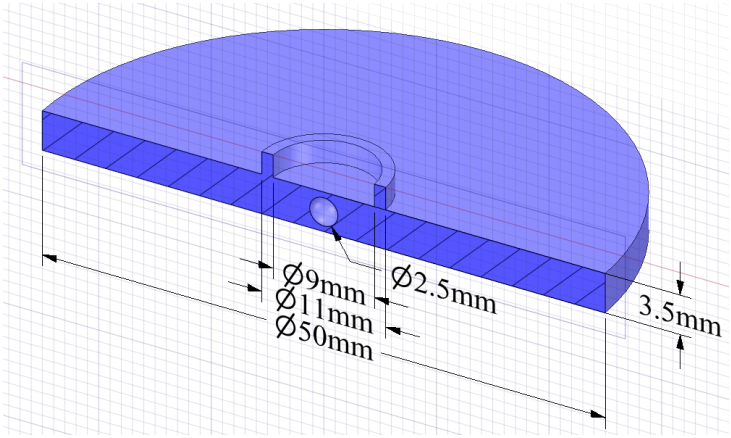

Figure 5.4: A 3D model of the internal cavity test specimen. Adopted from [1].

(a) (b)

Figure 5.5: Example prints of the artificial cavity specimens. The green specimen (a) was printed from a transparent filament only to illustrate the specimens' internal structure, whereas the gray specimen (b) (depicted prior to the application of surface finish) would be subsequently employed in the experiment.

specimens were printed from a *polyethylene terephthalate glycol* (PETG) filament using a *Prusa* i3 MK3S 3D printer. A 3D model illustrating the design and dimensions of the printed specimens is shown in Figure 5.4. Concerning the print parameters, the finest available print layer resolution of 50 µm was chosen to ensure as regular shape of the cavity as possible. Naturally, the printing infill was set to 100 % so that no additional, unwanted cavities would be formed. Default print nozzle and heated bed temperatures were employed, i.e., for the first layer 240/85 °C, respectively, and the other layers 250/90 °C, respectively. The default filament flow rate was slightly reduced to prevent the prolapse of material into the artificial cavity during the print. As shown in Figure 5.4, a rim was added to the specimen's upper surface. The purpose of the rim was to facilitate the subsequent placement of the specimen in between the electrodes.

5.1.3.2 Resulting prints, aluminum surface finish

Two examples of specimen prints are shown in Figure 5.5. Even though the electrodes' diameters were more than twice as large as the cavity's, an aluminum surface finish was applied to both faces of the specimen to homogenize the internal electric field of the cavity further. Moreover, the surface finish was designed to ensure better (electrical) contact between the specimen and the electrodes and serve as an additional countermeasure against oil ingress into the cavity. The evaporative deposition was employed to apply the aluminum surface finish.

5.1.4 Experimental data acquisition

At first, the test specimen was inserted between the electrodes, and the PD measurement configuration was calibrated using a train of 1-nC strong discharges generated by a PD calibrator. Next, the test

specimen was preconditioned for about 45 minutes under full test voltage (18 kV_{RMS}, 50 Hz only). The preconditioning was required to incept the PD activity (see section 2.3.1.4) and stabilize it for measurement purposes.

After acquiring reference data for the calibration of the analytical PD model, a 2-kHz oscillation was placed in the positive amplitude of the fundamental 50-Hz waveform (phase angle of 90°). Three 60-second-long PD measurements were performed to obtain the values of individual statistical parameters and the PRPD pattern of the discharge activity. Subsequently, the oscillation's frequency was increased by 1 kHz, and the measurement sequence was replicated. The procedure was repeated until the highest designated oscillation frequency of 9 kHz was reached. Afterward, the oscillation's frequency was set to 8 kHz, while its position was changed to a phase angle of 324°. Analogously, three 60-second-long PD measurements were performed. In the following steps, the oscillation's placement was altered by +18° each time, until the phase angle of 108° (468° – 360°) was reached. With all the required data gathered, the oscillation was removed, and the occurring PD activity was compared to the initial one to confirm that no substantial changes of both the cavity and discharge activity occurred.

5.2 Analytical PD model

5.2.1 Operating principle

Principles and modeling of partial discharge activity in an internal cavity were already described in sections 2.3.1 and 2.3.3, respectively. As was mentioned above, the electrostatic PD model variant was employed due to its satisfactory accuracy and fast computation speed. Initially, the FEM implementation of the model was used to obtain the time development of the main field and its contribution to the internal cavity field (see Figure 2.12). Since the main field is invariant to the PD activity and its aftereffects, its initial calculation would be valid for the entirety of the simulation. By using several simplifications listed below, the remaining space-charge component of the cavity field could be calculated analytically. The model then operated as follows: the first virgin PD was determined solely from the FEM-calculated field, as no space charge was present. When the initial PD occurred, the space-charge contribution to the internal field was calculated and superposed on the predetermined main field contribution. The simulation then continued using the newly obtained field values, and the process was repeated for each successive PD.

Namely, the implemented simplifications were:

- The discharge both incepts and propagates along the cavity's vertical axis (see Figure 7a, d, j, and g in [108]) → the inception field condition (Eq. 2.40) needs to be evaluated only along this axis.
- The internal cavity field is quasihomogeneous before the occurrence of a PD (see Figure 6.1 in [104] or Figure 7c in [108]) → field needs to be calculated only at a single point inside the cavity. Due to the above remark, the ideal point is the cavity's center.
- Surface charge deposits exclusively in small areas around the cavity' top and bottom poles (see Figure 7b and k in [108]) → the space-charge field can be approximately calculated as transferred charge during a discharge divided by the cavity's diameter.
- The amount of transferred charge during a discharge is proportional to the field difference before and after the event (Eq. 2.41) → the model does not need to employ charge variables and can be solved using only the field variables.

Combining the individual simplifications above makes it clear that only the value of both components of the internal cavity field in the cavity's center was required. With the main field component predetermined and the space-charge component easily calculable from its previous value and the difference between the instantaneous field strength and the extinction field strength, no time-intensive FEM modeling was needed. Furthermore, since the calculation of the key model parameters, electron availabilities, was already defined for field strength in the center of the cavity (see Eq. 2.42), no modifications were necessary.

5.2.2 Software implementation

The FEM and analytical calculations were carried out using Wolfram Mathematica 12.0 software. In the case of the former, the "NDSolve‘FEM‘" package was included in the program to create the mesh of the model geometry and calculate the electric potential and field distributions using the following equations:

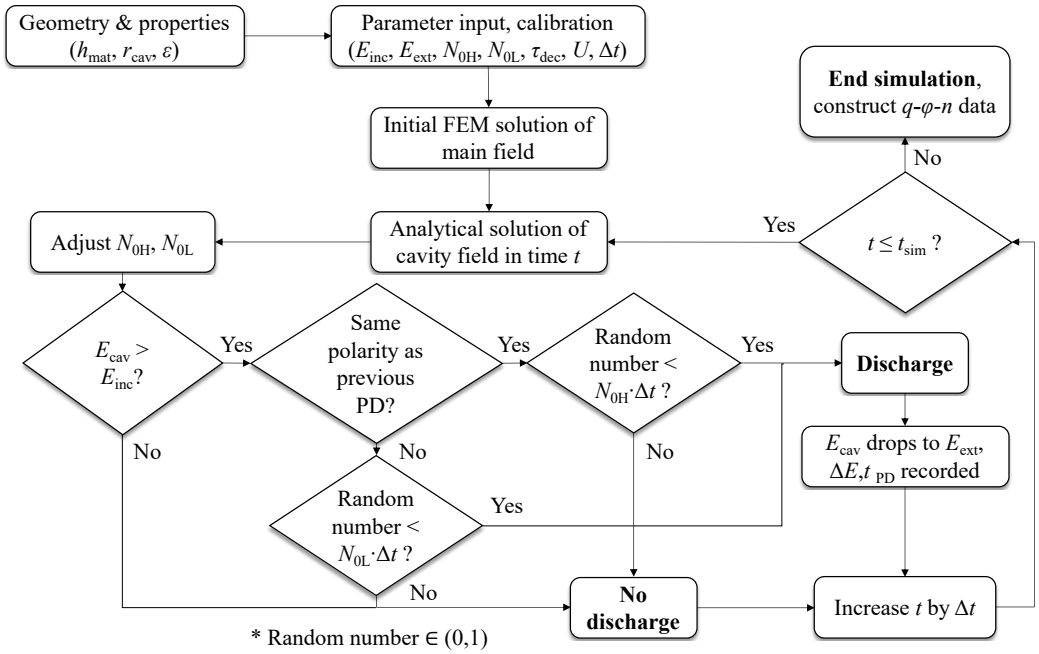

Figure 5.6: Flowchart of the employed PD model. The denotations of individual model parameters are explained in Table 5.1.

$$\nabla \cdot \varepsilon(\nabla\varphi) = -\rho, \tag{5.1}$$

$$\nabla\varphi = -\boldsymbol{E}. \tag{5.2}$$

Naturally, the package also implemented energy functional to the model to identify the correct solution with the least potential energy.

The obtained time development of the electric field strength in the center of the cavity was subsequently incorporated into the analytical model. Analogous to the FEM model, the analytical solution was calculated using the "NDSolve" command. In this case, two packages, "DifferentialEquations–'NDSolveProblems'" and "DifferentialEquations–'NDSolveUtilities'" needed to be included in the program. The "WhenEvent" subcommand of "NDSolve" ensured that the solved parameters (electric field strengths) could be changed at arbitrary moments. This capability was employed to simulate the discharge events as instantaneous changes in the respective field strengths. Additionally, the time evolution of free electron availability per equation 2.42 could also be employed. A flowchart of the simulation process is depicted in Figure 5.6 to explain how the model operates. A sample time-development of the cavity field and its components obtained by the analytical model can be seen in Figure 5.7.

5.2.3 Model parameters

An overview of the employed model parameters is given in Table 5.1. Some of the values could be determined readily from the experimental configuration (voltage waveform, test specimens' dimensions, and characteristics), some needed to be calculated (inception and extinction field strength), while the rest needed to be calibrated using the experimental results (electron availability, effective time decay; see section 5.2.4). The table also lists parameters employed in modeling PD activity due to the distorted waveforms – their meaning is explained in section 5.2.5.

5.2.4 Model calibration

Initially, a 60-s long PD measurement was carried out to provide reference data for the calibration of the analytical model. A purely sinusoidal waveform with a peak voltage of 24.5 kV (effective value of

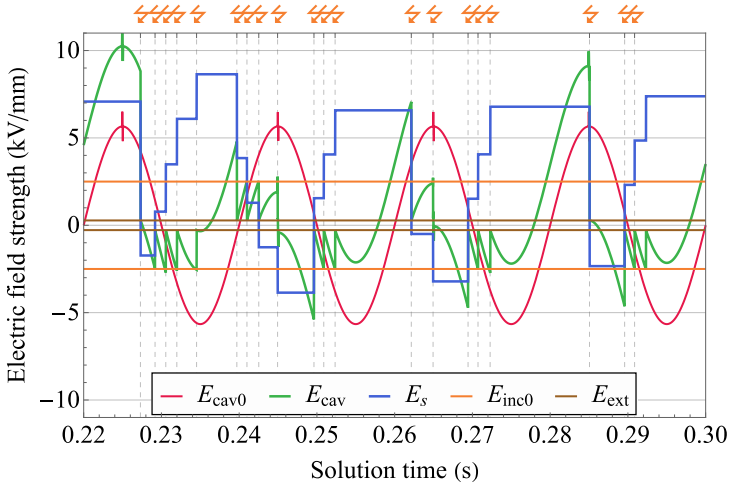

Figure 5.7: A sample of computed PD activity. The internal cavity field E_{cav} is obtained as a sum of the main-field contribution E_{cav0} and space-charge contribution E_s. A PD can only occur if the cavity field is stronger than the inception field strength E_{inc} and a free electron is available. Whenever a discharge takes place, the cavity field drops to the extinction field strength E_{ext}. The lightning symbols above the plot denote individual discharges. Adopted from [1].

Table 5.1: An overview of the employed model parameters and their values.

Parameter	**Denotation**	**Value**
Inception field strength	E_{inc}	2.5 kV/mm
Extinction field strength	E_{ext}	0.277 kV/mm
Electron availability, opposite polarity	N_{0H}	65 s^{-1}
Electron availability, same polarity	N_{0L}	1,250 s^{-1}
Surface charge decay time constant	τ_{dec}	2 ms
Simulation time	t_{sim}	60 s
Fundamental waveform	U	$24.5 \cdot \sin(2\pi \cdot 50 \cdot t)$ kV
Step size, normal	t_{step}	20 µs
Step size, during oscillation	$t_{step,osc}$	2.5 µs
Electron availability increase, oscillation	$N_{max,osc}$	$0.36 \cdot 10^{-4}$ $m \cdot V^{-1} s^{-1}$

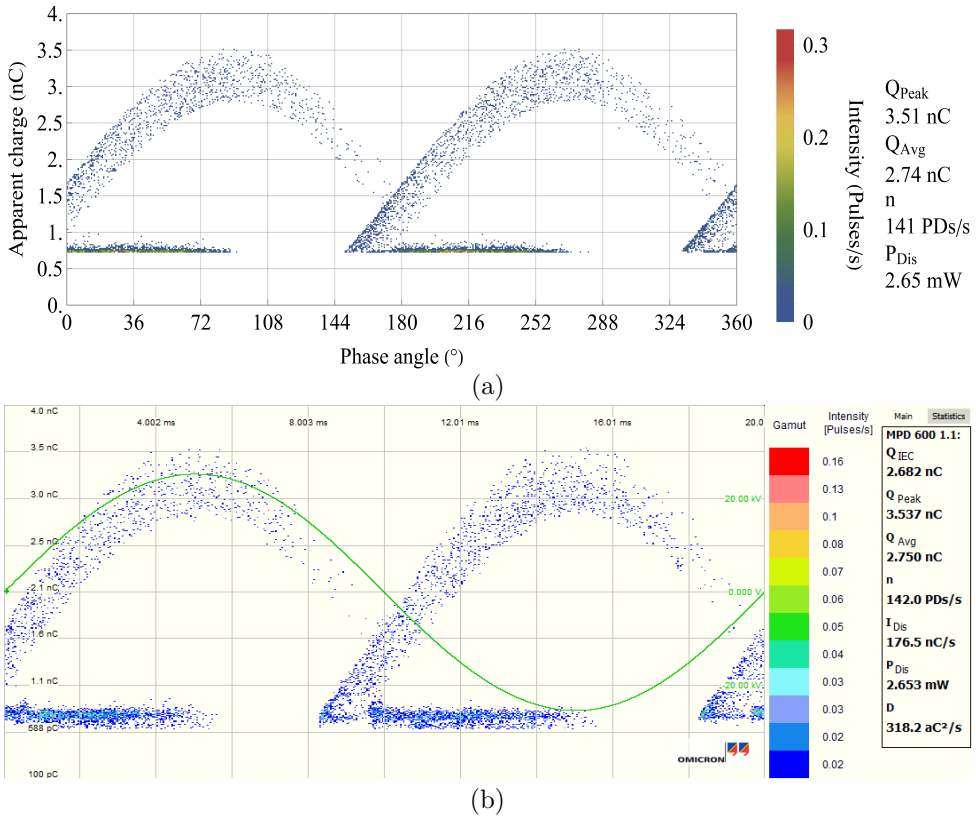

Figure 5.8: A comparison of the PRPD patterns obtained: (a) by the analytical model using the calibrated parameters; (b) from the experimental measurement. Adopted from [1].

18 kV_{RMS}) was employed. Apart from gathering the values of individual statistical parameters per IEC 60270 standard (namely Q_{Peak}, Q_{Avg}, n and P_{Dis}), the PRPD pattern of the discharge activity was also recorded.

The model was calibrated using the electron availability terms for both polarities. After each simulation, the above statistical parameters were calculated, and a PRPD pattern was constructed. The variables were then changed, and the simulation was repeated. At first, the N_{0H} and N_{0L} were cycled by steps of 100 s^{-1} and 10 s^{-1}, respectively. When a PRPD pattern vaguely resembling the measured one was obtained, the steps were reduced to 10 s^{-1} and 1 s^{-1}, respectively, and the parameters were altered until the relative difference between the calculated and measured statistical parameters was lower than 1 %. The PRPD pattern of the discharge activity modeled by employing the calibrated parameters (listed in Table 5.1) is depicted in Figure 5.8a, while Figure 5.8b shows the PRPD pattern of the discharge activity measured in the test specimen.

5.2.5 Implemented changes due to supraharmonic oscillations

Next, the experimental measurement was repeated using a waveform with an 8-kHz oscillation placed in the phase angle of 18°. Analogously, the statistical parameters and PRPD pattern were gathered. A simulation of PD activity under an identical waveform was performed by employing the parameters calibrated for the sinusoidal waveform. As evident from the PRPD pattern of the experimental discharge activity in Figure 5.9a, the oscillations manifested as intensive clustering of PD events in the positive halfwave of the oscillation (note that the oscillation in the shown voltage trend is largely suppressed owing to the transfer function of the measuring impedance). This clustering led to the disappearance of PD events in a small phase angle window just after the oscillation's positive halfwave. Surprisingly, this phenomenon was present only in the pulse-train cluster, i.e., for same-polarity PD events in the same halfwave.

As shown in Figure 5.9b, the analytical model did not entirely reflect the observed discharge event distribution. Even though significantly more PD events took place in the positive halfwave, the characteristic

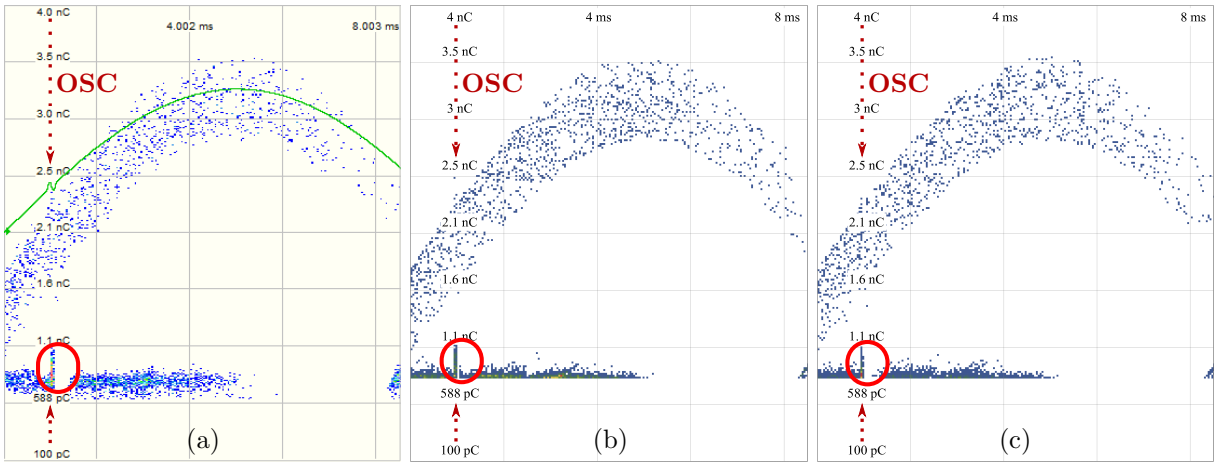

Figure 5.9: A comparison of the PRPD patterns obtained: (a) from the experimental measurements; (b) by the analytical model using the unmodified Eq. 2.42; (c) by the analytical model incorporating Eq. 5.3. Adopted from [1].

"trench" in the pulse-train cluster was not obtained. This "trench" signifies that virtually all the theoretically possible PDs take place during the positive halfwave, while the subsequent discharges can only occur after the cavity field again reaches the inception field criterion. This phenomenon leads to the observed timeframe (phase angle range) where no discharge events are present. Therefore, it was speculated that the free electron availability must be further increased during the oscillation's positive halfwave. An increase in the availability due to the much higher instantaneous value of $\mathrm{d}V/\mathrm{d}t$ ratio ($\mathrm{d}E/\mathrm{d}t$) was therefore assumed and incorporated into the model by redefining the free electron availability term $N_{\mathrm{es}}(t)$ as:

$$N_{\mathrm{es}}\left(t\right) = \begin{cases} N_{\mathrm{es}}\left(t\right) + N_{\mathrm{max,osc}} \cdot \frac{\mathrm{d}E_{\mathrm{cav}}(t)}{\mathrm{d}t} & \text{if } t \in t_{\mathrm{osc}} \wedge \frac{E_{\mathrm{cav}}(t)}{E_{\mathrm{cav}}(t_{\mathrm{PD}})} \geq 0 \\ N_{\mathrm{es}}\left(t\right) \quad \text{(per Eq. 2.42)} & \text{otherwise,} \end{cases} \tag{5.3}$$

where t_{osc} is the time range during which the oscillation is present, and $N_{\mathrm{max,osc}}$ is the maximum increase in electron availability during the oscillation. Analogous to the other two electron availability terms, the latter's value needs to be calibrated as well (see Table 5.1). A PRPD pattern obtained by employing the modified analytical model is depicted in Figure 5.9c. Clearly, the distinct separation of PD events is addressed substantially better by this model variant, and it was hence used in the simulation of all PD activities under the distorted voltage waveforms.

Finally, it should be noted that the standard time step size of 20 µs was reduced to 2.5 µs during oscillations to accommodate the more rapid change in electric field strengths.

5.3 Results and discussion

5.3.1 Measured and modeled statistical parameters

Four fundamental parameters were determined from each measurement/simulation for the oscillation's effect analysis. These were the average charge Q_{Avg}, the peak charge Q_{Peak}, discharge power P_{Dis}, and pulse repetition rate n. Unfortunately, the test specimen's PDIV and PDEV could not be employed in the analysis, as the initial electron availability was extremely low. In other words, reliable determination of the two parameters would require a step voltage protocol with fine step size and dwell times of at least several minutes. Since such a procedure would be necessary for each waveform, the two parameters were disregarded.

The statistical parameters gathered from the experimental measurements using waveforms with variable oscillation frequency (f_{osc}) are listed in Table 5.2. Likewise, those obtained using waveforms with variable oscillation placement (ϕ) are listed in Table 5.3. Each value represents an arithmetic average of the three gathered readings.

Table 5.2: An overview of the **measured** statistical parameters; variable oscillation **frequency** approach, oscillation's placement set to 90° phase angle.

f_{osc} (kHz)	Q_{Avg} (nC)	Q_{Peak} (nC)	P_{Dis} (mW)	n (PD/s)
None	2.75	3.56	2.66	142
2	2.75	3.70	2.76	157
3	2.75	3.66	2.75	153
4	2.77	3.74	2.86	158
5	2.75	3.70	2.68	150
6	2.75	3.66	2.75	154
7	2.73	3.67	2.71	152
8	2.74	3.68	2.64	151
9	2.72	3.74	2.63	149

Table 5.3: An overview of the **measured** statistical parameters; variable oscillation **placement** approach, oscillation's frequency set to 8 kHz.

ϕ (°)	Q_{Avg} (nC)	Q_{Peak} (nC)	P_{Dis} (mW)	n (PD/s)
324	2.77	3.60	2.71	142
342	2.76	3.60	2.67	138
0	2.77	3.56	2.69	140
18	2.80	3.55	2.81	147
36	2.75	3.55	2.61	135
54	2.77	3.54	2.69	141
72	2.77	3.70	2.78	148
90	2.74	3.68	2.64	151
108	2.79	3.57	2.76	143

Both data sets are also visualized as plots in Figure 5.10, and include error bars determined from the range of the gathered readings.

Similarly, the statistical parameters obtained from the modeled PD activities are listed in Table 5.4 (variable frequency) and Table 5.5 (variable position) and visualized in Figure 5.11.

Comparison of Figures 5.10 and 5.11 implies that the analytical model simulated the experimentally observed PD activities very well. Therefore, the model's use in analyzing the oscillation's effect on the discharge activity seems to be justified.

Table 5.4: An overview of the **modeled** statistical parameters; variable oscillation **frequency** approach, oscillation's placement set to 90° phase angle.

f_{osc} (kHz)	Q_{Avg} (nC)	Q_{Peak} (nC)	P_{Dis} (mW)	n (PD/s)
None	2.75	3.51	2.67	143
2	2.79	3.74	2.88	162
3	2.80	3.76	2.89	162
4	2.78	3.78	2.84	159
5	2.80	3.76	2.85	159
6	2.79	3.75	2.83	158
7	2.78	3.73	2.78	155
8	2.77	3.73	2.79	155
9	2.78	3.75	2.79	157

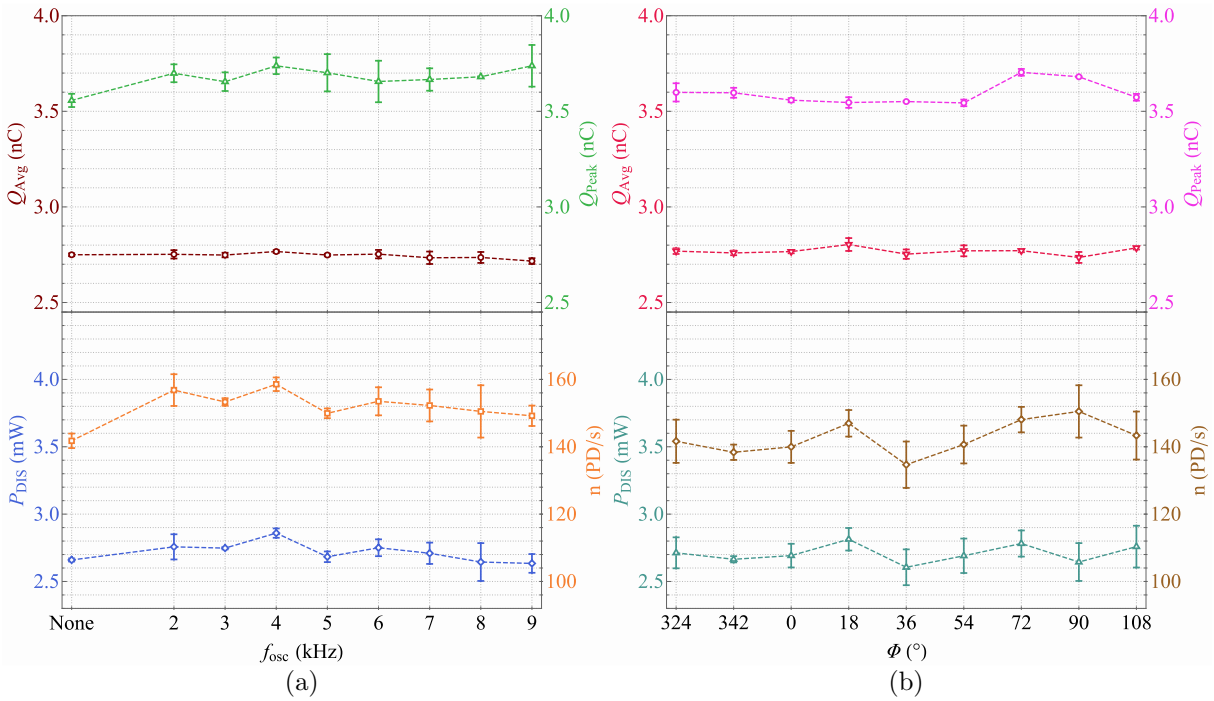

Figure 5.10: The dependence of the four statistical parameters of the **measured** PD activities on (a) the oscillation's frequency; (b) the oscillation's position. Adopted from [1].

Table 5.5: An overview of the **modeled** statistical parameters; variable oscillation **placement** approach, oscillation's frequency set to 8 kHz.

ϕ (°)	$Q_{\mathbf{Avg}}$ (nC)	$Q_{\mathbf{Peak}}$ (nC)	$P_{\mathbf{Dis}}$ (mW)	n (PD/s)
324	2.75	3.50	2.67	142
342	2.74	3.50	2.65	142
0	2.76	3.50	2.75	146
18	2.76	3.50	2.71	144
36	2.76	3.50	2.69	142
54	2.76	3.51	2.69	142
72	2.79	3.68	2.79	152
90	2.77	3.73	2.79	155
108	2.75	3.60	2.72	149

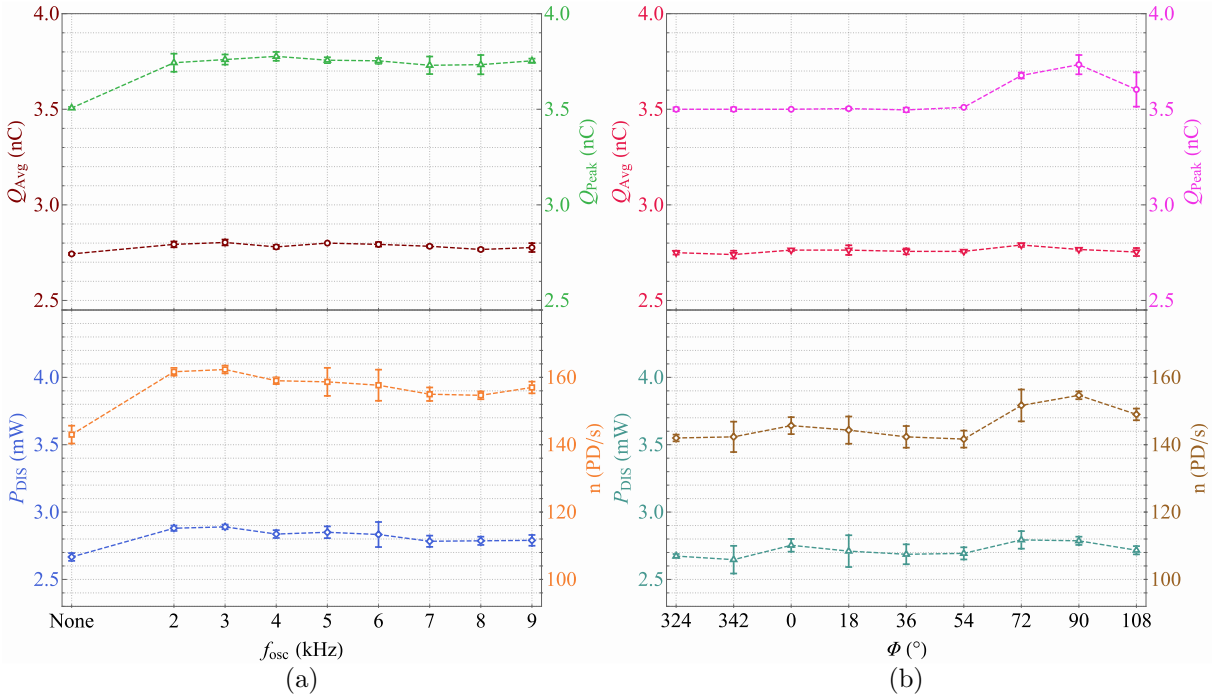

Figure 5.11: The dependence of the four statistical parameters of the **modeled** PD activities on (a) the oscillation's frequency; (b) the oscillation's position. Adopted from [1].

5.3.2 Analysis of the oscillation's effect

5.3.2.1 Average charge (Q_{Avg})

The average charge seems to be the only parameter unaffected by the presence of the oscillation. Both its trends for the variable oscillation frequency and position are practically flat and show only minimum deviation from the reference value. This observation is valid both for the measured and modeled trends.

An explanation for the parameter's invariance might lie in the specific way the oscillation affects the discharge activity. As shown in Figure 5.12, the oscillation in the positive halfwave's peak splits the negative halfwave's "rabbit-ear" cluster into two distinct parts. The reason for that is the suitable placement of the oscillation, which causes a temporally increase in the cavity field just before it gradually decreases according to the fundamental waveform's shape. This way, discharges that could not normally be incepted due to the insufficient field might take place instead. If such a discharge occurs, the now-opposite space-charge field will be strengthened. However, when the main field starts to switch polarity, the space-charge will be instead added to it, and owing to its enhanced value, the inception field criterion will be met earlier in the phase. As a result, discharges might occur in earlier phase angles than before and create the observed second "rabbit ear." The described phenomenon is illustrated in Figure 5.7, where it gave rise to the 9^{th} and 14^{th} PD.

A consequence of the identified phenomenon is an increased number of PD events per time unit, as described in section 5.3.2.3 below. In general, the average charge is independent of the number of discharges and should therefore be immune to this effect. However, the additional discharges are expected to be slightly weaker since they occur at the end of the pulse-train cluster (charge close to Q_{min}) and then earlier during the second halfwave, when the free electron availability is higher (discharges occur at lower fields on average). The reason for the higher free electron availability is the shorter time between successive discharges, during which the surface charge can decay. On the other hand, due to the presence of the second "rabbit ear," discharges stronger than is normally possible can take place, as the entire cavity field trend is shifted downward (toward the negative polarity) by the amplitude of the oscillation. Nonetheless, according to both the measured and modeled results, these two effects seem to cancel each other in terms of average charge.

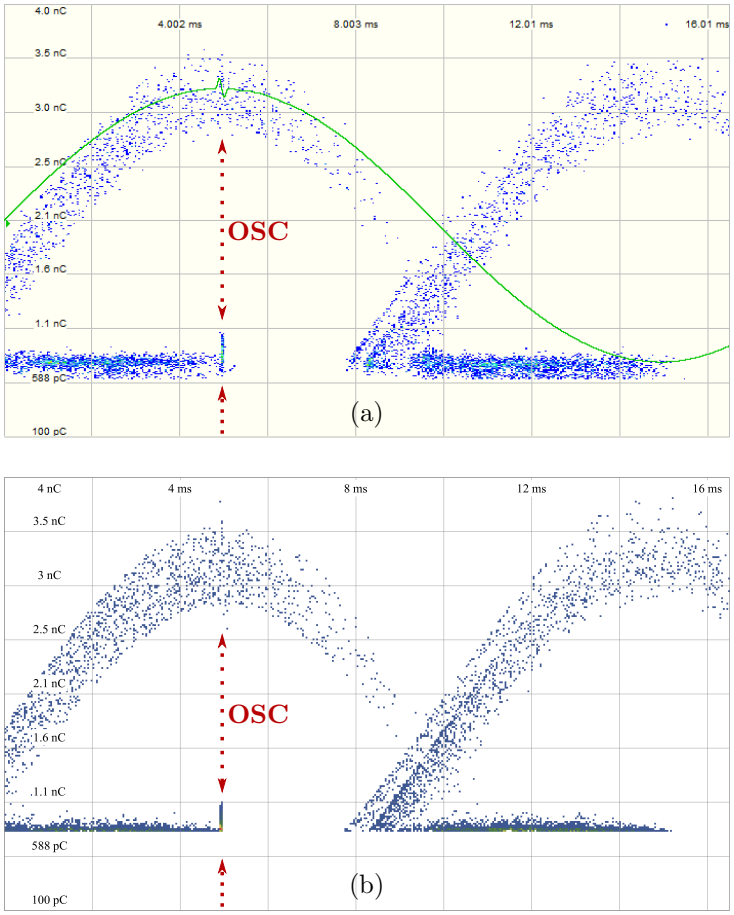

Figure 5.12: PRPD pattern details of measured (a) and modeled (b) PD activity. Oscillation parameters: $f_{\text{osc}} = 8$ kHz, $\phi = 90°$. Adopted from [1].

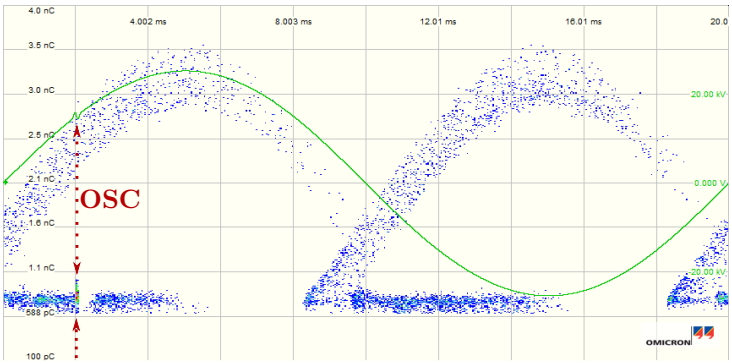

Figure 5.13: The PRPD pattern of the measured discharge activity showing the absence of the second "rabbit-ear" cluster. Oscillation parameters: $f_{\mathrm{osc}} = 8$ kHz, $\phi = 36°$.

5.3.2.2 Peak charge (Q_{Peak})

The second effect identified in the previous paragraph seems to have played a definitive role in the increase of the peak charge observed for waveforms with oscillations placed between 72° and 108°. This range should roughly correspond to the phase angle range, in which the superposition of the fundamental waveform and the oscillation increases the overall peak voltage. Outside of this range, the second "rabbit" ear cluster is not formed, as, for example, evident from the PRPD pattern shown in Figure 5.13 (oscillation placement $\phi = 36°$).

It is worth noting that the maximum increase of peak charge should be present for the oscillation placed at a phase angle of 90°. However, PD events around this phase angle that are also part of the second "rabbit ear" are sporadic, and, hence, there is a high probability that discharges with magnitudes close to the theoretical maximum will not occur during the observed timeframe of three minutes. Naturally, this can result in situations where a larger peak charge is observed for other phase angles, as was the case in the experimental measurements (compare Q_{peak} of $\phi = 72°$ and $\phi = 90°$ in Table 5.3).

5.3.2.3 Pulse repetition rate (n)

As already discussed in section 5.3.2.1, the placement of an oscillation into the vicinity of the fundamental waveform's amplitude can lead to the occurrence of additional PDs. Naturally, this phenomenon directly increases the pulse repetition rate, as can be seen from the respective trends in Figure 5.10b as well as in Figure 5.11b for oscillation placements $\phi = 72°$ to $\phi = 108°$.

Further analysis of the PRPD patterns revealed that the window of opportunity in which discharges can occur is also enlarged for the oscillation placement $\phi = 324°$, as shown in Figure 5.14. Theoretically, if a PD takes place "prematurely" due to the oscillation, more discharge events could fit in the subsequent pulse train (i.e., up to the phase angle of 90°). However, in this case, it seems that either the time shift is insufficient or the number of additional events statistically insignificant, as no apparent increase in the pulse repetition rate was identified.

While both average and peak charges showed no dependence on the oscillation's natural frequency, the pulse repetition rate seems to be affected by it. As can be seen in Figures 5.10a and 5.11a, the pulse repetition trends imply that the parameter slightly decreases with the rising oscillation frequency. The comparison depicted in Figure 5.15 demonstrates that the 2-kHz oscillation leads to substantially more discharges at the end of the pulse train cluster than its 8-kHz counterpart. Since the discharges are, on average, stronger, they lead to the formation of the above-described additional "rabbit-ear" cluster. By comparing the respective PRPD pattern details in Figure 5.15, one might notice that number of discharges in this cluster is also much larger in the case of the 2-kHz oscillation. The reason for that is presumably the longer duration of the oscillation's positive halfwave, which also strengthens discharges that would occur only at the standard magnitude in the case of the 8-kHz oscillation. Normally, this would be offset by the oscillation's longer negative halfwave, but due to the asymmetry between the number of discharges during oscillation's positive and negative halfwaves, for example, illustrated in Figure 5.9a, the effect of the negative halfwave is negligible. Indeed, when the oscillation's negative halfwave is disregarded, the average voltage around the waveform's peak is higher, meaning that the discharges should be slightly stronger for lower oscillation frequencies. As a result, more discharges take

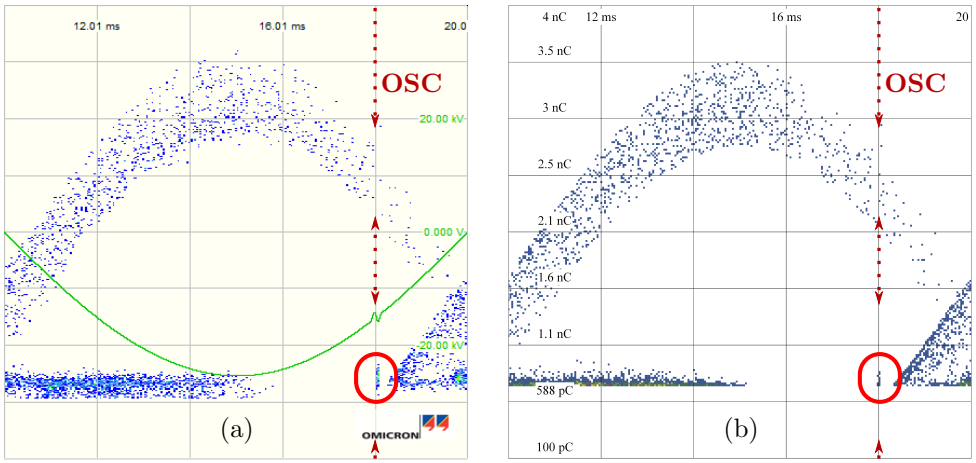

Figure 5.14: PRPD pattern details of measured (a) and modeled (b) PD activity showing additional discharge events due to the oscillation. Oscillation parameters: $f_{\text{osc}} = 8$ kHz, $\phi = 324°$.

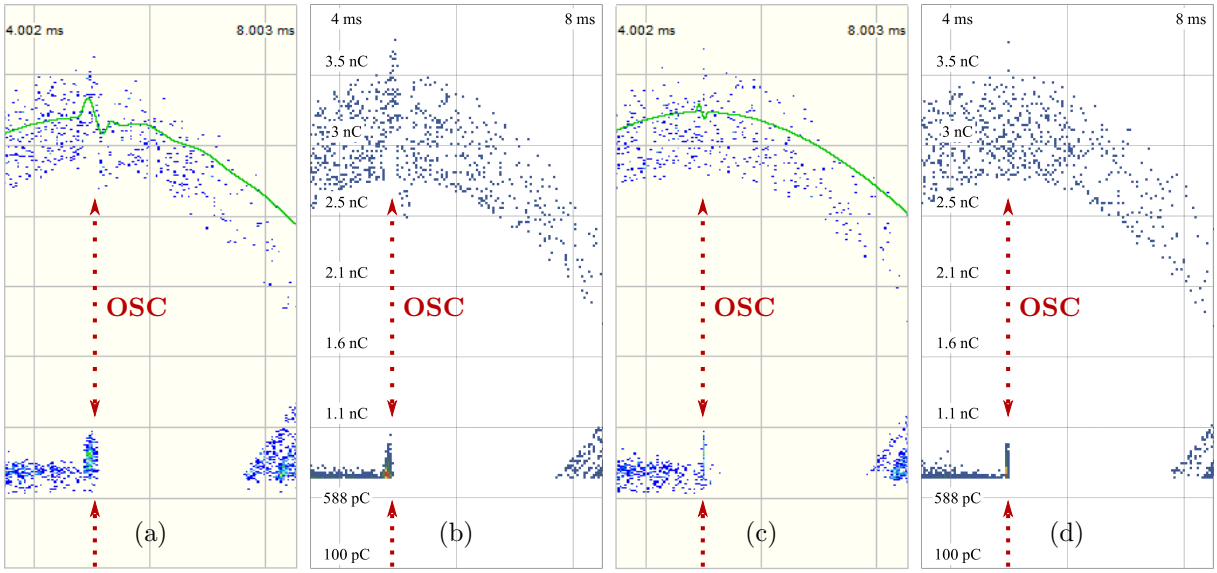

Figure 5.15: A comparison of PRPD patterns constructed from the (a) measured and (b) modeled PD activity under the waveform $f_{\text{osc}} = 2$ kHz, $\phi = 90°$ and (c) measured and (d) modeled PD activity under the waveform $f_{\text{osc}} = 8$ kHz, $\phi = 90°$. Adopted from [1].

place in the additional "rabbit-ear" cluster, increasing the total number of PDs per time unit.

5.3.2.4 Discharge power (P_{Dis})

Since the analysis of the oscillation's effect on discharge power is tied to its definition, it might be convenient to reiterate it. Per IEC 60270, the parameter is expressed as:

$$P_{\text{Dis}} = \frac{1}{T_{\text{ref}}} \prod_{i=1}^{N} q_i u_i, \tag{5.4}$$

where T_{ref} is the reference time interval, u_i is the instantaneous voltage at the moment of the i^{th} discharge, and q_i is its apparent charge magnitude. In this case, the capital N denotes the number of detected discharges during T_{ref}, and is not to be confused with the pulse repetition rate n.

From Eq. 5.4, it is clear that the discharge power is directly linked to both average charge and pulse repetition rate. Since practically no changes were observed in the average charge, the trends of the

discharge power should duplicate those of the pulse repetition rate. Indeed, that was precisely the case, as evident from Figures 5.10 and 5.11.

Other than that, a slight discrepancy between the discharge power of the measured and modeled PD activities was observed. This discrepancy might partially originate from the improper voltage measurement via the coupling capacitor, which naturally suppresses higher-frequency components. Consequently, the supraharmonic oscillation is detected with a much smaller amplitude (compare Figure 5.15a and c; both oscillations had similar peak-to-peak voltage). As a result, the contribution ($q \cdot u$ product) of the oscillation-induced discharges toward the dissipated power parameter is reduced. While the frequency range of the voltage measurement is commonly given (< 400 Hz for the employed MPD 600), its relation to the discharge power parameter might not always be evident at first.

5.4 Conclussion

The experiment identified a clear impact of the added supraharmonic oscillation on the discharge activity in an artificial spherical cavity specimen. By employing an analytical PD model, an explanation of the origin of the observed effects was proposed. The results of the work can be summarized and generalized as follows:

- Typical 3D printers based on the fused deposition modeling method can be employed to prepare test specimens with arbitrary defects (cavities) using the PET-G material. However, these specimens cannot be repeatedly used in long-term (several hours) experiments, as the cavity surface degrades relatively quickly, and the discharge activity changes afterward. In such a case, a more suitable material than the employed PET-G or a completely different fabrication method is required.
- When oscillations or distortions pollute the fundamental waveform, the occurring PD activity seems to be the strongest when these components are present at the peak of the waveform. The activity-magnifying effect is evident primarily from the pulse repetition rate and dissipated power metrics.
- The effect is most likely connected to the occurrence of additional PD events at the end of the pulse-train cluster and the additional "rabbit-ear" cluster. In rare cases, the latter cluster can give rise to stronger discharges than what would be possible in the absence of oscillations. Specifically, an average increase in the peak discharge of 3 to 7 % was identified from the results.
- While infrequent, the magnified peak charges might incept degradation processes (such as treeing) earlier, as their rate generally shows an exponential dependence on energy. A suitable example might be the cathode bombardment, in which the obtained kinetic energy is directly tied to the field strength at the moment of discharge. Other effects, such as the release of radicals or heating of cavity surface, would also be affected.
- Intensified free electron detrapping from the cavity's surface during the oscillations was indicated by discrepancies between the measured and modeled PRPD patterns. The effect was assumed to originate from the increased $\mathrm{d}V/\mathrm{d}t$ ratio during the oscillations. Hence, a $\mathrm{d}V/\mathrm{d}t$-based term was added to the free electron availability term of the analytical model. The addition resulted in a much better match between the PRPD patterns and is therefore recommended for further modeling of PDs under similar waveforms.
- While the PDIV could not be reliably determined, it is expected that the presence of oscillations or distortions in the fundamental waveform's peaks would reduce its value.

Even though the works reviewed in section 2.3.4 chiefly identified a direct impact of the added components on the PDIV and apparent charge parameters, no such inferences were obtained in this case. However, the individual effects listed above suggest that the PD activity would be enhanced, nonetheless. It might thus be suitable to evaluate PD measurements using the whole spectrum of available metrics and not to limit it to just average or apparent charge and PDIV to avoid erroneous conclusions.

Regarding the degradation effects, the work implies that the presence of supraharmonic components in the voltage waveform could be harmful in two ways. Apart from the possible premature inception, the discharge activity would also intensify, implying that the afflicted insulation system would degrade quicker than expected. Naturally, it would be suitable to investigate the magnitude of this degradation-enhancing effect and consider it while designing the respective power system.

Thesis Conclusions & Outlooks

Note: Each experimental chapter has a specific conclusion of its own and it is suggested that the reader refers to those if they seek further information.

The thesis consisted of three individual experimental works, which strived to investigate the effect of voltage waveforms with supraharmonic content on the aging rate of polymeric insulation materials. Each work identified that such waveforms could accelerate aging processes in the respective systems, which were represented by various test specimens. By analyzing the results, it can be concluded that:

- *Aging of Medium-Voltage Cable Termination Specimens.* A model of a photovoltaic power station and its neighboring network showed that supraharmonics could substantially distort the system's voltage waveform. A distorted waveform, similar to the one obtained by the model, and a reference sinusoidal waveform were respectively employed in cable termination specimens' long-term combined (thermal + electrical) aging. Loss tangent and partial discharge measurements were performed on the specimens throughout the aging experiment, and, afterward, their short-term breakdown strength was tested. The results indicated that the distorted waveform substantially enhanced the aging rate of cable termination specimens. The original contribution of this work was the investigation of the direct impacts of supraharmonics on actual insulation systems, represented by the cable termination specimens. Regarding the state-of-the-art knowledge and practical utilization, the work could provide a part of the basis for the choice of cable termination designs or suitable filtering methods in systems prone to the presence of supraharmonics or, possibly, other higher-frequency components.

- *Aging of XLPE and nano-XLPE Specimens.* A similarly distorted voltage waveform was used in the long-term electrical aging of XLPE and nano-XLPE film specimens. With ten specimens tested for each of the four materials, three stress levels, and two waveform types, the results could be treated by Weibull statistics to provide data for fitting of aging models. Inverse power law and two variants of the Crine aging model were chosen as suitable models for determining the supraharmonics' impacts. The models implied that aging transpired faster and that the operating field strength might have been reduced, both due to the presence of supraharmonics. Concerning the effect of nanoparticles, adding 1wt% and 3wt% nano alumina(nano-Al_2O_3) into the XLPE resulted in poorer insulation performance, whereas the 5wt% nanofiller content slightly increased the expected lifetime in comparison to the base material. The original contribution of this work was the investigation of the direct impacts of supraharmonics on both unmodified and nano-alumina-filled film specimens, which represented the main insulation of medium-voltage cable systems. Regarding the state-of-the-art knowledge and practical utilization, the results could be applied in the optimization process of cable insulation system dimensioning or, analogously, the choice of suitable filtering methods in systems prone to the presence of supraharmonics or other higher-frequency distortions.

- *Impacts of Low-Order Supraharmonics on Partial Discharges.* A 3D-printed specimen with an artificial cavity was employed to analyze the impact of supraharmonics on partial discharge activity. Sinusoidal waveforms with a superposed, single-per-period oscillation of various (supraharmonic) frequency and phase-angle placement were applied to the test specimen, and the resulting PD activity was gathered. An analytical PD model was constructed and used to simulate discharge activity under identical conditions. Both the measured and modeled results indicated that the discharge activity was increased due to the supraharmonic oscillation, particularly in the case of lower natural frequencies and placement in the peak of the fundamental waveform. The analytical model was employed to explain the observed changes in both statistical parameters and PRPD patterns. The original contribution of this work was the use of 3D-printed internal cavity speci-

mens for analysis of PDs, investigation of PD activity under sinusoidal waveforms with superposed supraharmonic oscillations, and introduction of a $\mathrm{d}V/\mathrm{d}t$-dependent term of free electron availability into the fundamental equation of an analytical electrostatic PD model. Regarding the state-of-the-art knowledge and practical utilization, the work sheds light on the impacts of supraharmonics and possibly other high-frequency components on the actual internal cavity processes and electric field time-development that constitute the observable PD activity. The detected increase in PD activity could provide further incentive to tighten the regulations of permissible apparent charge or PDIV in power energy (insulation) systems designed for use in networks prone to the presence of supraharmonics.

Overall, the thesis should illustrate that the presence of supraharmonics in electrical power systems could pose a much greater threat to their insulation systems than what is generally accepted. Therefore, the gathered findings could instigate the power engineering community to further discuss and investigate the issue and possibly review whether present-day restrictions on harmonic pollution in the supraharmonic range, i.e., 2 to 150 kHz, are sufficient. Another vital discussion could be led concerning the right way to deal with the issue, meaning whether it would be preferable, technical- and cost-wise, to dimension the insulation system with slight redundance or design the filtering method accordingly. Naturally, such a decision should also consider another significant impact of supraharmonics: interference.

Concerning the significance of the thesis for future research, the limitations of the individual constituent experiments should be identified and outlook for subsequent works mentioned. Firstly, the accelerated aging tests of cable termination specimens were performed on the commonly employed designs of cable terminations. However, a specific design, which should resolve the issue of the uneven field distribution due to higher-frequency voltage components, had already been proposed. Therefore, it would be suitable to include this type in a new run of this experiment to determine whether the said cable termination design would eliminate the observed additional aging effect.

Secondly, the long-term aging test of unmodified and nano-alumina-filled XLPE film specimens included only one base material. While XLPE is still widely employed, there are environmental concerns about its further use due to its non-recyclability. Therefore, a similar experiment on film specimens of the more environment-friendly LDPE or polypropylene materials could be valuable. Analogously, a study of the long-term insulation performance of their nanocomposites should provide equally beneficial results.

Thirdly and finally, the investigation of discharge activity inside of a single internal cavity concluded that the PD activity could be magnified due to the presence of supraharmonics in the test voltage waveform. While the results seem convincing, it would be appropriate to study the phenomenon using an actual insulation system. Considering the systems prone to the presence of supraharmonics, medium-voltage cable systems or epoxy resin encapsulated transformers seem to be the ideal candidates.

Bibliography

[1] O. Sefl and R. Prochazka, "Investigation of supraharmonics' influence on partial discharge activity using an internal cavity sample," *International Journal of Electrical Power & Energy Systems*, vol. 134, pp. 1–10, 2022.

[2] M. Knenicky, R. Prochazka, J. Hlavacek, and O. Sefl, "Impact of high-frequency voltage distortion emitted by large photovoltaic power plant on medium voltage cable systems," *IEEE Transactions on Power Delivery*, vol. 36, no. 3, pp. 1882–1891, 2021.

[3] O. Sefl and R. Prochazka, "Study on aging rate of XLPE and its nanocomposites under nonstandard voltage stresses." Submitted to IEEE Conference on Electrical Insulation and Dielectric Phenomena 2021.

[4] O. Sefl and R. Prochazka, "XLPE ageing under non-standard voltage stresses," in *Proceedings of the 10th International Scientific Symposium on Electrical Power Engineering, ELEKTROENERGETIKA 2019*, (Stara Lesna, Slovakia), pp. 521–524, Technical University of Kosice, 2019.

[5] O. Sefl, M. Knenicky, and R. Prochazka, "Life-time of oil filled insulation paper under nonstandard voltage stresses," in *2018 International Conference on Diagnostics in Electrical Engineering (Diagnostika)*, (Prague, CZ), Czechoslovakia Section IEEE, 2018.

[6] R. Prochazka and O. Sefl, "Influence of voltage distortion shape on partial discharge activity in internal voids," in *2020 International Conference on Diagnostics in Electrical Engineering (Diagnostika)*, (Pilsen, Czech Republic), pp. 1–4, IEEE, 2020.

[7] R. Prochazka and O. Sefl, "Simulation model of partial discharges in internal void," in *Proceedings of the 10th International Scientific Symposium on Electrical Power Engineering, ELEKTROENERGETIKA 2019*, (Stara Lesna, Slovakia), pp. 202–206, Technical University of Kosice, 2019.

[8] R. Prochazka, O. Sefl, and M. Knenicky, "Partial discharges activity within an internal void at AC voltage disturbed by high frequency components," in *Proceedings of 2018 IEEE International Conference on High Voltage Engineering and Application*, (Divani Caravel Hotel,Athens), IEEE (Institute of Electrical and Electronics Engineers), 2018.

[9] M. Knenicky, R. Prochazka, and O. Sefl, "Influence of nonstandard voltage stresses on transformer insulation paper," in *Proceedings of 2017 IEEE Conference on Electrical Insulation and Dielectric Phenomena*, (Piscataway, US), IEEE, 2017.

[10] O. Sefl, "Aging of insulation materials under nonstandard voltage stresses," 2017.

[11] J. C. Das, *Power system analysis*. Boca Raton: CRC Press, 2nd ed ed., 2012.

[12] K. Yang, M. H. J. Bollen, and E. O. A. Larsson, "Aggregation and amplification of wind-turbine harmonic emission in a wind park," *IEEE Transactions on Power Delivery*, vol. 30, no. 2, pp. 791–799, 2015.

[13] M. H. J. Bollen and S. K. Ronnberg, "Primary and secondary harmonics emission; harmonic interaction - a set of definitions," in *2016 17th International Conference on Harmonics and Quality of Power (ICHQP)*, (Belo Horizonte, Brazil), pp. 703–708, IEEE, 2016.

[14] J. Sun, "On the zero-crossing distortion in single-phase PFC converters," *IEEE Transactions on Power Electronics*, vol. 19, no. 3, pp. 685–692, 2004.

[15] M. Bollen, M. Olofsson, A. Larsson, S. Ronnberg, and M. Lundmark, "Standards for supraharmonics (2 to 150 kHz)," *IEEE Electromagnetic Compatibility Magazine*, vol. 3, no. 1, pp. 114–119, 2014.

[16] S. K. Rönnberg, M. H. Bollen, H. Amaris, G. W. Chang, I. Y. Gu, Łukasz H. Kocewiak, J. Meyer, M. Olofsson, P. F. Ribeiro, and J. Desmet, "On waveform distortion in the frequency range of 2 kHz–150 kHz—review and research challenges," *Electric Power Systems Research*, no. vol. 150, pp. 1–10, 2017.

[17] V. Khokhlov, J. Meyer, A. Grevener, T. Busatto, and S. Ronnberg, "Comparison of measurement methods for the frequency range 2–150 kHz (supraharmonics) based on the present standards framework," *IEEE Access*, vol. 8, pp. 77618–77630, 2020.

[18] L. Paulsson, B. Ekehov, S. Halen, T. Larsson, L. Palmqvist, A. Edris, D. Kidd, A. Keri, and B. Mehraban, "High-frequency impacts in a converter-based back-to-back tie; the eagle pass installation," *IEEE Transactions on Power Delivery*, vol. 18, no. 4, pp. 1410–1415, 2003.

[19] H. Bai, X. Wang, F. Blaabjerg, and P. C. Loh, "Harmonic analysis and mitigation of low-frequency switching voltage source inverter with auxiliary VSI," *IEEE Journal of Emerging and Selected Topics in Power Electronics*, vol. 6, no. 3, pp. 1355–1365, 2018.

[20] Y. A.-R. I. Mohamed, "Mitigation of dynamic, unbalanced, and harmonic voltage disturbances using grid-connected inverters with LCL filter," *IEEE Transactions on Industrial Electronics*, vol. 58, no. 9, pp. 3914–3924, 2011.

[21] S. Jiang and Y. Liu, "EMI noise reduction for the single-phase grid-connected inverter with a modified harmonic filter design," *IEEE Transactions on Electromagnetic Compatibility*, pp. 1–13, 2020 (Early Access).

[22] R. N. Beres, X. Wang, F. Blaabjerg, M. Liserre, and C. L. Bak, "Optimal design of high-order passive-damped filters for grid-connected applications," *IEEE Transactions on Power Electronics*, vol. 31, no. 3, pp. 2083–2098, 2016.

[23] M. H. Rashid, *Power Electronics Handbook*. Saint Louis: Elsevier Science & Technology, 3rd ed., 2011.

[24] A. Trzynadlowski, N. Patriciu, F. Blaabjerg, and J. Pedersen, "A hybrid, current-source/voltage-source power inverter circuit," *IEEE Transactions on Power Electronics*, vol. 16, no. 6, pp. 866–871, 2001.

[25] Y. Levron, H. Kim, and R. W. Erickson, "Design of EMI filters having low harmonic distortion in high-power-factor converters," *IEEE Transactions on Power Electronics*, vol. 29, no. 7, pp. 3403–3413, 2014.

[26] W. Chen, X. Yang, and Z. Wang, "An active EMI filtering technique for improving passive filter low-frequency performance," *IEEE Transactions on Electromagnetic Compatibility*, vol. 48, no. 1, pp. 172–177, 2006.

[27] S. Jiang, Y. Liu, W. Liang, J. Peng, and H. Jiang, "Active EMI filter design with a modified LCL-LC filter for single-phase grid-connected inverter in vehicle-to-grid application," *IEEE Transactions on Vehicular Technology*, vol. 68, no. 11, pp. 10639–10650, 2019.

[28] W. Wu, Z. Xie, Y. Chen, J. Liu, J. Guo, Y. Xu, H. Wang, and A. Luo, "Analysis and suppression of high-frequency oscillation between converter-based source and loads in an island power system," *International Journal of Electrical Power & Energy Systems*, vol. 117, no. 105616, pp. 1–13, 2020.

[29] R. Kirlin, M. Bech, and A. Trzynadlowski, "Analysis of power and power spectral density in PWM inverters with randomized switching frequency," *IEEE Transactions on Industrial Electronics*, vol. 49, no. 2, pp. 486–499, 2002.

[30] M. Vilathgamuwa, J. Deng, and K. Tseng, "EMI suppression with switching frequency modulated DC-DC converters," *IEEE Industry Applications Magazine*, vol. 5, no. 6, pp. 27–33, 1999.

[31] S. Rönnberg, A. Larson, M. Bollen, and J.-L. Schanen, "A simple model for interaction between equipment at a frequency of some tens of kHz," in *Proceedings of CIRED 21st International Conference on Electricity Distribution, 2011*, (Frankfurt, Germany), pp. 1–4, CIRED, 2011.

[32] N. Uribe-Pérez, I. Angulo, L. Hernández-Callejo, T. Arzuaga, D. de la Vega, and A. Arrinda, "Study of unwanted emissions in the CENELEC-A band generated by distributed energy resources and their influence over narrow band power line communications," *Energies*, vol. 9, no. 12, pp. 1–24, 2016.

[33] K. Yang, M. Bollen, and L. Yao, "Theoretical emission study of windpark grids," in *11th International Conference on Electrical Power Quality and Utilisation*, (Lisbon, Portugal), pp. 1–6, IEEE, 2011.

[34] K. Yang, "On harmonic emission, propagation and aggregation in wind power plants," 2015.

[35] E. O. A. Larsson, M. H. J. Bollen, M. G. Wahlberg, C. M. Lundmark, and S. K. Ronnberg, "Measurements of high-frequency (2–150 kHz) distortion in low-voltage networks," *IEEE Transactions on Power Delivery*, vol. 25, no. 3, pp. 1749–1757, 2010.

[36] A. Küchler, *High voltage engineering*. Berlin: Springer Vieweg, 5th ed. ed., 2018.

[37] E. Kuffel, W. S. Zaengl, and J. Kuffel, *High voltage engineering*. Boston: Butterworth-Heinemann, 2nd ed ed., 2000.

[38] O. Gallot-Lavallée, *Dielectric Materials and Electrostatics*. Hoboken, USA: Wiley, 1st ed. ed., 2013.

[39] A. D. McNaught and A. Wilkinson, *Compendium of chemical terminology*. Cambridge: Blackwell, 2nd ed ed., 1997.

[40] S. Grzybowski and R. Dobroszewski, "Influence of partial discharges on the development of electrical treeing in polyethylene insulated cables," in *1978 IEEE International Conference on Electrical Insulation*, (Philadelphia, PA, USA), pp. 122–125, IEEE, 1978.

[41] J. Crine, "Electrical aging and breakdown of crosslinked polyethylene cables," in *Annual Report Conference on Electrical Insulation and Dielectric Phenomena*, pp. 23–26, IEEE, 2002.

[42] S. Ray and R. P. Cooney, "Chapter 9 - thermal degradation of polymer and polymer composites," in *Handbook of Environmental Degradation of Materials*, pp. 185–206, Norwich, NY, USA: William Andrew, 3rd ed. ed., 2018.

[43] C. Dang, J.-L. Parpal, and J.-P. Crine, "Electrical aging of extruded dielectric cables," *IEEE Transactions on Dielectrics and Electrical Insulation*, vol. 3, no. 2, pp. 237–247, 1996.

[44] J.-L. Parpal, J.-P. Crine, and C. Dang, "Electrical aging of extruded dielectric cables. a physical model," *IEEE Transactions on Dielectrics and Electrical Insulation*, vol. 4, no. 2, pp. 197–209, 1997.

[45] S. B. Vardeman, *Statistics for engineering problem solving*. Boston: PWS Pub. Co., c1994.

[46] P. Muller, "Glossary of terms used in physical organic chemistry (IUPAC recommendations 1994)," *Pure and Applied Chemistry*, vol. 66, no. 5, pp. 1077–1184, 1994-01-1.

[47] K. J. Laidler, "A glossary of terms used in chemical kinetics, including reaction dynamics (IUPAC recommendations 1996)," *Pure and Applied Chemistry*, vol. 68, no. 1, pp. 149–192, 1996-01-1.

[48] T. S. Ramu, *Diagnostic Testing and Life Estimation of Power Equipment*. New Delhi, India: New Age Science, 2nd ed. ed., 2009.

[49] W. Nelson, "Graphical analysis of accelerated life test data with the inverse power law model," *IEEE Transactions on Reliability*, vol. R-21, no. 1, pp. 2–11, 1972.

[50] L. Simoni, "A new approach to the voltage-endurance test on electrical insulation," *IEEE Transactions on Electrical Insulation*, vol. EI-8, no. 3, pp. 76–86, 1973.

[51] G. Bahder, T. Garrity, M. Sosnowski, R. Eaton, and C. Katz, "Physical model of electric aging and breakdown of extruded polymeric insulated power cables," *IEEE Transactions on Power Apparatus and Systems*, vol. PAS-101, no. 6, pp. 1379–1390, 1982.

[52] T. W. Dakin, "Electrical insulation deterioration treated as a chemical rate phenomenon," *Transactions of the American Institute of Electrical Engineers*, vol. 67, no. 1, pp. 113–122, 1948.

[53] T. W. Dakin and S. A. Studniarz, "The voltage endurance of cast epoxy resins," in *1978 IEEE International Conference on Electrical Insulation*, (Philadelphia, PA, USA), pp. 216–221, IEEE, 1978.

[54] T. Hibma and H. R. Zeller, "Direct measurement of space-charge injection from a needle electrode into dielectrics," *Journal of Applied Physics*, vol. 59, no. 5, pp. 1614–1620, 1986.

[55] J.-P. Crine, "Comparison between Lewis and Crine models for the electrical aging of dielectric polymers," in *1999 Annual Report Conference on Electrical Insulation and Dielectric Phenomena (Cat. No.99CH36319)*, (Austin, TX, USA), pp. 508–511, IEEE, 1999.

[56] J. Crine, "A molecular model for the electrical aging of XLPE," in *2007 Annual Report - Conference on Electrical Insulation and Dielectric Phenomena*, (Vancouver, BC, Canada), pp. 608–610, IEEE, 2007.

[57] J.-P. Crine, "Cable life predictions from breakdown and accelerated aging tests," in *2009 IEEE Electrical Insulation Conference*, (Montreal, Canada), pp. 435–438, IEEE, 2009.

[58] G. Wypych, *Handbook of Polymers*. Toronto, Canada: ChemTec Publishing, 2nd ed. ed., 2016.

[59] J. S. Bergstrom, *Mechanics of Solid Polymers*. Amsterdam, Netherlands: Elsevier Science & Technology Books, 1st ed. ed., 2015.

[60] S. N. Zhurkov, V. A. Zakrevskyi, V. E. Korsukov, and V. S. Kuksenko, "Mechanism of submicrocrack generation in stressed polymers," *Journal of Polymer Science Part A-2: Polymer Physics*, vol. 10, no. 8, pp. 1509–1520, 1972.

[61] G. Bahder, M. Sosnowski, C. Katz, R. Eaton, and K. Kleinr, "Electrical breakdown characteristics and testing of high voltage XLPE and EPR insulated cables," *IEEE Transactions on Power Apparatus and Systems*, vol. PAS-102, no. 7, pp. 2173–2185, 1983.

[62] G. Montanari and L. Simoni, "Aging phenomenology and modeling," *IEEE Transactions on Electrical Insulation*, vol. 28, no. 5, pp. 755–776, 1993.

[63] J. C. L. Hageman, G. A. de Wijs, R. A. de Groot, and R. J. Meier, "Bond scission in a perfect polyethylene chain and the consequences for the ultimate strength," *Macromolecules*, vol. 33, no. 24, pp. 9098–9108, 2000.

[64] L. Simoni, "General equation of the decline in the electric strength for combined thermal and electrical stresses," *IEEE Transactions on Electrical Insulation*, vol. EI-19, no. 1, pp. 45–52, 1984.

[65] L. Simoni, G. Mazzanti, G. Montanari, and L. Lefebre, "A general multi-stress life model for insulating materials with or without evidence for thresholds," *IEEE Transactions on Electrical Insulation*, vol. 28, no. 3, pp. 349–364, 1993.

[66] W. Standring and R. Hughes, "Breakdown under impulse voltages of solid and liquid dielectrics in combination," *Proceedings of the IEE Part A: Power Engineering*, vol. 103, no. 12, pp. 583–597, 1956.

[67] P. Sun, W. Sima, X. Jiang, D. Zhang, J. He, and L. Ye, "Review of accumulative failure of winding insulation subjected to repetitive impulse voltages," *High Voltage*, vol. 4, no. 1, pp. 1–11, 2019.

[68] W. Yin, "Failure mechanism of winding insulations in inverter-fed motors," *IEEE Electrical Insulation Magazine*, vol. 13, no. 6, pp. 18–23, 1997.

[69] P. Bidan, T. Lebey, G. Montseny, and J. Saint-Michel, "Transient voltage distribution in inverter fed motor windings," *IEEE Transactions on Power Electronics*, vol. 16, no. 1, pp. 92–100, 2001.

[70] B. Gao, G. Wu, J. He, and K. Lei, "Investigation on aging mechanism of winding insulation used in inverter-fed traction motors," in *2007 Annual Report - Conference on Electrical Insulation and Dielectric Phenomena*, (Vancouver, Canada), pp. 107–111, IEEE, 2007.

[71] A. Cavallini, D. Fabiani, H. Hiroshi, N. Masayuki, H. Joachim, L. June-Ho, S. Greg, S. Howard, D. John, C. A. Batista, E. Fermin, C. Albert, D. J. Park, and H. Yamashita, *Insulation degradation under fast, repetitive voltage pulses*. Paris, France: CIGRE, 2017.

[72] T. Guillod, R. Farber, F. Krismer, C. M. Franck, and J. W. Kolar, "Computation and analysis of dielectric losses in MV power electronic converter insulation," in *2016 IEEE Energy Conversion Congress and Exposition (ECCE)*, (Milwaukee, USA), pp. 1–8, IEEE, 2016.

[73] S. Fujita, N. Hosokawa, and Y. Shibuya, "Experimental investigation of high frequency voltage oscillation in transformer windings," *IEEE Transactions on Power Delivery*, vol. 13, no. 4, pp. 1201–1207, 1998.

[74] Y. Shibuya, K. Wada, and H. Muto, "Analysis of high-frequency oscillations in voltage transformers," *Electrical Engineering in Japan*, vol. 163, no. 1, pp. 8–15, 2008-04-15.

[75] L. Ming, F. Sahlen, S. Halen, G. Brosig, and L. Palmqvist, "Impacts of high-frequency voltage on cable-terminations with resistive stressgrading," in *Proceedings of the 2004 IEEE International Conference on Solid Dielectrics*, (Toulouse, France), pp. 300–303, IEEE, 2004.

[76] F. Espino-Cortes, S. Jayaram, and E. Cherney, "Stress grading materials for cable terminations under fast-rise time pulses," *IEEE Transactions on Dielectrics and Electrical Insulation*, vol. 13, no. 2, pp. 430–435, 2006.

[77] J. Bellomo, P. Castelan, and T. Lebey, "The effect of pulsed voltages on dielectric material properties," *IEEE Transactions on Dielectrics and Electrical Insulation*, vol. 6, no. 1, pp. 20–26, 1999.

[78] H. Ren, Y. Tanaka, H. Miyake, K. Endo, Q. Li, H. Gao, C. Li, and Z. Wang, "Research on the effect of unipolar pulse wave voltage on space charge characteristics for high-frequency equipment insulation," *IEEE Transactions on Dielectrics and Electrical Insulation*, vol. 28, no. 1, pp. 150–157, 2021.

[79] R. Färber, "Endurance of polymeric insulation under mixed-frequency medium-voltage stresses," 2019.

[80] R. Färber, T. Guillod, F. Krismer, J. Kolar, and C. Franck, "Endurance of polymeric insulation foil exposed to DC-biased medium-frequency rectangular pulse voltage stress," *Energies*, vol. 13, no. 1, pp. 1–17, 2020.

[81] K. Niayesh and E. Gockenbach, "On the aging mechanism of solid insulating materials exposed to repetitive high voltage pulses," *IEEE Transactions on Dielectrics and Electrical Insulation*, vol. 21, no. 1, pp. 304–310, 2014.

[82] J. Luszcz, "Motor cable influence on the conducted EMI emission of the converter fed AC motor drive," in *Electromagnetic Interference Issues in Power Electronics and Power Systems*, pp. 77–95, Sharjah, UAE: Bentham Science Publishers, 1st ed. ed., 2011.

[83] B. Sonerud, T. Bengtsson, J. Blennow, and S. Gubanski, "Dielectric heating in insulating materials subjected to voltage waveforms with high harmonic content," *IEEE Transactions on Dielectrics and Electrical Insulation*, vol. 16, no. 4, pp. 926–933, 2009.

[84] U. Patel, S. H. Jayaram, A. El-Hag, and R. Seetahpathy, "MV cable termination failure assessment in the context of increased use of power electronics," in *2011 Electrical Insulation Conference (EIC)*, (Annapolis, USA), pp. 418–422, IEEE, 2011.

[85] Y. O. Shaker, A. H. El-Hag, U. Patel, and S. H. Jayaram, "Thermal modeling of medium voltage cable terminations under square pulses," *IEEE Transactions on Dielectrics and Electrical Insulation*, vol. 21, no. 3, pp. 932–939, 2014.

[86] S. S. Bamji, A. T. Bulinski, and R. J. Densley, "Evidence of near-ultraviolet emission during electrical-tree initiation in polyethylene," *Journal of Applied Physics*, vol. 61, no. 2, pp. 694–699, 1987-01-15.

[87] T. Lebey and C. Laurent, "Charge injection and electroluminescence as a prelude to dielectric breakdown," *Journal of Applied Physics*, vol. 68, no. 1, pp. 275–282, 1990.

[88] H. R. Zeller and W. R. Schneider, "Electrofracture mechanics of dielectric aging," *Journal of Applied Physics*, vol. 56, no. 2, pp. 455–459, 1984-07-15.

[89] G. Stone, R. V. Heeswijk, and R. Bartnikas, "Electroluminescence in epoxy insulation," *IEEE Transactions on Electrical Insulation*, vol. 27, no. 2, pp. 221–232, 1992.

[90] G. Stone, R. V. Heeswijk, and R. Bartnikas, "Electrical aging and electroluminescence in epoxy under repetitive voltage surges," *IEEE Transactions on Electrical Insulation*, vol. 27, no. 2, pp. 233–244, 1992.

[91] D. Konig, N. Hardt, and V. Scherb, "Comparitive insulation tests with DC and AC at 50 Hz and 50 kHz," in *1998 Annual Report Conference on Electrical Insulation and Dielectric Phenomena (Cat. No.98CH36257)*, (Atlanta, USA), pp. 702–705, IEEE, 1998.

[92] M. G. Niasar and W. Zhao, "Aging of oil-impregnated paper at different frequencies," in *2021 IEEE International Conference on the Properties and Applications of Dielectric Materials (ICPADM)*, (Johor Bahru, Malaysia), pp. 430–433, IEEE, 2021-7-12.

[93] Q. Dai, Y. Liu, and G. Cheng, "The mathematical model of dissipation factor with temperature–frequency effect for oil-impregnated paper bushings," *AIP Advances*, vol. 10, no. 11, pp. 1–7, 2020-11-01.

[94] L. Niemeyer, "A generalized approach to partial discharge modeling," *IEEE Transactions on Dielectrics and Electrical Insulation*, vol. 2, no. 4, pp. 510–528, 1995.

[95] F. Gutfleisch and L. Niemeyer, "Measurement and simulation of PD in epoxy voids," *IEEE Transactions on Dielectrics and Electrical Insulation*, vol. 2, no. 5, pp. 729–743, 1995.

[96] W. A. Thue, *Electrical power cable engineering.* Boca Raton, USA: CRC Press LLC, 2nd ed. ed., 2003.

[97] C. Pan, G. Chen, J. Tang, and K. Wu, "Numerical modeling of partial discharges in a solid dielectric-bounded cavity," *IEEE Transactions on Dielectrics and Electrical Insulation*, vol. 26, no. 3, pp. 981–1000, 2019.

[98] A. Gemant and W. Phililppoff, "Die Funkenstrecke mit Vorkondensator," *Zeitschrift für technische Physik*, vol. 13, no. 9, pp. 425–430, 1932.

[99] I. McAllister, "Electric field theory and the fallacy of void capacitance," *IEEE Transactions on Electrical Insulation*, vol. 26, no. 3, pp. 458–459, 1991.

[100] T. S. Negm, M. Refaey, and A. A. Hossam-Eldin, "Modeling and simulation of internal partial discharges in solid dielectrics under variable applied frequencies," in *2016 Eighteenth International Middle East Power Systems Conference (MEPCON)*, (Cairo, Egypt), pp. 639–644, IEEE, 2016.

[101] K. Wu, C. Pan, Y. Meng, and Y. Cheng, "Dynamic behavior of surface charge distribution during partial discharge sequences," *IEEE Transactions on Dielectrics and Electrical Insulation*, vol. 20, no. 2, pp. 612–619, 2013.

[102] H. Illias, M. Tunio, A. Bakar, H. Mokhlis, and G. Chen, "Partial discharge phenomena within an artificial void in cable insulation geometry," *IEEE Transactions on Dielectrics and Electrical Insulation*, vol. 23, no. 1, pp. 451–459, 2016.

[103] H. A. Illias, G. Chen, and P. L. Lewin, "The influence of spherical cavity surface charge distribution on the sequence of partial discharge events," *Journal of Physics D: Applied Physics*, vol. 44, no. 24, pp. 1–15, 2011-06-22.

[104] H. A. Illias, "Measurement and simulation of partial discharges within a spherical cavity in a solid dielectric material," 2011.

[105] C. Forssen and H. Edin, "Partial discharges in a cavity at variable applied frequency part 2," *IEEE Transactions on Dielectrics and Electrical Insulation*, vol. 15, no. 6, pp. 1610–1616, 2008.

[106] H. A. Illias, G. Chen, A. H. A. Bakar, H. Mokhlis, and M. A. Tunio, "Partial discharges within two spherical voids in an epoxy resin," *Journal of Physics D: Applied Physics*, vol. 46, no. 33, pp. 1–10, 2013-08-21.

[107] O. E. Gouda, A. A. ElFarskoury, A. R. Elsinnary, and A. A. Farag, "Investigating the effect of cavity size within medium-voltage power cable on partial discharge behaviour," *IET Generation, Transmission & Distribution*, vol. 12, no. 5, pp. 1190–1197, 2018.

[108] A. Villa, L. Barbieri, M. Gondola, A. R. Leon-Garzon, and R. Malgesini, "A PDE-based partial discharge simulator," *Journal of Computational Physics*, vol. 345, pp. 687–705, 2017.

[109] P. Romano, G. Presti, A. Imburgia, and R. Candela, "A new approach to partial discharge detection under DC voltage," *IEEE Electrical Insulation Magazine*, vol. 34, no. 4, pp. 32–41, 2018.

[110] P. Romano, A. Parastar, A. Imburgia, J. Blennow, M. Bongiorno, A. D. Tommaso, T. Hammarstrom, and Y. Serdyuk, "Partial discharge measurements under DC voltages containing harmonics produced by power electronic devices," in *2018 IEEE Conference on Electrical Insulation and Dielectric Phenomena (CEIDP)*, (Cancun, Mexico), pp. 558–561, IEEE, 2018.

[111] B. Du, G. F. Zhao, Z. L. Li, and C. L. Han, "Effects of harmonic component on electrical tree in EPDM for HVDC cable accessories insulation," *IEEE Transactions on Dielectrics and Electrical Insulation*, vol. 28, no. 2, pp. 578–585, 2021.

[112] P. Romano, A. Imburgia, G. Rizzo, G. Ala, and R. Candela, "A new approach to partial discharge detection under dc voltage," *IEEE Electrical Insulation Magazine*, vol. 37, no. 2, pp. 18–32, 2021.

[113] M. A. Fard, A. J. Reid, and D. M. Hepburn, "Analysis of HVDC superimposed harmonic voltage effects on partial discharge behavior in solid dielectric media," *IEEE Transactions on Dielectrics and Electrical Insulation*, vol. 24, no. 1, pp. 7–16, 2017.

[114] M. Florkowski, M. Kuniewski, and P. Zydron, "Partial discharges in HVDC insulation with superimposed AC harmonics," *IEEE Transactions on Dielectrics and Electrical Insulation*, vol. 27, no. 6, pp. 1906–1914, 2020.

[115] D. Kaneko, T. Maeda, T. Ito, Y. Ohki, T. Konishi, Y. Nakamichi, and M. Okashita, "Role of number of consecutive voltage zero-crossings in propagation of water trees in polyethylene," *IEEE Transactions on Dielectrics and Electrical Insulation*, vol. 11, no. 4, pp. 708–714, 2004.

[116] M. Ghassemi, "Accelerated insulation aging due to fast, repetitive voltages," *IEEE Transactions on Dielectrics and Electrical Insulation*, vol. 26, no. 5, pp. 1558–1568, 2019.

[117] T. J. A. Hammarstrom, "Combination of adjustable inverter level and voltage rise time for electrical stress reduction in PWM driven motor windings," *IEEE Electrical Insulation Magazine*, vol. 37, no. 1, pp. 17–26, 2021.

[118] M. Florkowski, P. Blaszczyk, and P. Klimczak, "Partial discharges in insulation systems subjected to multilevel converters," in *2016 IEEE International Power Modulator and High Voltage Conference (IPMHVC)*, (San Francisco, USA), pp. 320–324, IEEE, 2016.

[119] L. Benmamas, P. Teste, E. Odic, G. Krebs, and T. Hamiti, "Contribution to the analysis of PWM inverter parameters influence on the partial discharge inception voltage," *IEEE Transactions on Dielectrics and Electrical Insulation*, vol. 26, no. 1, pp. 146–152, 2019.

[120] P. Wang, H. Xu, J. Wang, W. Wang, and A. Cavallini, "Effect of repetitive impulsive voltage duty cycle on partial discharge features and insulation endurance of enameled wires for inverter-fed low voltage machines," *IEEE Transactions on Dielectrics and Electrical Insulation*, vol. 24, no. 4, pp. 2123–2131, 2017.

[121] M. Kaufhold, H. Aninger, M. Berth, J. Speck, and M. Eberhardt, "Electrical stress and failure mechanism of the winding insulation in PWM-inverter-fed low-voltage induction motors," *IEEE Transactions on Industrial Electronics*, vol. 47, no. 2, pp. 396–402, 2000.

[122] E. Lindell, T. Bengtsson, J. Blennow, and S. Gubanski, "Influence of rise time on partial discharge extinction voltage at semi-square voltage waveforms," *IEEE Transactions on Dielectrics and Electrical Insulation*, vol. 17, no. 1, pp. 141–148, 2010.

[123] G. C. Stone and I. Culbert, "Review of stator insulation problems in medium voltage motors fed from voltage source PWM drives," in *Proceedings of 2014 International Symposium on Electrical Insulating Materials*, (Niigata, Japan), pp. 50–53, IEEE, 2014.

[124] T. J. A. Hammarstrom, "Partial discharge characteristics of electrical treeing in XLPE insulation utilizing multi level PWM waveforms," in *2019 22nd International Conference on Electrical Machines and Systems (ICEMS)*, (Harbin, China), pp. 1–6, IEEE, 2019.

[125] T. Koltunowicz, A. Cavallini, D. Djairam, G. C. Montanari, and J. Smit, "The influence of square voltage waveforms on transformer insulation break down voltage," in *2011 Annual Report Con-*

ference on Electrical Insulation and Dielectric Phenomena, (Cancun, Mexico), pp. 48–51, IEEE, 2011.

[126] B. Florkowska, M. Florkowski, and P. Zydron, "The role of harmonic components on partial discharge mechanism and degradation processes in epoxy resin insulation," in *2007 IEEE International Conference on Solid Dielectrics*, (Winchester, UK), pp. 560–563, IEEE, 2007.

[127] M. Florkowski, B. Florkowska, and P. Zydron, "Influence of high voltage harmonics on partial discharge patterns modulation," in *2014 ICHVE International Conference on High Voltage Engineering and Application*, (Poznan, Poland), pp. 1–4, IEEE, 2014.

[128] M. Florkowski, B. Florkowska, J. Furgal, and P. Zydron, "Impact of high voltage harmonics on interpretation of partial discharge patterns," *IEEE Transactions on Dielectrics and Electrical Insulation*, vol. 20, no. 6, pp. 2009–2016, 2013.

[129] L. Cao and S. Grzybowski, "Accelerated aging study on 15 kV XLPE and EPR cables insulation caused by switching impulses," *IEEE Transactions on Dielectrics and Electrical Insulation*, vol. 22, no. 5, pp. 2809–2817, 2015.

[130] J. Wu, A. R. Mor, and J. J. Smit, "The effects of superimposed impulse transients on partial discharge in XLPE cable joint," *International Journal of Electrical Power & Energy Systems*, vol. 110, pp. 497–509, 2019.

[131] J. Wu, A. R. Mor, and J. J. Smit, "Partial discharges activated by impulses and superimposed voltages in a high voltage cable model," *International Journal of Electrical Power & Energy Systems*, vol. 120, pp. 1–11, 2020.

[132] J. Wu, A. R. Mor, P. V. van Nes, and J. J. Smit, "Measuring method for partial discharges in a high voltage cable system subjected to impulse and superimposed voltage under laboratory conditions," *International Journal of Electrical Power & Energy Systems*, vol. 115, pp. 1–12, 2020.

[133] S. M. Lebedev, O. S. Gefle, and I. Y. Zakurdaev, "Usage of LLDPE for producing large-size hv polymeric insulation," in *2013 International Siberian Conference on Control and Communications (SIBCON)*, (Krasnoyarsk, Russia), pp. 1–3, IEEE, 2013.

[134] E. Peschke, R. Schroth, and R. v. Olskausen, "Extension of XLPE cables to 500 kv based on progress in technology," in *JICABLE 95, 4th International Conference on Insulated Power Cables*, (Paris), pp. 1–5, 1995.

[135] T. Andritsch, A. Vaughan, and G. C. Stevens, "Novel insulation materials for high voltage cable systems," *IEEE Electrical Insulation Magazine*, vol. 33, no. 4, pp. 27–33, 2017.

[136] X. Huang, J. Zhang, P. Jiang, and T. Tanaka, "Material progress toward recyclable insulation of power cables. part 1," *IEEE Electrical Insulation Magazine*, vol. 35, no. 5, pp. 7–19, 2019.

[137] R. E. James and Q. Su, *Condition Assessment of High Voltage Insulation in Power System Equipment*. London, United Kingdom: The Institution of Engineering and Technology, 1st ed. ed., 2008.

[138] "XLPE land cable systems, user's guide," ABB, 5th rev., 2010.

[139] J. C. Hernandez-Mejia, "Cable diagnostic focused initiative (CDFI), Chapter 6 Dissipation factor," Georgia Institute of Technology NEETRAC, Georgia, USA, 2016.

[140] K. Aljoumaa and Z. Ajji, "Mechanical and electrical properties of gamma-irradiated silane crosslinked polyethylene (si-xlpe)," *Journal of Radioanalytical and Nuclear Chemistry*, vol. 307, no. 2, pp. 1391–1399, 2016.

[141] L. Dissado, "Understanding electrical trees in solids," *IEEE Transactions on Dielectrics and Electrical Insulation*, vol. 9, no. 4, pp. 483–497, 2002.

[142] T. Tanaka and T. Imai, "Advances in nanodielectric materials over the past 50 years," *IEEE Electrical Insulation Magazine*, vol. 29, no. 1, pp. 10–23, 2013.

[143] T. Tanaka, M. Kozako, N. Fuse, and Y. Ohki, "Proposal of a multi-core model for polymer nanocomposite dielectrics," *IEEE Transactions on Dielectrics and Electrical Insulation*, vol. 12, no. 4, pp. 669–681, 2005.

[144] T. Tanaka and T. Imai, *Advanced Nanodielectrics*. Singapore: Jenny Stanford Publishing, 2017-7-6.

[145] T. Tanaka, A. Bulinski, J. Castellon, M. Frechette, S. Gubanski, J. Kindersberger, G. Montanari, M. Nagao, P. Morshuis, Y. Tanaka, S. Pelissou, A. Vaughan, Y. Ohki, C. Reed, S. Sutton, and S. Han, "Dielectric properties of XLPE/SiO2 nanocomposites based on CIGRE WG D1.24 cooperative test results," *IEEE Transactions on Dielectrics and Electrical Insulation*, vol. 18, no. 5, pp. 1482–1517, 2011.

[146] W. Lei, K. Wu, Y. Wang, Y. Cheng, X. Zheng, L. A. Dissado, S. J. Dodd, N. M. Chalashkanov, J. C. Fotherglll, C. Zhang, and W. Li, "Are nano-composites really better DC insulators? a study using silica nanoparticles in XLPE," *IEEE Transactions on Dielectrics and Electrical Insulation*, vol. 24, no. 4, pp. 2268–2270, 2017.

[147] M. Roy, J. K. Nelson, R. K. MacCrone, and L. S. Schadler, "Candidate mechanisms controlling the electrical characteristics of silica/XLPE nanodielectrics," *Journal of Materials Science*, vol. 42, no. 11, pp. 3789–3799, 2007.

[148] T. Tanaka, A. Nose, Y. Ohki, and Y. Murata, "PD resistance evaluation of LDPE/MgO nanocomposite by a rod-to-plane electrode system," in *2006 IEEE 8th International Conference on Properties and applications of Dielectric Materials*, (Bali, Indonesia), pp. 319–322, IEEE, 2006.

[149] M. Nagao, S. Watanabe, Y. Murakami, Y. Murata, Y. Sekiguchi, and M. Goshowaki, "Water tree retardation of MgO/LDPE and MgO/XLPE nanocomposites," in *2008 International Symposium on Electrical Insulating Materials (ISEIM 2008)*, (Yokkaichi, Japan), pp. 483–486, IEEE, 2008.

[150] A. Paramane, X. Chen, C. Dai, H. Guan, L. Yu, and Y. Tanaka, "Electrical insulation performance of cross-linked polyethylene/MgO nanocomposite material for ±320-kV high-voltage direct-current cables," *Polymer Composites*, vol. 41, no. 5, pp. 1936–1949, 2020.

[151] S. Wang, P. Chen, S. Yu, P. Zhang, J. Li, and S. Li, "Nanoparticle dispersion and distribution in XLPE and the related DC insulation performance," *IEEE Transactions on Dielectrics and Electrical Insulation*, vol. 25, no. 6, pp. 2349–2357, 2018.

[152] Y.-J. Park, J.-Y. Sim, K.-J. Lim, J.-H. Nam, and W.-G. Park, "Electrical conduction of a XLPE nanocomposite," *Journal of the Korean Physical Society*, vol. 65, no. 2, pp. 248–252, 2014.

[153] D. Boxue, "Trap property and charge transmission in PE," in *Electrical Insulation Breakdown and Its Theory, Process, and Prevention*, pp. 129–155, Tianjin University, China: IGI Global, 2020.

[154] C. Watanabe, Y. Itou, H. Sasaki, Y. Murata, M. Suizu, M. Sakamaki, M. Watanabe, and S. Katakai, "Practical application of ±250-kV DC-XLPE cable for hokkaido-honshu HVDC link," *Electrical Engineering in Japan*, vol. 191, no. 3, pp. 18–31, 2015.

[155] M. Knenicky, "Impact of high-frequency voltage distortion on medium voltage cable systems," 2020.

[156] G. Mazzanti and G. Montanari, "A comparison between XLPE and EPR as insulating materials for HV cables," *IEEE Transactions on Power Delivery*, vol. 12, no. 1, pp. 15–28, 1997.

[157] H. Sarma, E. Cometa, and J. Densley, "Accelerated ageing tests on polymeric cables using water-filled tanks - a critical review," *IEEE Electrical Insulation Magazine*, vol. 18, no. 2, pp. 15–26, 2002.

[158] S. Nikolajevic, "The behavior of water in XLPE and EPR cables and its influence on the electric characteristics of insulation," *IEEE Transactions on Power Delivery*, vol. 14, no. 1, pp. 39–45, 1999.

[159] Y. Okazaki, M. Kozako, M. Hikita, and T. Tanaka, "Effects of addition of nano-scale alumina and silica fillers on thermal conductivity and dielectric strength of epoxy / alumina microcomposites," in *2010 10th IEEE International Conference on Solid Dielectrics*, (Potsdam, Germany), pp. 1–4, IEEE, 2010.

[160] A. M. Nobrega, M. L. B. Martinez, and A. A. A. de Queiroz, "Investigation and analysis of electrical aging of XLPE insulation for medium voltage covered conductors manufactured in Brazil," *IEEE Transactions on Dielectrics and Electrical Insulation*, vol. 20, no. 2, pp. 628–640, 2013.

[161] C. Unger, K. Kruger, M. Sonnenschein, and R. Zurowski, "Disturbances due to voltage distortion in the kHz range-experiences and mitigation measures," in *18th International Conference and Exhibition on Electricity Distribution (CIRED 2005)*, (Turin, Italy), pp. v2–23–v2–23, IEE, 2005.